Electronic and Impurity Doping in Colloidal Semiconductor Nanocrystals

Alina Marie Schimpf

A dissertation

submitted in partial fulfillment of the

requirements for the degree of

Doctor of Philosophy

University of Washington

2014

Reading Committee:

Daniel R. Gamelin, chair

Brandi M. Cossairt

Xiaosong Li

David J. Masiello

Program authorized to offer degree:

Department of Chemistry

University of Washington

Abstract

Electronic and Impurity Doping in Colloidal Semiconductor Nanocrystals

Alina Marie Schimpf

Chair of the Supervisory Committee:
Professor Daniel R. Gamelin
Department of Chemistry

This thesis presents investigations of semiconductor nanocrystals doped with impurity ions, excess charge carriers, or both. The introduction of excess charge carriers into colloidal semiconductor nanocrystals constitutes a longstanding challenge in the development of nanocrystal building blocks for various technologies including solar cells, photovoltaic devices and electroluminescent devices. Chapter 1 discusses methods for electronic doping in semiconductor nanocrystals, focusing on photodoping and aliovent doping strategies. Of the various successful strategies for electronic doping, photodoping is particularly useful as a post-synthetic method for reversible and quantifiable tuning of carrier density. Alternatively, aliovalently doped nanocrystals are attractive due to the great stability of charge carriers.

Chapter 2 presents a comparative study of conduction-band electrons in colloidal ZnO nanocrystals added via photodoping or aliovalent doping. The studies show that, although they have very similar spectroscopic properties, the reactivites of the electrons are vastly different, owing to the relative mobilities of their charge-compensating cations. Chapters 3, 4 and 5 present

investigations of the ability to add excess electrons to a variety of systems via photodoping. The study in Chapter 3 shows that the maximum number of elecrons that may be added photochemically is dependent on the nanocrystal volume, such that all nanocrystals may be photodoped to the same electron density. Furthermore, the identities of the sacrifical reductant and the charge-compensating cation determine the maximum photodoping density. For the first time, alkyl borohydrides were used as sacrificial reductants to photodope ZnO, leading to much larger carrier densities than previously observed. These findings informed the first demonstration of photodoping in CdE (E= S, Se, Te) nanocrystals, presented in Chapter 4. Chapter 5 presents a combination of photodoping and aliovalent doping in In_2O_3 nanocrystals to investigate the redox chemistries in In_2O_3 and ITO nanocrystals. The study shows that all nanocrystals have the same Fermi level, and Sn^{4+} stabilizes that conduction band to allow accumulation of excess delocalized electrons. Moreover, regardless of Sn^{4+} doping and therefore of initial carrier density, all nanocrystals have the same number of electrons that may be added photochemically. These results, in conjunction with those presented in Chapters 3 and 4, suggest maximum photodoping density is thermodynamically limited, and is not an intrinsic property of the nanocrystal, nor a result of competition between productive hole-quenching and non-productive Auger recombination in the photoexcited nanocrystals.

The ability to reversibly tune the carrier densities in colloidal semiconductor nanocrystals via photodoping allows new photophsyical investigations of electronically doped systems. Chapters 5 and 6 use photodoping to investigate the properties of plasmon resonances in ZnO and In_2O_3 nanocrystals. Chapter 5 shows that the plasmon energy is affected by both carrier density and Sn^{4+} doping. Chapter 6 shows that plasmons in ZnO nanocrystals are subject to quantum confinement and therefore may not be understood with a classical Drude picture.

The large magnetic exchange interaction between charge carriers and magnetic dopants make diluted magnetic semiconductors (DMSs) particularly attractive for spin-based information processing. Chapter 7 uses pulsed electron paramagnetic resonance (pEPR) spectroscopy to investigate the affect of excess electrons on the Mn^{2+} spin dynamics in doped ZnO nancorystals, showing that Mn^{2+} spin relaxation is greatly accelerated by the presence of even one conduction-band electron. Chapter 8 uses pEPR to investigate the intrinsic spin dynamics of Mn^{2+} in a variety of II-VI colloidal semiconductor nanocrystals. Finally, Chapter 9 shows the ability to tune the effective *g* value in DMSs at low fields using temperature.

For Jesse

Acknowledgements

The order in which people are mentioned is dictated largely by story-flow, and is not intended as a reflection of my relative level of gratefulness.

I must start by thanking Prof. Daniel Gamelin, as he is the one who truly made this work possible. I continue to be amazed by Daniel's ability to bring together knowledge from a wide range of topics and use this to generate new ideas. This way of thinking has shaped me as a scientist and is one that I will always strive to emulate throughout the rest of my career. I am grateful for Daniel's excellent mentorship, as well as his willingness to let me try my own ideas. I am also grateful for his promotion of a good lab dynamic. From weekly, post-group-meeting Big Time outings to the Moisture Festival to lab hikes, Daniel encouraged the lab members to be friends in addition to colleagues.

I have many coworkers to thank for their contributions to my scientific efforts, but perhaps even more so for their roles as friends, confidants, role models, and overall fun people. Especially during the last few months, when a large portion of my time was spent writing at my desk, the co-habitants of the CHB 212 office were crucial for keeping the days enjoyable and productive. I am particularly grateful for my many coffee breaks, library runs and good laughs with Michael De Siena. I have had many great conversations and fun times with Troy Kilburn and Heidi Nelson. I also look forward to getting to know the newest inhabitants, Jose Araujo and Kira Hughes.

Kimberly Hartstein has been especially supportive, as both a friend and coworker. I am so lucky to sit only a few feet away from someone with whom I can turn around and share every idea that pops into my head. Kimberly was brave enough to take on the daunting fields of semiconductor plasmons and magnetism and it has been exciting to work with her and watch her grow as a scientist. I am happy to move on knowing that she will be taking over many of my unfinished ideas.

Outside of my office-mates, a number of coworkers have helped me along the way. Liam Bradshaw, who started and finished grad school with me, could always be relied upon, whether for help with instruments or for a much-needed post-lab beer and chat. During the last couple months of graduate school, I had the opportunity to work with Mike Carroll, who has brought exciting new ideas and a great skillset to the world of photodoping. I am excited for the new discoveries that will be made in photodoping as he finishes his graduate studies. I want to thank Charlie Barrows and Emily McLaurin, who could always be relied upon for help with nanocrystal synthesis questions. Although I had very little overlap with them scientifically, they became close friends and are people I admire for their strength of character. I also want to acknowledge Kathryn Knowles and Emily Tsui, who are incredible scientists and role models. I am grateful for the advice they gave me when I was searching for postdoc positions and putting together my thesis defense. I hope to follow in their footsteps as I move forward in my scientific career.

Much of my thesis work would not have been possible without the efforts of my incredible undergraduate researchers, Carolyn Gunthardt and Xing Yee Gan. I am grateful for their endless hard work and their willingness to sometimes just trust me. I am equally grateful for their friendship. Carolyn was supportive during some of the most frustrating times of graduate school, and remains one of my best friends. Xing Yee has been a reliable friend and amazing roommate during the latter part of my graduate school career. I am excited for both of them as they prepare for their graduate school careers.

A number of my studies were made possible by various collaborations. Prof. Delia Milliron and Raffaella Buonsanti provided me with a great opportunity to experience working at Lawrence

Berkeley Lab. In addition to the great experience of working at a national lab, many fruitful discussions and studies came from my interactions with Delia and Raffa. I have also had many wonderful in-house collaborations. Prof. David Masiello and Niket Thakkar gave us new insights into semiconductor plasmons. I am grateful that I was able to work with them while Daniel was abroad, almost as if I had a secondary advisor. Prof. Xiaosong Li, Joseph May and Joshua Goings offered wisdom I many areas of nanocrystal electronic structure that enlightened experimental results. Prof. Jim Mayer and Carolyn Valdez had valuable knowledge about molecular reactivity that informed new discoveries in nanocrystal reactivity. I am grateful to have had the opportunity to work closely with and learn from all of these people. These experiences were invaluable to expanding my knowledge into many different areas.

There were a number of senior graduate students and postdocs who helped me get started when I first joined the Gamelin lab. Stefan Ochsenbein taught me almost everything I know about EPR, and it was a wonderful learning experience to fill his shoes as the resident expert. It was because of following in Stefan's footsteps that I initially got involved in photodoping, which ended up defining the majority of my graduate career. During my very first months in the lab, I learned nearly all of my synthetic and spectroscopic techniques from Vlad Vlaskin and Alicia Cohn. As I started to have my own direction, I had great scientific conversations with and gained a lot of inspiration from Jillian Dempsey, Kevin Kittilstved and Rémi Beaulac. Nils Janßen was a great source of knowledge about optics as well as a great, fun-loving friend.

I can unequivocally say that I would not be where I am without the love and support of Jeff Rinehart. When Jeff started as a postdoc in our lab, I was excited to make a new friend and have someone to watch football games with. As I got to know Jeff, I became inspired by him both as a scientist and as a person. Jeff is one of the smartest, kindest and most fun people I have known. He has continuously supported me in my goals, and has done everything possible to help me accomplish them. I can rely on Jeff for anything from thoughtful scientific discussions to paper editing to emotional support. He is one of my biggest inspirations in science and beyond.

I would like to acknowledge the late Claire Chapman, who welcomed me into her home as soon as I moved to Seattle. I would also like to thank Nancy Colton, who introduced me to Claire, and whose visits to Seattle always gave me something to look forward to. The positive attitudes and endless energy of both Nancy and Claire have been inspirational.

I have mentioned many people that helped me throughout my graduate school career, but I must also thank those who helped me get there. My parents, Martin and Maya Schimpf, have lovingly pushed me and supported me for as long as I can remember, and it makes me happy to know that I have made them proud. Their success and happiness is a constant source of inspiration. Perhaps the best thing they did was to give me a younger brother, Jesse. Being almost twelve years old when he was born, I got to experience Jesse as a baby, and to watch him grow into a smart, loving, reliable young man. Even with the large separation in age, I see my brother as a close friend and confidant. He is my hero, more so than he understands.

I had a number of undergraduate professors that influenced my career path, but none more than my undergraduate research advisor, Prof. Don Warner. I had Don for organic chemistry, which I still have a soft spot for even though my research interests have taken me in a very different direction. Knowing that I was both a math and chemistry major, Don asked me to join his lab to work on a project that combined synthesis and electronic structure calculations. My experience in his lab played a major role in my decision to go to graduate school. Don's excellent mentorship extended beyond research. One of my first memories of him as an advisor is when he pushed me to apply for a Goldwater Scholarship, even though I didn't think I was good enough. I received

the scholarship, and learned a valuable lesson that sticks with me still whenever I think about applying for fellowships. I am grateful to have learned from Prof. Eric Brown, who got me interested in inorganic chemistry, and the late Prof. Jeffrey Peloquin, who got me interested in spectroscopy. I must also thank Prof. Susan Shadle for encouraging me to look into Daniel as a research advisor. Her knack for understanding the needs of students, both in the classroom and beyond, is inspirational.

Many others helped me throughout my undergraduate career. Marcy Harmer and Prof. Helen Lojek made the Dean's office a great place to be, whether for academic help or just good conversation. I would like to specifically thank Prof. Charles Hanna for teaching me to love physics. I would also like to thank Prof. Otis Kenny, Prof. Jodi Mead and Prof. Mary Jarratt Smith for teaching such great classes that I couldn't resist doing a double major in math.

Finally, I must thank everyone who supported me through my recovery from the head injury. The Departments of Chemistry and Mathematics, as well as numerous individuals at Boise State University and beyond, sent their support in the form of flowers, cards or hospital visits. Dr. Ron Jutzy supported my post-injury ambitions, no matter how difficult others told me they would be. The outpouring of support from family, friends and colleagues motivated me to get through my injury and to not let it limit me.

There are many people not specifically listed that have influenced my path to where I am now. I am grateful for all of my family and friends, who have supported me and given me many reasons to smile, and who I know will continue to do so as I begin the next chapter of my scientific career.

Table of Contents

Figures and Schemes

Abbreviations and Chemical Formulas

AZO	Aluminum-doped zinc oxide
$[BAr_F]^-$	Tetrakis(3,5-trifluoromethylphenylborate)
$[Bu_4N]^+$	Tetrabutylammonium
CB	Conduction band
$[C_{12}H_{10}]^{\bullet-}$	Biphenyl radical
$CoCp^*_2$	Decamethylcobaltocene
$CrCp^*_2$	Decamethylchromocene
CW	Continuous wave
DDA	Dodecylamine
DMS	Diluted magnetic semiconductor
DMSO	Dimethylsulfoxide
DPPH	Diphenylpicrylhydrazyl
e^-_{CB}	Conduction-band electron
ENDOR	Electron nuclear double resonance
EPR	Electron paramagnetic resonance
ESEEM	Electron spin echo envelope modulation
$[Et_3BH]^-$	Triethylborohydride
EtOAc	Ethyl acetate
EtOH, EtOD	Ethanol, deuterated ethanol
$[FeCp^*_2]^+$	Decamethylferrocenium
FTO	Fluorine-doped tin oxide
HDA	Hexadecylamine
$[H(Et_2O)_2]^+$	Diethyl ether oxonium (“Brookhart’s acid”)
h^+_{VB}	Valence-band hole
HWHM	Half width at half maximum
ICP-AES	Inductively coupled plasma detected by atomic emission spectroscopy
ICP-MS	Inductively coupled plasma detected by mass spectroscopy
In_2O_3	Indium oxide
IR	Infrared
IRF	Instrument response function

ITO	Tin-doped indium oxide
LMB	Leucomethylene blue
LSPR	Localized surface plasmon resonance
MB	Methylene blue
MCD	Magnetic circular dichroism
$[Me_2NBH_3]^-$	Dimethylaminoborohydride
$[N(C_6H_4Br\text{-}4)_3]^+$	Tris(4-bromo-phenyl)aminium hexa-chloridoantimonate (“magic blue”)
NIR	Near infrared
NMR	Nuclear magnetic resonance
$[NO]^+$	Nitrosonium
$(OAc)^-$	Acetate
ODE	Octadecene
ODPA	Octadecylphosphonic acid
pEPR	Pulsed electron paramagnetic resonance
$[PF_6]^-$	Hexafluorophosphonate
PL	Photoluminescence
PLMA	Poly(lauryl methacrylate)
PTFE	Polytetrafluoroethylene
pXRD	Powder X-ray diffraction
QD	Quantum dot
SQUID	Superconducting quantum interference device
THF	Tetrahydrofuran
TM	Transition metal
TMAH	Tetramethylammonium hydroxide pentahydrate
Tol, tol-d_8	Toluene, deuterated toluene
TOP	Tri-n-octylphosphine
TOPO	Tri-n-octylphosphine oxide
UV	Ultraviolet
VB	Valence band

Chapter 1

Introduction

1.1 Introduction to electronically doped colloidal semiconductor nanocrystals

Semiconductors that are capable of supporting band-like charge-carriers are amongst the most vital materials for current and future technological advancement of solar cell, photovoltaic, transistor, photodetector, electroluminescent and plasmonic technologies. A relatively recent class of semiconducting materials, colloidal semiconductor nanocrystals, offers the additional advantages of scalable solution-processing and size-tunable quantum properties. The introduction of excess charge carriers to colloidal semiconductor nanocrystals is often challenging, however, due to the relatively large surface area, which provides a myriad of possible localized charge states. For example, in aliovalently doped nanocrystals such as Al^{3+}-doped ZnO (AZO) or Sn^{4+}-doped In_2O_3 (ITO), only a small fraction of the dopants are compensated by excess band-like electrons, while the majority are compensated by localized charges arising from surface nonstoichiometries or even ligands.[1-4] In some cases such localized states on the surface or in the nanocrystal solution may serve to limit the number of charge carriers that may be added by pinning the Fermi level.[5] In many chalcogenide colloidal semiconductor nanocrystals such as CdSe or CdS, the introduction of a large number of excess carriers may be difficult due to the abundance of localized trap states.[6] A wide variety of successful strategies have been employed for electronic doping of semiconductor nanocrystals. include remote chemical doping[7-15] photodoping,[4,6,8,16-20] electrochemical oxidation or reduction,[13,20-27] and aliovalent[1,3,28-40] or vacancy[41-46] defect doping. This thesis will focus largely on those added photochemically. As discussed in Chapter 2, regardless of how excess carriers are added, they have analogous spectroscopic properties.[3] This section will discuss the spectroscopic

signatures required to conclusively detrmine the existence of band-like charge carriers in semiconductor nanocrystals, as well as highlight the advances in electronic doping of colloidal semiconductor nanocrystals.

1.1.1 Spectroscopic signatures of band-like charge carriers in semiconductors. To understand the spectroscopic signatures of electronic doping it is first necessary to clarify the requirements to classify a semiconductor nanocrystal as carrier-doped. Analogous to bulk semiconductor physics, *n*- or *p*-doping is defined here as the addition of delocalized electrons or holes to the conduction or valence bands, respectively. This requires the Fermi level (E_F) to be raised or lowered enough such that the conduction or valence bands may be thermally populated with electrons or holes[47] (Scheme 1.1). Mathematically, this doping regime is defined by equation 1.1, where N_e is the free-carrier density. For an intrinsic semiconductor, where E_F is in the middle of the bandgap, raising or lowering E_F slightly results in no change of N_e. It is only when E_F is near or above the conduction band that raising it changes N_e.

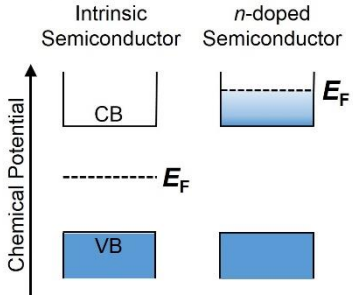

Scheme 1.1. Schematic representations of carrier-doping in semiconductor nanocrystals. An intrinsic semiconductor nanocrystal has its Fermi level (E_F) in the middle of the band gap. When E_F resides near or above the conduction-band (CB) edge, excess band-like electrons are introduced and the nanocrystal becomes *n*-type. A similar diagram applies for *p*-doping.

$$\frac{\partial N_e}{\partial E_F} \neq 0 \qquad (1.1)$$

The addition of excess charge carriers has two primary concomitant spectroscopic signatures that can be used to monitor *n*- or *p*-doping: Bleach of the band-edge absorption and appearance of new intraband absorption. Figure 1.1 illustrates these signatures for the case of photochemical electronic doping of colloidal CdSe nanocrystals (discussed in detail in Chapter 4). For Figure 1.1, d = 3.8 nm CdSe nanocrystals were doped with an average ($\langle n_e \rangle$) of 0–1 electrons per nanocrystal. Increased electron accumulation is indicated by the arrows. The addition of one conduction-band electron to a nanocrystal places E_F above the conduction band edge (Scheme1.1). With added electrons, a simultaneous bleach of the exciton absorption and appearance of new IR absorption is clearly observed (top). The lower panel plots the absorption difference ($\Delta A = A_{doped} - A_{undoped}$) at $<n_e> = 1$. When $<n_e> = 1$ is reached, the exciton absorption is 50% bleached,[15] corresponding to a 50% filling at the conduction-band edge. This is illustrated schematically by the inset. In an undoped nanocrystal (left) band-edge absorption is fully allowed. Addition of conduction-band electrons blocks the band-edge transition, leading to a bleach (middle). These conduction-band electrons can be excited to higher conduction-band levels, leading to new IR absorption. In many cases, the bleach and the IR absorption are increased even further by the accumulation of multiple electrons in the conduction band.

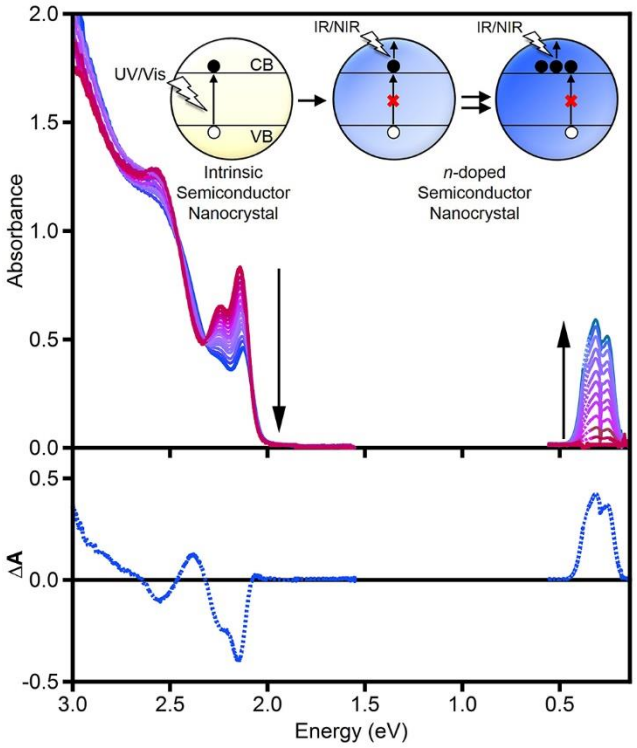

Figure 1.1. Spectroscopic signatures of excess band-like charge carriers. The addition of conduction-band electrons to CdSe nanocrystals leads to a bleach in the band-edge absorption and a new intraband absorption. The top panel plots the visible and IR absorption with various amounts of electrons. Arrows show increased electron accumulation from $\langle n_e \rangle$ = 0–1. The bottom panel plots the absorption difference ($\Delta A = A_{doped} - A_{undoped}$) at $\langle n_e \rangle$ = 1. The inset shows a schematic representation of the mechanism for these spectroscopic signatures. In undoped CdSe nanocrystals, band-gap absorption is fully allowed. As the conduction-band edge is filled, this transition is blocked, leading to a bleach. The conduction-band electrons undergo a new intraband transition. Adapted from ref. 6.

1.1.2 Photodoping of colloidal semiconductor nanocrystals. Photodoping offers distinct advantages over other methods of electronic doping because it may be done post-synthetically, is completely tunable and reversible and requires oxidants or reductants that are less harsh than those required for direct chemical oxidation or reduction. Studies presented in this thesis will focus on photochemical addition to of excess conduction-band electrons, illustrated schematically in Scheme 1.2. Above band-gap illumination of semiconductor nanocrystals

excites an electron across the band gap and, in the presence of a sacrificial reductant, or hole quencher, (ZQ), the photogenerated valence-band hole may be irreversibly reduced. This chemistry deposits conduction-band electrons and charge-compensating cations (Z^+) on the nanocrystals. In many cases, extended illumination leads to accumulation of multiple conduction-band electrons per nanocrystal (Scheme 1.2). This type of electronic doping has been demonstrated in a variety of systems,[4,6,8,16-20,48,49] and the maximum number of accumulated electrons varies depending on the identities of the semiconductor and the sacrificial reductant.[18] To date, photodoping has been used exclusively for the introduction of excess electrons. It should, in principle, also be a viable hole-doping mechanism, given an appropriate sacrificial oxidant.

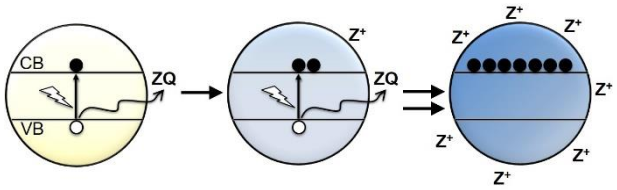

Scheme 1.2. Photochemical reduction of semiconductor nanocrystals. Above band-gap illumination promotes an electron to the conduction band (CB), leaving behind a valence-band (VB) hole. Under anaerobic conditions and in the presence of a hole quencher (ZQ), this hole may be rapidly quenched, leaving a conduction-band electron. The hole quencher deposits a cation to compensate the stranded electron. Extended illumination allows for the accumulation of multiple conduction-band electrons.

Upon exposure to air or other oxidants, photodoped electrons can be removed and the nanocrystals returned to their original oxidation state. This chemistry allows excess conduction-band electrons to be quantified via chemical titration with a mild oxidant, another distinct advantage of photochemically reduced nanocrystals. The ability to directly count the number of electrons added via photodoping is central to understanding the limitations to photochemical reduction and to evaluating the photophysical processes in these reduced systems.

A large portion of this thesis will focus on advances in the understanding of the photodoping process and on the photophysical process that can be investigated in doped semiconductor nanocrystals. Chapter 2 discusses the comparison of both reactivities and spectroscopic features of electrons added photochemically and those added by aliovalent doping. Chapters 3–5 discuss the factors that govern the ability to photodope including the identity of the hole quencher and the host nanocrystal. These studies suggest a thermodynamic limit to the number of electrons that may be added photochemically. Chapters 6 and 7 will present some of the photophysical process that may be investigated because of photodoping. First, in Chapter 6, the ability to tune and independently count excess electrons allows investigation of the plasmonic properties in ZnO nanocrystals. Second, in Chapter 7, the addition of excess electrons is used to study the spin interactions between magnetic dopants and excess carriers in $Zn_{1-x}Mn_xO$ nanocrystals.

1.1.3 Aliovalent or vacancy defect-doping in colloidal semiconductor nanocrystals. Recent advances in colloidal nanocrystal synthesis have led to a wide variety of nanocrystals that are electronically doped due to the purposeful introduction of defects. In these cases, aliovalent dopants[1,3,28-40] or vacancies[41-46] are used to generate charge carriers. This strategy is important because it has the advantage of often generating to very stable *n*- or *p*-type semiconductor nanocrystals. Aliovalent dopants or vacancies have an associated positive or negative charge that must be compensated. In many cases, these charges are compensated by localized charges such as ligands or surface defects. In some cases, however, a percentage of defect charges are compensated by excess conduction-band electrons or valence-band holes, leading to electronic doping. For example, in ITO nanocrystals Sn^{4+} cations substitute at In^{3+} sites, leading to an extra positive charge for each Sn^{4+} dopant. Some of these charges are compensated by conduction-band electrons. Although the exact chemical origin of these electrons is unclear, they must come

from oxidation of the nanocrystal precursors during synthesis. Figure 1.2a shows absorption spectra of colloidal In_2O_3 and ITO nanocrystals containing various amounts of Sn dopants.[4] With increased Sn^{4+}-doping, increased NIR absorption is clearly observed. Additionally, some bleaching of the band-edge absorption is apparent. These spectroscopic signatures are representative of the heavy *n*-type doping known to occur in ITO.

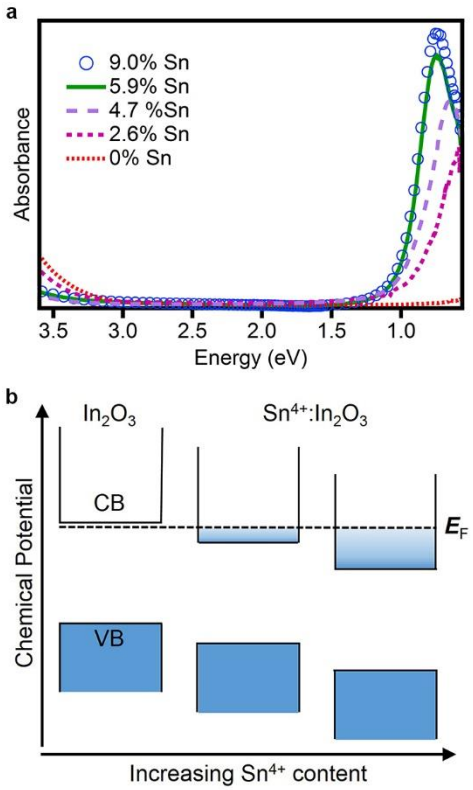

Figure 1.2. Addition of conduction-band electrons to colloidal semiconductor nanocrystals via aliovalent doping. (a) Absorption spectra show loss of band-edge absorption and increase in NIR absorption with increased Sn^{4+} incorporation. (b) Schematic representation of shift in the conduction band edge with added Sn^{4+}. Stabilization of the conduction-band edge by Sn^{4+} below E_F allows for electrons to accumulate in the conduction band. Adapted from ref. 4.

Although the recent synthetic advances have made defect-doped nanocrystals the most prevalent class of electronically doped colloidal semiconductor nanocrystals, the effects of impurity ions are not fully understood. For example, isovalent dopants such as Mg^{2+} and Cd^{2+} are known to affect the band energies of ZnO nanocrystals,[50-52] but their effect on the intraband transitions in reduced ZnO nanocrystals has not been explored. In aliovalently doped nanocrystals, it is difficult to isolate the influence of impurity ions from those off added carriers, making their effects even more complicated to investigate. Chapter 5 uses a combination of photodoping and aliovalent doping in In_2O_3 nanocrystals to separate the effects of excess electrons and added Sn^{4+} dopants on the plasmon resonances in doped semiconductor nanocrystals.

1.2 Introduction to magnetically doped semiconductor nanocrystals

Magnetically doped semiconductor nanocrystals are of great interest for the development of spin-based information technologies. Diluted magnetic semiconductors (DMSs) exhibit impressive magneto-optical phenomena owing to the strong exchange interactions between photogenerated charge carriers and localized dopants. Spintronics device structures, such as spin filters and spin light-emitting diodes, have taken advantage of these exchange interactions.[53] Although the mechanism of this interactions is well-understood, its effect on spin dynamics in DMSs is less clear. In Chapter 7, pulsed electron paramagnetic resonance spectroscopy (pEPR) is used to investigate the spin dynamics of Mn^{2+} dopants in the presence of stable conduction-band electrons in $Zn_{1-x}Mn_xO$ nanocrystals. The study suggests that the presence of excess electrons introduces new relaxation pathways in for the Mn^{2+} dopant spins. Chapter 8 uses pEPR to study the Mn^{2+} spins in the absence of excess electrons. It is demonstrated that nuclear spins

from surrounding ligand and solvent molecules also play a significant role in the spin dynamics of magnetic dopants in DMSs. Finally, in Chapter 9, exchange interactions are investigated by magnetic circular dichroism spectroscopy. In this study, temperature is used to tune and invert the field-induced excitonic splitting. The results presented in Chapters 7–9 have relevance for understanding the timescales and interaction strengths of spin dynamics in DMSs that may be useful for emerging spintronics technologies.

1.3 References

1. Wang, T.; Radovanovic, P. V. Free Electron Concentration in Colloidal Indium Tin Oxide Nanocrystals Determined by Their Size and Structure. *J. Phys. Chem. C* **2011**, *115*, 406.

2. Mendelsberg, R. J.; Garcia, G.; Li, H.; Manna, L.; Milliron, D. J. Understanding the Plasmon Resonance in Ensembles of Degenerately Doped Semiconductor Nanocrystals. *J. Phys. Chem. C* **2012**, *116*, 12226.

3. Schimpf, A. M.; Ochsenbein, S. T.; Buonsanti, R.; Milliron, D. J.; Gamelin, D. R. Comparison of Extra Electrons in Colloidal *n*-Type Al^{3+}-Doped and Photochemically Reduced ZnO Nanocrystals. *Chem. Commun.* **2012**, *48*, 9352.

4. Schimpf, A. M.; Runnerstrom, E. L.; Lounis, S. D.; Milliron, D. J.; Gamelin, D. R. Redox Energies and Plasmon Resonance Energies of Photodoped In_2O_3 and Sn-doped In_2O_3 Nanocrystals. *J. Am. Chem. Soc.* **2014**.

5. Bard, A. J.; Bocarsly, A. B.; Fan, F. R. F.; Walton, E. G.; Wrighton, M. S. The Concept of Fermi Level Pinning at Semiconductor/Liquid Junctions. Consequences for Eenergy Conversion Efficiency and Selection of Useful Solution Redox Couples in Solar Devices. *J. Am. Chem. Soc.* **1980**, *102*, 3671.

6. Rinehart, J. D.; Schimpf, A. M.; Weaver, A. L.; Cohn, A. W.; Gamelin, D. R. Photochemical Electronic Doping of Colloidal CdSe Nanocrystals. *J. Am. Chem. Soc.* **2013**, *135*, 18782.

7. Shim, M.; Guyot-Sionnest, P. *n*-Type Colloidal Semiconductor Nanocrystals. *Nature* **2000**, *407*, 981.

8. Shim, M.; Guyot-Sionnest, P. Organic-Capped ZnO nanocrystals: Synthesis and *n*-Type Character. *J. Am. Chem. Soc.* **2001**, *123*, 11651.

9. Valdez, C. N.; Braten, M.; Soria, A.; Gamelin, D. R.; Mayer, J. M. Effect of Protons on the Redox Chemistry of Colloidal Zinc Oxide Nanocrystals. *J. Am. Chem. Soc.* **2013**, *135*, 8492.

10. Koh, W.-k.; Koposov, A. Y.; Stewart, J. T.; Pal, B. N.; Robel, I.; Pietryga, J. M.; Klimov, V. I. Heavily Doped *n*-type PbSe and PbS Nanocrystals Using Ground-State Charge Transfer from Cobaltocene. *Sci. Rep.* **2013**, *3*, 2004.

11. Wheeler, L. M.; Neale, N. R.; Chen, T.; Kortshagen, U. R. Hypervalent Surface Interactions for Colloidal Stability and Doping of Silicon Nanocrystals. *Nat. Commun.* **2013**, *4*.

12. Palomaki, P. K. B.; Miller, E. M.; Neale, N. R. Control of Plasmonic and Interband Transitions in Colloidal Indium Nitride Nanocrystals. *J. Am. Chem. Soc.* **2013**, *135*, 14142.

13. Yu, D.; Wang, C.; Guyot-Sionnest, P. *n*-Type Conducting CdSe Nanocrystal Solids. *Science* **2003**, *300*, 1277.

14. Jeong, K. S.; Deng, Z.; Keuleyan, S.; Liu, H.; Guyot-Sionnest, P. Air-Stable n-Doped Colloidal HgS Quantum Dots. *J. Phys. Chem. Lett.* **2014**, *5*, 1139.

15. Shim, M.; Wang, C.; Guyot-Sionnest, P. Charge-Tunable Optical Properties in Colloidal Semiconductor Nanocrystals. *J. Phys. Chem. B* **2001**, *105*, 2369.

16. Haase, M.; Weller, H.; Henglein, A. Photochemistry and Radiation Chemistry of Colloidal Semiconductors. 23. Electron Storage on ZnO Particles and Size Quantization. *J. Phys. Chem.* **1988**, *92*, 482.

17. Liu, W. K.; Whitaker, K. M.; Kittilstved, K. R.; Gamelin, D. R. Stable Photogenerated Carriers in Magnetic Semiconductor Nanocrystals. *J. Am. Chem. Soc.* **2006**, *128*, 3910.

18. Cohn, A. W.; Schimpf, A. M.; Gunthardt, C. E.; Gamelin, D. R. Size-Dependent Trap-Assisted Auger Recombination in Semiconductor Nanocrystals. *Nano Lett.* **2013**, *13*, 1810.

19. Cohn, A. W.; Janßen, N.; Mayer, J. M.; Gamelin, D. R. Photocharging ZnO Nanocrystals: Picosecond Hole Capture, Electron Accumulation, and Auger Recombination. *J. Phys. Chem. C* **2012**, *116*, 20633.

20. Germeau, A.; Roest, A. L.; Vanmaekelbergh, D.; Allan, G.; Delerue, C.; Meulenkamp, E. A. Optical Transitions in Artificial Ffew-Electron Atoms Strongly Confined Inside ZnO Nanocrystals. *Phys. Rev. Lett.* **2003**, *90*, 097401.

21. Wang, C. J.; Shim, M.; Guyot-Sionnest, P. Electrochromic Nanocrystal Quantum Dots. *Science* **2001**, *291*, 2390.

22. Roest, A. L.; Kelly, J. J.; Vanmaekelbergh, D.; Meulenkamp, E. A. Staircase in the Electron Mobility of a ZnO Quantum Dot Assembly due to Shell Filling. *Phys. Rev. Lett.* **2002**, *89*, 036801.

23. Wehrenberg, B. L.; Guyot-Sionnest, P. Electron and Hole Injection in PbSe Quantum Dot Films. *J. Am. Chem. Soc.* **2003**, *125*, 7806.

24. Roest, A. L.; Houtepen, A. J.; Kelly, J. J.; Vanmaekelbergh, D. Electron-Conducting Quantum-Dot Solids with Ionic Charge Compensation. *Faraday Discuss.* **2004**, *125*, 55.

25. Guyot-Sionnest, P. Charging Colloidal Quantum Dots by Electrochemistry. *Microchim. Acta* **2008**, *160*, 309.

26. Jha, P. P.; Guyot-Sionnest, P. Photoluminescence Switching of Charged Quantum Dot Films. *J. Phys. Chem. C* **2007**, *111*, 15440.

27. Wehrenberg, B. L.; Yu, D.; Ma, J.; Guyot-Sionnest, P. Conduction in Charged PbSe Nanocrystal Films. *J. Phys. Chem. B* **2005**, *109*, 20192.

28. Hammarberg, E.; Prodi-Schwab, A.; Feldmann, C. Microwave-Assisted Polyol Synthesis of Aluminium- and Indium-Doped ZnO Nanocrystals. *J. Colloid Interf. Sci.* **2009**, *334*, 29.

29. Kanehara, M.; Koike, H.; Yoshinaga, T.; Teranishi, T. Indium Tin oxide Nanoparticles with Compositionally Tunable Surface Plasmon Resonance Frequencies in the Near-IR Region. *J. Am. Chem. Soc.* **2009**, *131*, 17736.

30. Buonsanti, R.; Llordes, A.; Aloni, S.; Helms, B.; Milliron, D. Tunable Infrared Absorption and Visible Transparency of Colloidal Aluminum-Doped Zinc Oxide Nanocrystals. *Nano Lett.* **2011**, *11*, 4706.

31. Garcia, G.; Buonsanti, R.; Runnerstrom, E. L.; Mendelsberg, R. J.; Llordes, A.; Anders, A.; Richardson, T. J.; Milliron, D. J. Dynamically Modulating the Surface Plasmon Resonance of Doped Semiconductor Nanocrystals. *Nano Lett.* **2011**, *11*, 4415.

32. Herklotz, F.; Lavrov, E. V.; Weber, J.; Mamin, G. V.; Kutin, Y. S.; Volodin, M. A.; Orlinskii, S. B. Identification of Shallow Al Donors in ZnO. *Phys. Stat. Sol. B* **2011**, *248*, 1532.

33. Chou, L. W.; Shin, N.; Sivaram, S. V.; Filler, M. A. Tunable Mid-Infrared Localized Surface Plasmon Resonances in Silicon Nanowires. *J. Am. Chem. Soc.* **2012**, *134*, 16155.

34. De Trizio, L.; Buonsanti, R.; Schimpf, A. M.; Llordes, A.; Gamelin, D. R.; Simonutti, R.; Milliron, D. J. Nb-Doped Colloidal TiO_2 Nanocrystals with Tunable Infrared Absorption. *Chem. Mater.* **2013**, *25*, 3383.

35. Diroll, B. T.; Gordon, T. R.; Gaulding, E. A.; Klein, D. R.; Paik, T.; Yun, H. J.; Goodwin, E. D.; Damodhar, D.; Kagan, C. R.; Murray, C. B. Synthesis of *n*-Type Plasmonic Oxide Nanocrystals and the Optical and Electrical Characterization of their Transparent Conducting Films. *Chem. Mater.* **2014**, *26*, 4579.

36. Liang, X.; Ren, Y.; Bai, S.; Zhang, N.; Dai, X.; Wang, X.; He, H.; Jin, C.; Ye, Z.; Chen, Q.; Chen, L.; Wang, J.; Jin, Y. Colloidal Indium-Doped Zinc Oxide Nanocrystals with Tunable Work Function: Rational Synthesis and Optoelectronic Applications. *Chem. Mater.* **2014**.

37. Lounis, S. D.; Runnerstrom, E. L.; Bergerud, A.; Nordlund, D.; Milliron, D. J. Influence of Dopant Distribution on the Plasmonic Properties of Indium Tin Oxide Nanocrystals. *J. Am. Chem. Soc.* **2014**, *136*, 7110.

38. Lounis, S. D.; Runnerstrom, E. L.; Llordes, A.; Milliron, D. J. Defect Chemistry and Plasmon Physics of Colloidal Metal Oxide Nanocrystals. *J. Phys. Chem. Lett.* **2014**, *5*, 1564.

39. Ye, X.; Fei, J.; Diroll, B. T.; Paik, T.; Murray, C. B. Expanding the Spectral Tunability of Plasmonic Resonances in Doped Metal-Oxide Nanocrystals through Cooperative Cation–Anion Codoping. *J. Am. Chem. Soc.* **2014**, *136*, 11680.

40. Stavrinadis, A.; Rath, A. K.; de Arquer, F. P. G.; Diedenhofen, S. L.; Magén, C.; Martinez, L.; So, D.; Konstantatos, G. Heterovalent Cation Substitutional Doping for Quantum Dot Homojunction Solar Cells. *Nat. Commun.* **2013**, *4*, 2981.

41. Luther, J.; Jain, P.; Ewers, T.; Alivisatos, A. Localized Surface Plasmon Resonances Arising from Free Carriers in Doped Quantum Dots. *Nat. Mater.* **2011**, *10*, 361.

42. Xie, Y.; Riedinger, A.; Prato, M.; Casu, A.; Genovese, A.; Guardia, P.; Sottini, S.; Sangregorio, C.; Miszta, K.; Ghosh, S.; Pellegrino, T.; Manna, L. Copper Sulfide Nanocrystals with Tunable Composition by Reduction of Covellite Nanocrystals with Cu+ Ions. *J. Am. Chem. Soc.* **2013**, *135*, 17630.

43. Manthiram, K.; Alivisatos, A. Tunable Localized Surface Plasmon Resonances in Tungsten Oxide Nanocrystals. *J. Am. Chem. Soc.* **2012**, *134*, 3995.

44. Dorfs, D.; Härtling, T.; Miszta, K.; Bigall, N. C.; Kim, M. R.; Genovese, A.; Falqui, A.; Povia, M.; Manna, L. Reversible Tunability of the Near-Infrared Valence Band Plasmon Resonance in $Cu_{2-x}Se$ Nanocrystals. *J. Am. Chem. Soc.* **2011**, *133*, 11175.

45. Zhao, Y.; Pan, H.; Lou, Y.; Qiu, X.; Zhu, J.; Burda, C. Plasmonic $Cu_{2-x}S$ Nanocrystals: Optical and Structural Properties of Copper-Deficient Copper(I) Sulfides. *J. Am. Chem. Soc.* **2009**, *131*, 4253.

46. Polking, M. J.; Jain, P. K.; Bekenstein, Y.; Banin, U.; Millo, O.; Ramesh, R.; Alivisatos, A. P. Controlling Localized Surface Plasmon Resonances in GeTe Nanoparticles Using an Amorphous-to-Crystalline Phase Transition. *Phys. Rev. Lett.* **2013**, *111*, 037401.

47. Kittel, C. *Introduction to Solid State Physics*; Wiley, 2004.

48. Liu, W. K.; Whitaker, K. M.; Smith, A. L.; Kittilstved, K. R.; Robinson, B. H.; Gamelin, D. R. Room-Temperature Electron Spin Dynamics in Free-Standing ZnO Quantum Dots. *Phys. Rev. Lett.* **2007**, *98*, 186804.

49. Schrauben, J.; Hayoun, R.; Valdez, C.; Braten, M.; Fridley, L.; Mayer, J. Titanium and Zinc Oxide Nanoparticles Are Proton-Coupled Electron Transfer Agents. *Science* **2012**, *336*, 1298.

50. Cohn, A. W.; Kittilstved, K. R.; Gamelin, D. R. Tuning the Potentials of "Extra" Electrons in Colloidal n-type ZnO Nanocrystals via Mg^{2+} Substitution. *J. Am. Chem. Soc.* **2012**, *134*, 7937.

51. Wang, X.; Jin, Y. Z.; He, H. P.; Yang, F.; Yang, Y. F.; Ye, Z. Z. Bandgap Engineering and Shape Control of Colloidal $Cd_xZn_{1-x}O$ Nanocrystals. *Nanoscale* **2013**, *5*, 6464.

52. Yang, Y. F.; Jin, Y. Z.; He, H. P.; Wang, Q. L.; Tu, Y.; Lu, H. M.; Ye, Z. Z. Dopant-Induced Shape Evolution of Colloidal Nanocrystals: The Case of Zinc Oxide. *J. Am. Chem. Soc.* **2010**, *132*, 13381.

53. Fiederling, R.; Keim, M.; Reuscher, G.; Ossau, W.; Schmidt, G.; Waag, A.; Molenkamp, L. W. Injection and Detection of a Spin-Polarized Current in a Light-Emitting Diode. *Nature* **1999**, *402*, 787.

Chapter 2

Comparison of Extra Electrons in *n*-Type Al^{3+}-Doped and Photochemically Reduced ZnO Nanocrystals

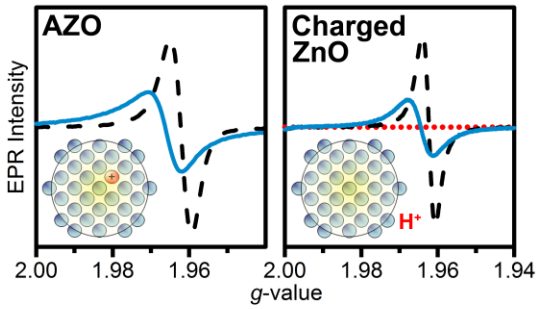

Adapted from: Schimpf, A. M.; Ochsenbein, S. T.; Buonsanti, R.; Milliron, D. J.; Gamelin, D. R. *Chem. Comm.* **2012**, *48*, 9352.

2.1 Overview

The extra electrons in colloidal *n*-type ZnO nanocrystals formed by aliovalent doping and photochemical reduction are compared. Whereas the two are similar spectroscopically, they show very different electron-transfer reactivities, attributable to their different charge-compensating cations (Al^{3+} versus H^+).

2.2 Introduction

Semiconductors containing excess delocalized charge carriers (extra conduction-band electrons or valence-band holes) are of enormous technological importance. Such carriers are usually introduced by doping with shallow donor or acceptor impurities (*n*- or *p*-type, respectively). In contrast with bulk semiconductors, there has been relatively little success generating band-like charge carriers in colloidal semiconductor nanocrystals via aliovalent doping. Most *n*- or *p*-type colloidal semiconductor nanocrystals are instead prepared by remote doping[1] and photochemical[2-5] or electrochemical[6-8] reduction. Aliovalent doping of colloidal semiconductor nanocrystals to yield band-like charge carriers remains a major obstacle to the preparation of nanocrystal-based devices for information processing, solar energy conversion, or

other technologies.

Among colloidal II-VI, III-V, and IV-VI semiconductor nanocrystals, the doping chemistry of ZnO nanocrystals has proved to be particularly rich. Colloidal transition-metal-doped ZnO nanocrystals ($Zn_{1-x}TM_xO$) have been prepared across the entire series of $0 < x < 1$.[9] Colloidal *n*-type ZnO nanocrystals containing additional conduction-band-like electrons have been prepared by photochemical,[2-5,10-13] electrochemical,[7] or chemical[3] reduction. Most recently, colloidal Al^{3+}-doped ZnO (AZO) nanocrystals have been reported in which Al^{3+} acts as an ionized shallow donor.[14] Electronic absorption spectroscopy shows excess band-like electrons in these AZO nanocrystals. From a practical standpoint, processable colloidal AZO nanocrystals may offer new low-cost routes to transparent-conducting-oxide device components. From a fundamental standpoint, these AZO nanocrystals provide a rare opportunity to study the properties of charge carriers introduced into colloidal semiconductor nanocrystals via aliovalent doping. Here, we use electron paramagnetic resonance (EPR) and electronic absorption spectroscopies along with chemical reactivity to compare the conduction-band-like electrons in colloidal AZO nanocrystals with those in photochemically reduced ZnO nanocrystals.

2.3 Results and discussion

Colloidal ZnO and AZO nanocrystals were synthesized following literature procedures.[14,15] Details may be found in Appendix A. Figure 2.1 shows representative TEM images of (a) 2.5% AZO and (b) undoped ZnO nanocrystals synthesized as described previously.[14-16] The nanocrystals are not spherical but show facets that reflect the hexagonal ZnO crystal structure. Both sets of nanocrystals have an average radius of ~5 nm. Figure 2.1c shows room-temperature X-band EPR spectra of colloidal 1.8% (also ~5 nm) and 2.5% AZO nanocrystals. Resonances at

$g \approx 1.96$ are observed for both samples, consistent with shallow donor resonances in bulk ZnO.[6] Increasing the Al^{3+} concentration from 1.8 to 2.5% broadens the EPR signal, increases its *g* value from 1.962 to 1.966, and increases its intensity (determined by double integration). Aluminum is a shallow donor in bulk ZnO with a donor binding energy of ~50 meV.[17,18] The EPR spectra in Figure 2.1c confirm that aluminum is also a shallow donor in these AZO nanocrystals.

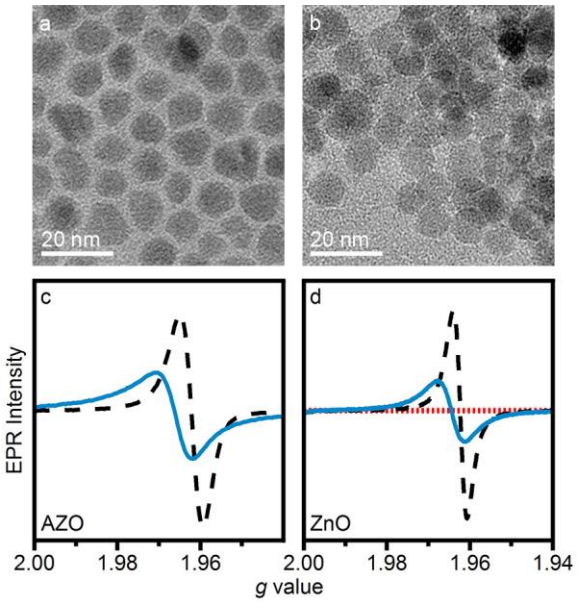

Figure 2.1. Physical and spectroscopic comparison of Al^{3+}-doped ZnO and ZnO nanocrystals. TEM images of (a) 2.5% AZO and (b) ZnO nanocrystals. (c) EPR spectra of colloidal 1.8% (dashed black) and 2.5% (solid blue) AZO nanocrystals in 1:1 hexane/octane (18 μM). (d) EPR spectra of as-prepared (dotted red), lightly photodoped (dashed black) and highly photodoped (solid blue) dodecylamine-capped ZnO nanocrystals in toluene (6 μM). EPR spectra were collected at room-temperature.

For comparison with the AZO nanocrystals, extra electrons were added to the ZnO nanocrystals via photochemical reduction (photodoping). UV irradiation in the presence of ethanol or other hole quenchers leaves behind conduction-band electrons (e^-_{CB}) compensated by protons.[2-5,10-13] These electrons are kinetically stable under rigorously anaerobic conditions.[5]

Longer UV irradiation leads to accumulation of multiple electrons.[4,11,13] The EPR spectra of these nanocrystals at various levels of photochemical reduction are shown in Figure 2.1d. Consistent with previous results,[11] increasing the number of e^-_{CB} per ZnO nanocrystal leads to EPR line broadening, an increase in *g* value (from 1.962 to 1.965), and increased EPR intensity. Because these nanocrystals are too large to show size-dependent *g* values,[12] these EPR changes can be attributed solely to the addition of multiple electrons, and not to size heterogeneity. EPR spectroscopy is thus sensitive to the number of e^-_{CB} per nanocrystal.

ZnO nanocrystal reduction is accompanied by a blue shift of the band-gap absorption edge and growth of an intense electronic absorption band in the IR.[3,5,11,13] Figure 2.2 compares the absorption spectra of these AZO and ZnO nanocrystals. All show increased NIR absorption and blue-shifted band-edge absorption relative to the undoped ZnO nanocrystals. The NIR absorbance increases as more electrons are added photochemically or more Al^{3+} is incorporated. Overall, by EPR and electronic absorption spectroscopies, these AZO and photodoped ZnO nanocrystals are essentially indistinguishable.

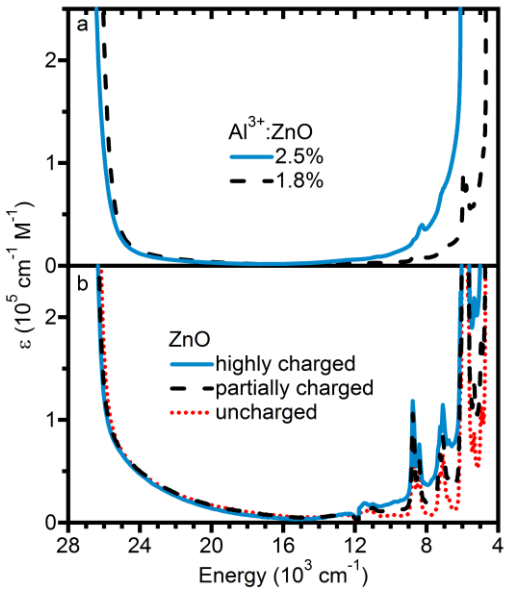

Figure 2.2. Comparison of Al^{3+}-doped ZnO and ZnO nanocrystals by electronic absorption. (a) 1.8% (dashed black) and 2.5% (solid blue) AZO nanocrystals in 1:1 hexane/octane (18 μM). (b) As-prepared (dotted red), partially photodoped (dashed black), and highly photodoped (solid blue) ZnO nanocrystals in toluene (6 μM).

In photodoped ZnO nanocrystals, the number of e^-_{CB} per nanocrystal can be quantified by anaerobic titration with an appropriate oxidant (See Appendix B for details).[4,11,13,19] Here, titration was performed with $[FeCp^*_2][BAr_F]$.[13] Figure 2.3a shows NIR absorption spectra of ZnO nanocrystals before photodoping, after maximum photodoping, and following anaerobic addition of increasing amounts of $[FeCp^*_2][BAr_F]$. The inset plots the 1550 nm NIR absorbance of the ZnO nanocrystals versus added $[FeCp^*_2][BAr_F]$. The $[FeCp^*_2]^+$ concentration at which the NIR absorbance returns to that of the as-prepared nanocrystals provides the average number of e^-_{CB} per nanocrystal. By this method, the maximally photodoped ZnO nanocrystals were determined to contain an average of ~48 e^-_{CB} per nanocrystal, and the highly photodoped ZnO nanocrystals of Figures 2.1 and 2.2 were determined to contain an average of ~32 e^-_{CB} per nanocrystal. Although at first 48 e^-_{CB} per nanocrystal appears anomalously large relative to

previous reports, [4,11,13] it actually corresponds to a slightly smaller electron *density* (9.2×10^{19} cm^{-3} versus 1.1×10^{20} cm^{-3} for r = 2.3 nm nanocrystals [Ref. 11], 1.3×10^{20} cm^{-3} for r = 1.95 nm nanocrystals [Ref. 13], and 1.5×10^{20} cm^{-3} for r = 2.5 nm nanocrystals [Ref. 4]). As discussed in Chapter 5, this high number of conduction-band electrons in photodoped ZnO nanocrystals is due to the large volume of the nanocrystals.[19]

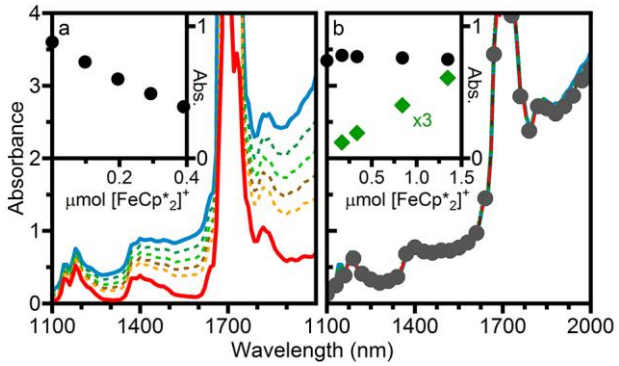

Figure 2.3. Oxidative stabilities of AZO versus photodoped ZnO nanocrystals. Electronic absorption spectra of (a) photodoped ZnO and (b) 5.4% AZO nanocrystals before (solid blue) and after anaerobic mixing with various amounts of $[FeCp^*_2]^+$. The insets plot the NIR absorption at 1550 nm versus added $[FeCp^*_2]^+$ (black circles). The inset in (b) also plots the absorption at 782 nm (×3), corresponding to $[FeCp^*_2]^+$ (green triangles). Both sets of nanocrystals are capped with dodecylamine and suspended in 1:1 toluene/THF.

The number of electrons per AZO nanocrystal cannot be determined by the same method due to the greater stability of AZO against oxidation (*vide infra*), but can be estimated from EPR and absorption spectroscopies. The very similar EPR and absorption spectra of the highly photodoped ZnO and 2.5% AZO nanocrystals in Figures 2.1 and 2.2 suggest these two samples contain similar numbers of conduction-band electrons (~30 e^-_{CB} per nanocrystal). The NIR absorbance of the 1.8% AZO nanocrystals is ~5 times smaller, suggesting they have ~6 e^-_{CB} per nanocrystal. Although these numbers are approximate, there are clearly far fewer conduction-band electrons than Al^{3+} ions per nanocrystal. At r = 5 nm, the average AZO nanocrystal

contains a total of ~22000 cations and approximately 400 or 550 Al^{3+} ions (for 1.8 or 2.5% Al^{3+}, respectively). Evidently, roughly 95% of the Al^{3+} ions in these AZO nanocrystals are not compensated by conduction-band electrons. Similar ratios have been reported for Sn^{4+}-doped In_2O_3 (ITO) nanocrystals.[20,21] We note that many Al^{3+} ions are at or near the nanocrystal surfaces, where charge compensation by other means may be favored. This observation highlights a major general challenge confronting aliovalent doping of colloidal semiconductor nanocrystals: most dopants will reside near the surface, where charge compensation can be achieved by changes in surface ion or ligand stoichiometry without introducing band-like charge carriers.

Despite their spectroscopic similarities, the AZO and photochemically reduced ZnO nanocrystals possess very different chemical reactivities. Specifically, the AZO nanocrystals are completely stable against oxidation by air, in stark contrast with the rapid oxidation of the photochemically reduced nanocrystals in air.[2-5,10-13] To illustrate this distinction, the reactivities of AZO and photodoped ZnO nanocrystals toward various stoichiometric oxidants were examined. Figure 2.3b shows NIR absorption spectra of 5.4% AZO nanocrystals obtained upon $[FeCp^*_2]^+$ titration under identical conditions as described above. As anticipated from the aerobic stability of these AZO nanocrystals, $[FeCp^*_2]^+$ addition does not diminish the AZO NIR absorption. Instead, only growth of $[FeCp^*_2]^+$ absorption at ~725 nm is observed (Figures 2.3b inset and C.1), indicating coexistence of AZO electrons and $[FeCp^*_2]^+$ in solution, *i.e.*, electrons are not transferred from the AZO nanocrystals to $[FeCp^*_2]^+$. Similarly, photochemically photodoped ZnO nanocrystals rapidly reduce methylene blue (MB^+), whereas no reaction is detected between AZO nanocrystals and MB^+ (Figure C.2).

The different reactivities of the AZO and photodoped ZnO nanocrystals reflect different free-

energy changes for oxidation of these two-electron donors. We hypothesize that this difference is not due to a particular stability of electrons in AZO nanocrystals but rather to the formation of high-energy products upon electron transfer from these nanocrystals. A critical difference between AZO and photochemically reduced ZnO nanocrystals is the source of electron charge compensation. In the former, the electron is compensated by a lattice-bound Al^{3+} ion, whereas in the latter it is compensated by a proton either at the surface or within the lattice.[4,13,22] Removing the electron from an AZO nanocrystal strands a lattice-bound Al^{3+} without local compensation, resulting in a high-energy configuration (Scheme 2.1, left). In contrast, electron transfer from a photochemically reduced ZnO nanocrystal can be accompanied by proton stabilization. For example, proton stabilization may occur due to proton-coupled electron transfer[13] (*e.g.*, in the reactions with O_2 and MB^+), as illustrated in Scheme 2.1, right, or via short-range electrostatic stabilization by anionic surface ligands, counter ions, or dipoles (*e.g.*, in the outer-sphere electron-transfer reaction with $[FeCp^*_2][BAr_F]$). The reactivity difference between AZO and photodoped ZnO nanocrystals is thus ultimately attributable to their different charge-compensating cations (H^+ versus Al^{3+}).

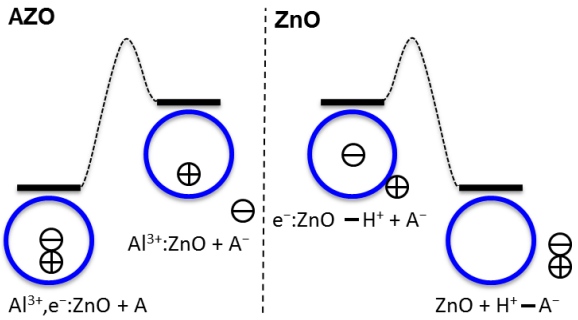

Scheme 2.1. Oxidative stabilities of AZO versus ZnO nanocrystals. Left: Electron transfer from an AZO nanocrystal to an acceptor (A) strands an uncompensated Al^{3+} ion and is not thermodynamically favorable. Right: Electron transfer from a photochemically reduced ZnO nanocrystal can be accompanied by proton transfer to the acceptor (depicted) or other local proton charge stabilization (not depicted), and is thermodynamically favorable. The relative free energies are for illustrative purposes only and are not to scale.

2.4 Summary and conclusions

In summary, AZO and photochemically reduced ZnO nanocrystals are essentially indistinguishable when examined spectroscopically, yet display qualitatively different chemical reactivities. The electrostatic interaction between lattice-bound Al^{3+} and e^-_{CB} appears to lend oxidative stability to AZO nanocrystals that is not found in photodoped ZnO nanocrystals, where charge compensation involves protons. This comparison provides general insights into the challenge of generating and stabilizing extra charge carriers in colloidal semiconductor nanocrystals, with implications extending to other colloidal nanocrystals of interest for potential device applications or as tunable chemical redox agents.

2.5 Experimental methods

ZnO and Al^{3+}-doped ZnO nanocrystal synthesis and general characterization are described in Appendix A. Photodoping and titration methods are described in Appendix B. EPR spectra were

collected using a Bruker E580 X-band spectrometer with a SHQE resonator operating at 9.8 GHz. The *g* values were measured in reference to DPPH (g = 2.0036).

2.6 References

1. Shim, M.; Guyot-Sionnest, P. *n*-Type Colloidal Semiconductor Nanocrystals. *Nature* **2000**, *407*, 981.

2. Haase, M.; Weller, H.; Henglein, A. Photochemistry and Radiation Chemistry of Colloidal Semiconductors. 23. Electron Storage on ZnO Particles and Size Quantization. *J. Phys. Chem.* **1988**, *92*, 482.

3. Shim, M.; Guyot-Sionnest, P. Organic-Capped ZnO nanocrystals: Synthesis and *n*-Type Character. *J. Am. Chem. Soc.* **2001**, *123*, 11651.

4. Wood, A.; Giersig, M.; Mulvaney, P. Fermi Level Equilibration in Quantum Dot-Metal Nanojunctions. *J. Phys. Chem. B* **2001**, *105*, 8810.

5. Liu, W. K.; Whitaker, K. M.; Kittilstved, K. R.; Gamelin, D. R. Stable Photogenerated Carriers in Magnetic Semiconductor Nanocrystals. *J. Am. Chem. Soc.* **2006**, *128*, 3910.

6. Wang, C. J.; Shim, M.; Guyot-Sionnest, P. Electrochromic Nanocrystal Quantum Dots. *Science* **2001**, *291*, 2390.

7. Roest, A. L.; Kelly, J. J.; Vanmaekelbergh, D.; Meulenkamp, E. A. Staircase in the Electron Mobility of a ZnO Quantum Dot Assembly due to Shell Filling. *Phys. Rev. Lett.* **2002**, *89*, 036801.

8. Guyot-Sionnest, P. Charging Colloidal Quantum Dots by Electrochemistry. *Microchim. Acta* **2008**, *160*, 309.

9. White, M. A.; Ochsenbein, S. T.; Gamelin, D. R. Colloidal Nanocrystals of Wurtzite $Zn_{1-x}Co_xO$ ($0 \leq x \leq 1$): Models of Spinodal Decomposition in an Oxide Diluted Magnetic Semiconductor. *Chem. Mater.* **2008**, *20*, 7107.

10. van Dijken, A.; Meulenkamp, E. A.; Vanmaekelbergh, D.; Meijerink, A. Influence of Adsorbed Oxygen on the Emission Properties of Nanocrystalline ZnO Particles. *J. Phys. Chem. B* **2000**, *104*, 4355.

11. Liu, W. K.; Whitaker, K. M.; Smith, A. L.; Kittilstved, K. R.; Robinson, B. H.; Gamelin, D. R. Room-Temperature Electron Spin Dynamics in Free-Standing ZnO Quantum Dots. *Phys. Rev. Lett.* **2007**, *98*, 186804.

12. Whitaker, K. M.; Ochsenbein, S. T.; Polinger, V. Z.; Gamelin, D. R. Electron Confinement Effects in the EPR Spectra of Colloidal n-Type ZnO Quantum Dots. *J. Phys. Chem. C* **2008**, *112*, 14331.

13. Schrauben, J.; Hayoun, R.; Valdez, C.; Braten, M.; Fridley, L.; Mayer, J. Titanium and Zinc Oxide Nanoparticles Are Proton-Coupled Electron Transfer Agents. *Science* **2012**, *336*, 1298.

14. Buonsanti, R.; Llordes, A.; Aloni, S.; Helms, B.; Milliron, D. Tunable Infrared Absorption and Visible Transparency of Colloidal Aluminum-Doped Zinc Oxide Nanocrystals. *Nano Lett.* **2011**, *11*, 4706.

15. Schwartz, D. A.; Norberg, N. S.; Nguyen, Q. P.; Parker, J. M.; Gamelin, D. R. Magnetic Quantum Dots: Synthesis, Spectroscopy, and Magnetism of Co^{2+}- and Ni^{2+}-Doped ZnO Nanocrystals. *J. Am. Chem. Soc.* **2003**, *125*, 13205.

16. Norberg, N. S.; Gamelin, D. R. Influence of Surface Modification on the Luminescence of Colloidal ZnO Nanocrystals. *J. Phys. Chem. B* **2005**, *109*, 20810.

17. Klingshirn, C. ZnO: Material, Physics and Applications. *Chem. Phys. Chem.* **2007**, *8*, 782.

18. Herklotz, F.; Lavrov, E. V.; Weber, J.; Mamin, G. V.; Kutin, Y. S.; Volodin, M. A.; Orlinskii, S. B. Identification of Shallow Al Donors in ZnO. *Phys. Stat. Sol. B* **2011**, *248*, 1532.

19. Schimpf, A. M.; Gunthardt, C. E.; Rinehart, J. D.; Mayer, J. M.; Gamelin, D. R. Controlling Carrier Densities in Photochemically Reduced Colloidal ZnO Nanocrystals: Size Dependence and Role of the Hole Quencher. *J. Am. Chem. Soc.* **2013**, *135*, 16569.

20. Wang, T.; Radovanovic, P. V. Free Electron Concentration in Colloidal Indium Tin Oxide Nanocrystals Determined by Their Size and Structure. *J. Phys. Chem. C* **2011**, *115*, 406.

21. Mendelsberg, R. J.; Garcia, G.; Li, H.; Manna, L.; Milliron, D. J. Understanding the Plasmon Resonance in Ensembles of Degenerately Doped Semiconductor Nanocrystals. *J. Phys. Chem. C* **2012**, *116*, 12226.

22. Roest, A. L.; Houtepen, A. J.; Kelly, J. J.; Vanmaekelbergh, D. Electron-Conducting Quantum-Dot Solids with Ionic Charge Compensation. *Faraday Discuss.* **2004**, *125*, 55.

Chapter 3

Controlling Carrier Densities in Photochemically Reduced Colloidal ZnO Nanocrystals: Size Dependence and Role of the Hole Quencher

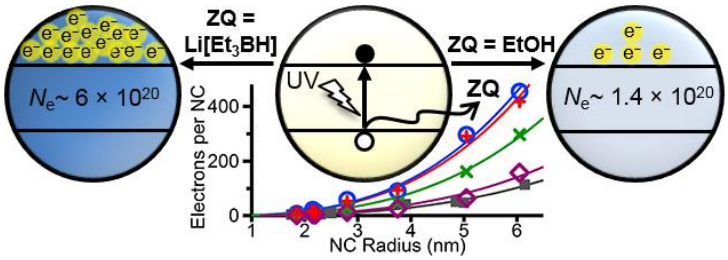

Adapted from: Schimpf, A. M.; Gunthardt, C. E; Rinehart, J. D.; Gamelin, D. R. *J. Am. Chem. Soc.* **2013**, *135*, 16569.

3.1 Overview

Photodoped colloidal ZnO nanocrystals are model systems for understanding the generation and physical or chemical properties of excess delocalized charge carriers in semiconductor nanocrystals. Typically, ZnO photodoping is achieved using EtOH as a sacrificial reductant. Curiously, different studies have reported over an order of magnitude spread in the maximum number of conduction-band electrons that can be accumulated by photochemical oxidation of EtOH. Here, we demonstrate that this apparent discrepancy results from a strong size dependence of the average maximum number of excess electrons per nanocrystal, $\langle n_{max} \rangle$. We demonstrate that $\langle n_{max} \rangle$ increases in proportion to nanocrystal volume, such that the maximum carrier density remains constant for all nanocrystal sizes. $\langle n_{max} \rangle$ is found to be largely insensitive to precise experimental conditions such as solvent, ligands, protons or other cations, photolysis conditions, and nanocrystal or EtOH concentrations. These results reconcile the broad range of literature results obtained with EtOH as the hole quencher. Furthermore, we

demonstrate that $<n_{max}>$ depends on the identity of the hole quencher, and is thus not an intrinsic property of the multiply reduced ZnO nanocrystals themselves. Using a series of substituted borohydride hole quenchers, we show that it is possible to increase the nanocrystal carrier densities over fourfold relative to previous photodoping reports. When excess lithium and potassium triethylborohydrides are used in the photodoping, formation of Zn^0 is observed. The relationship between metallic Zn^0 formation and ZnO surface electron traps is discussed.

3.2 Introduction

The introduction of extra charge carriers into free-standing colloidal semiconductor nanocrystals constitutes a long-standing challenge in the development of nanocrystal building blocks for quantum dot solar cells, transistors, photodetectors, and electroluminescent devices. Successful strategies for introducing extra band-like charge carriers into colloidal semiconductor nanocrystals have included remote doping,[1,2] defect- or vacancy-induced doping,[3,4] photochemical[2,5-10] or electrochemical reduction,[7,11-13] and aliovalent doping.[10,14-16] Among free-standing colloidal nanocrystals, the extra electrons of reduced colloidal ZnO nanocrystals are arguably the most extensively investigated.[1,2,5-10,17] Most commonly, these electrons have been generated by photochemical oxidation of EtOH,[5,6,8-10,17] as described by equation 3.1.[18-20] UV illumination of ZnO nanocrystals excites an electron across the band gap and, in the presence of EtOH or other hole quenchers (ZQ), the photogenerated valence-band hole (h^+_{VB}) can be captured irreversibly. This chemistry deposits conduction-band electrons (e^-_{CB}) and charge-compensating protons or other cations (Z^+). Remarkably, extended UV irradiation leads to accumulation of multiple conduction-band electrons per colloidal ZnO nanocrystal (Scheme 3.1).[6,9] Under rigorously anaerobic conditions, these extra electrons are stable indefinitely,

allowing their handling and detailed investigation by physical and chemical techniques.[8,9] Upon exposure to air or other oxidants, these electrons can be removed and the ZnO nanocrystals returned to their original oxidation state. Such chemistry thus offers a post-synthetic method of tuning nanocrystal carrier densities that has proven attractive for numerous physical and chemical investigations.[8-10,17,21-27]

$$e^-_{CB},h^+_{VB}\text{:ZnO} + CH_3CH_2OH \rightarrow 2e^-_{CB}\text{:ZnO} + 2H^+ + CH_3CHO \qquad (3.1)$$

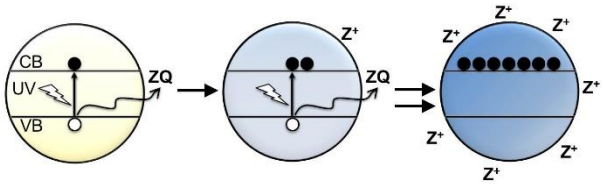

Scheme 3.1. Photochemical reduction of ZnO nanocrystals. UV illumination promotes an electron to the conduction band (CB), leaving behind a valence-band (VB) hole. Under anaerobic conditions and in the presence of a hole quencher (ZQ), this hole may be rapidly quenched, leaving a conduction-band electron. The hole quencher deposits a cation to compensate the stranded electron. Extended UV exposure allows for the accumulation of multiple conduction-band electrons.

Recently, it was demonstrated that photochemical accumulation of multiple conduction-band electrons is made possible by the fact that hole quenching with EtOH is markedly faster than Auger recombination of the charged exciton.[26] Although this observation explains how more than one electron may be injected photochemically, salient questions remain pertaining to the level of electron doping that can be achieved by this method. Previous studies have reported disparate values for the maximum number of electrons per nanocrystal (denoted $\langle n_{max} \rangle$ when averaged over the ensemble) that can be added to colloidal ZnO nanocrystals via photochemical oxidation of EtOH. Titrations have shown $\langle n_{max} \rangle$ = 4 (ref. 17), 6 (ref. 9), 10 (ref. 6), and 48 (ref. 10) electrons per ZnO nanocrystal. The cause of this large spread in experimental $\langle n_{max} \rangle$ values

has not been examined or clarified. Furthermore, the role of the hole quencher in determining $<n_{max}>$ has not been examined.

Here, we present a systematic investigation of the maximum number of electrons that can be added to ZnO nanocrystals via photochemical oxidation of EtOH. We demonstrate that $<n_{max}>$ varies strongly with nanocrystal radius (r) in a well-behaved fashion, covering nearly two orders of magnitude in $<n_{max}>$ with only a factor of four variation in r. Specifically, $<n_{max}>$ is found to scale with nanocrystal volume, yielding nearly constant maximum electron *densities* over all nanocrystal radii. For photodoping using EtOH, $<n_{max}>$ is largely independent of solvent, surface-capping ligands, photoexcitation rates, and other experimental variations. We further demonstrate that for a given nanocrystal size, $<n_{max}>$ is not intrinsic to the nanocrystal but depends on the specific hole quencher used. We introduce the use of lithium and potassium triethylborohydrides as particularly effective hole quenchers for photodoping ZnO nanocrystals, and demonstrate systematic trends in $<n_{max}>$ that relate to the properties of these hole quenchers. Comparison of these hole quenchers with tetrabutylammonium triethylborohydride reveals that the cations can also play an important role in determining $<n_{max}>$. These results improve upon existing methods for photodoping ZnO nanocrystals, and shed light onto the fundamental factors governing this nanocrystal photodoping. Ultimately, this knowledge may contribute to the development of new routes to functionalization of colloidal semiconductor nanocrystals for a variety of chemical, optical, or technological applications.

3.3 Results and analysis

Figure 3.1 shows UV/vis, IR, and EPR spectra of colloidal r = 2.8 nm ZnO nanocrystals collected before and after various durations of UV exposure in the presence of EtOH. As

reported previously,[2,9] electron accumulation is accompanied by a bleach of the band edge absorption (Figure 3.1a), corresponding to filling of the conduction band, and by growth of an intense absorption band in the IR (Figure 3.1b) attributable to intra-conduction-band transitions. With electron accumulation, the IR band increases in intensity and shifts to higher energy. The appearance of the EPR signal at $g \approx 1.96$ (Figure 3.1c), and its dependence on nanocrystal radius,[21] confirms that these extra electrons are delocalized in the conduction band. This photodoping is completely reversed upon exposure of the nanocrystals to air or other appropriate oxidants, returning the spectroscopic properties to their original values.

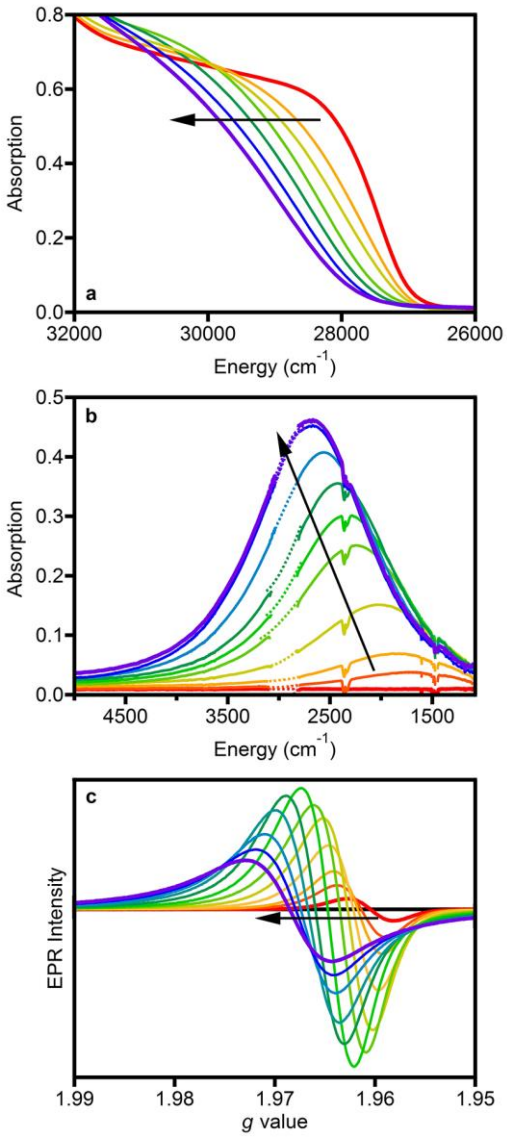

Figure 3.1. Spectroscopic signatures of photodoping in colloidal ZnO nanocrystals. Photochemical addition of conduction-band electrons leads to (a) a bleach in the UV absorption, (b) growth of IR absorption, and (c) appearance of a $g \approx 1.96$ EPR signal. The arrows indicate increased UV irradiation time. The region of intense ligand and solvent C–H stretches (~2800–3100 cm^{-1}) in panel (b) has been interpolated for clarity (dotted lines). Spectra are shown for ~10 μM in 1:1 toluene/THF (absorption) and ~100 μM in toluene (EPR) colloidal TOPO-capped r = 2.8 nm ZnO nanocrystals.

Photodoping experiments were performed on colloidal ZnO nanocrystals with average radii ranging from r = 1.75 to 6.15 nm using EtOH as the hole quencher. For each sample, $\langle n_{max} \rangle$ was

determined by titration against $[FeCp^*_2][BAr_F]$ (see Appendix B for photodoping and titration methods).[10,17] Figure 3.2a presents a double-log plot of the resulting $<n_{max}>$ values (blue squares) versus nanocrystal radius. The entire data set spans nearly two orders of magnitude in $<n_{max}>$, showing a strong and well-behaved dependence on nanocrystal radius. The present data agree remarkably well with data reported in previous studies of ZnO nanocrystals in which EtOH was the hole quencher (red circles).[6,9,10,17] This data set includes nanocrystals with amine, TOPO/phosphonate, or acetate/hydroxide surface capping ligands that are suspended in toluene, toluene/THF, or EtOH solvents (Appendix D.1). Photolysis was performed at different nanocrystal concentrations with different excitation rates and in different laboratories. Nevertheless, all of these data fall on the same line in Figure 3.2a, indicating that $<n_{max}>$ is not particularly sensitive to precise experimental conditions such as solvent, ligands, photolysis conditions, and nanocrystal or EtOH concentrations. The disparate literature values thus follow a rational and fundamentally meaningful trend. Fitting these data to a phenomenological power law expression (equation 3.2) yields the solid black line plotted in Figure 3.2a with a best fit exponential value of $p = 2.8 \pm 0.2$. For comparison, the dashed line in Figure 3.2a shows the best fit obtained when fixing $p = 3.0$, demonstrating that $<n_{max}>$ varies roughly in proportion to the nanocrystal volume. As a consequence of this size dependence, the average maximum electron *density* ($<N_{max}>$) remains essentially constant across this entire set of samples. To illustrate this point, Figure 3.2b plots the data from Figure 3.2a as $<N_{max}>$ versus nanocrystal radius. All nanocrystals display similar maximum electron densities of $<N_{max}> \approx 1–2 \times 10^{20}$ cm^{-3}. The dashed line represents the average value of $<N_{max}>$ over all sizes of nanocrystals, $<<N_{max}^{EtOH}>> = 1.4 \pm 0.4 \times 10^{20}$ cm^{-3}.

$$< n_{max} > \; = \; a r^{p} \tag{3.2}$$

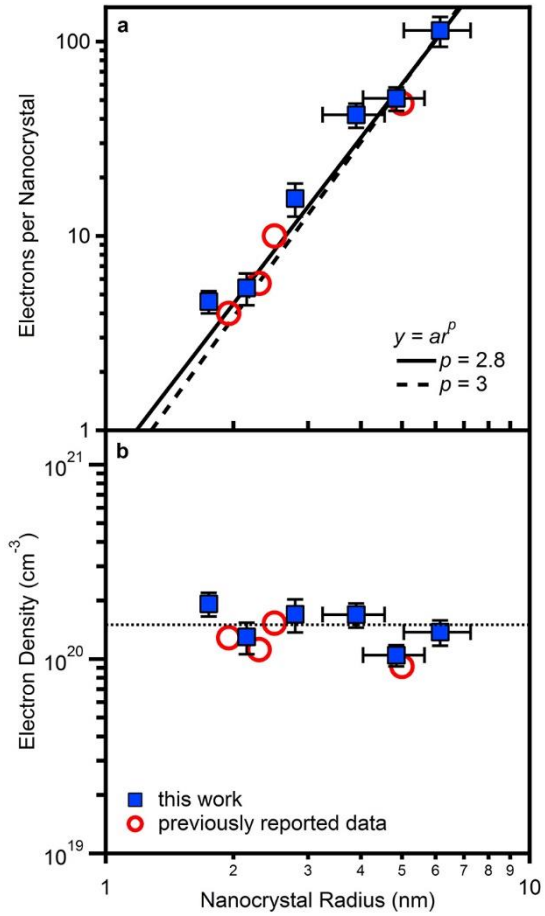

Figure 3.2. Size dependence of the maximum photodoping level in colloidal ZnO nanocrystals using EtOH as the hole quencher. (a) Average maximum number of electrons per nanocrystal (<n_{max}>) plotted versus nanocrystal radius on logarithmic scales. The solid blue squares are data points from the present study. The red open circles show literature data points, one each from refs. [6,9,10,17]. The solid line represents the best fit to equation 3.2, which yields p = 2.8. The dashed line shows the best fit for p = 3.0. (b) The data from (a) plotted as the average maximum electron density (<N_{max}>) versus nanocrystal radius on logarithmic scales. The dotted line is the maximum electron density averaged over all nanocrystal sizes (<<N_{max}^{EtOH}>> = 1.4 ± 0.4 × 10^{20} cm^{-3}).

To date, the influence of the hole quencher on <n_{max}> in colloidal ZnO nanocrystals has not been explored. To investigate this variable, colloidal ZnO nanocrystals were photoexcited in the

presence of four additional hole quenchers, defined here as ZQ. These hole quenchers included two different anions (Q^-): triethylborohydride and dimethylaminoborohydride ($[Et_3BH]^-$ and $[Me_2NBH_3]^-$, respectively). For the $[Et_3BH]^-$ anion, three different charge-compensating cations (Z^+) were investigated: Li^+, K^+, and tetrabutylammonium ($[Bu_4N]^+$). Similar to EtOH, the hydrides successfully quench photogenerated holes and lead to electron accumulation in ZnO nanocrystals photoexcited under anaerobic conditions. For these hole quenchers, the net photochemical reactions are not yet known, but we speculate that they may be summarized as shown in equation 3.3, where Z^+ represents Li^+, K^+, or $[Bu_4N]^+$. This representation assumes "current doubling" analogous to that reported for EtOH (equation 3.1),[18,20] but current doubling with these hydride hole quenchers has not been confirmed. The results presented below do not rely on any assumptions about current doubling.

$$e^-_{CB},h^+_{VB}\text{:ZnO} + Z[Et_3BH] \rightarrow 2e^-_{CB}\text{:ZnO} + H^+ + Z^+ + BEt_3 \quad (3.3a)$$

$$e^-_{CB},h^+_{VB}\text{:ZnO} + Li[Me_2NBH_3] \rightarrow 2e^-_{CB}\text{:ZnO} + H^+ + Li^+ + Me_2NBH_2 \quad (3.3b)$$

Figure 3.3a shows IR absorption spectra of r = 2.8 nm nanocrystals after maximum photodoping in the presence of EtOH, $Li[Et_3BH]$, $K[Et_3BH]$, $[Bu_4N][Et_3BH]$, or $Li[Me_2NBH_3]$. These experiments demonstrate that $\langle n_{max} \rangle$ can be markedly increased by changing the hole quencher. Figure 3.3b plots the $\langle n_{max} \rangle$ values obtained using the various hole quenchers as a function of nanocrystal radius (Appendix D.2). As with EtOH in Figure 3.2, $\langle n_{max} \rangle$ is a strong function of nanocrystal radius for each hole quencher, in every case changing roughly in proportion to the nanocrystal volume. For the hydrides, fits of these data to equation 3.2 all yield values of p close to 3 (Appendix D.3). The solid lines in Figure 3.3b show fits obtained with p

fixed to a value of 3.0. This fitting allows meaningful information to be extracted from the coefficient a: The ratio of a^{ZQ} to a^{EtOH} represents the maximum photodoping achieveable with the various hydride hole quenchers, relative to EtOH. Multiplying this ratio by $\langle\langle N_{max}^{EtOH}\rangle\rangle$ thus yields $\langle\langle N_{max}^{ZQ}\rangle\rangle$. The results of this fitting are summarized in Table 3.1. Floating p yields slightly different values but the same trend (Appendix D.3).

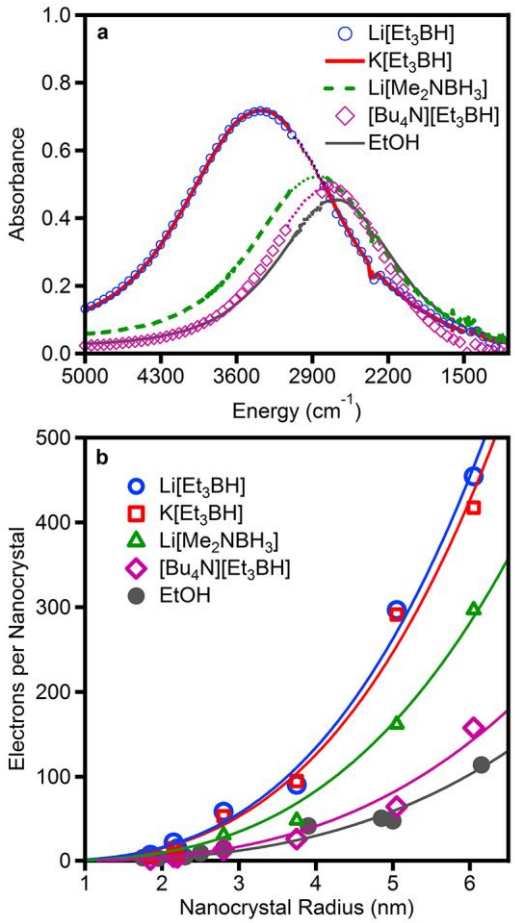

Figure 3.3. Dependence of photodoping on the hole quencher. (a) IR absorption of colloidal r = 2.8 nm ZnO nanocrystals (TOPO-capped in 1:1 toluene/THF) photodoped in the presence of EtOH (solid gray line), $[Bu_4N][Et_3BH]$ (purple diamonds), $Li[Me_2NBH_3]$ (dashed green line), $K[Et_3BH]$ (solid red line) and $Li[Et_3BH]$ (blue circles) hole quenchers. The region of intense ligand and solvent C–H stretches (~2800–3100 cm^{-1}) has been interpolated for clarity (dotted lines). (b) Size dependence of $\langle n_{max}\rangle$ of ZnO nanocrystals photodoped using the hole quenchers from (a). The solid lines show fits to equation 3.2 in which p is fixed to 3.0.

Table 3.1. Summary of the size dependence of ZnO nanocrystal photodoping using various hole quenchers (ZQ). These parameters were obtained by fitting the data of Figure 3.3b to equation 3.2 with p fixed at 3.0. Here, a^{ZQ} is the scaling coefficient (proportional to $\langle\langle N_{max}\rangle\rangle$) and a^{ZQ}/a^{EtOH} represents the scaling coefficient relative to EtOH. The maximum photodoping was calculated as $\langle\langle N_{max}^{ZQ}\rangle\rangle = (a^{ZQ}/a^{EtOH})\ \langle\langle N_{max}^{EtOH}\rangle\rangle$, with $\langle\langle N_{max}^{EtOH}\rangle\rangle = 1.4 \pm 0.4 \times 10^{20}$ cm^{-3}. Typical errors in a are small ($< \pm 0.1$), and all uncertainties in $\langle\langle N_{max}^{ZQ}\rangle\rangle$ are thus estimated to be within ~30% based on the uncertainty in $\langle\langle N_{max}^{EtOH}\rangle\rangle$.

ZQ	a	a^{ZQ}/a^{EtOH}	$\left\langle\left\langle N_{max}^{ZQ}\right\rangle\right\rangle$ (10^{20} cm^{-3})
EtOH	0.5	1	1.4
$[Bu_4N][Et_3BH]$	0.7	1.4	2.0
$Li[Me_2NBH_3]$	1.3	2.7	3.8
$K[Et_3BH]$	2.0	4.1	5.7
$Li[Et_3BH]$	2.1	4.4	6.1

To test whether the high carrier densities achieved with some hydrides still involve delocalized electrons, EPR measurements were performed. Figure 3.4a shows the EPR spectra of colloidal r = 2.15 nm ZnO nanocrystals at various stages of UV irradiation in the presence of $Li[Et_3BH]$. As with ZnO nanocrystals photodoped using EtOH (Figure 3.1c), increased UV irradiation causes an increase in g value and a broadening of the EPR signal.[9] Figure 3.4b plots EPR spectra of the same ZnO nanocrystals photodoped to their maximum extent using EtOH or $Li[Et_3BH]$ as the hole quencher. Consistent with the absorption experiments, the higher g value and broader line width of the latter confirms that photodoping using $Li[Et_3BH]$ as the hole quencher yields higher densities of conduction-band electrons in colloidal ZnO nanocrystals.

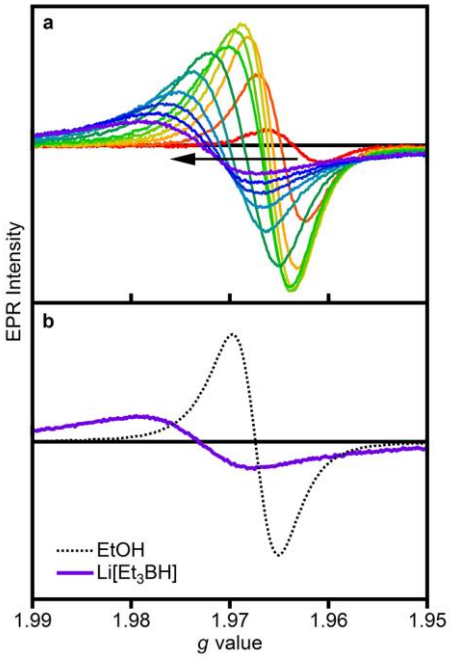

Figure 3.4. EPR spectra of photodoped ZnO nanocrystals with different hole quenchers. (a) Spectra recorded at various stages of UV irradiation in the presence of $Li[Et_3BH]$. (b) Comparison of the same nanocrystals photodoped to the maximum extent using EtOH (dotted black line) or $Li[Et_3BH]$ (solid purple line) as the hole quencher. Spectra are for colloidal r = 2.15 nm TOPO-capped ZnO nanocrystals in toluene.

To gain further insight into the reactivity of the borohydride hole quenchers, electron accumulation kinetics were measured with various hole quenchers. Anaerobic solutions of r = 2.8 nm ZnO nanocrystals were prepared in the presence of each hole quencher and exposed to UV illumination under identical conditions. Figure 3.5a plots the relative NIR absorption intensities ($A_{photodoped} - A_{as\text{-}prepared}$ at 1400 nm) as a function of UV irradiation time. For a given sample, these values are directly proportional to the average number of accumulated electrons per nanocrystal, $\langle n \rangle$. In all cases, $\langle n \rangle$ increases rapidly before leveling off at $\langle n_{max} \rangle$. A salient observation from these measurements is that photodoping with the hydride hole quenchers reaches $\langle n_{max} \rangle$ much more quickly than with EtOH, despite the fact that EtOH is added at concentrations ~40 times greater than the hydrides in these experiments. To test if the difference

in rates between the hydrides and EtOH may simply relate to the addition of cations such as Li^+, parallel photodoping measurements were performed using EtOH with added $Li[PF_6]$. The addition of $Li[PF_6]$ has only a minor effect on the ZnO photodoping kinetics and no effect on $\langle n_{max} \rangle$ (Figure 3.5a). Similarly, addition of the acid $[H(Et_2O)_2][BAr_F]$ before or during photodoping has no effect on $\langle n_{max} \rangle$ (Appendix D.4). The difference between the hydrides and EtOH is also not linked to the absolute magnitude of $\langle n_{max} \rangle$, because $[Bu_4N][Et_3BH]$ and EtOH yield very similar $\langle n_{max} \rangle$ values even though photoreduction is much faster when using $[Bu_4N][Et_3BH]$. We note that both EtOH curves in Figure 3.5a show a small amount (~10%) of rapid photodoping within the first 30 sec, followed by slower photodoping over the course of many minutes.

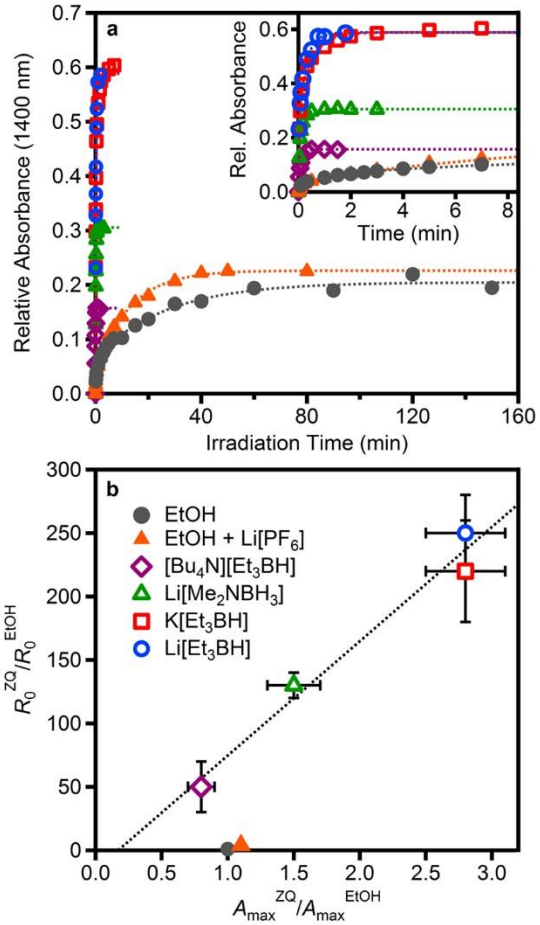

Figure 3.5. Kinetics of photodoping ZnO with various hole quenchers. (a) Relative absorbance at 1400 nm of colloidal r = 2.8 nm ZnO nanocrystals (TOPO-capped in 1:1 toluene/THF) irradiated with UV light in the presence of EtOH (filled gray circles), $[Bu_4N][Et_3BH]$ (open purple diamonds), $Li[Me_2NBH_3]$ (open green triangles), $K[Et_3BH]$ (open red squares), $Li[Et_3BH]$ (open blue circles), and EtOH with added $Li[PF_6]$ (open orange triangles). All solutions had the same nanocrystal concentration (~5 μM). The dashed lines show double exponential fits to the data. (b) Plot of R_0^{ZQ}/R_0^{EtOH} versus $A_{max}^{ZQ}/A_{max}^{EtOH}$ for EtOH (closed symbols) and hydride (open symbols) hole quenchers. The dotted line is a linear fit to the hydride data. Hydride and $Li[PF_6]$ concentrations were ~500 equivalents per nanocrystal, while EtOH concentrations were ~2 × 10^4 equivalents per nanocrystal.

To quantify the above observations, the data in Figure 3.5a were fit to a double exponential function (dotted lines) to extract initial photodoping rates ($R_0 = \left(dA/dt\right)\big|_{t=0}$) and asymptotic absorbance values (A_{max}, which represents the absorbance at $<n_{max}>$).[28] The trends in these two

parameters are largely insensitive to the precise form of the fitting function (*e.g.*, bi- versus multi-exponential). The details of this analysis are provided in the Appendix D.5, and the results are summarized in Table 3.2. The ratio $A_{max}^{ZQ}/A_{max}^{EtOH}$ in Table 3.2 reflects the ratio $<N_{max}^{ZQ}>/<N_{max}^{EtOH}>$ for these measurements and is analogous to the data of Figure 3.3b summarized in Table 3.1, except not averaged over multiple nanocrystal radii and measured at only one absorption wavelength. The trends summarized in Table 3.2 capture (*i*) the faster photodoping achieved with all of the hydrides relative to EtOH, and (*ii*) the greater photodoping levels achieved with some hydrides relative to EtOH. Although R_0 increases rapidly from EtOH to $[Bu_4N][Et_3BH]$ and $Li[Me_2NBH_3]$, there is no corresponding increase in $A_{max}^{ZQ}/A_{max}^{EtOH}$. Among the hydrides alone, however, R_0 and A_{max} ($<N_{max}>$) appear strongly correlated. To illustrate this point, Figure 3.5b plots R_0^{ZQ}/R_0^{EtOH} versus $A_{max}^{ZQ}/A_{max}^{EtOH}$ for each hole quencher. The hydride data all fall onto the same line, whereas the EtOH data lie well below this line.

Table 3.2. Summary of the time dependence for colloidal r = 2.8 nm ZnO nanocrystal photodoping in the presence of various hole quenchers, based on analysis of the data in Figure 3.5a.

ZQ	R_0^{ZQ}/R_0^{EtOH}	$A_{max}^{ZQ}/A_{max}^{EtOH}$
EtOH	1	1
EtOH + $Li[PF_6]$	4 ± 1	1.1 ± 0.1
$[Bu_4N][Et_3BH]$	50 ± 20	0.8 ± 0.1
$Li[Me_2NBH_3]$	130 ± 10	1.5 ± 0.2
$K[Et_3BH]$	220 ± 40	2.8 ± 0.3
$Li[Et_3BH]$	250 ± 30	2.8 ± 0.3

Finally, we note the observation of Zn^{2+} reduction to form metallic Zn^0 when photodoping is performed in the presence of excess $Li[Et_3BH]$, $Li[Me_2NBH_3]$, and to lesser extent, $K[Et_3BH]$

hole quenchers. Zn^0 is not observed when photodoping is performed in the presence of excess EtOH or $[Bu_4N][Et_3BH]$. The formation of a metallic species was noticed by a brown/black coloration of the ZnO nanocrystal suspensions upon photolysis (Appendix D.6). Considerably more coloration is observed when UV photodoping is performed in the presence of a large excess of hydride compared to when small aliquots of hydride are titrated in during the photodoping process. Within experimental uncertainty, the same value of $\langle n_{max} \rangle$ was achieved for any given hole quencher, regardless of how much coloration was observed. Under the conditions used for the data presented above, metallic Zn^0 could not be detected analytically, for example, by pXRD or TEM, suggesting its presence in trace quantities. Eventually, metallization was confirmed by pXRD of samples exposed to prolonged UV irradiation (24 h) in the presence of a very large excess of $Li[Et_3BH]$ ($>10^4$ equivalents, Appendix D.6). These conditions are extreme compared to those used for the data presented above (~3–10 min irradiation with $\leq$ 500 equivalents hydride). The collected byproduct showed sharp pXRD peaks attributable to relatively large Zn^0 metal particles, as well as weaker, similarly sharp peaks that were unidentifiable but may reflect formation of a Li_xZn intermetallic similar to that observed following electrochemical reduction of ZnO nanowires in the presence of Li^+.[29]

3.4 Discussion

The data presented above allow three primary conclusions to be drawn about colloidal ZnO nanocrystal photodoping: (*i*) Photodoping using EtOH as the hole quencher shows a strong volume dependence and no evident dependence on other experimental variables (ligand, solvent, concentration, photolysis conditions, added cations, luminescence quantum yield), such that the entire collection of present and literature data is described well by a single average maximum

electron density of $<<N_{max}^{EtOH}>> = 1.4 \pm 0.4 \times 10^{20}$ cm^{-3}; (*ii*) Similar volume dependence is observed with other hole quenchers (ZQ), but $<<N_{max}>>$ depends on ZQ and can be increased substantially by switching from EtOH to Li[Et_3BH] or K[Et_3BH]; (*iii*) Under specific photodoping conditions, metallic Zn^0 is formed, indicating electron localization that appears to be aided by Li^+ and, to a lesser extent, K^+.

The strong dependence of $<n_{max}>$ on volume when using EtOH as the hole quencher, and its weak dependence on other experimental parameters, is a central result from this work that raises fundamental questions about the microscopic origins of this doping limit in ZnO nanocrystals. Bulk ZnO shows a similar *n*-type doping limit ($N_{max} \sim 10^{21}$ cm^{-3}),[30] which has been proposed to arise from enhanced formation of compensating Zn^{2+}-vacancy centers under heavy *n*-type aliovalent doping conditions.[31] Analogously, in ZnO nanocrystals, *n*-doping by Al^{3+} substitution may be viewed as being limited by the capacity of localized surface charges to compensate the aliovalent dopants.[10] Nanocrystal photodoping, however, is likely limited by the photoprocesses themselves. Reaching an $<n_{max}>$ means that the net photodoping probability decreases to zero as $<n>$ (or $<N>$) increases.

As discussed previously,[2,26] one possible photophysical origin of $<n_{max}>$ in photodoped ZnO nanocrystals could be the competition between hole quenching and multicarrier Auger recombination. For example, after successful addition of one extra conduction-band electron to a ZnO nanocrystal, the addition of a second electron must proceed via a negative trion. If trion Auger recombination occurs before the valence band hole is transferred to the hole quencher, a second electron will not be accumulated in the nanocrystal. A similar competition applies to quenching of trapped holes.[27] Thus, to add more than one e^-_{CB} per nanocrystal, hole quenching must compete kinetically with multicarrier Auger recombination. Because multicarrier Auger

recombination rates increase with the number of excess charge carriers,[32] Auger recombination should become progressively more competitive with hole quenching and could thus determine $\langle n_{max} \rangle$. Recently, however, it was shown that hole capture by EtOH is roughly an order of magnitude faster (<15 ps) than trion Auger recombination (~150 ps, ref. 33, both size dependent) and should therefore be kinetically competent for the accumulation of multiple conduction-band electrons.[26] Furthermore, the exciton lifetime was shown to *increase* with increasing $\langle n \rangle$, all the way up to $\langle n_{max} \rangle$,[26] whereas exciton lifetimes limited by multicarrier Auger recombination would decrease with increasing $\langle n \rangle$. Consequently, we conclude that $\langle n_{max} \rangle$ is not limited solely by multicarrier Auger recombination.

A second possibility is that $\langle n_{max} \rangle$ is determined primarily by the properties of the hole quencher, ZQ. This possibility was investigated by using Li[Et_3BH], K[Et_3BH], Li[Me_2NBH_3], and [Bu_4N][Et_3BH] in place of EtOH. For a given nanocrystal sample, $\langle n_{max} \rangle$ could be increased more than fourfold by using a more reactive hole quencher. Thus, $\langle n_{max} \rangle$ clearly depends on the identity of ZQ. Moreover, the data suggest that both the anionic (Q^-) and cationic (Z^+) portions of ZQ influence photodoping. For example, $[Et_3BH]^-$ is a common reducing agent whose alkyl electron-donating groups make it more reducing than an unsubstituted borohydride. Conversely, the electron-withdrawing nitrogen of $[Me_2NBH_3]^-$ makes this species less reducing than an unsubstituted borohydride. Both of these hydrides are expected to be much better reductants than EtOH. Based on these qualitative considerations, the trend in $\langle n_{max} \rangle$ for a given ZnO sample could be anticipated to be $[Et_3BH]^- > [Me_2NBH_3]^- >$ EtOH, which agrees well with the experimental trend of Li[Et_3BH] ≈ K[Et_3BH] > Li[Me_2NBH_3] > EtOH (Table 3.1). This correlation indicates that $\langle n_{max} \rangle$ is in some way affected by the strength of Q^- as a reductant.

Still, the effect is relatively modest, with only three times higher $<n_{max}>$ for $Li[Et_3BH]$ than for EtOH despite the much greater reducing power of the borohydride.

The outlier in the above trend is $[Bu_4N][Et_3BH]$, which is unable to reduce the nanocrystals to the same extent as its Li^+ and K^+ counterparts can and is only slightly more effective than EtOH. This result indicates that the cations also play an important role. On one hand, the smaller $<n_{max}>$ obtained with $[Bu_4N][Et_3BH]$ could be attributed to poorer stabilization of ZnO electrons by the bulky $[Bu_4N]^+$ cation. This interpretation would be consistent with the greater effect of Li^+ than Bu_4N^+ on the band-edge energies of bulk ZnO. It is also consistent with recent work demonstrating greater chemical reduction of ZnO nanocrystals when using protons rather than bulky metallocene cations for electron charge compensation.[34] It is conceivable, however, that the bulky $[Bu_4N]^+$ cation merely limits the effective surface hydride concentration and thereby reduces the probability of hole capture, despite a sufficient thermodynamic driving force.

The insensitivity of $<n_{max}>$ to added $Li[PF_6]$ or $[H(Et_2O)][BAr_F]$ when using EtOH as the hole quencher is a particularly striking result, given the previous demonstration that protons shift colloidal ZnO nanocrystal conduction-band-edge potentials and thereby tune $<n_{max}>$ when using chemical reductants such as $CoCp^*_2$ or $CrCp^*_2$.[34] A clear conclusion can be drawn that the photochemical $<n_{max}>$ is not directly determined by the same equilibrium thermodynamics as the chemical $<n_{max}>$. For photodoping, the potentials of the photogenerated holes are probably more relevant than the equilibrium Fermi levels of the reduced nanocrystals, and these holes are likely always sufficiently powerful to oxidize the hydrides explored here.

It is noteworthy that all of the hydrides examined here yield substantially faster photochemical electron accumulation than EtOH does (Figure 3.5a) despite their lower solution concentration. We hypothesize that this faster photodoping reflects greater effective

concentrations of the hydrides at the ZnO nanocrystal surfaces compared to EtOH. For example, it is possible that EtOH is only reactive when bound dissociatively to the ZnO surface,[35,36] a condition that would limit its effective concentration. Indeed, Figure 3.5a shows an initial fast component to photodoping with EtOH (up to ~10% of A_{max}), followed by slower photodoping for the remaining 90%. This behavior would be consistent with EtOH pre-association and subsequent photodoping rates limited by EtOH configuration. EtOH is thus qualitatively different from the hydrides. When just the hydrides are considered, the initial photodoping rates correlate well with $<n_{max}>$ (Figure 3.5b).

Overall, we conclude that $<n_{max}>$ for any given nanocrystal sample is directly determined by ZQ, whereas the volumetric scaling of $<n_{max}>$ is universal for all ZQ and hence is intrinsic to the ZnO nanocrystals. One explanation is that $<n_{max}>$ is determined primarily by unfavorable hole-capture kinetics at large $<n>$, possibly ultimately arising from hole stabilization and contraction due to Coulomb interaction with the multiple accumulated electrons, as described previously.[26]

Finally, we address the formation of metallic Zn^0. The formation of Zn^0 metal has been reported following UV illumination of ZnO sol-gel films[37] and single crystals,[38] accompanied by marked coloration. Black precipitates were also observed in early studies of the photoreduction of ZnO nanocrystals suspended in propanol, and the band-edge absorption bleach upon UV irradiation was therefore initially interpreted entirely in terms of surface Zn^{2+} reduction to Zn^0 metal.[39] It was subsequently recognized by the same authors that delocalized electrons were being stored within the ZnO nanocrystals following photoreduction.[5] The possibility of electron localization in reduced ZnO nanocrystals has since been heavily debated.[7,40,41] The results presented here demonstrate unambiguously that localization of excess electrons in ZnO nanocrystals can occur under specific experimental conditions. Strikingly, Zn^0 forms with only

three of our five hole quenchers, and without any apparent correlation to $\langle n_{max} \rangle$. Specifically, only those hole quenchers involving Li^+, and to a far lesser extent K^+, show evidence of Zn^0 formation. Under identical conditions, photodoping with $Li[Et_3BH]$ leads to far more coloration than $K[Et_3BH]$ despite their nearly identical $\langle n_{max} \rangle$, and no coloration is observed with $[Bu_4N][Et_3BH]$. Likewise, under identical conditions, photodoping with $Li[Me_2NBH_3]$ leads to much more coloration than with $K[Et_3BH]$, despite nearly a factor of two smaller $\langle n_{max} \rangle$. Overall, these results implicate the cations of ZQ as non-innocent in the electron-localization process. We hypothesize that Zn^{2+} reduction is facilitated by Li^+ (and to a lesser extent by K^+), which shifts the surface $Zn^{2+/0}$ potential more positive relative to the ZnO conduction-band edge by interacting strongly with surface oxo anions. Li_2O has a greater lattice energy than K_2O, making Zn^0 formation more thermodynamically favorable with Li^+. In support of this interpretation, we note that research into the use of ZnO nanostructures as Li^+ battery anodes[29] has demonstrated that extensive electrochemical reduction in the presence of Li^+ electrolyte severely disrupts the ZnO lattice, eventually converting it to amorphous Li_2O and Zn^0 metal. We propose that similar chemistries occur to a lesser extent under our photochemical reduction conditions when using Li^+-containing hole quenchers.

It remains an open question why more Zn^0 is observed with a large excess of $Li[Et_3BH]$ or $K[Et_3BH]$ compared to when the same quantities of these hole quenchers are added in small aliquots, and why it is not observed in nanocrystals photochemically reduced with EtOH in the presence of $Li[PF_6]$. These observations may implicate an unrelated dark chemical reaction of the hydride. In any case, Zn^0 constitutes a trace side product whose formation appears to be unrelated to $\langle n_{max} \rangle$. Overall, the observation of Zn^0 precipitates under specific photodoping

conditions is both cautionary and potentially revealing of the roles of hard Lewis acids in compensating the charges of added electrons in ZnO nanostructures.

3.5 Summary and conclusions

In summary, the maximum number of kinetically stable, conduction-band electrons that can be added to colloidal ZnO nanocrystals by photochemical oxidation of EtOH increases rapidly with increasing nanocrystal radius, scaling roughly as $\langle n_{max} \rangle \propto r^3$. These numbers are remarkably independent of other experimental parameters. Consequently, ZnO nanocrystals of all radii may be reduced to similar maximum electron *densities* ($\langle\langle N_{max}^{EtOH} \rangle\rangle = 1.4 \pm 0.4 \times 10^{20}$ cm^{-3}) when EtOH is the hole quencher. By switching from EtOH to hydride hole quenchers, $\langle N_{max} \rangle$ can be increased up to ~6×10^{20} cm^{-3}. This is a very high value, corresponding to one added electron per ~70 Zn^{2+} ions in the nanocrystal. Work is ongoing to define the structures of these highly reduced nanocrystals, which may be better described as $ZnLi_xO$. Further investigation into this chemistry will be of interest both fundamentally and in relation to nanostructured Li^+/ZnO ion battery electrodes. These data suggest that ZnO photodoping limits are determined by the specific identity of ZQ, correlating with the reducing ability of Q^- and influenced by the identity of the countercation. These results are interpreted in terms of competing hole capture and non-productive recombination channels, a competition that evolves with $\langle n \rangle$. The observation of Zn^0 formation in the presence of Li^+ cations, and to a lesser extent K^+, but not with H^+ or $[Bu_4N]^+$, indicates that electron localization can occur under specific conditions.

The results presented here reconcile the disparate values of electron accumulation reported previously for colloidal ZnO nanocrystals photodoped using EtOH and expand the range of

carrier densities achievable in such nanocrystals via photochemical reduction. This ability to tune carrier densities in colloidal semiconductor nanocrystals over a broad range promises to have interesting ramifications in many areas including nanocrystal redox chemistries, nanocrystal doping, and quantum dot plasmonics.

3.6 Experimental methods

Synthesis and general characterization are described in Appendix A. CW EPR measurements were collected using a Bruker EMX X-band spectrometer with a SHQE resonator operating at 9.8 GHz. The *g* values were measured in reference to DPPH (g = 2.0036).

3.6.1 ***Photodoping.*** General photodoping considerations are provided in Appendix B. For kinetic measurements, TOPO-capped r = 2.8 nm nanocrystals suspended in 1:1 toluene/THF were used. Nanocrystal solutions were prepared to contain ~5 μM nanocrystals. The samples photodoped using hydrides were prepared with ~500 equivalents of hydride. The samples photodoped using EtOH and EtOH/Li[PF_6] were prepared with ~2 × 10^4 equivalents EtOH and ~2 × 10^4 equivalents EtOH plus ~500 equivalents Li[PF_6], respectively. All samples were stirred while irradiating.

3.6.2 ***Electron counting.*** The average number of excess electrons per ZnO nanocrystal (<n>) photodoped using EtOH was determined by titration with [$FeCp^*_2$][BAr_F].[10,17] Details and example titration data are provided in Appendix B. For the other hole quenchers, <n> was determined ratiometrically by comparing their NIR absorption (integrated between 800 and 1400 nm, far in the high-energy tail of the IR absorption band) with that of the same nanocrystals photodoped using EtOH (see Appendix D.2 for details). In select cases, these reduced nanocrystals were also titrated against [$FeCp^*_2$][BAr_F], and good agreement between the titration

and ratiometric optical methods was observed. All size-dependent electron-counting data presented in this chapter were fit in original (linear) form. For fits obtained using the log-log form of the data, see Appendix D.3.

3.7 References

1. Shim, M.; Guyot-Sionnest, P. *n*-Type Colloidal Semiconductor Nanocrystals. *Nature* **2000**, *407*, 981.

2. Shim, M.; Guyot-Sionnest, P. Organic-Capped ZnO nanocrystals: Synthesis and *n*-Type Character. *J. Am. Chem. Soc.* **2001**, *123*, 11651.

3. Luther, J.; Jain, P.; Ewers, T.; Alivisatos, A. Localized Surface Plasmon Resonances Arising from Free Carriers in Doped Quantum Dots. *Nat. Mater.* **2011**, *10*, 361.

4. Manthiram, K.; Alivisatos, A. Tunable Localized Surface Plasmon Resonances in Tungsten Oxide Nanocrystals. *J. Am. Chem. Soc.* **2012**, *134*, 3995.

5. Haase, M.; Weller, H.; Henglein, A. Photochemistry and Radiation Chemistry of Colloidal Semiconductors. 23. Electron Storage on ZnO Particles and Size Quantization. *J. Phys. Chem.* **1988**, *92*, 482.

6. Wood, A.; Giersig, M.; Mulvaney, P. Fermi Level Equilibration in Quantum Dot-Metal Nanojunctions. *J. Phys. Chem. B* **2001**, *105*, 8810.

7. Vanmaekelbergh, D.; Roest, A. L.; Germeau, A.; Kelly, J. J.; Meulenkamp, E. A.; Allan, G.; Delerue, C. Vanmaekelbergh et al. Reply. *Phys. Rev. Lett.* **2003**, *91*, 169704.

8. Liu, W. K.; Whitaker, K. M.; Kittilstved, K. R.; Gamelin, D. R. Stable Photogenerated Carriers in Magnetic Semiconductor Nanocrystals. *J. Am. Chem. Soc.* **2006**, *128*, 3910.

9. Liu, W. K.; Whitaker, K. M.; Smith, A. L.; Kittilstved, K. R.; Robinson, B. H.; Gamelin, D. R. Room-Temperature Electron Spin Dynamics in Free-Standing ZnO Quantum Dots. *Phys. Rev. Lett.* **2007**, *98*, 186804.

10. Schimpf, A. M.; Ochsenbein, S. T.; Buonsanti, R.; Milliron, D. J.; Gamelin, D. R. Comparison of Extra Electrons in Colloidal *n*-Type Al^{3+}-Doped and Photochemically Reduced ZnO Nanocrystals. *Chem. Commun.* **2012**, *48*, 9352.

11. Wang, C. J.; Shim, M.; Guyot-Sionnest, P. Electrochromic Nanocrystal Quantum Dots. *Science* **2001**, *291*, 2390.

12. Roest, A. L.; Kelly, J. J.; Vanmaekelbergh, D.; Meulenkamp, E. A. Staircase in the Electron Mobility of a ZnO Quantum Dot Assembly due to Shell Filling. *Phys. Rev. Lett.* **2002**, *89*, 036801.

13. Guyot-Sionnest, P. Charging Colloidal Quantum Dots by Electrochemistry. *Microchim. Acta* **2008**, *160*, 309.

14. Kanehara, M.; Koike, H.; Yoshinaga, T.; Teranishi, T. Indium Tin oxide Nanoparticles with Compositionally Tunable Surface Plasmon Resonance Frequencies in the Near-IR Region. *J. Am. Chem. Soc.* **2009**, *131*, 17736.

15. Wang, T.; Radovanovic, P. V. Free Electron Concentration in Colloidal Indium Tin Oxide Nanocrystals Determined by Their Size and Structure. *J. Phys. Chem. C* **2011**, *115*, 406.

16. Buonsanti, R.; Llordes, A.; Aloni, S.; Helms, B.; Milliron, D. Tunable Infrared Absorption and Visible Transparency of Colloidal Aluminum-Doped Zinc Oxide Nanocrystals. *Nano Lett.* **2011**, *11*, 4706.

17. Schrauben, J.; Hayoun, R.; Valdez, C.; Braten, M.; Fridley, L.; Mayer, J. Titanium and Zinc Oxide Nanoparticles Are Proton-Coupled Electron Transfer Agents. *Science* **2012**, *336*, 1298.

18. Markham, M. C.; Hannan, M. C.; Paternostro, R.; Rose, C. B. Oxidation of Alcohols Catalyzed by Zinc Oxide and Light. *J. Am. Chem. Soc.* **1958**, *80*, 5394.

19. Gomes, W. P.; Freund, T.; Morrison, S. R. Chemical Reactions Involving Holes at the Zinc Oxide Single Crystal Anode. *J. Electrochem. Soc.* **1968**, *115*, 818.

20. Cunningham, J.; Hodnett, B. K. Kinetic Studies of Secondary Alcohol Photo-oxidation on ZnO and TiO2 at 348 K Studied by Gas-Chromatographic Analysis. *J. Chem. Soc., Faraday Trans. 1* **1981**, *77*, 2777.

21. Whitaker, K. M.; Ochsenbein, S. T.; Polinger, V. Z.; Gamelin, D. R. Electron Confinement Effects in the EPR Spectra of Colloidal n-Type ZnO Quantum Dots. *J. Phys. Chem. C* **2008**, *112*, 14331.

22. Ochsenbein, S. T.; Feng, Y.; Whitaker, K. M.; Badaeva, E.; Liu, W. K.; Li, X.; Gamelin, D. R. Charge-Controlled Magnetism in Colloidal Doped Semiconductor Nanocrystals. *Nat. Nanotechnol.* **2009**, *4*, 681.

23. Whitaker, K. M.; Ochsenbein, S. T.; Smith, A. L.; Echodu, D. C.; Robinson, B. H.; Gamelin, D. R. Hyperfine Coupling in Colloidal *n*-Type ZnO Quantum Dots: Effects on Electron Spin Relaxation. *J. Phys. Chem. C* **2010**, *114*, 14467.

24. Hayoun, R.; Whitaker, K. M.; Gamelin, D. R.; Mayer, J. M. Electron Transfer Between Colloidal ZnO Nanocrystals. *J. Am. Chem. Soc.* **2011**, *133*, 4228.

25. Cohn, A. W.; Kittilstved, K. R.; Gamelin, D. R. Tuning the Potentials of "Extra" Electrons in Colloidal n-type ZnO Nanocrystals via Mg^{2+} Substitution. *J. Am. Chem. Soc.* **2012**, *134*, 7937.

26. Cohn, A. W.; Janßen, N.; Mayer, J. M.; Gamelin, D. R. Photocharging ZnO Nanocrystals: Picosecond Hole Capture, Electron Accumulation, and Auger Recombination. *J. Phys. Chem. C* **2012**, *116*, 20633.

27. Cohn, A. W.; Schimpf, A. M.; Gunthardt, C. E.; Gamelin, D. R. Size-Dependent Trap-Assisted Auger Recombination in Semiconductor Nanocrystals. *Nano Lett.* **2013**, *13*, 1810.

28. Strictly speaking, these curves are apparent rates of appearance of conduction-band electrons under the specific photolysis conditions. The relative rates likely mostly reflect the change in photodoping quantum yield as a function of $\langle n_e \rangle$. The relative rates are informative because the photolysis conditions and lamp intensity were kept quite constant over all the experiments, as described in the Supporting Information.

29. Kushima, A.; Liu, X. H.; Zhu, G.; Wang, Z. L.; Huang, J. Y.; Li, J. Leapfrog Cracking and Nanoamorphization of ZnO Nanowires During In Situ Electrochemical Lithiation. *Nano Lett.* **2011**, *11*, 4535.

30. Agashe, C.; Kluth, O.; Hupkes, J.; Zastrow, U.; Rech, B.; Wuttig, M. Efforts to Improve Carrier Mobility in Radio Frequency Sputtered Aluminum Doped Zinc Oxide Films. *J. Appl. Phys.* **2004**, *95*, 1911.

31. Noh, J.-Y.; Kim, H.; Kim, Y.-S.; Park, C. H. Electron Doping Limit in Al-Doped ZnO by Donor-Acceptor Interactions. *J. Appl. Phys.* **2013**, *113*, 153703.

32. Klimov, V. I.; Mikhailovsky, A. A.; McBranch, D. W.; Leatherdale, C. A.; Bawendi, M. G. Quantization of Multiparticle Auger Rates in Semiconductor Quantum Dots. *Science* **2000**, *287*, 1011.

33. Yamamoto, S. Photoenhanced Band-Edge Luminescence in ZnO Nanocrystals Dispersed in Ethanol. *J. Phys. Chem. C* **2011**, *115*, 21635.

34. Valdez, C. N.; Braten, M.; Soria, A.; Gamelin, D. R.; Mayer, J. M. Effect of Protons on the Redox Chemistry of Colloidal Zinc Oxide Nanocrystals. *J. Am. Chem. Soc.* **2013**, *135*, 8492.

35. Nagao, M.; Morimoto, T. Adsorption of Alcohols on Zinc Oxide Surfaces. *J. Phys. Chem.* **1980**, *84*, 2054.

36. Vohs, J. M.; Barteau, M. A. Dehydration and Dehydrogenation of Ethanol and 1-Propanol on the Polar Surfaces of Zinc Oxide. *Surf. Sci.* **1989**, *221*, 590.

37. Asakuma, N.; Hirashima, H.; Fukui, T.; Toki, M.; Awazu, K.; Imai, H. Photoreduction of Amorphous and Crystalline ZnO Films. *Jpn. J. Appl. Phys.* **2002**, *41*, 3909.

38. Khan, E. H.; Langford, S. C.; Dickinson, J. T.; Boatner, L. A.; Hess, W. P. Photoinduced Formation of Zinc Nanoparticles by UV Laser Irradiation of ZnO. *Langmuir* **2009**, *25*, 1930.

39. Koch, U.; Fojtik, A.; Weller, H.; Henglein, A. Photochemistry of Semiconductor Colloids. Preparation of Extremely Small ZnO Particles, Fluorescence Phenomena and Size Quantization Effects. *Chem. Phys. Lett.* **1985**, *122*, 507.

40. Hoyer, P.; Weller, H. Potential-Dependent Electron Injection in Nanoporous Colloidal ZnO Films. *J. Phys. Chem.* **1995**, *99*, 14096.

41. Shim, M.; Guyot-Sionnest, P. Comment on "Staircase in the Electron Mobility of a ZnO Quantum Dot Assembly Due to Shell Filling" and "Optical Transitions in Artificial Few-Electron Atoms Strongly Confined Inside ZnO Nanocrystals". *Phys. Rev. Lett.* **2003**, *91*, 169703.

Chapter 4

Photochemical Electronic Doping of CdSe Nanocrystals

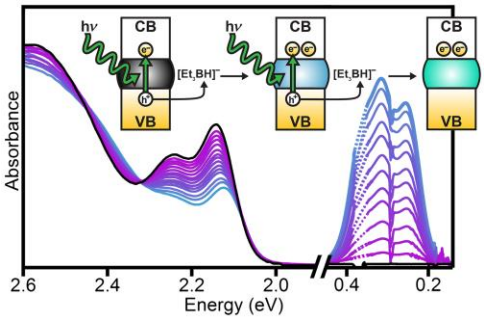

Adapted from: Rinehart, J. D.; Schimpf, A. M.; Weaver, A. L.; Cohn, A. W.; Gamelin, D. R. *J. Am. Chem. Soc.* 2013, *135*, 18782.

4.1 Overview

A method for electronic doping of colloidal CdSe nanocrystals is reported. Anaerobic photoexcitation of CdSe nanocrystals in the presence of a borohydride hole quencher, Li[Et_3BH], yields colloidal *n*-type CdSe nanocrystals possessing extra conduction-band electrons compensated by cations deposited by the hydride hole quencher. The photodoped nanocrystals possess excellent optical quality and display the key spectroscopic signatures associated with nanocrystal *n*-doping, including a bleach at the absorption edge, appearance of a new IR absorption band, and Auger quenching of the excitonic photoluminescence. Although stable under anaerobic conditions, these spectroscopic changes are all reversed completely upon exposure of the *n*-doped nanocrystals to air. Chemical titration of the added electrons confirms previous correlations between absorption bleach and electron accumulation, and provides a means of quantifying the extent of electron trapping in some nanocrystals. The generality of this photodoping method is demonstrated by initial results on colloidal CdE (E = S, Te) nanocrystals as well as on CdSe quantum dot films.

4.2 Introduction

The generation and manipulation of charge carriers in semiconductor nanostructures is central to emerging solar,[1-5] battery,[6,7] nanoelectronics,[8] and nanospintronics[9-11] technologies, as well as to nanocrystal blinking and multi-carrier Auger processes that impact the use of such nanostructures as phosphors in display, lasing, or imaging technologies.[12-14] To study the physical properties of semiconductor nanostructures possessing extra charge carriers, chemical reduction of colloidal nanocrystals,[15] electrochemical reduction of quantum dot solids,[16] and low-temperature charge separation[17] have been used to introduce the carriers. Many of these processes involve harsh reductants, require precipitation and ligand exchange, or only occur at cryogenic temperatures. A general method for introducing additional charge carriers to free-standing colloidal nanocrystals would enable a wide variety of experiments and applications involving electronically doped semiconductor nanocrystals.

Photochemistry offers a convenient in situ method for modulating carrier densities in colloidal nanocrystals. For photochemical *n*-doping, capture of photogenerated holes by suitable hole quenchers strands extra electrons inside the nanocrystals, compensated by cations deposited upon quencher oxidation. This method has been applied successfully with several oxide semiconductor nanocrystals.[18-21] Despite the fact that chalcogenide semiconductor nanocrystals are frequently used as sensitizers in solar photochemistry, photovoltaic, and photoelectrochemical devices because of their strong visible absorption and ability to separate photogenerated charges,[1-5] photochemical electronic doping of this class of nanomaterials has not been explored. In contrast with oxides, chalcogenides such as CdE (E = S, Se, Te) possess shallow valence bands and are consequently not as reactive toward many hole quenchers commonly used with oxides. For generality, more reactive hole quenchers are thus required.

Here, we report facile and reversible photodoping of colloidal CdSe nanocrystals using a reactive borohydride, Li[Et_3BH], as the hole quencher. This photodoping allows formation of kinetically stable colloidal *n*-type CdSe nanocrystals without the surface degradation caused by chemical reductants examined previously. Moreover, this approach allows CdSe nanocrystal doping even in the presence of ZnSe shells that impede direct electron injection. Although the present work is focused on colloidal CdSe quantum dots, it is expected to be broadly applicable for preparing *n*-type nanocrystals in various forms. Proof-of-concept results confirm successful CdE (E = S, Te) quantum dot photodoping, as well as photodoping of CdSe quantum dot solids.

4.3 Results and discussion

Colloidal TOPO-capped CdSe nanocrystals with average diameters (*d*) of 3.8 and 7.0 nm were prepared by established synthetic procedures.[22] These nanocrystals were transferred to dry, deoxygenated toluene and stored in the presence of excess TOPO under inert atmosphere. Under these conditions, exposure to visible or UV radiation does not alter the nanocrystal spectra or cause sample degradation. After addition of Li[Et_3BH] to these suspensions, exposure to light exceeding the band gap energy causes a bleach of the first excitonic absorption feature (Figure 4.1). This bleach occurs even with excitation solely by ambient room light, but no absorption changes are detected without photoexcitation (Appendix E.1).

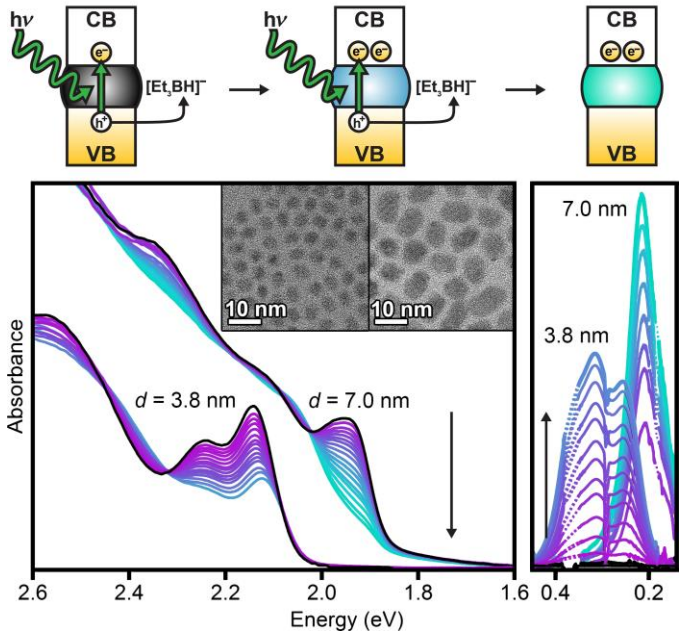

Figure 4.1. Photochemical electron accumulation in CdSe nanocrystals. Top: Schematic description of nanocrystal photodoping using $[Et_3BH]^-$. A photogenerated hole (h^+) is quenched by $[Et_3BH]^-$, leaving an electron (e^-) in the conduction band. Extended photoexcitation can add more electrons. Bottom: Absorption spectra of d = 3.8 nm and d = 7.0 nm CdSe nanocrystals and the same nanocrystals at various stages of photodoping starting from as-prepared (black) to maximum photodoping (teal). The arrows show increased exposure to UV illumination. The data show the exciton bleach and growth of IR absorption with increased photodoping. Inset: TEM images of these nanocrystals.

The observed absorption bleach approaches an asymptotic limit with extended photoexcitation. When the absorption spectrum is unchanged over ~30 s of photoexcitation, the samples are considered to have reached their maximum photodoping level. Photodoping can be stopped at any intermediate stage. Partially photodoped CdSe nanocrystals can be used for spectroscopic measurements and the photoexcitation can be resumed to increase photodoping up the asymptotic limit. Exposure of the reduced nanocrystals to an appropriate oxidant completely reverses the absorption bleach and returns their as-prepared spectroscopic properties (*vide infra).*

The absorption bleach is a signature of the presence of one or more delocalized electrons in the quantum-confined CdSe nanocrystal conduction band.[15] This bleach is accompanied by a

concurrent redshift of the first two excitonic absorption bands (*e.g.*, ~−15 meV for the d = 3.8 nm CdSe nanocrystals at maximum photodoping in Figure 4.2, (Appendix E.2). This redshift is comparable to that of trion luminescence relative to neutral exciton luminescence in other CdSe quantum dots[23,24] and is thus tentatively attribute to the reduced energy required for trion formation by photoexcitation of *n*-doped CdSe nanocrystals. Electrostatic exciton stabilization by localized charges may also contribute to the redshift. IR absorption spectroscopy verifies the presence of extra quantum-confined electrons, showing intense new absorption corresponding to intraband excitations of the newly introduced conduction electrons (Figure 4.1), with an energy that increases with decreasing nanocrystal diameter. A per-electron molar extinction coefficient of $8.9 \pm 0.6 \times 10^4$ $M_e^{-1}cm^{-1}$ is estimated at the IR absorption maximum (0.32 eV) of d = 3.8 nm CdSe nanocrystals (Appendix E.3). This IR absorption verifies that the added electrons do not simply reside in localized trap states. Interestingly, the IR absorption of the smaller nanocrystals shows distinct structure. Similar structure has been seen previously in chemically reduced CdSe nanocrystals[15] and may reflect a low-symmetry splitting of the $1P_e$ degeneracy. The IR absorption grows with photodoping (Figure 4.1), and in some cases blueshifts slightly. These blueshifts are small compared to those observed in ZnO nanocrystals heavily photodoped (average electron density, $<N_{max}>$, $\approx 6 \times 10^{20}$ cm^{-3}) using the same hole quencher,[21] suggesting smaller carrier densities in the photodoped CdSe nanocrystals. The IR spectroscopic changes are also fully reversed upon nanocrystal reoxidation by exposure to air.

To quantify the maximum (average) number of excess electrons per nanocrystal ($<n_{max}>$) achievable by these methods, the magnitude of the absorption bleach was analyzed. Previous studies have established a linear correlation between the number of CdSe conduction-band electrons and the fractional bleach at the first excitonic absorption maximum, where a 100%

bleach corresponds to 2 conduction band electrons.[19,25] By Gaussian deconvolution of the absorption bleach data (Appendix E.2), we find a maximum bleach of 41% for the d = 3.8 nm CdSe nanocrystals and 98% for the d = 7.0 nm CdSe nanocrystals. The data in Figure 4.1 thus suggest $\langle n_{max} \rangle \approx 0.8$ ($\langle N_{max} \rangle \approx 2.8 \times 10^{19}$ cm^{-3}) and 2 (($\langle N_{max} \rangle \approx 1.1 \times 10^{19}$ cm^{-3}), respectively.

An attractive aspect of the photodoping method described here is that the resulting *n*-type nanocrystals are amenable to direct chemical titration of the added electrons, something not possible with chemically reduced nanocrystals because of the excess reductant present under equilibrium conditions. Chemical titration of excess electrons in chalcogenide nanocrystals has not been described previously. Figure 4.2 shows electronic absorption spectra of the 3.8 nm CdSe nanocrystals from Figure 4.1 before photodoping, at maximum photodoping, and at various stages of reoxidation by [$FeCp^*_2$][BAr_F]. Titration of these 3.8 nm nanocrystals yields an $\langle n_{max} \rangle$ of 0.97, consistent with the spectroscopic estimation. Titrations were also performed on d = 4.6 nm and 7.0 nm CdSe samples (Appendix E.4). Titration of the 4.6 nm nanocrystals yields $\langle n_{max} \rangle$ = 1.1, similar to the 1.4 estimated using absorption spectroscopy. By contrast, although the absorption bleach of the 7.0 nm CdSe suggests ~2.0 conduction-band electrons per nanocrystal, titration requires nearly 30 equivalents of [$FeCp^*_2$][BAr_F]. This divergence suggests substantial electron trapping in these nanocrystals, for example by surface di-selenide bonds.[26] This interpretation is supported by the fact that the same nanocrystal sample with different handling/storage history can hold different numbers of electrons (Appendix E.4). Many previous experiments have suggested the existence of near-band-edge electron traps in CdSe nanocrystals. Such traps have been proposed to play major roles in blinking and other physical processes,[5,13,27] but little is known about their potentials, densities, or redox reactivities. These results emphasize that titration is also sensitive to other electrons accessible at the potential defined by the titrant,

such as trapped electrons that do not contribute to the band-edge absorption bleach, and titration therefore complements the spectroscopic evaluation described above.

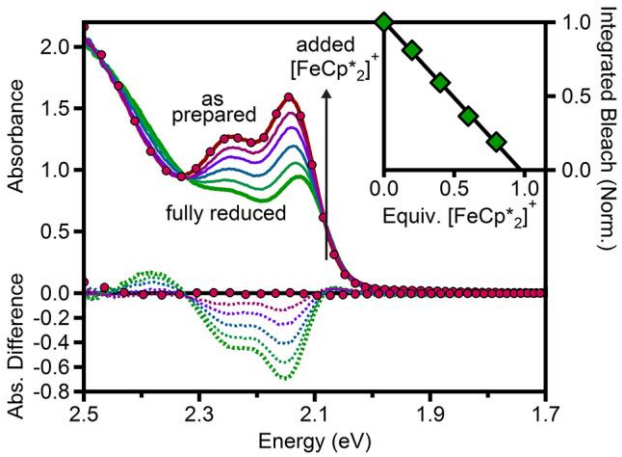

Figure 4.2. Titration of photodoped CdSe nanocrystals. Absorption spectra of d = 3.8 nm (43 μM) CdSe nanocrystals collected during redox titration in 1:1 toluene/THF. The red spectrum shows data collected before introduction of Li[Et_3BH]. The solid green spectrum is of the maximally photodoped nanocrystals, and the red circles represent the nanocrystals after re-oxidation in air. The intermediate spectra were collected following incremental oxidation by addition of $[FeCp^*_2]^+$ aliquots. The corresponding difference spectra ($A - A_{as\text{-}prepared}$) are plotted as dotted lines. Inset: Integrated absorption bleach of the first excitonic feature as a function of $[FeCp^*_2]^+$ equivalents, with a solid line showing the best linear fit to the data. The crossing of this line with zero indicates 0.97 electrons per nanocrystal.

A second attractive feature of this photodoping methodology is that the resulting colloidal *n*-type nanocrystals are of high spectroscopic quality, making them well suited for advanced characterization by various spectroscopic techniques. For illustration, Figure 4.3 summarizes the changes in room-temperature photoluminescence of d = 4.6 nm CdSe nanocrystals upon photodoping. For these measurements, thin ZnSe shells were grown around the nanocrystals to passivate surface traps and hence suppress nonradiative decay. Prior to photodoping, these nanocrystals show single-exponential excitonic photoluminescence decay with a time constant of

τ = 16 ns. After photodoping to <*n*> ~ 0.5 (estimated by absorption spectroscopy), their steady-state photoluminescence is quenched by ~80% (Figure 4.3, inset), and the two characteristic signatures of trion decay are observed in their photoluminescence decay curves: (1) an increase in luminescence intensity at short times (<500 ps) relative to the neutral nanocrystals, and (2) appearance of a fast decay component attributable to Auger recombination. The persistence of a slow decay component in the photodoped sample reflects the presence of some undoped CdSe nanocrystals, as expected for <*n*> ~ 0.5. Analysis of these data yields a trion decay time of τ_{X-} = 750 ps that agrees well with those reported previously for electrochemically reduced CdSe/CdS core/shell nanocrystals in films,[28] but here has been collected on a high-optical-quality colloidal suspension with minimal sample perturbation.

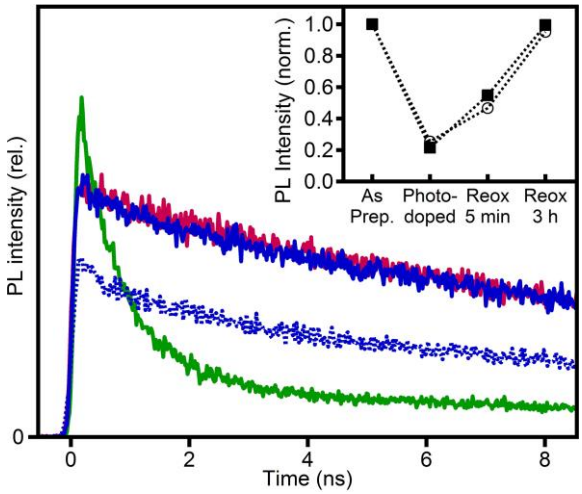

Figure 4.3. Auger recombination in photodoped CdSe nanocrystals. Time-resolved PL decays of *d* = 4.6 nm CdSe/ZnSe nanocrystals measured before photodoping (red), after photodoping (green), after 5 min re-oxidation in air (dotted blue), and after 3 h in air (solid blue). Inset: Normalized steady-state (squares) and time-resolved (at 7.5 ns, circles) PL intensities showing slow re-oxidation in air.

Like absorption, the PL also recovers completely upon introduction of air, but this recovery is markedly slower than the absorption recovery. Whereas absorption recovers within seconds of

exposure to air, both the time-resolved and steady-state luminescence intensities have not fully recovered even after 5 min in air (Figure 4.3 inset). This discrepancy indicates that the nanocrystal PL is sensitive not only to the presence of conduction-band electrons but also to other changes induced upon photodoping, which we tentatively associate with electron trapping. These results suggest that deeply trapped electrons react more slowly with air than conduction electrons do, as could be anticipated from Marcus-theory considerations. The reactivities and reaction dynamics of redox-active traps in semiconductor nanocrystals have been of central interest to many aspects of nanocrystal photophysics and electronics,[3,5,13,27] and the present results illustrate a promising new avenue for deliberate investigation of such trap chemistries.

A final important feature of this photodoping methodology that distinguishes it from all other chalcogenide nanocrystal reduction strategies reported to date is that electrons are placed in the conduction band by photoexcitation, not by equilibrium electron injection. Photodoping is fundamentally governed by the reactivities of the quenchers toward the photogenerated holes.[21] This property may be valuable for applications in which *n*-type nanostructures are encapsulated within barrier heterostructures or in cases where competing redox reactions may interfere with direct nanocrystal reduction. To illustrate the power of photochemical reduction, it was compared with chemical reduction in CdSe nanocrystals with and without a barrier. To do this a ZnSe shell was added (~1 nm thick, ~4 monolayers, Appendix E.5) to the d = 4.6 nm CdSe nanocrystals and both sets (shelled and unshelled) were reduced chemically (with $Na[C_{12}H_{10}]$) and photochemically. The results of this comparison are presented in Figure 4.4.

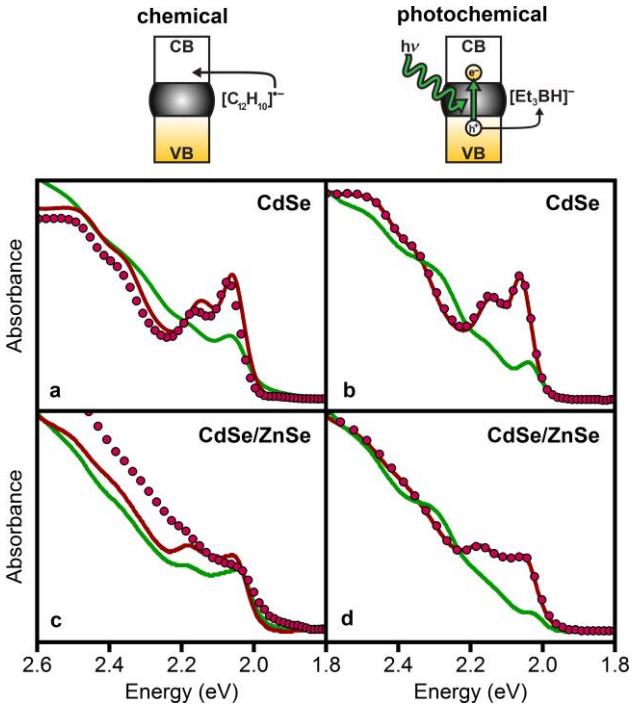

Figure 4.4. Comparison of chemical and photochemical reduction methods in CdSe nanocrystals with and without a barrier. Top: Scheme outlining chemical and photochemical doping methods. Absorption spectra of d = 4.6 nm CdSe nanocrystals with and without a ~1 nm ZnSe shell, measured before reduction (red lines), after maximum reduction (green lines), and after re-oxidation by air (red circles). Panels (a) and (c) show reduction of core and core/shell nanocrystals using 10^3 and 10^4 equivalents of Na[$C_{12}H_{10}$], respectively. Panels (b) and (d) show photodoping of the same core and core/shell nanocrystals, respectively, using ~50 equivalents of Li[Et_3BH].

Figure 4.4a shows that addition of 10^3 equivalents of Na[$C_{12}H_{10}$] reduces the core d = 4.6 nm CdSe nanocrystals, consistent with literature results.[15] The absorption bleach is similar to that achieved photochemically with the same nanocrystals (Figure 4.4b, both ~60%), albeit with the appearance of a small sub-bandgap tail and less complete reversibility in the case of chemical reduction. The core/shell nanocrystals show markedly different results: Incremental addition of up to 10^4 equivalents of Na[$C_{12}H_{10}$] causes only a small (~20%) bleach of the first excitonic absorption (Figure 4.4c). A large sub-bandgap absorption tail and an offset at higher energy are observed, suggestive of scattering due to nanocrystal clustering or absorption due to trapped

electrons. Furthermore, the spectral changes are only partially reversed upon exposure to air, suggesting substantial nanocrystal degradation. These irreversible changes are attributed to deleterious side reactions of the chemical reductant, $Na[C_{12}H_{10}]$. In contrast, photodoping the same core/shell nanocrystals (Figure 4.4d) yields a clean ~85% bleach of the first exciton that is rapidly and completely reversed upon exposure to air. These data demonstrate superior results with photodoping compared to chemical reduction. The high optical quality of the photodoped nanocrystal samples and the excellent reversibility of the photodoping will facilitate future spectroscopic and electronic structure studies of these and related *n*-type nanostructures.

Although this study has focused on colloidal CdSe quantum dots, preliminary results have also been obtained for colloidal CdE (E = S, Te) nanocrystals and CdSe quantum dot films (Appendix E.6). CdE (E = S, Te) nanocrystals of d = 6.0 and 4.1 nm, respectively, were prepared by established methods.[29,30] Anaerobic photoexcitation of these nanocrystals in the presence of $Li[Et_3BH]$ leads to successful photodoping as evidenced by a band-edge absorption bleach or new IR absorption similar to that obtained for photodoped CdSe nanocrystals. Perhaps more intriguingly, anaerobic photoexcitation of CdSe quantum dot solids prepared by co-deposition of d = 7.0 colloidal CdSe nanocrystals with $Li[Et_3BH]$ onto fluorine-doped tin oxide (FTO) electrodes also yields comparable *n*-doping to that found in solution. In all cases, these changes are fully reversed upon re-oxidation in air. These results, in conjunction with our recent demonstration of enhanced ZnO nanocrystal photodoping using $Li[Et_3BH]$,[21] demonstrate this as a general and versatile approach for preparing *n*-type semiconductor nanocrystals, both in colloidal suspensions and in solids. The precise roles played by the charge-compensating cations (Li^+, H^+) in this chemistry remains an open topic for future research. In ZnO nanocrystals, bulky

cations slow photodoping,[21] but it is not yet known whether small cations associate with the surfaces or can intercalate into the internal volumes of such photodoped nanocrystals.

4.4 Summary and conclusions

In summary, a new method for preparation of colloidal *n*-type CdSe nanocrystals has been demonstrated that involves photodoping using $Li[Et_3BH]$ as a hole quencher. This hydride is commercially available, shelf-stable, and compatible with the solvents and ligands commonly used for colloidal semiconductor nanocrystals. The *n*-type CdSe nanocrystals prepared by this method are kinetically stable, show excellent optical quality, and are readily returned to their original oxidation state upon exposure to air. Photodoping is successful even for CdSe/ZnSe core/shell heterostructures that are significantly more difficult to reduce directly with $Na[C_{12}H_{10}]$. This photodoping methodology is also applicable to other colloidal chalcogenide and oxide nanocrystals, offering a facile general approach to in situ nanocrystal electronic doping. As such, this methodology will enable a broad range of fundamental science experiments to address *n*-type doped nanocrystal electronic structures, electron spin dynamics, quantum dot plasmonics, and inter-nanocrystal electron-transfer processes, among other intriguing topics. It is equally attractive for in situ, non-destructive, tunable carrier doping of quantum dot solids currently of interest in more applied areas of quantum dot photovoltaics, photodetectors, and transistors.

4.5 Experimental methods

Synthetic methods are described in Appendix A. Photodoping and titration methods are detailed in Appendix B.

4.5.1 Photoluminescence. Time resolved photoluminescence measurements were taken by exciting with the frequency doubled output of a Ti:Sapphire with the repetition rate reduced from 76 MHz to 500 kHz using a pulse picker (400 nm, 150 fs pulse with, 0.7 nJ/pulse) and detected using a streak camera coupled to a monochromator with an IRF of ~ 15 ps. Concurrent quasi-CW measurements were detected using a perpendicular Ocean Optics 2000+ spectrometer.

4.6 References

1. Nozik, A. J.; Beard, M. C.; Luther, J. M.; Law, M.; Ellingson, R. J.; Johnson, J. C. Semiconductor Quantum Dots and Quantum Dot Arrays and Applications of Multiple Exciton Generation to Third-Generation Photovoltaic Solar Cells. *Chem. Rev.* **2010**, *110*, 6873.

2. Kramer, I. J.; Sargent, E. H. Colloidal Quantum Dot Photovoltaics: A Path Forward. *ACS Nano* **2011**, *5*, 8506.

3. Ip, A. H.; Thon, S. M.; Hoogland, S.; Voznyy, O.; Zhitomirsky, D.; Debnath, R.; Levina, L.; Rollny, L. R.; Carey, G. H.; Fischer, A.; Kemp, K. W.; Kramer, I. J.; Ning, Z.; Labelle, A. J.; Chou, K. W.; Amassian, A.; Sargent, E. H. Hybrid Passivated Colloidal Quantum Dot Solids. *Nature Nanotechnol.* **2012**, *7*, 577.

4. Kamat, P. V. Quantum Dot Solar Cells. *The Next Big Thing* in Photovoltaics. *J. Phys. Chem. Lett.* **2013**, *4*, 908.

5. Zhu, H.; Song, N.; Lian, T. Charging of Quantum Dots by Sulfide Redox Electrolytes Reduces Electron Injection Efficiency in Quantum Dot Sensitized Solar Cells. *J. Am. Chem. Soc.* **2013**, *135*, 11461.

6. Su, Q.; Chang, L.; Zhang, J.; Du, G.; Xu, B. In Situ TEM Observation of the Electrochemical Process of Individual CeO2/Graphene Anode for Lithium Ion Battery. *J. Phys. Chem. C* **2013**, *117*, 4292.

7. Gregorczyk, K. E.; Liu, Y.; Sullivan, J. P.; Rubloff, G. W. In Situ Transmission Electron Microscopy Study of Electrochemical Lithiation and Delithiation Cycling of the Conversion Anode RuO₂. *ACS Nano* **2013**, *7*, 6354.

8. Hetsch, F.; Zhao, N.; Kershaw, S. V.; Rogach, A. L. Quantum Dot Field Effect Transistors. *Mater. Today* **2013**, *16*, 312.

9. Loss, D.; DiVincenzo, D. P. Quantum Computation with Quantum Dots. *Phys. Rev. A* **1998**, *57*, 120.

10. Hanson, R.; Kouwenhoven, L. P.; Petta, J. R.; Tarucha, S.; Vandersypen, L. M. K. Spins in Few-Electron Quantum Dots. *Rev. Mod. Phys.* **2007**, *79*, 1217.

11. Dzurak, A. S.; Petta, J. R.; Hu, E. L.; Bassett, L. C.; Awschalom, D. D. Quantum Spintronics: Engineering and Manipulating Atom-Like Spins in Semiconductors. *Science* **2013**, *339*, 1174.

12. Mahler, B.; Spinicelli, P.; St; Buil, p.; Quelin, X.; Hermier, J.-P.; Dubertret, B. Towards Non-Blinking Colloidal Quantum Dots. *Nature Mater.* **2008**, *7*, 659.

13. Galland, C.; Ghosh, Y.; Steinbrück, A.; Sykora, M.; Hollingsworth, J. A.; Klimov, V. I.; Htoon, H. Two Types of Luminescence Blinking Revealed by Spectroelectrochemistry of Single Quantum Dots. *Nature* **2011**, *479*, 203.

14. Chen, O.; Zhao, J.; Chauhan, V. P.; Cui, J.; Wong, C.; Harris, D. K.; Wei, H.; Han, H. S.; Fukumura, D.; Jain, R. K.; Bawendi, M. G. Compact High-Quality CdSe-CdS Core-Shell Nanocrystals with Narrow Emission Linewidths and Suppressed Blinking. *Nature Mater.* **2013**, *12*, 445.

15. Shim, M.; Guyot-Sionnest, P. *n*-Type Colloidal Semiconductor Nanocrystals. *Nature* **2000**, *407*, 981.

16. Yu, D.; Wehrenberg, B. L.; Jha, P.; Ma, J.; Guyot-Sionnest, P. Electronic Transport of *n*-Type CdSe Quantum Dot Films: Effect of Film Treatment. *J. App. Phys.* **2006**, *99*, 104315.

17. Nguyen, T.-L.; Tamarat, P.; Mulvaney, P.; Sinito, C.; Potzner, C.; Lounis, B.; Louyer, Y.; Fernée, M. J. Magneto-Optical Properties of Trions in Non-Blinking Charged Nanocrystals Reveal an Acoustic Phonon Bottleneck. *Nature Commun.* **2012**, *3*, 1287.

18. Haase, M.; Weller, H.; Henglein, A. Photochemistry and Radiation Chemistry of Colloidal Semiconductors. 23. Electron Storage on ZnO Particles and Size Quantization. *J. Phys. Chem.* **1988**, *92*, 482.

19. Shim, M.; Wang, C.; Guyot-Sionnest, P. Charge-Tunable Optical Properties in Colloidal Semiconductor Nanocrystals. *J. Phys. Chem. B* **2001**, *105*, 2369.

20. Liu, W. K.; Whitaker, K. M.; Smith, A. L.; Kittilstved, K. R.; Robinson, B. H.; Gamelin, D. R. Room-Temperature Electron Spin Dynamics in Free-Standing ZnO Quantum Dots. *Phys. Rev. Lett.* **2007**, *98*, 186804.

21. Schimpf, A. M.; Gunthardt, C. E.; Rinehart, J. D.; Mayer, J. M.; Gamelin, D. R. Controlling Carrier Densities in Photochemically Reduced Colloidal ZnO Nanocrystals: Size Dependence and Role of the Hole Quencher. *J. Am. Chem. Soc.* **2013**, *135*, 16569.

22. Carbone, L.; Nobile, C.; De Giorgi, M.; Sala, F. D.; Morello, G.; Pompa, P.; Hytch, M.; Snoeck, E.; Fiore, A.; Franchini, I. R.; Nadasan, M.; Silvestre, A. F.; Chiodo, L.; Kudera, S.; Cingolani, R.; Krahne, R.; Manna, L. Synthesis and Micrometer-Scale Assembly of

Colloidal CdSe/CdS Nanorods Prepared by a Seeded Growth Approach. *Nano Lett.* **2007**, *7*, 2942.

23. Shimizu, K. T.; Woo, W. K.; Fisher, B. R.; Eisler, H. J.; Bawendi, M. G. Surface-Enhanced Emission from Single Semiconductor Nanocrystals. *Phys. Rev. Lett.* **2002**, *89*, 117401.

24. Patton, B.; Langbein, W.; Woggon, U. Trion, Biexciton, and Exciton Dynamics in Single Self-Assembled CdSe Quantum Dots. *Phys. Rev. B* **2003**, *68*, 125316.

25. Wang, C. J.; Shim, M.; Guyot-Sionnest, P. Electrochromic Nanocrystal Quantum Dots. *Science* **2001**, *291*, 2390.

26. Voznyy, O.; Thon, S. M.; Ip, A. H.; Sargent, E. H. Dynamic Trap Formation and Elimination in Colloidal Quantum Dots. *J. Phys. Chem. Lett.* **2013**, *4*, 987.

27. Tice, D. B.; Frederick, M. T.; Chang, R. P. H.; Weiss, E. A. Electron Migration Limits the Rate of Photobrightening in Thin Films of CdSe Quantum Dots in a Dry N-2 (g) Atmosphere. *J. Phys. Chem. C* **2011**, *115*, 3654.

28. Jha, P. P.; Guyot-Sionnest, P. Trion Decay in Colloidal Quantum Dots. *ACS Nano* **2009**, *3*, 1011.

29. Yu, W. W.; Peng, X. G. Formation of High-Quality CdS and Other II-VI Semiconductor Nanocrystals in Noncoordinating Solvents: Tunable Reactivity of Monomers. *Angew. Chem. Int. Ed.* **2002**, *41*, 2368.

30. Yu, W. W.; Qu, L.; Guo, W.; Peng, X. Experimental Determination of the Extinction Coefficient of CdTe, CdSe, and CdS Nanocrystals. *Chem. Mater.* **2003**, *15*, 2854.

Chapter 5

Photodoped In_2O_3 and Sn-Doped In_2O_3 Nanocrystals

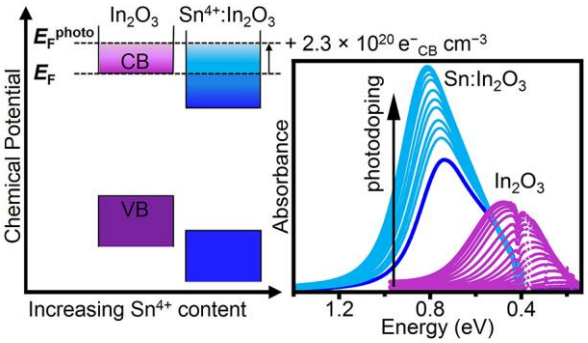

Adapted from: Schimpf, A. M.; Lounis, S. D.; Runnerstrom, E. L.; Milliron, D. J.; Gamelin, D. R. *J. Am. Chem. Soc.* **2014**, *Accepted Manuscript*, doi: 10.1021/ja5116953.

5.1 Overview

Plasmonic doped semiconductor nanocrystals promise exciting opportunities for new technologies, but basic features of the relationships between their structures, compositions, electronic structures, and optical properties remain poorly understood. Here, we report a quantitative assessment of the impact of composition on the energies of localized surface plasmon resonances (LSPRs) in colloidal tin-doped indium oxide (ITO) nanocrystals. Using a combination of aliovalent doping and photodoping, the effects of added electrons and impurity ions on the energies of LSPRs in colloidal In_2O_3 and ITO nanocrystals have been evaluated. Photodoping allows electron densities to be tuned post-synthetically in ITO nanocrystals, independent of their Sn content. Because electrons added photochemically are easily titrated, photodoping also allows independent quantitative determination of the dependence of the LSPR energy on nanocrystal composition and changes in electron density. The data show that ITO LSPR energies are affected by both electron and Sn concentrations, with composition yielding a broader plasmon tuning range than achievable by tuning carrier densities alone. Aspects of the photodoping energetics, as well as magneto-optical properties of these ITO LSPRs, are also discussed.

5.2 Introduction

LSPRs in semiconductor nanocrystals have recently attracted broad attention,[1-6] in part because of their tunability in both energy and intensity via tunable carrier densities. Charge-carrier densities in semiconductor nanocrystals have been modulated by various techniques including remote doping,[7-13] vacancy generation,[14-17] aliovalent doping,[18-25] electrochemical doping,[26-29] and photodoping,[8,21,28,30-40] each offering specific advantages. For example, aliovalently doped colloidal nanocrystals such as Sn-doped In_2O_3 (ITO)[18,19,41-44] and Al-doped ZnO (AZO)[20,21,45] contain conduction-band electrons that are stable in air, making them attractive for potential aerobic applications. Alternatively, photodoped ZnO nanocrystals contain reactive conduction-band electrons that can be readily titrated against mild oxidants,[21,31,33,37,38] making the carrier densities associated with their LSPRs directly quantifiable.[46] The reactivities of these electrons also provide opportunities for fundamental studies of interfacial electron-transfer reactions involving semiconductor nanostructures.[10,11,36,37,47]

Characterization of the electronic structures of doped semiconductor nanocrystals poses interesting challenges. For example, using photodoped ZnO nanocrystals, we have recently observed that the LSPR energies of doped semiconductors are strongly coupled to the one-electron intraband transition energies, causing divergence from the classical Drude model when in the quantum confinement size regime.[46] A second potentially important feature of doped nanocrystal electronic structure that has not received sufficient attention in LSPR analyses is the impact of the sizeable electronic-structural changes that frequently accompany the introduction of lattice defects (*e.g.*, impurities, vacancies) even in the absence of free carriers. Such effects are widely discussed in the context of band-gap engineering[36,48,49] but have not been thoroughly explored for the purposes of plasmon engineering in semiconductor nanocrystals. For example,

isovalent Mg^{2+} doping is known to shift the potentials of extra conduction-band electrons in *n*-type $Zn_{1-x}Mg_xO$ nanocrystals,[36] and it would be reasonable to expect that it might also tune LSPR energies. Although LSPRs in $Cu_{2-x}E$ (E = S, Se, Te) nanocrystals are generally attributed to formation of nonstoichiometric compositions,[14-16,50] the impact of the compositional changes alone on LSPR energies has not been addressed. Typically, these ancillary compositional changes are difficult to disentangle from the effects of changing free-carrier density, and to our knowledge, this issue has not been previously addressed for any plasmonic semiconductor nanocrystals.

Here, we use a combination of aliovalent doping and photodoping to separately evaluate the effects of added electrons and impurity ions on the LSPR energies in In_2O_3-based nanocrystals. We demonstrate controlled photodoping of both In_2O_3 and ITO nanocrystals using EtOH as a sacrificial reductant. The added conduction-band electrons can be titrated using mild oxidants, allowing them to be quantified without reliance on modeling of absorption energies and bandshapes based on the Drude approximation or Mie theory. The results reveal that the LSPR energies are affected separately by *both* electron *and* Sn concentrations, with compositional engineering offering a greater range in LSPR energies than can be achieved by tuning carrier densities alone. Surprisingly, the maximum number of electrons that can be added photochemically is independent of the number of electrons already present due to Sn doping, providing general insight into the factors governing nanocrystal photodoping. Finally, magnetic circular dichroism (MCD) spectroscopy of the ITO LSPR reveals properties similar to those of metal nanoparticles and heavily *n*-doped ZnO nanocrystals. The large magneto-optical responses from the IR LSPRs of doped semiconductor nanocrystals may have interesting ramifications for applications such as IR chiral imaging or sensing.

5.3 Results and analysis

In_2O_3 and ITO nanocrystals were synthesized as described previously.[43] Absorption spectra of all samples are provided in Appendix F (Figure F.1). In_2O_3 and ITO nanocrystals were photodoped in the same manner as detailed for ZnO nanocrystals[32,33,38] (see section 5.5, Appendix B). Specifically, exposure to UV illumination under rigorously anaerobic conditions and in the presence of a sacrificial reductant (EtOH) leads to the accumulation of conduction-band electrons (Figure 5.1, top). Photodoping is evident from the appearance and growth of a new IR absorption band in the case of In_2O_3 nanocrystals, and from an increase and blue shift of the existing IR absorption band in the case of ITO nanocrystals (Figure 5.1, bottom). Note that the new IR absorption resulting from ITO photodoping has a similar energy and bandshape as the IR absorption of the as-prepared ITO nanocrystals. As observed with ZnO nanocrystals,[33,38] a maximum photodoping level is approached asymptotically under these conditions. Importantly, this photodoping is completely reversible, with the In_2O_3 and ITO nanocrystals returning to their as-prepared state upon exposure to air or other mild oxidants.

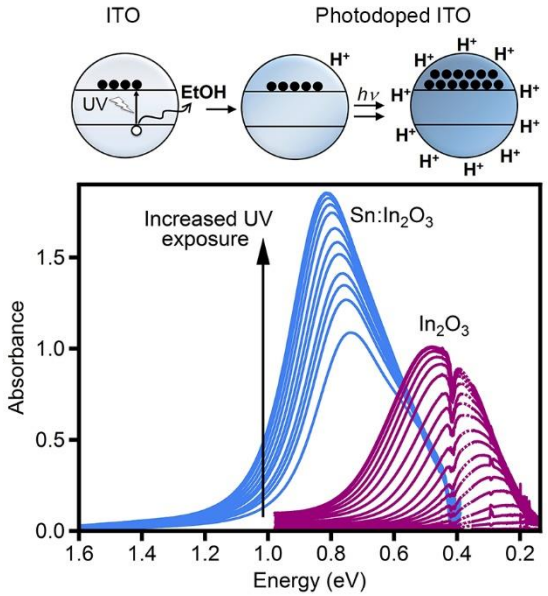

Figure 5.1. Photodoping of In_2O_3 and ITO nanocrystals. Top: Scheme depicting photodoping of In_2O_3 and ITO nanocrystals. Bottom: Absorption spectra before and following various extents of photodoping of In_2O_3 (right, ~0.4 eV) and 9.0% Sn-doped In_2O_3 (left, ~0.8 eV) nanocrystals (~20 μM in 7:1 toluene/EtOH). The arrows show the direction of increasing photodoping.

The reversibility of this photodoping allows the number of photogenerated electrons to be counted via oxidative titration.[21,31,33,37,38,46] Oxidants such as air or $[FeCp^*_2]^+$ remove the electrons (equation 5.1) added photochemically but have no effect on those arising from Sn doping, indicating greater stability of the latter. Using stronger oxidants such as Ce^{4+}, $[NO]^+$, or $[N(C_6H_4Br\text{-}4)_3]^+$, roughly half of the remaining ITO electrons could be removed (Figure F.2), but this chemistry leads to nanocrystal precipitation. Nevertheless, this result confirms the greater chemical stability of electrons generated via aliovalent doping than of those added photochemically, despite their spectroscopic similarity (Figure 5.1). Greater stability of electrons added via aliovalent doping over photochemically added ones is also observed in AZO nanocrystals.[21]

$$e^-_{CB}:NC + [FeCp^*_2]^+ \rightarrow NC + FeCp^*_2 \quad (5.1)$$

NC = In_2O_3 or ITO nanocrystal

Figure 5.2a shows infrared absorption spectra of photodoped 5.9% Sn:In_2O_3 nanocrystals as a function of added titrant. Addition of $[FeCp^*_2]^+$ to the maximally photodoped nanocrystals (top, solid blue) decreases the LSPR intensity (dotted green) until the spectrum of the as-prepared ITO nanocrystals is recovered (solid purple). The inset of Figure 5.2a plots the integrated absorption intensity versus equivalents of $[FeCp^*_2]^+$. The solid line is a linear fit to the data. These intensities are normalized such that the as-prepared nanocrystals have a relative integrated absorbance of 1.0. The intersection of the fitted line with 1.0 thus defines the average number of electrons per nanocrystal added photochemically ($\langle n_{photo} \rangle$). Furthermore, extrapolation of this line to zero absorption represents the average total number of electrons present in the maximally photodoped nanocrystals ($\langle n_{tot} \rangle$). The difference, $\langle n_{tot} \rangle - \langle n_{photo} \rangle$, describes the number of electrons initially present in the as-prepared ITO nanocrystals ($\langle n_{as\text{-}prepared} \rangle$). For the sample of Figure 5.2a, this analysis yields $\langle n_{photo} \rangle = 28$, $\langle n_{as\text{-}prepared} \rangle = 46$, and $\langle n_{tot} \rangle = 74$. We note that this extrapolation may underestimate $\langle n_{as\text{-}prepared} \rangle$ because the plasmon intensity is only linear with $\langle n \rangle$ when integrating over the entire spectrum, and the data in Figure 5.2a are limited by solvent absorption and the spectrometer sensitivity window (see section 5.5 for details). Fortunately, the spectra of samples with large $\langle n_{as\text{-}prepared} \rangle$ can be mostly integrated (*e.g.*, Figure 5.2a), and the spectra that cannot be as completely measured come from samples with smaller values of $\langle n_{as\text{-}prepared} \rangle$ that require less extrapolation.

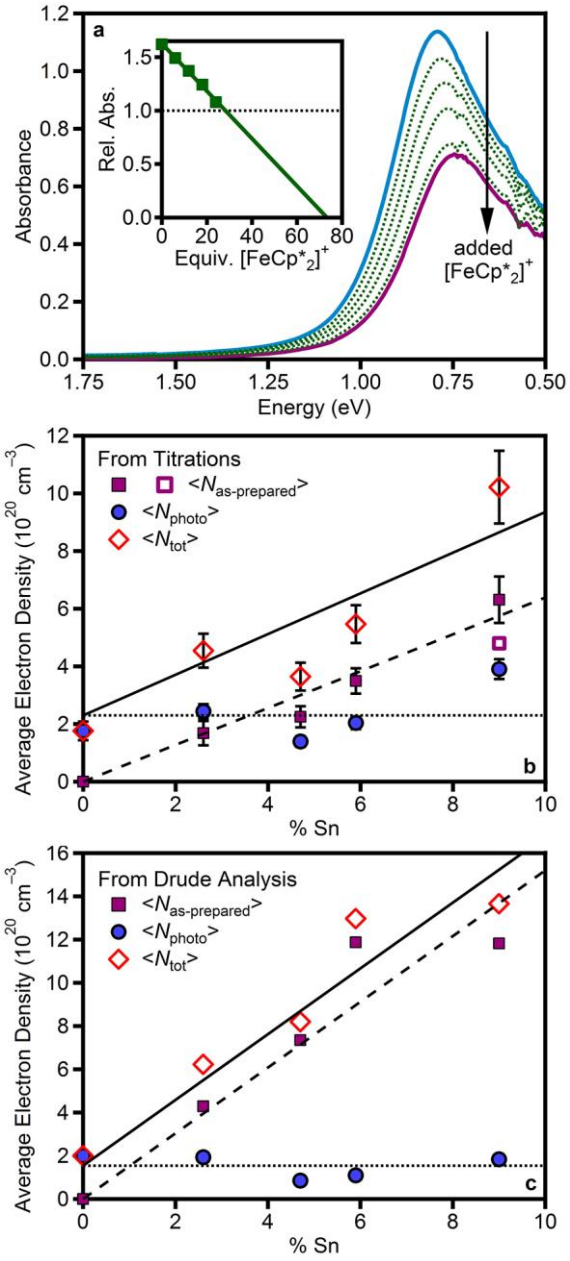

Figure 5.2. Quantification of the number of electrons per In_2O_3 or ITO nanocrystal. (a) Absorption spectra of as-prepared (bottom, purple) and maximally photodoped (top, blue) 5.9% Sn:In_2O_3 nanocrystals (0.6 μM in 1:1 toluene/THF with 3×10^5 equivalents EtOH). The intermediate spectra (dotted, green) were measured after adding various amounts of $[FeCp^*_2][BAr_F]$ to the maximally photodoped nanocrystals. The arrow indicates increasing $[FeCp^*_2][BAr_F]$. Inset: Relative integrated IR absorption as a function of added $[FeCp^*_2][BAr_F]$. The solid line is a linear fit to the data. (b,c) Electron densities, $\langle N_{as\text{-}prepared} \rangle$ (squares), $\langle N_{photo} \rangle$ (circles), and $\langle N_{tot} \rangle$ (diamonds) obtained from titrations and Drude analysis, respectively, plotted versus nanocrystal Sn content. The lines are guides to the eye, fitted such that $\langle N_{tot} \rangle = \langle N_{as\text{-}prepared} \rangle + \langle N_{photo} \rangle$ across the range of Sn content.

To probe the role of Sn, samples of ITO nanocrystals with Sn contents ranging from 0.0–9.0% were each photodoped to the maximum extent and then their electrons were titrated as described above. To correct for volume effects,[38] the resulting data are presented as average electron densities, $\langle N \rangle$. Figure 5.2b plots the electron densities, $\langle N_{\text{as-prepared}} \rangle$, $\langle N_{\text{photo}} \rangle$, and $\langle N_{\text{ot}} \rangle$ as a function of Sn concentration. The error bars in the experimental data were determined from multiple titrations on each sample and from error bars in the quantitative concentration measurements.

$\langle N_{\text{as-prepared}} \rangle$ increases rougly linearly from the origin as the Sn content increases, consistent with the role of Sn as an *n*-type dopant. Figure 5.2b shows that $\langle N_{\text{tot}} \rangle$ also increases linearly with increasing Sn content, but no longer starts at zero for 0% Sn. Quite unexpectedly, $\langle N_{\text{photo}} \rangle$ is almost completely insensitive to Sn concentration, and is therefore essentially independent of $\langle N_{\text{as-prepared}} \rangle$. Averaging over all samples yields $\langle\langle N_{\text{photo}} \rangle\rangle = 2.3 \pm 0.8 \times 10^{20}$ cm^{-3}. This value is slightly higher than that found for ZnO nanocrystals photodoped under the same conditions ($1.4 \pm 0.4 \times 10^{20}$ cm^{-3}).[38]

These titrations determine carrier densities without relying on a model-dependent analysis of LSPR energies, which presents an opportunity for critical comparison with use of the extended Drude model to analyze carrier concentrations in ITO nanocrystals based on LSPR spectra.[43,51,52] Spectra of the as-prepared ITO and all the photodoped nanocrystals were fit using a parametrized dielectric function that included a frequency-dependent damping function, as typically found for ITO.[53-55] The extracted electron concentrations $\langle n_{\text{as-prepared}} \rangle$ and $\langle n_{\text{tot}} \rangle$ trend monotonically and approximately linearly upwards with Sn content (Figure 5.2c). Notably, for photodoped In_2O_3 quantitative agreement is found between the titration-derived $\langle N_{\text{photo}} \rangle$ and the value determined by fitting. In addition, $\langle N_{\text{photo}} \rangle$ is found to have a constant value across Sn content, consistent

with the results of the titration. Hence, the trends in carrier densities determined by the model-free titration approach and analysis based on fitting to the extended Drude model agree well.

The independence of $\langle N_{photo} \rangle$ from Sn content in ITO nanocrystals is revealing. This observation indicates that the maximum photodoping level is *not* determined by competitive Auger recombination dynamics. Instead, it appears to be determined thermodynamically, *i.e.*, by the chemical potentials of the photogenerated carriers. A similar scenario was considered for photodoped ZnO nanocrystals, but kinetic limitations could not be ruled out.[38] This new result can be rationalized as follows: Prior to photodoping, each conduction-band electron within an ITO nanocrystal is compensated by a Sn^{4+} ion in the same nanocrystal. These Sn^{4+} ions stabilize the extra electrons to such an extent that the nanocrystals are not oxidized upon exposure to air. Subsequent photodoping introduces electrons stabilized by charge-compensating protons delivered from the EtOH oxidation reaction. As a consequence, the chemical potentials (V_{photo}) of these photogenerated electrons are essentially the same in all of the nanocrystals, independent of Sn content or initial electron density (Scheme 5.1).

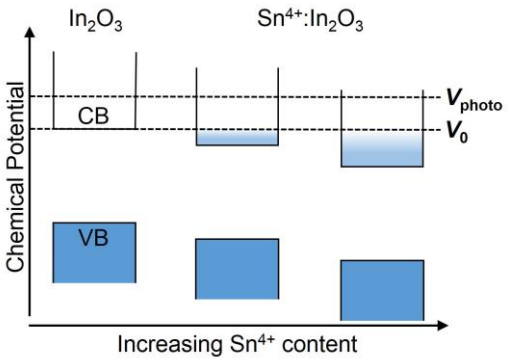

Scheme 5.1 Stabilization of the In_2O_3 conduction band by aliovalent doping with Sn^{4+}. As-prepared nanocrystals have the same E_F, determined by the solution potential, regardless of Sn-doping. Stabilization of the conduction-band by Sn^{4+} allows more electrons to be accumulated before reaching E_F. Photodoping allows E_F to be increased by an amount that is constant across all samples.

Three control experiments confirm this interpretation. In the first, the as-prepared 9.0% ITO and In_2O_3 nanocrystals were mixed and the absorption spectra monitored for evidence of electron transfer, which would imply an elevated chemical potential in the ITO nanocrystals. Figure 5.3a shows the absorption spectra of as-prepared In_2O_3 and 9.0% Sn:In_2O_3 nanocrystals prepared separately. The absorption spectrum measured after adding the ITO nanocrystals to the In_2O_3 nanocrystals is a simple superposition of the two independent absorption spectra. This result shows that electron transfer from as-prepared ITO nanocrystals to as-prepared In_2O_3 nanocrystals does not occur, and hence that the Fermi level of the ITO nanocrystals is not above the conduction-band edge of the In_2O_3 nanocrystals. In the second experiment, this mixture of as-prepared nanocrystals was photodoped and monitored spectroscopically, with the observation that electrons are added to both types of nanocrystals concurrently (Figure F.3). In the third experiment, as-prepared ITO nanocrystals were added to photodoped In_2O_3 nanocrystals (1 equivalents) and the absorption spectrum monitored for evidence of electron transfer. The spectrum of this mixture is shown in Figure 5.3b, and is essentially identical to that of the mixture of the same nanocrystal samples photodoped concurrently (Figure F.3), but at roughly half the intensity (Figure F.4). This result demonstrates that electrons do indeed transfer between nanocrystals to equilibrate chemical potentials.

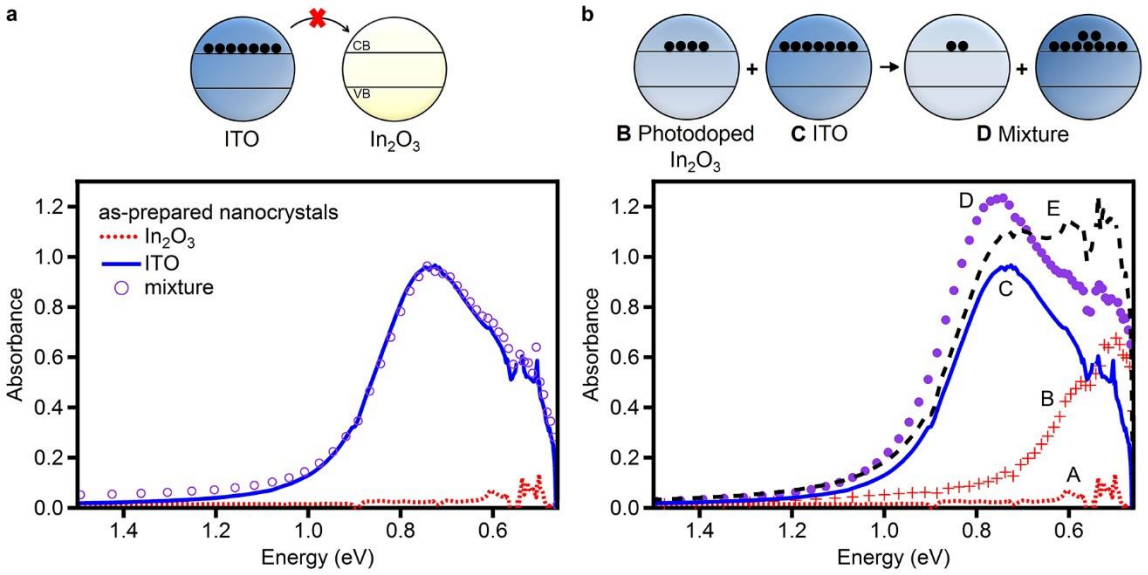

Figure 5.3. Electron transfer between In_2O_3 and ITO nanocrystals. (a) Absorption spectra of as-prepared In_2O_3 nanocrystals (dotted), 9.0% Sn:In_2O_3 nanocrystals (solid), and an anaerobic mixture of the two (circles, both 1μM in 1:1 toluene/THF). The resulting spectrum shows no indication of electron transfer from the ITO to In_2O_3 nanocrystals. (b) Absorption spectra of: (A) As-prepared In_2O_3 nanocrystals (1μM in 1:1 toluene/THF with ~3×10^5 equivalents EtOH, anaerobic); (B) The same nanocrystals after maximal photodoping; (C) As-prepared 9.0% Sn:In_2O_3 nanocrystals; (D) After adding one equivalent of maximally photodoped In_2O_3 nanocrystals to a solution of as-prepared 9.0% Sn:In_2O_3 nanocrystals. Spectrum E is a numerical summation of absorption spectra B and C. Spectrum E does not match spectrum D, confirming inter-particle electron transfer in mixture of spectrum D.

Collectively, these results strongly support the alignment of as-prepared nanocrystal chemical potentials (V_0) as depicted in Scheme 5.1. The picture that emerges is thus that Sn doping does not raise the nanocrystal Fermi level, but instead it *stabilizes* the band edges relative to external redox couples (or vacuum), as summarized in Scheme 5.1. Under air-free conditions, irreversible photochemical oxidation of EtOH then raises the electron chemical potential to V_{photo} (Scheme 5.1), as dictated by the photoredox reaction and the stability of its products. The striking result of Figure 5.2b is that this increase is independent of the amount of Sn or the number of conduction-band electrons initially within the as-prepared nanocrystals.

With the electron densities of these nanocrystals defined, it is now possible to quantify the effect of Sn on ITO LSPR energies independent of the effects of free carriers. Nanocrystals with different Sn concentrations were photodoped to the same final electron density and their IR LSPRs compared. Figure 5.4 plots the NIR absorption spectra of three such ITO nanocrystal samples (d = 6.1, 6.8, 6.4 nm; [Sn] = 2.6, 4.7, 5.9%, respectively), all photodoped to the same total electron density of ~3.65×10^{20} cm^{-3}. For a fixed carrier density, increasing the Sn content from 2.6 to 5.9% increases the LSPR energy by ~0.2 eV. The inset to Figure 5.4 plots these LSPR energies as a function of the Sn content and reveals a linear relationship with a slope of 0.06 eV/%Sn. Quantum confinement cannot be responsible for this increase in LSPR energies[46] because these ITO nanocrystals are substantially larger than the electron in In_2O_3. Moreover, the trend in Figure 5.4 (inset) does not track the small differences in nanocrystal diameter within this series. The change in the high-frequency dielectric constant (ε_∞) also cannot account for the magnitude of this Sn dependence, because the refractive indices of In_2O_3 and SnO_2 are experimentally indistinguishable (1.8–2.0). Instead, this blue shift is attributed to the disruptive impact of Sn on the electronic structure of In_2O_3, in the same way as composition control allows semiconductor band-gap engineering. Microscopically, the misalignment of In and Sn empty valence orbitals in ITO causes minima in the In_2O_3 conduction-band wavefunction amplitudes at each Sn site.

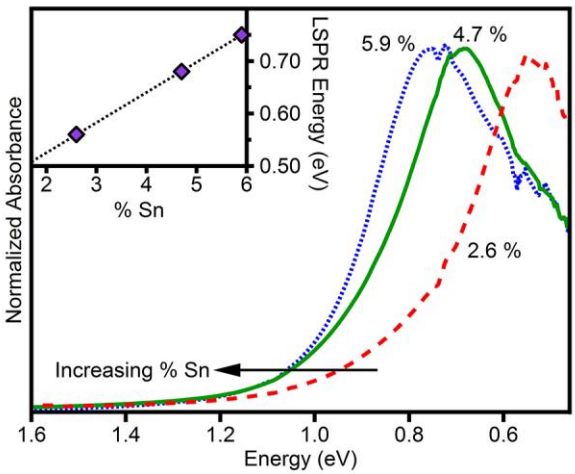

Figure 5.4. Compositional engineering of LSPRs. Absorption spectra of ITO nanocrystals with 2.6% (dashed red) 4.7% (solid green) and 5.9% (dotted blue) Sn content, all having the same carrier density of 3.65×10^{20} cm^{-3}. Inset: Plot of the LSPR energy versus Sn cation mole fraction (%) at this carrier density.

The results presented above thus demonstrate that the LSPR energies of ITO nanocrystals are affected separately by *both* the number of conduction-band electrons *and* the number of impurity ions in the nanocrystal: Greater Sn incorporation leads to higher LSPR energies even without introducing more conduction-band electrons. More generally, these data highlight the observation that the relationship between carrier density and LSPR energy frequently invoked in recent literature[1-3,14] is not as straightforward as generally assumed. For example, similar perturbations of the band structure and carrier dynamics must also accompany vacancy formation in plasmonic semiconductors such as $Cu_{2-x}E$ (E = S, Se, Te).[14-16,50,56] Quantitative analysis of the LSPR energies of those semiconductors without accounting for such effects will therefore yield incorrect carrier densities. Even LSPRs generated by redox doping may be affected by perturbations due to the presence of counterions, although such perturbations are likely small compared to those from aliovalent substitution or lattice vacancy formation. This sensitivity of LSPR frequencies to lattice defects, combined with the possibility of strong quantum

confinement effects,[40] identifies doped semiconductor nanocrystals as highly flexible platforms for tuning IR plasmons.

Finally, we address the magneto-optical properties of these nanocrystals. Recently, magnetic circular dichroism (MCD) spectroscopy has been demonstrated as a powerful probe of the LSPRs of both metal nanoparticles[57,58] and electronically doped semiconductor nanocrystals.[46] Large magneto-optical responses have been reported in both classes of plasmonic materials. For high-carrier-density ZnO nanocrystals, the LSPR magneto-optical spectra closely resemble those of metal nanoparticles. To probe the analogous magneto-optical properties of these ITO nanocrystals, low-temperature spectroscopic measurements were performed on 9.0% Sn:In_2O_3 nanocrystals embedded into PLMA matrices as frozen solutions. The transfer from toluene to PLMA has little effect on the LSPR band (Figure F.5). The LSPR absorption spectrum is nearly independent of temperature (Figure F.6). Figure 5.5a plots the absorption spectrum collected at 20K, and Figure 5.5b plots variable-field MCD spectra of the same film collected at 1.8 K. As in metal nanoparticles and *n*-type ZnO nanocrystals, the LSPR gives rise to an intense derivative-shaped MCD signal with its crossing point red shifted slightly from the absorption maximum. The inset of Figure 5.5b plots relative integrated MCD intensity as a function of magnetic field at 1.8 K. Importantly, this intensity is linear with field and shows no evidence of saturation at high fields, indicating that it does not derive from ground-state Curie paramagnetism. Additionally, the MCD spectrum shows no temperature dependence (Figure F.7). The similarities between these data and those of other plasmonic nanocrystals support the proposal[40] that these characteristics (linear field dependence and no temperature dependence) are signatures of LSPRs in doped semiconductor nanocrystals. This behavior is identical to that of LSPRs in metals,[57] and is consistent with the classical notion of magnetoplasmonic free-carrier excitations.[58]

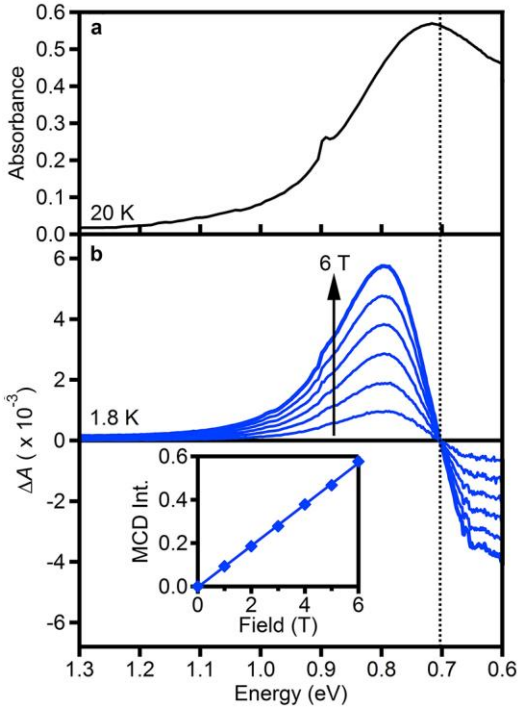

Figure 5.5. Magnetic circular dichroism of plasmons in ITO nanocrystals. (a) 20 K absorption and (b) 1.8 K variable-field MCD spectra of 9.0% Sn:In_2O_3 nanocrystals in a PLMA matrix. The inset plots the MCD intensity at 1.8 K as a function of applied magnetic field. The solid line is a linear fit to the data.

5.4 Summary and conclusions

In summary, photodoping allows the LSPRs of colloidal In_2O_3 and ITO nanocrystals to be tuned post-synthetically. Titration of the photochemically added electrons against mild oxidants allows direct quantification of the carrier densities without relying on models, which may be inaccurate especially at very low carrier densities, under quantum confinement, or for alloyed compositions. Surprisingly, the maximum number of extra electrons that can be added photochemically is largely unaffected by the starting number of electrons introduced via aliovalent doping with Sn^{4+}, suggesting that the maximum number of electrons added photochemically is not limited by competing fast multi-carrier Auger recombination processes but is instead determined thermodynamically. By chemical titration of the charge carriers in

these nanocrystals, we have been able to separately evaluate the effects of added electrons and added impurity ions on the energies of the LSPRs. The results reveal that the perturbation of the nanocrystal electronic structure by the added impurity is considerable, and that the final plasmon energies across a series of ITO compositions are significantly affected by this perturbation. Compositional plasmon engineering can thus be used to tune the energies of LSPRs in doped semiconductor nanocrystals beyond the ranges normally accessible via tunable carrier densities. These findings have broad implications for the analysis of LSPRs in doped semiconductor nanocrystals in general, where until now, such effects have not been explicitly separated experimentally. Finally, the observation of strong IR magneto-optical responses arising from these nanocrystal LSPRs bolsters prior analysis of doped ZnO nanocrystal plasmonic magneto-optics and may have interesting ramifications for low-energy plasmonic sensing or imaging technologies.

5.5 Experimental methods

5.5.1 Nanocrystal synthesis and general characterization. In_2O_3 and $Sn:In_2O_3$ nanocrystals were synthesized as reported previously.[43] Nanocrystals were dried, pumped into a N_2 glove box, and dispersed in toluene for storage. Tri-n-octylphosphine oxide (99%) was added to the nanocrystal solutions to aid in colloidal stability during photodoping and titrations. Nanocrystal and dopant concentrations were determined via inductively coupled plasma optical emission spectroscopy using a Perkin Elmer Optima 8300. UV/visible/near-IR spectra (4.1–0.4 eV) were measured using a Cary 500 spectrometer. IR spectra (1.0–0.1 eV) were measured using a Bruker Vector 33 spectrometer. Nanocrystal diameters were determined via statistical analysis of TEM

images taken on a JEOL 2100 microscope. All nanocrystals had average diameters of 5.5–6.8 nm.

5.5.2 Photodoping and determination of electron densities. In_2O_3 and ITO nanocrystals could be photodoped in the same manner as ZnO nanocrystals, detailed in Appendix B. The data in Figure 5.1 were collected using a Bruker Vector 33 IR spectrometer. The nanocrystal solution was loaded into an air-free IR cell with a 50 μm Teflon spacer between two CaF_2 windows. To the photodoped nanocrystals, aliquots of $[FeCp^*_2][BAr_F]$ in THF were added anaerobically and the absorption spectra monitored after each addition. As titrations required larger volume and adequate diffusion, these experiments were conducted in a 2 mm air-free quartz cuvette and measured on a Cary 500 spectrophotometer.

5.5.3 Low-temperature absorption and MCD spectroscopy. A 10 μl aliquot of ~2 μM 5.4% Sn-doped In_2O_3 nanocrystals was added to 50 μl of ~2% poly(lauryl methacrylate) in toluene. The ITO-PLMA solution was evaporated to ~5 μl, sandwiched between two quartz discs, and heated for 2 h at 75 ºC. The resulting film had a slightly red-shifted LSPR from that of the colloidal nanocrystals (see Figure F.5). For low-temperature absorption measurements, the sample was mounted in a closed-cycle helium refrigerator and spectra were collected with a Cary 500 spectrometer. For MCD measurements, the film was mounted in a high-field superconducting magneto-optical cryostat (Cryo-Industries SMC-1659 OVT) with a variable-temperature sample compartment oriented in the Faraday configuration. Spectra were measured using an Aviv 40DS spectropolarimeter with an InGaAs detector (Teledyne-Judson).

5.6 References

1. Routzahn, A. L.; White, S. L.; Fong, L.-K.; Jain, P. K. Plasmonics with Doped Quantum Dots. *Israel J. Chem.* **2012**, *52*, 983.

2. Scotognella, F.; Valle, G.; Srimath Kandada, A.; Zavelani-Rossi, M.; Longhi, S.; Lanzani, G.; Tassone, F. Plasmonics in Heavily-Doped Semiconductor Nanocrystals. *Eur. Phys. J. B* **2013**, *86*, 1.

3. Comin, A.; Manna, L. New Materials for Tunable Plasmonic Colloidal Nanocrystals. *Chem. Soc. Rev.* **2014**, *43*, 3957.

4. Faucheaux, J. A.; Stanton, A. L. D.; Jain, P. K. Plasmon Resonances of Semiconductor Nanocrystals: Physical Principles and New Opportunities. *J. Phys. Chem. Lett.* **2014**, *5*, 976.

5. Lounis, S. D.; Runnerstrom, E. L.; Llordes, A.; Milliron, D. J. Defect Chemistry and Plasmon Physics of Colloidal Metal Oxide Nanocrystals. *J. Phys. Chem. Lett.* **2014**, *5*, 1564.

6. Hartland, G. Designing Plasmon Resonances. *J. Phys. Chem. Lett.* **2014**, *5*, 1583.

7. Shim, M.; Guyot-Sionnest, P. *n*-Type Colloidal Semiconductor Nanocrystals. *Nature* **2000**, *407*, 981.

8. Shim, M.; Guyot-Sionnest, P. Organic-Capped ZnO nanocrystals: Synthesis and *n*-Type Character. *J. Am. Chem. Soc.* **2001**, *123*, 11651.

9. Engel, J. H.; Surendranath, Y.; Alivisatos, A. P. Controlled Chemical Doping of Semiconductor Nanocrystals Using Redox Buffers. *J. Am. Chem. Soc.* **2012**, *134*, 13200.

10. Valdez, C. N.; Braten, M.; Soria, A.; Gamelin, D. R.; Mayer, J. M. Effect of Protons on the Redox Chemistry of Colloidal Zinc Oxide Nanocrystals. *J. Am. Chem. Soc.* **2013**, *135*, 8492.

11. Palomaki, P. K. B.; Miller, E. M.; Neale, N. R. Control of Plasmonic and Interband Transitions in Colloidal Indium Nitride Nanocrystals. *J. Am. Chem. Soc.* **2013**, *135*, 14142.

12. Koh, W.-k.; Koposov, A. Y.; Stewart, J. T.; Pal, B. N.; Robel, I.; Pietryga, J. M.; Klimov, V. I. Heavily Doped *n*-type PbSe and PbS Nanocrystals Using Ground-State Charge Transfer from Cobaltocene. *Sci. Rep.* **2013**, *3*, 2004.

13. Wheeler, L. M.; Neale, N. R.; Chen, T.; Kortshagen, U. R. Hypervalent Surface Interactions for Colloidal Stability and Doping of Silicon Nanocrystals. *Nat. Commun.* **2013**, *4*.

14. Luther, J.; Jain, P.; Ewers, T.; Alivisatos, A. Localized Surface Plasmon Resonances Arising from Free Carriers in Doped Quantum Dots. *Nat. Mater.* **2011**, *10*, 361.

15. Dorfs, D.; Härtling, T.; Miszta, K.; Bigall, N. C.; Kim, M. R.; Genovese, A.; Falqui, A.; Povia, M.; Manna, L. Reversible Tunability of the Near-Infrared Valence Band Plasmon Resonance in $Cu_{2-x}Se$ Nanocrystals. *J. Am. Chem. Soc.* **2011**, *133*, 11175.

16. Kriegel, I.; Jiang, C.; Rodríguez-Fernández, J.; Schaller, R. D.; Talapin, D. V.; da Como, E.; Feldmann, J. Tuning the Excitonic and Plasmonic Properties of Copper Chalcogenide Nanocrystals. *J. Am. Chem. Soc.* **2011**, *134*, 1583.

17. Manthiram, K.; Alivisatos, A. Tunable Localized Surface Plasmon Resonances in Tungsten Oxide Nanocrystals. *J. Am. Chem. Soc.* **2012**, *134*, 3995.

18. Kanehara, M.; Koike, H.; Yoshinaga, T.; Teranishi, T. Indium Tin oxide Nanoparticles with Compositionally Tunable Surface Plasmon Resonance Frequencies in the Near-IR Region. *J. Am. Chem. Soc.* **2009**, *131*, 17736.

19. Wang, T.; Radovanovic, P. V. Free Electron Concentration in Colloidal Indium Tin Oxide Nanocrystals Determined by Their Size and Structure. *J. Phys. Chem. C* **2011**, *115*, 406.

20. Buonsanti, R.; Llordes, A.; Aloni, S.; Helms, B.; Milliron, D. Tunable Infrared Absorption and Visible Transparency of Colloidal Aluminum-Doped Zinc Oxide Nanocrystals. *Nano Lett.* **2011**, *11*, 4706.

21. Schimpf, A. M.; Ochsenbein, S. T.; Buonsanti, R.; Milliron, D. J.; Gamelin, D. R. Comparison of Extra Electrons in Colloidal *n*-Type Al^{3+}-Doped and Photochemically Reduced ZnO Nanocrystals. *Chem. Commun.* **2012**, *48*, 9352.

22. De Trizio, L.; Buonsanti, R.; Schimpf, A. M.; Llordes, A.; Gamelin, D. R.; Simonutti, R.; Milliron, D. J. Nb-Doped Colloidal TiO_2 Nanocrystals with Tunable Infrared Absorption. *Chem. Mater.* **2013**, *25*, 3383.

23. Diroll, B. T.; Gordon, T. R.; Gaulding, E. A.; Klein, D. R.; Paik, T.; Yun, H. J.; Goodwin, E. D.; Damodhar, D.; Kagan, C. R.; Murray, C. B. Synthesis of *n*-Type Plasmonic Oxide Nanocrystals and the Optical and Electrical Characterization of their Transparent Conducting Films. *Chem. Mater.* **2014**, *26*, 4579.

24. Liang, X.; Ren, Y.; Bai, S.; Zhang, N.; Dai, X.; Wang, X.; He, H.; Jin, C.; Ye, Z.; Chen, Q.; Chen, L.; Wang, J.; Jin, Y. Colloidal Indium-Doped Zinc Oxide Nanocrystals with Tunable Work Function: Rational Synthesis and Optoelectronic Applications. *Chem. Mater.* **2014**.

25. Ye, X.; Fei, J.; Diroll, B. T.; Paik, T.; Murray, C. B. Expanding the Spectral Tunability of Plasmonic Resonances in Doped Metal-Oxide Nanocrystals through Cooperative Cation–Anion Codoping. *J. Am. Chem. Soc.* **2014**.

26. Wang, C. J.; Shim, M.; Guyot-Sionnest, P. Electrochromic Nanocrystal Quantum Dots. *Science* **2001**, *291*, 2390.

27. Roest, A. L.; Kelly, J. J.; Vanmaekelbergh, D.; Meulenkamp, E. A. Staircase in the Electron Mobility of a ZnO Quantum Dot Assembly due to Shell Filling. *Phys. Rev. Lett.* **2002**, *89*, 036801.

28. Vanmaekelbergh, D.; Roest, A. L.; Germeau, A.; Kelly, J. J.; Meulenkamp, E. A.; Allan, G.; Delerue, C. Vanmaekelbergh et al. Reply. *Phys. Rev. Lett.* **2003**, *91*, 169704.

29. Wehrenberg, B. L.; Guyot-Sionnest, P. Electron and Hole Injection in PbSe Quantum Dot Films. *J. Am. Chem. Soc.* **2003**, *125*, 7806.

30. Haase, M.; Weller, H.; Henglein, A. Photochemistry and Radiation Chemistry of Colloidal Semiconductors. 23. Electron Storage on ZnO Particles and Size Quantization. *J. Phys. Chem.* **1988**, *92*, 482.

31. Wood, A.; Giersig, M.; Mulvaney, P. Fermi Level Equilibration in Quantum Dot-Metal Nanojunctions. *J. Phys. Chem. B* **2001**, *105*, 8810.

32. Liu, W. K.; Whitaker, K. M.; Kittilstved, K. R.; Gamelin, D. R. Stable Photogenerated Carriers in Magnetic Semiconductor Nanocrystals. *J. Am. Chem. Soc.* **2006**, *128*, 3910.

33. Liu, W. K.; Whitaker, K. M.; Smith, A. L.; Kittilstved, K. R.; Robinson, B. H.; Gamelin, D. R. Room-Temperature Electron Spin Dynamics in Free-Standing ZnO Quantum Dots. *Phys. Rev. Lett.* **2007**, *98*, 186804.

34. Whitaker, K. M.; Ochsenbein, S. T.; Polinger, V. Z.; Gamelin, D. R. Electron Confinement Effects in the EPR Spectra of Colloidal n-Type ZnO Quantum Dots. *J. Phys. Chem. C* **2008**, *112*, 14331.

35. Whitaker, K. M.; Ochsenbein, S. T.; Smith, A. L.; Echodu, D. C.; Robinson, B. H.; Gamelin, D. R. Hyperfine Coupling in Colloidal *n*-Type ZnO Quantum Dots: Effects on Electron Spin Relaxation. *J. Phys. Chem. C* **2010**, *114*, 14467.

36. Cohn, A. W.; Kittilstved, K. R.; Gamelin, D. R. Tuning the Potentials of "Extra" Electrons in Colloidal n-type ZnO Nanocrystals via Mg^{2+} Substitution. *J. Am. Chem. Soc.* **2012**, *134*, 7937.

37. Schrauben, J.; Hayoun, R.; Valdez, C.; Braten, M.; Fridley, L.; Mayer, J. Titanium and Zinc Oxide Nanoparticles Are Proton-Coupled Electron Transfer Agents. *Science* **2012**, *336*, 1298.

38. Schimpf, A. M.; Gunthardt, C. E.; Rinehart, J. D.; Mayer, J. M.; Gamelin, D. R. Controlling Carrier Densities in Photochemically Reduced Colloidal ZnO Nanocrystals: Size Dependence and Role of the Hole Quencher. *J. Am. Chem. Soc.* **2013**, *135*, 16569.

39. Rinehart, J. D.; Schimpf, A. M.; Weaver, A. L.; Cohn, A. W.; Gamelin, D. R. Photochemical Electronic Doping of Colloidal CdSe Nanocrystals. *J. Am. Chem. Soc.* **2013**, *135*, 18782.

40. Cohn, A. W.; Rinehart, J. D.; Schimpf, A. M.; Weaver, A. L.; Gamelin, D. R. Size Dependence of Negative Trion Auger Recombination in Photodoped CdSe Nanocrystals. *Nano Lett.* **2014**, *14*, 353−358.

41. Choi, S.-I.; Nam, K. M.; Park, B. K.; Seo, W. S.; Park, J. T. Preparation and Optical Properties of Colloidal, Monodisperse, and Highly Crystalline ITO Nanoparticles. *Chem. Mater.* **2008**, *20*, 2609.

42. Gilstrap, R. A.; Capozzi, C. J.; Carson, C. G.; Gerhardt, R. A.; Summers, C. J. Synthesis of a Nonagglomerated Indium Tin Oxide Nanoparticle Dispersion. *Adv. Mater.* **2008**, *20*, 4163.

43. Garcia, G.; Buonsanti, R.; Runnerstrom, E. L.; Mendelsberg, R. J.; Llordes, A.; Anders, A.; Richardson, T. J.; Milliron, D. J. Dynamically Modulating the Surface Plasmon Resonance of Doped Semiconductor Nanocrystals. *Nano Lett.* **2011**, *11*, 4415.

44. Lounis, S. D.; Runnerstrom, E. L.; Bergerud, A.; Nordlund, D.; Milliron, D. J. Influence of Dopant Distribution on the Plasmonic Properties of Indium Tin Oxide Nanocrystals. *J. Am. Chem. Soc.* **2014**, *136*, 7110.

45. Hammarberg, E.; Prodi-Schwab, A.; Feldmann, C. Microwave-Assisted Polyol Synthesis of Aluminium- and Indium-Doped ZnO Nanocrystals. *J. Colloid Interf. Sci.* **2009**, *334*, 29.

46. Schimpf, A. M.; Thakkar, N.; Gunthardt, C. E.; Masiello, D. J.; Gamelin, D. R. Charge-Tunable Quantum Plasmons in Colloidal Semiconductor Nanocrystals. *ACS Nano* **2013**, *8*, 1065.

47. Hayoun, R.; Whitaker, K. M.; Gamelin, D. R.; Mayer, J. M. Electron Transfer Between Colloidal ZnO Nanocrystals. *J. Am. Chem. Soc.* **2011**, *133*, 4228.

48. Wang, X.; Jin, Y. Z.; He, H. P.; Yang, F.; Yang, Y. F.; Ye, Z. Z. Bandgap Engineering and Shape Control of Colloidal $Cd_xZn_{1-x}O$ Nanocrystals. *Nanoscale* **2013**, *5*, 6464.

49. Yang, Y. F.; Jin, Y. Z.; He, H. P.; Wang, Q. L.; Tu, Y.; Lu, H. M.; Ye, Z. Z. Dopant-Induced Shape Evolution of Colloidal Nanocrystals: The Case of Zinc Oxide. *J. Am. Chem. Soc.* **2010**, *132*, 13381.

50. Kriegel, I.; Rodríguez-Fernández, J.; Wisnet, A.; Zhang, H.; Waurisch, C.; Eychmüller, A.; Dubavik, A.; Govorov, A. O.; Feldmann, J. Shedding Light on Vacancy-Doped Copper Chalcogenides: Shape-Controlled Synthesis, Optical Properties, and Modeling of Copper Telluride Nanocrystals with Near-Infrared Plasmon Resonances. *ACS Nano* **2013**, *7*, 4367.

51. Mendelsberg, R. J.; Garcia, G.; Li, H.; Manna, L.; Milliron, D. J. Understanding the Plasmon Resonance in Ensembles of Degenerately Doped Semiconductor Nanocrystals. *J. Phys. Chem. C* **2012**, *116*, 12226.

52. Mendelsberg, R. J.; Garcia, G.; Milliron, D. J. Extracting Reliable Electronic Properties From Transmission Spectra of Indium Tin Oxide Thin Films and Nanocrystal Films by Careful Application of the Drude Theory. *J. Appl. Phys.* **2012**, *111*, 063515.

53. Hamberg, I.; Granqvist, C. G. Optical Properties of Transparent and Heat-Reflecting Indium Tin Oxide Films: The Role of Ionized Impurity Scattering. *Appl. Phys. Lett.* **1984**, *44*, 721.

54. Hamberg, I.; Granqvist, C. G. Evaporated Sn-doped In_2O_3 films: Basic optical properties and applications to energy-efficient windows. *J. Appl. Phys.* **1986**, *60*, R123.

55. Gerlach, E. Carrier Scattering and Transport in Semiconductors Treated by the Energy-Loss Method. *J. Phys. C Solid State* **1986**, *19*, 4585.

56. Xie, Y.; Riedinger, A.; Prato, M.; Casu, A.; Genovese, A.; Guardia, P.; Sottini, S.; Sangregorio, C.; Miszta, K.; Ghosh, S.; Pellegrino, T.; Manna, L. Copper Sulfide Nanocrystals with Tunable Composition by Reduction of Covellite Nanocrystals with Cu+ Ions. *J. Am. Chem. Soc.* **2013**, *135*, 17630.

57. Zaitoun, M. A.; Mason, W. R.; Lin, C. T. Magnetic Circular Dichroism Spectra for Colloidal Gold Nanoparticles in Xerogels at 5.5 K. *J. Phys. Chem. B* **2001**, *105*, 6780.

58. Pineider, F.; Campo, G.; Bonanni, V.; Fernandez, C. J.; Mattei, G.; Caneschi, A.; Gatteschi, D.; Sangregorio, C. Circular Magnetoplasmonic Modes in Gold Nanoparticles. *Nano Lett.* **2013**, *13*, 4785.

Chapter 6

Charge-Tunable Quantum Plasmons in Colloidal Semiconductor Nanocrystals

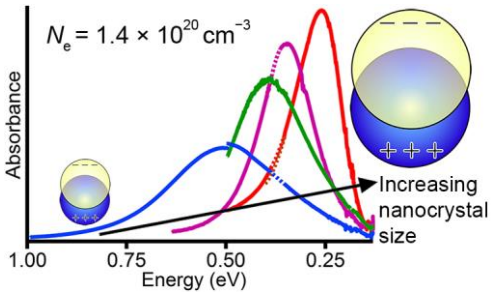

Adapted from: Schimpf, A. M.; Thakkar, N.; Gunthardt, C. E.; Masiello, D. J.; Gamelin, D. R. *ACS Nano* 2014, *8*, 1065.

6.1 Overview

Nanomaterials exhibiting plasmonic optical responses are impacting sensing, information processing, catalysis, solar, and photonics technologies. Recent advances have expanded the portfolio of plasmonic nanostructures into doped semiconductor nanocrystals, which allow dynamic manipulation of carrier densities. Once interpreted as intra-band single-electron transitions, the infrared absorption of doped semiconductor nanocrystals is now commonly attributed to localized surface plasmon resonances and analyzed using the classical Drude model to determine carrier densities. Here, we show that the experimental plasmon resonance energies of photodoped ZnO nanocrystals with controlled sizes and carrier densities diverge from classical Drude model predictions at small sizes, revealing quantum plasmons in these nanocrystals. A Lorentz oscillator model more adequately describes the data and illustrates a closer link between plasmon resonances and single-electron transitions in semiconductors than in metals, highlighting a fundamental contrast between these two classes of plasmonic materials.

6.2 Introduction

Carrier-doped semiconductor nanocrystals are envisioned as essential components of future information processing, solar energy conversion, and other technologies. Nanocrystal carrier

doping generates new infrared (IR) absorption bands similar to localized surface plasmon resonances (LSPRs) of metal nanoparticles. Semiconductor nanocrystals showing such LSPRs have recently attracted broad attention,[1,2] in part because of the wide range of carrier densities achievable in such systems. Over just the past few years, LSPRs have been reported in many semiconductor nanocrystals with excess charge carriers introduced by aliovalent,[3-7] vacancy-induced,[8-10] or redox[11,12] doping. Central to any analysis of these LSPRs is an assessment of the carrier density. Many investigations have applied the classical Drude model to estimate carrier densities from IR absorption energies.[3-6,8,10-12] Others have assumed stoichiometric relationships between defects and carriers.[9] In semiconductor nanocrystals, however, a large fraction of aliovalent dopants or electronic defects can be compensated by localized surface charges,[13] and impurity doping of any type perturbs carrier wavefunctions.[14] Additionally, in some cases the carriers may be partially localized.[15] These factors complicate determination of carrier densities using the Drude model. Moreover, the Drude model itself may not even be adequate for semiconductor nanocrystals, which have much smaller carrier densities than metals, but this model has not been quantitatively tested. Finally, quantum confinement effects are not accounted for in the Drude model and have also not yet been investigated in LSPR-supporting semiconductors. Here, we analyze the IR absorption spectra of photodoped colloidal ZnO nanocrystals with tunable radii (r) and carrier densities (N_e) to assess the applicability of the Drude model in this case. These experimental data expose fundamental shortcomings of the Drude model when applied to semiconductor nanocrystals, revealing the existence of quantum plasmons in semiconductor nanocrystals and highlighting important contrasts between LSPRs in semiconductor and metal nanostructures.

Photodoped ZnO nanocrystals are among the best characterized carrier-doped colloidal semiconductor nanocrystals[13,14,16-21] and offer a unique platform for turning on, tuning, and investigating semiconductor LSPRs. Anaerobic UV irradiation in the presence of an appropriate hole quencher allows accumulation of delocalized conduction-band electrons, achieving average carrier densities tunable from zero up to ~6×10^{20} cm^{-3}.[16] Unlike in other systems investigated to date, these carrier densities are readily determined by direct titration against mild redox reagents,[13,16,19,20,22,23] *providing a model-independent measure of this critical quantity*. Previous studies have described a new IR absorption band that accompanies the added conduction-band electrons,[19,24-26] but its interpretation remains ambiguous. It has generally been interpreted in terms of single-electron intra-conduction-band transitions,[19,24-26] but has recently also been interpreted in terms of LSPRs,[12] and similar IR absorption in Al^{3+}-doped ZnO nanocrystals has also been described as LSPRs.[27,28] If indeed this IR band is due to LSPRs, the relationship between these collective excitations and the anticipated single-electron excitations has yet to be revealed.

6.3 Results and analysis

Figure 6.1 shows IR absorption spectra of two anaerobic ZnO nanocrystal suspensions (r = 1.75 and 6 nm), each prepared and photodoped using ethanol for hole quenching as detailed previously (see Appendix B for details).[16] Spectra collected at various UV irradiation times are shown, with increasing IR absorption reflecting increasing electron density.[19,26] The maximum photodoping corresponds to an electron density of $1.4 \pm 0.4 \times 10^{20}$ cm^{-3} for both samples (Appendix G.1).[16] With added electrons, the IR absorption maxima blue shift while increasing in intensity. A similar blue shift has been reported in r = 2.1 nm ZnO nanocrystals,[26] where it was

interpreted as arising from the increased energy spacings of intra-conduction-band single-electron transitions. The experimental shifts are slightly greater than predicted from tight-binding calculations,[26] but are comparable to expectations from the classical Drude model (Figure G.4a). Similar shifts are observed in all sizes of nanocrystals (Figure G.4b), even though the smallest have a maximum of ~3 conduction-band electrons while the largest have up to ~130. This similarity suggests that the blue shift is correlated with electron *density* rather than number. Additionally, from tight binding calculations,[26] a significant blue shift is not expected in large nanocrystals, where intraband spacings are nearly constant. Although it is conceivable that the blue shift reflects preferential reduction of larger nanocrystals, because intraband spacings are size-dependent and electrons can transfer rapidly from one nanocrystal to another,[14,18] the average radius (6 nm) for the larger ZnO nanocrystals of Figure 6.1 is well beyond the quantum confinement size regime (≤3.5 nm), allowing the conclusion that size heterogeneity is not responsible. Based on these considerations, the IR blue shift with increased photodoping is consistent with assignment of this IR band as an LSPR.

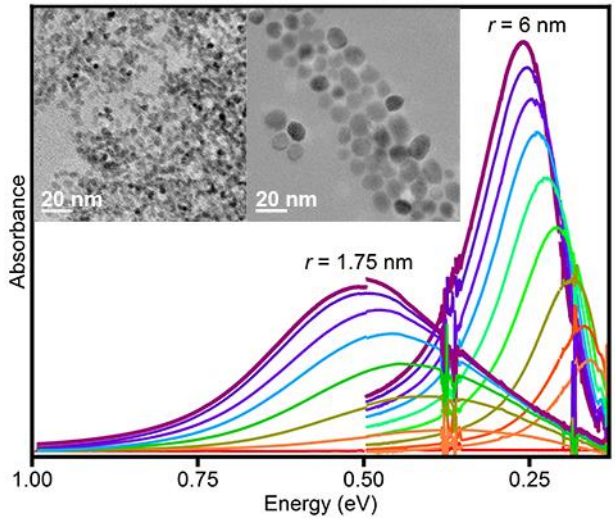

Figure 6.1. Infrared absorption spectra of photodoped ZnO nanocrystals. IR absorption spectra of r = 1.75 and 6 nm colloidal photodoped ZnO nanocrystals. For each sample, the increased IR absorption corresponds to progressively greater photodoping. Both samples display the same maximum photodoping level of 1.4 ± 0.4 × 10^{20} cm^{-3}. This density corresponds to a maximum average occupancy of 3.2 ± 0.9 and 116 ± 22 electrons per nanocrystal for the small and large nanocrystals, respectively. Inset: TEM images of the r = 1.75 nm (left) and r = 6 nm (right) nanocrystals.

Magnetic circular dichroism (MCD) spectroscopy provides strong support for assignment of the IR band in photodoped ZnO nanocrystals as an LSPR. Figure 6.2 shows room-temperature absorption (a) and variable-field MCD (b) spectra of photodoped r = 1.55 nm ZnO nanocrystals. The MCD intensity is very large ($|\Delta A/A_0|$ ~ 0.01) but does not maximize at the absorption maximum, instead crossing zero close to the absorption maximum. The MCD intensity is temperature independent (Figure G.5) and shows a linear dependence on magnetic field, even at 2 K (Figure 6.2, inset). Strikingly similar MCD data have been reported for the LSPRs of colloidal Au nanoparticles,[29] which also show very large ($|\Delta A/A_0|$ ~ 0.001) and temperature-independent derivative-shaped MCD intensities. These similarities support the assignment of the ZnO IR peak as an LSPR.

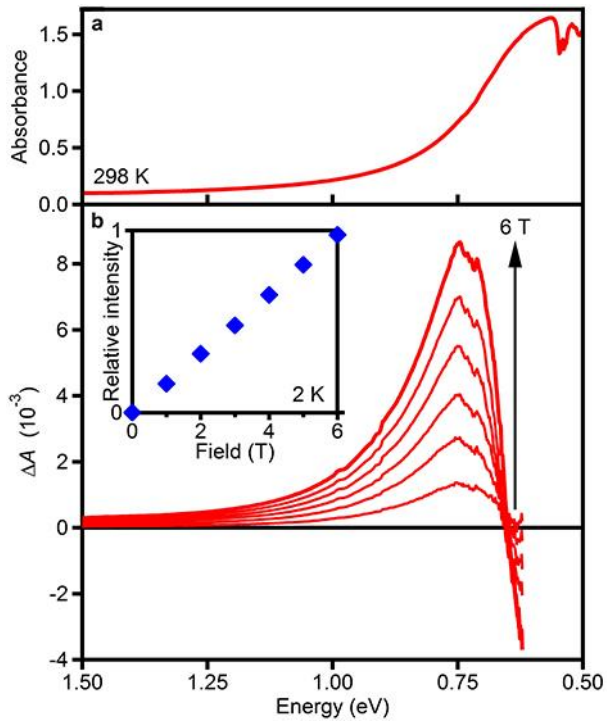

Figure 6.2. Infrared magnetic circular dichroism spectra of photodoped ZnO nanocrystals. Room-temperature (a) absorption and (b) MCD spectra of heavily photodoped colloidal r = 1.55 nm ZnO nanocrystals. The arrow indicates increasing magnetic field strength in 1 T steps. The dip in panel (a) at ~0.55 eV is due to imperfect subtraction of solvent vibrations. Inset: Relative 2 K IR MCD intensities plotted as a function of magnetic field strength. The MCD spectra terminate at the instrumental limit of ~0.6 eV.

Temperature-independent derivative-like band shapes are typically characteristic of *A*-term MCD intensities,[30] which derive from the effects of magnetic fields on excited states rather than from magnetization of the ground state (*C*-term).[30] Previous MCD spectra of plasmons in Au nanoparticles have been interpreted in this way.[29] For the photodoped ZnO nanocrystals, this interpretation is surprising because of the strong correlation between IR absorption and the ground-state g = 1.96 electron paramagnetic resonance (EPR) intensity from the delocalized electrons within these nanocrystals.[19,21] Paramagnets typically display *C*-term MCD intensity that increases rapidly with decreasing temperature (in proportion to $1/T$ for simple Curie-type paramagnets, see Figure G.6) and therefore dominates at low temperatures. The MCD of these

photodoped ZnO nanocrystals is thus not typical of paramagnetic chromophores. We propose that the temperature independence of the plasmon MCD intensities in these nanocrystals may alternatively reflect Pauli-type paramagnetism, a characteristic of conduction electrons in most nonferromagnetic metals.[31]

Several samples of colloidal ZnO nanocrystals were prepared with average radii ranging from 1.75 to 6 nm. All photodoped to the same electron density of $1.4 \pm 0.4 \times 10^{20}$ cm^{-3}, which was independently verified.[23] Figure 6.3a shows IR absorption spectra of these nanocrystals and illustrates a key result of this study: At a constant carrier density, the IR absorption blue shifts substantially with decreasing nanocrystal radius. Figure 6.3b plots the energies of the absorption maxima as a function of nanocrystal radius (blue circles). For large radii ($\gtrsim$ 5 nm), this energy approaches an asymptote of ~0.25 eV, agreeing well with the LSPR energies of ZnO thin films[32] (which should be greater by a factor of ~1.2). This size dependence is very similar to that observed for the first excitonic absorption maximum in ZnO nanocrystals arising from quantum confinement,[33] but it is qualitatively different from that anticipated by the classical Drude model.

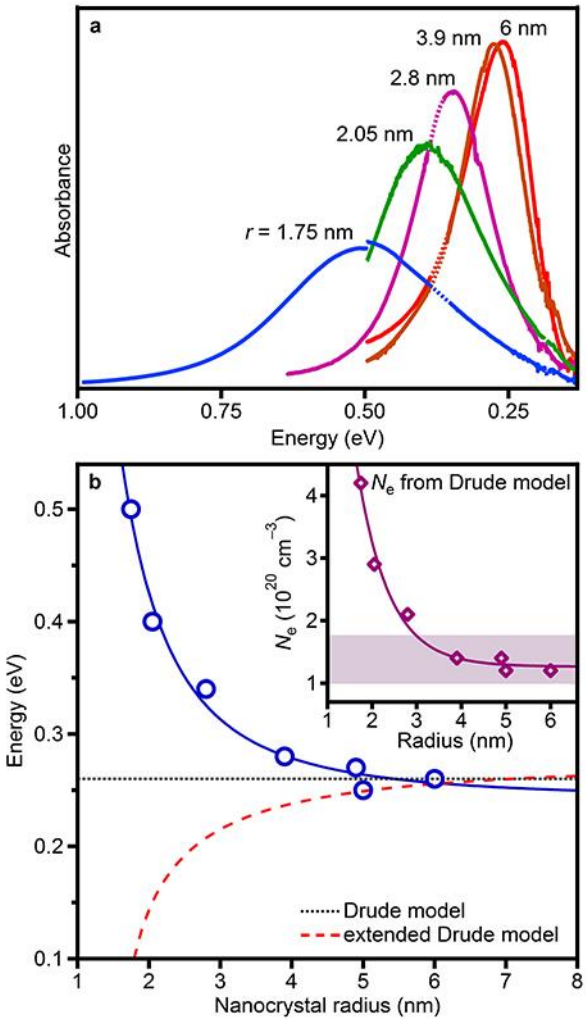

Figure 6.3. Size dependence of LSPR energies in colloidal photodoped ZnO nanocrystals. (a) IR absorption spectra of a series of colloidal ZnO nanocrystals with different radii, each photodoped to an average carrer density of N_e = 1.4 ± 0.4 × 10^{20} cm^{-3}. Dotted lines indicate the region of intense C–H stretches. (b) IR peak maxima versus nanocrystal radius (blue circles). The dotted black line shows the Drude model (equation 6.1) prediction for LSPR energies at N_e = 1.4 ± 0.4 × 10^{20} cm^{-3}. The dashed red line extends this model to account for increased surface scattering in small nanocrystals (equation 6.2). Inset: Predicted (diamonds, from equation 6.1) and experimental (shaded region) carrier densities plotted versus nanocrystal radius. Solid lines are guides to the eye.

The LSPR frequencies predicted by the classical Drude model are given by

$$\omega_{sp} = \sqrt{\frac{N_e e^2}{\varepsilon_0 m_e \left(\varepsilon_\infty + 2\varepsilon_m\right)} - \gamma^2} \,. \qquad (6.1)$$

This relationship has been widely employed in the analysis of heavily doped semiconductor nanocrystals. Here, $\gamma = \gamma_{bulk}$ is the bulk scattering frequency, e is the elementary charge, ε_0 is the permittivity of vacuum, ε_m is the medium dielectric (estimated as 2.25 for toluene), ε_∞ is the high-frequency dielectric (3.72 for ZnO),[34] and $m_e = 0.28m_0$ is the mass of an electron in ZnO.[34] Application of equation 6.1 to predict the LSPR frequencies of ZnO nanocrystals photodoped to $N_e = 1.4 \times 10^{20}$ cm^{-3} yields the dotted line in Figure 6.3b. The Drude model accurately estimates ω_{sp} for the largest ZnO nanocrystals but fails for smaller nanocrystals. Equivalently, the inset of Figure 6.3b compares the experimental carrier densities (shaded) with those estimated from equation 6.1. Here, N_e values were calculated from the IR absorption using ω_{sp} and γ as the maxima and half-widths-at-half-maxima (HWHM), respectively. The Drude model accurately estimates the carrier density of the largest ZnO nanocrystals, yielding a value of 1.2×10^{20} cm^{-3}, but it predicts a carrier density roughly four times too large (4.2×10^{20} cm^{-3}) for the smallest nanocrystals. Furthermore, an extended Drude model that accounts for size-dependent surface scattering through modification of the scattering frequency,

$$\gamma = \gamma_{bulk} + \frac{Av_F}{r}, \tag{6.2}$$

actually predicts an absorption *red shift* with decreasing radius for a constant N_e (Figure 6.3b, dashed line). Here, v_F is the Fermi velocity (8.4×10^5 m/s in ZnO)[35] and A is an empirical constant whose value is debated in the literature.[36] Drude models thus fail to describe the IR absorption spectra of carrier-doped ZnO quantum dots. For accurate interpretation of this IR absorption, a more sophisticated model is needed.

To address these shortcomings, we introduce a quantum mechanical correction to the driving force on a classical Lorentz electron in an external electric field.[37] A similar semiclassical

approach was recently used to model a blue shift of Ag nanoparticle LSPR energies with decreasing radius.[38] We model electron motion within a spherical semiconductor nanocrystal as a collection of damped and driven harmonic oscillators, where the driving force is dependent on both the incident electric field and quantum mechanical responses to the boundary. Quantum confinement also alters the harmonic restoring force by discretizing the set of available transition frequencies, ω_{if}, where *i* and *f* are composite labels for initial and final quantum states. This model yields the dielectric function,

$$\varepsilon(\omega) = \varepsilon_{\mathrm{IB}}(\omega) - \omega_{\mathrm{p}}^2 \sum_{i,f} \frac{S_{if}}{\omega^2 + i\gamma\omega - \omega_{if}^2}, \tag{6.3}$$

where $\omega_{\mathrm{p}} = \sqrt{N_{\mathrm{e}} e^2 / \varepsilon_0 m_{\mathrm{e}}}$ is the bulk plasma frequency, S_{if} is the oscillator strength obeying the Thomas-Reiche-Kuhn sum rule, γ is the size-dependent scattering frequency (equation 6.2), and $\varepsilon_{\mathrm{IB}}(\omega)$ represents contributions from interband transitions.

To apply this dielectric function to photodoped ZnO nanocrystals, conduction electrons are modeled as noninteracting particles within an infinite spherical potential well. The quasi-spherical shapes of our nanocrystals are verified by transmission electron microscopy (Figure 6.1, inset). The many-electron character is introduced by imposing the Pauli exclusion principle and a hydrogenic shell-filling scheme with degeneracy $2n^2$ for each principle quantum number, n. Under these assumptions, the Fermi level, n_{F}, is determined by finding the nearest integer to the solution of

$$n_{\mathrm{e}} = \sum_{n=1}^{n_{\mathrm{F}}} 2n^2, \tag{6.4}$$

where $n_e = (4/3)\pi r^3 N_e$ is the total number of conduction electrons. Dominant contributions to the sum in equation 6.3 come from low-energy excitations around this value of n_F (Appendix G.5). Finally, interband transitions in ZnO occur above ~3.5 eV, far from the IR region. Therefore, it suffices to replace $\varepsilon_{IB}(\omega)$ with ε_∞ to impose consistency with the behavior of bulk ZnO. With this approach, LSPRs are found according to the Clausius-Mossotti relation at frequencies where

$$\mathrm{Re}\left[\varepsilon(\omega)\right] = -2\varepsilon_m . \tag{6.5}$$

Only frequencies in normal dispersion regimes ($(\partial/\partial\omega)\mathrm{Re}\left[\varepsilon(\omega)\right] > 0$) are considered. All calculations use the experimental carrier density of 1.4×10^{20} cm^{-3}.

Figure 6.4a presents $\mathrm{Re}\left[\varepsilon(\omega)\right]$ for various ZnO nanocrystal sizes (see Figure G.7 for $\mathrm{Im}\left[\varepsilon(\omega)\right]$). The corresponding normalized absorption efficiencies are shown in Figure 6.4b. LSPR energies, $\hbar\omega_{sp}$, were determined using equation 6.5 and are plotted on top of the absorption efficiencies (black circles). The single-electron transition energies, $\hbar\omega_{if}$, are also plotted in Figure 6.4b (white circles), with symbol opacities proportional to S_{if}. LSPRs are found in regions of high absorption efficiency, supporting the conclusion that plasmons dominate the ZnO nanocrystal IR absorption spectra at these experimental carrier densities. The single-electron transitions are relatively weak because they involve only one electron, whereas plasmon excitations involve many. As the radius decreases, the LSPR and lowest-energy single-electron transition energies converge. A similar convergence occurs for fixed radius as N_e is reduced (Figure G.7). The discontinuities in these calculations, which appear as jumps in Figure 6.4b, are a consequence of the shell-filling approximation used in our model (equation 6.4).

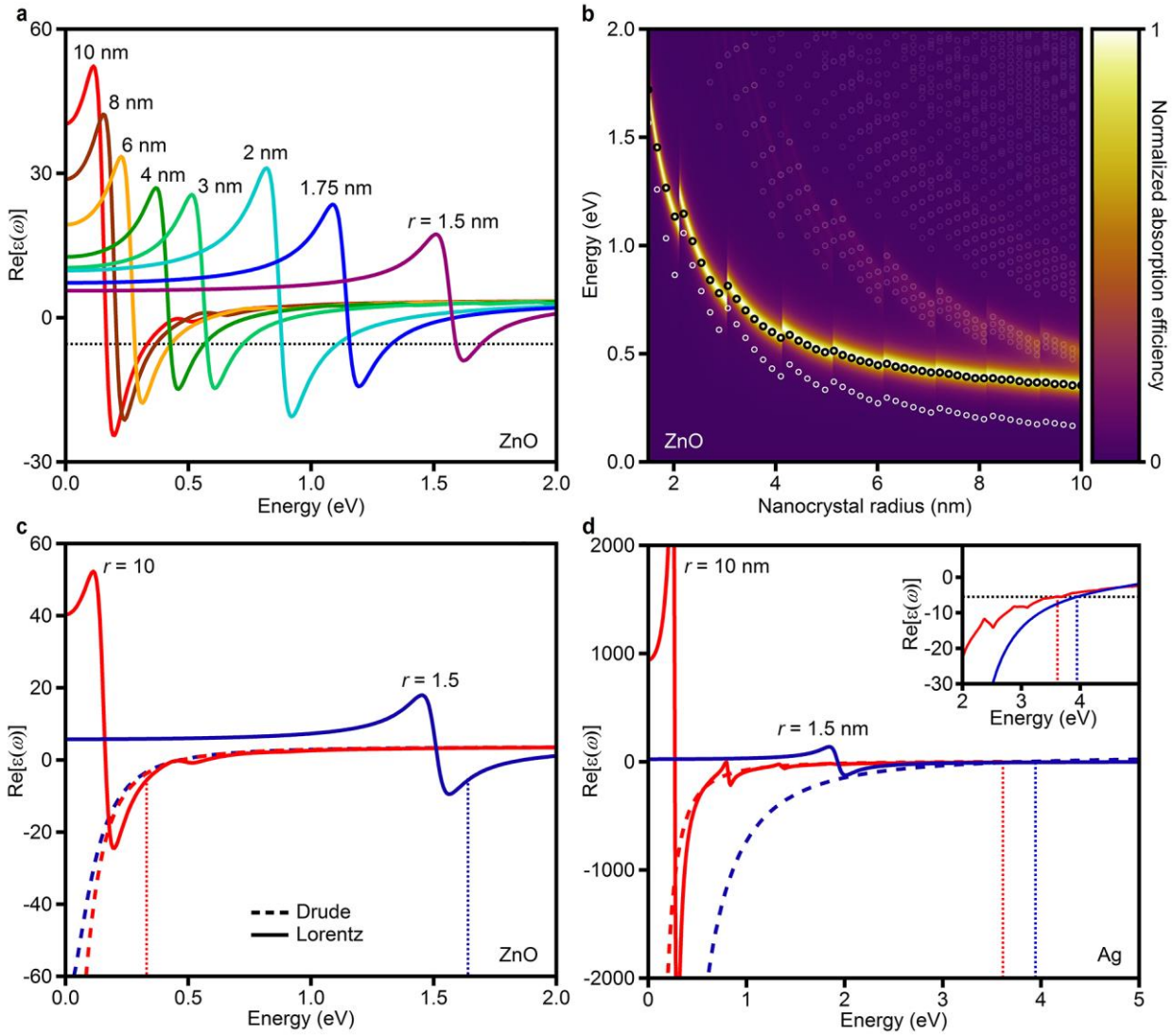

Figure 6.4. Calculated dependence of LSPR frequency on nanocrystal radius in photodoped ZnO and comprison to Au. Spectral dependence of (a) the real part of the ZnO dielectric function for various nanocrystal radii and of (b) the corresponding normalized absorption efficiencies as a function of nanocrystal radius. The dotted black line in panel (a) is positioned at $-2\varepsilon_m$. The crossings of this line with Re[ε(ω)] in regions of normal dispersion correspond to LSPR energies, $\hbar\omega_{sp}$, which are displayed as black open circles in panel (b). The white circles in panel (b) correspond to single-electron transitions and their opacities are scaled to their oscillator strengths. Also shown are the spectral dependencies of the real part of the dielectric functions for (c) ZnO and (d) Ag calculated with the Drude (dashed lines) and Lorentz (solid lines) models for two different sizes. The dotted vertical lines indicate the crossings of the Lorentz model with $-2\varepsilon_m = -5.5$ for the two different sizes (red and blue). All ZnO calculations use the experimental carrier density of 1.4×10^{20} cm^{-3}.

As observed experimentally, the calculated results of Figure 6.4b show an increase in $\hbar\omega_{sp}$ with decreasing radius, starting from bulk. We conclude that this model, although idealized and without any adjustable parameters, successfully captures the essence of the experimental observations. The calculated size dependence is steeper than observed experimentally, possibly because of the model's inability to account for electron tunneling beyond the nanocrystal surface ("spill-out").[39] Tunneling makes the smallest nanocrystals effectively larger and weakens the size dependence. Another factor could be the existence of delocalized surface states, such as Shockley or Tamm states.[40] Surface states could be important at high electron densities, particularly if the electron-charge-compensating protons from photodoping all reside at the ZnO nanocrystal surfaces. Confinement of such surface states is documented in metals, where electrons behave as particles in two-dimensional boxes.[41] The calculations of Figure 6.4 are based on an idealized model and do not account for surface states. We note that the experimental size dependence of the IR absorption is similar at both high and low electron densities (Figure G.4b), arguing against major contributions from surface states. Additional deviations from ideality may arise from nanocrystal shape anisotropies and surface ligation. Expansion of the model to include adjustable parameters accounting for such effects can indeed improve quantitative agreement with the experimental data (*e.g.*, Figure G.8), but it does not provide greater insight into the physical problem. Overall, the data in Figure 6.3b reveal large quantum size effects manifested in the LSPRs of doped semiconductor nanocrystals. *This result constitutes the first experimental demonstration of quantum confinement effects on LSPRs in semiconductors.* We stress that this size dependence is identified only because carrier densities

could be measured independently. Application of the Drude model to deduce carrier densities would have yielded a qualitatively different understanding of these semiconductor LSPRs.

It is interesting to note that, unlike in metals, LSPRs in photodoped ZnO nanocrystals occur spectrally near the regions of large anomalous dispersion (Figure 6.4c), placing them close to the most allowed single-electron transitions. In this regime, the Lorentz dielectric model is strongly non-Drude in character, and the free-electron picture used for metallic plasmons is qualitatively incorrect. Instead, the ZnO LSPRs become very sensitive to the most-dominant single-electron transitions, and converge to their energies in the limit of low carrier occupancy. Moreover, because this spectral proximity is a result of the relatively low carrier densities, it is not specific to ZnO or to nanocrystals. Carrier densities achievable in semiconductors are generally 2–3 orders of magnitude smaller than in metals, making this relationship between LSPRs and single-electron transitions universally significant. Figures 6.4c and 6.4d highlight this important contrast, comparing the calculated dielectric functions of photodoped ZnO nanocrystals and Ag nanoparticles at two radii. Because of its high carrier density, collective excitations in Ag occur far from the dominant single-electron transitions, within the free-electron (Drude) part of the Lorentz dielectric function. Consequently, they are spectrally distant from and relatively insensitive to the most-allowed single-electron transitions (Figure G.9). In stark contrast, the lower carrier densities of photodoped ZnO nanocrystals link the plasmons to dominant single-electron excitations, making them difficult to distinguish energetically. When these single-electron transitions shift due to changing nanocrystal radius, the collective excitations follow. These insights reconcile conflicting evidence for interpretation of the IR bands of doped semiconductor nanocrystals as plasmon resonances versus single-electron excitations.

6.4 Summary and conclusions

In summary, carrier-doped semiconductor nanocrystals offer a unique platform for tuning plasmons on nanometer length scales. The ability to control and quantify carrier densities in colloidal ZnO nanocrystals has allowed experimental assessment of the classical Drude model commonly applied to interpret IR absorption spectra of doped semiconductor nanocrystals. Investigating the relationship between nanocrystal size and IR absorption energy at constant carrier density has revealed that the Drude model fails for small nanocrystals in which electron wave functions are quantum confined. A Lorentz oscillator model that accounts for quantum-mechanical corrections qualitatively reproduces the experimental size dependence. Both the experimental and theoretical results bridge the single-electron and LSPR regimes, displaying quantum confinement in small nanocrystals and converging to classical bulk LSPRs in large nanocrystals. These findings shed new light on semiconductor plasmonics, with important ramifications for both fundamental investigations of doped semiconductor nanocrystals and future applications of this emerging class of materials.

6.5 Experimental methods

Synthesis and characterization of colloidal ZnO nanocrystals are provided in Appendix A. Photodoping and titration details are provided in Appendix B and Appendix G.

6.5.1 IR absorption measurements. For infrared (IR) absorption measurements on photodoped nanocrystals, nanocrystal solutions were prepared anaerobically to be ~0.15 M Zn^{2+} in toluene. These solutions were loaded into an air-free IR cell in an inert-atmosphere glove box, which was then removed from the glove box for subsequent experiments. The nanocrystals were photodoped by placing the IR cell in front of a 100 W Hg/Xe Oriel photolysis lamp for short

times (1−20 s between spectra). The IR absorption was monitored during photodoping until it stopped increasing. Residual EtOH from the synthesis and purification procedures is the hole quencher.[17]

6.5.2 MCD spectroscopy. For MCD measurements, a 200 μl sample of nanocrystals was prepared anaerobically in 2-methyltetrahydrofuran and to it added 2 μl of 1 M Li[Et_3BH], which serves as a hole quencher.[16] The sample was prepared in the glove box by dropping a small amount of this solution onto a polished quartz disc holding a Teflon spacer and placing another quartz disc on top. These nanocrystals were photodoped as described above and placed into the magneto-cryostat.

6.6 References

1. Routzahn, A. L.; White, S. L.; Fong, L.-K.; Jain, P. K. Plasmonics with Doped Quantum Dots. *Israel J. Chem.* **2012**, *52*, 983.

2. Scotognella, F.; Valle, G.; Srimath Kandada, A.; Zavelani-Rossi, M.; Longhi, S.; Lanzani, G.; Tassone, F. Plasmonics in Heavily-Doped Semiconductor Nanocrystals. *Eur. Phys. J. B* **2013**, *86*, 1.

3. Nütz, T.; zum Felde, U.; Haase, M. Wet-Chemical Synthesis of Doped Nanoparticles: Blue-Colored Colloids of *n*-Doped SnO_2:Sb. *J. Chem. Phys.* **1999**, *110*, 12142.

4. Wang, T.; Radovanovic, P. V. Free Electron Concentration in Colloidal Indium Tin Oxide Nanocrystals Determined by Their Size and Structure. *J. Phys. Chem. C* **2011**, *115*, 406.

5. Niezgoda, J. S.; Harrison, M. A.; McBride, J. R.; Rosenthal, S. J. Novel Synthesis of Chalcopyrite $Cu_xIn_yS_2$ Quantum Dots with Tunable Localized Surface Plasmon Resonances. *Chem. Mater.* **2012**, *24*, 3294.

6. Chou, L. W.; Shin, N.; Sivaram, S. V.; Filler, M. A. Tunable Mid-Infrared Localized Surface Plasmon Resonances in Silicon Nanowires. *J. Am. Chem. Soc.* **2012**, *134*, 16155.

7. De Trizio, L.; Buonsanti, R.; Schimpf, A. M.; Llordes, A.; Gamelin, D. R.; Simonutti, R.; Milliron, D. J. Nb-Doped Colloidal TiO_2 Nanocrystals with Tunable Infrared Absorption. *Chem. Mater.* **2013**, *25*, 3383.

8. Luther, J.; Jain, P.; Ewers, T.; Alivisatos, A. Localized Surface Plasmon Resonances Arising from Free Carriers in Doped Quantum Dots. *Nat. Mater.* **2011**, *10*, 361.

9. Manthiram, K.; Alivisatos, A. Tunable Localized Surface Plasmon Resonances in Tungsten Oxide Nanocrystals. *J. Am. Chem. Soc.* **2012**, *134*, 3995.

10. Polking, M. J.; Jain, P. K.; Bekenstein, Y.; Banin, U.; Millo, O.; Ramesh, R.; Alivisatos, A. P. Controlling Localized Surface Plasmon Resonances in GeTe Nanoparticles Using an Amorphous-to-Crystalline Phase Transition. *Phys. Rev. Lett.* **2013**, *111*, 037401.

11. Palomaki, P. K. B.; Miller, E. M.; Neale, N. R. Control of Plasmonic and Interband Transitions in Colloidal Indium Nitride Nanocrystals. *J. Am. Chem. Soc.* **2013**, *135*, 14142.

12. Faucheaux, J. A.; Jain, P. K. Plasmons in Photocharged ZnO Nanocrystals Revealing the Nature of Charge Dynamics. *J. Phys. Chem. Lett.* **2013**, *4*, 3024.

13. Schimpf, A. M.; Ochsenbein, S. T.; Buonsanti, R.; Milliron, D. J.; Gamelin, D. R. Comparison of Extra Electrons in Colloidal *n*-Type Al^{3+}-Doped and Photochemically Reduced ZnO Nanocrystals. *Chem. Commun.* **2012**, *48*, 9352.

14. Cohn, A. W.; Kittilstved, K. R.; Gamelin, D. R. Tuning the Potentials of "Extra" Electrons in Colloidal n-type ZnO Nanocrystals via Mg^{2+} Substitution. *J. Am. Chem. Soc.* **2012**, *134*, 7937.

15. Kriegel, I.; Rodríguez-Fernández, J.; Wisnet, A.; Zhang, H.; Waurisch, C.; Eychmüller, A.; Dubavik, A.; Govorov, A. O.; Feldmann, J. Shedding Light on Vacancy-Doped Copper Chalcogenides: Shape-Controlled Synthesis, Optical Properties, and Modeling of Copper Telluride Nanocrystals with Near-Infrared Plasmon Resonances. *ACS Nano* **2013**, *7*, 4367.

16. Schimpf, A. M.; Gunthardt, C. E.; Rinehart, J. D.; Mayer, J. M.; Gamelin, D. R. Controlling Carrier Densities in Photochemically Reduced Colloidal ZnO Nanocrystals: Size Dependence and Role of the Hole Quencher. *J. Am. Chem. Soc.* **2013**, *135*, 16569.

17. Cohn, A. W.; Janßen, N.; Mayer, J. M.; Gamelin, D. R. Photocharging ZnO Nanocrystals: Picosecond Hole Capture, Electron Accumulation, and Auger Recombination. *J. Phys. Chem. C* **2012**, *116*, 20633.

18. Hayoun, R.; Whitaker, K. M.; Gamelin, D. R.; Mayer, J. M. Electron Transfer Between Colloidal ZnO Nanocrystals. *J. Am. Chem. Soc.* **2011**, *133*, 4228.

19. Liu, W. K.; Whitaker, K. M.; Smith, A. L.; Kittilstved, K. R.; Robinson, B. H.; Gamelin, D. R. Room-Temperature Electron Spin Dynamics in Free-Standing ZnO Quantum Dots. *Phys. Rev. Lett.* **2007**, *98*, 186804.

20. Schrauben, J.; Hayoun, R.; Valdez, C.; Braten, M.; Fridley, L.; Mayer, J. Titanium and Zinc Oxide Nanoparticles Are Proton-Coupled Electron Transfer Agents. *Science* **2012**, *336*, 1298.

21. Whitaker, K. M.; Ochsenbein, S. T.; Polinger, V. Z.; Gamelin, D. R. Electron Confinement Effects in the EPR Spectra of Colloidal n-Type ZnO Quantum Dots. *J. Phys. Chem. C* **2008**, *112*, 14331.

22. Wood, A.; Giersig, M.; Mulvaney, P. Fermi Level Equilibration in Quantum Dot-Metal Nanojunctions. *J. Phys. Chem. B* **2001**, *105*, 8810.

23. Rinehart, J. D.; Schimpf, A. M.; Weaver, A. L.; Cohn, A. W.; Gamelin, D. R. Photochemical Electronic Doping of Colloidal CdSe Nanocrystals. *J. Am. Chem. Soc.* **2013**, *135*, 18782.

24. Shim, M.; Guyot-Sionnest, P. *n*-Type Colloidal Semiconductor Nanocrystals. *Nature* **2000**, *407*, 981.

25. Shim, M.; Guyot-Sionnest, P. Organic-Capped ZnO nanocrystals: Synthesis and *n*-Type Character. *J. Am. Chem. Soc.* **2001**, *123*, 11651.

26. Germeau, A.; Roest, A. L.; Vanmaekelbergh, D.; Allan, G.; Delerue, C.; Meulenkamp, E. A. Optical Transitions in Artificial Ffew-Electron Atoms Strongly Confined Inside ZnO Nanocrystals. *Phys. Rev. Lett.* **2003**, *90*, 097401.

27. Buonsanti, R.; Llordes, A.; Aloni, S.; Helms, B.; Milliron, D. Tunable Infrared Absorption and Visible Transparency of Colloidal Aluminum-Doped Zinc Oxide Nanocrystals. *Nano Lett.* **2011**, *11*, 4706.

28. Garcia, G.; Buonsanti, R.; Llordes, A.; Runnerstrom, E. L.; Bergerud, A.; Milliron, D. J. Near-Infrared Spectrally Selective Plasmonic ElectrochromicThin Films. *Adv. Opt. Mater.* **2013**, *1*, 215.

29. Zaitoun, M. A.; Mason, W. R.; Lin, C. T. Magnetic Circular Dichroism Spectra for Colloidal Gold Nanoparticles in Xerogels at 5.5 K. *J. Phys. Chem. B* **2001**, *105*, 6780.

30. Piepho, S. B.; Schatz, P. N. *Group Theory in Spectroscopy with Applications to Magnetic Circular Dichroism*; Wiley: New York, U.S.A., 1983.

31. Kondo, J. *The Physics of Dilute Magnetic Alloys*; Cambridge University Press: United Kingdom, 2012.

32. Sachet, E.; Losego, M. D.; Guske, J.; Franzen, S.; Maria, J. P. Mid-Infrared Surface Plasmon Resonance in Zinc Oxide Semiconductor Thin Films. *Appl. Phys. Lett.* **2013**, *102*, 051111.

33. Wood, A.; Giersig, M.; Hilgendorff, M.; Vilas-Campos, A.; Liz-Marzán, L. M.; Mulvaney, P. Size Effects in ZnO: The Cluster to Quantum Dot Transition. *Aust. J. Chem.* **2003**, *56*, 1051.

34. Madelung, O. *Semiconductors: Data Handbook*; Springer: New York, 2004.

35. Behera, H.; Mukhopadhyay, G. Strain-Tunable Band Parameters of ZnO Monolayer in Graphene-Like Honeycomb Structure. *Phys. Lett. A* **2012**, *376*, 3287.

36. Kreibig, U.; Genzel, L. Optical Absorption of Small Metallic Particles. *Surf. Sci.* **1985**, *156*, 678.

37. Dressel, M.; Grüner, G. *Electrodynamics of Solids*; Cambridge University Press: United Kingdom, 2002.

38. Scholl, J. A.; Koh, A. L.; Dionne, J. A. Quantum Plasmon Resonances of Individual Metallic Nanoparticles. *Nature* **2012**, *483*, 421.

39. Monreal, R. C.; Antosiewicz, T. J.; Apell, S. P. Competition Between Surface Screening and Size Quantization for Surface Plasmons in Nanoparticles. *New J. Phys.* **2013**, *15*, 083044.

40. Shockley, W. On the Surface States Associated with a Periodic Potential. *Phys. Rev.* **1939**, *56*, 317.

41. Crommie, M. F.; Lutz, C. P.; Eigler, D. M. Confinement of Electrons to Quantum Corrals on a Metal Surface. *Science* **1993**, *262*, 218.

Chapter 7

Acceleration of Mn^{2+} Spin Relaxation by Excess Charge Carriers in Colloidal *n*-Type $Zn_{1-x}Mn_xO$ Nanocrystals

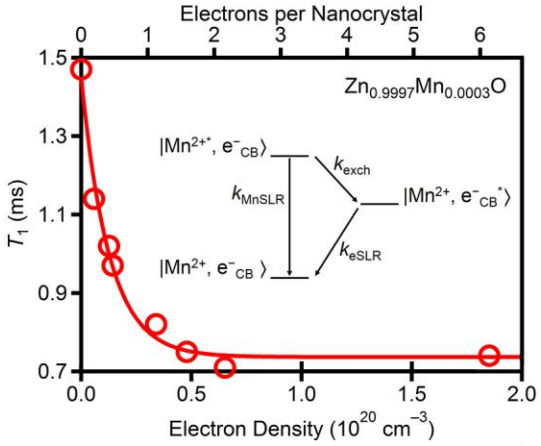

Adapted from: Schimpf, A. M.; Rinehart, J. D. Ochsenbein, S. T.; Gamelin, D. R. *In preparation.*

7.1 Overview

We present a quantitative analysis of how colloidal impurity-doped semiconductor nanostructures are affected by the introduction of excess charge carriers. Employing pulsed electron paramagnetic resonance (pEPR) spectroscopy enables us to probe the influence of excess electrons on the spin relaxation dynamics of Mn^{2+} doped into colloidal ZnO nanocrystals. We show that Mn^{2+} spin-lattice relaxation is strongly accelerated by the addition of one electron to the conduction band of the nanocrystals. We propose this increased relaxation rate in *n*-type $Zn_{1-x}Mn_xO$ nanocrystals is due to a new pathway not available in intrinsic $Zn_{1-x}Mn_xO$ nanocrystals and propose a kinetic model to quantify the enhancement. These findings are relevant to the design of DMS nanostructures for spin-based information processing technologies.

7.2 Introduction

Diluted magnetic semiconductor (DMS) nanocrystals are attractive targets for emerging spintronic and quantum computing applications[1-4] due to the large carrier-dopant magnetic

exchange interactions[5-7] and the ability to electronically and optically manipulate or read-out the magnetic dopant spins. One particular motif that has received broad attention involves the incorporation of Mn^{2+} cations into metal oxide nanocrystals. Substitutional Mn^{2+} incorporation has been demonstrated in nanoscale oxides from a distribution of many hundreds of Mn^{2+} cations per nanocrystal down to a single magnetic dopant per nanocrystal. Previous studies employing this motif have demonstrated that dopant-dopant exchange interactions and spin polarizations can be effectively manipulated by the introduction and removal of excess free carriers[8] or excitons. Less is known, however, about the effects of these free carriers on the dynamics of the Mn^{2+} spins. Such dynamics will eventually govern many of the device characteristics from polarization switching frequencies to the available timescale for coherent operations.

A distinct advantage of colloidal DMS nanocrystals is that many such systems can be easily photodoped to introduce a well-defined number of stable, delocalized electrons.[8-13] This chemistry turns on interactions between the delocalized electrons and the $S = 5/2$ Mn^{2+} ions, allowing the effects of delocalized charges on spin relaxation times to be varied systematically. Quantitative understanding of the effects of proximate electrons or holes on spin-lattice relaxation and quantum coherence times of magnetic dopants is vital to developing technologies based on DMS nanocrystal architectures. Here, we use electron paramagnetic resonance (EPR) spectroscopy to explore the effects of added electrons on the spin-lattice and spin-spin relaxation of Mn^{2+} dopants in colloidal ZnO nanocrystals.

7.3 Results

EPR experiments are detailed in Appendix H. Colloidal $Zn_{1-x}Mn_xO$ nanocrystals were synthesized and capped with trioctylphosphine oxide ligands as described previously (Appendix

A.1).[14] For these studies, three samples were examined: d = 3.7 nm $Zn_{0.9997}Mn_{0.0003}O$, d = 3.7 nm $Zn_{0.996}Mn_{0.004}O$ and d = 7.8 nm $Zn_{0.997}Mn_{0.003}O$ nanocrystals, with the focus primarily on the first two. Figure 7.1a shows the room-temperature continuous wave (CW) EPR spectrum of the 3.7 nm $Zn_{0.996}Mn_{0.004}O$ nanocrystals (red). The rich Mn^{2+} hyperfine structure is similar to that observed in bulk $Zn_{1-x}Mn_xO$, indicative of substitutional doping of the ZnO nanocrystals.[15]

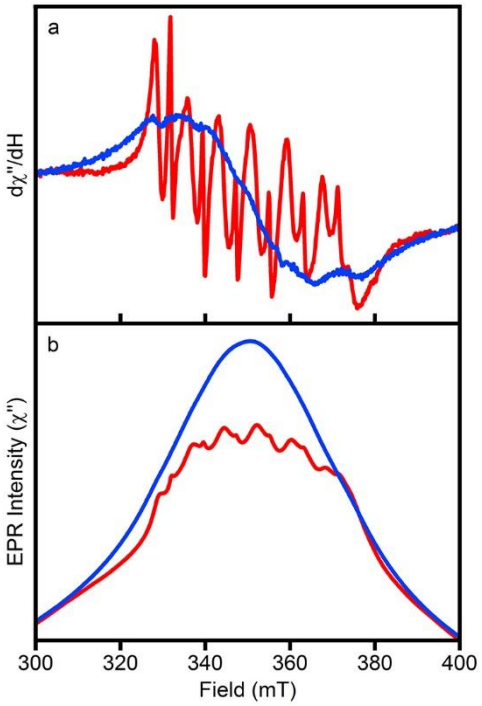

Figure 7.1. Effect of excess conduction-band electrons on the Mn^{2+} EPR spectrum in of $Zn_{1-x}Mn_xO$ nanocrystals. Room temperature X-band CW EPR spectra of as prepared (red) and maximally photodoped (blue) 3.7 nm $Zn_{0.996}Mn_{0.004}O$ nanocrystals in (a) derivative and (b) absorptive mode.

Extra electrons were added to the conduction bands of these $Zn_{1-x}Mn_xO$ nanocrystals via photochemical reduction.[10-13] Briefly, UV illumination under anaerobic conditions generates and excitonic hole that may be quenched by ethanol or other hole acceptors, leaving behind kinetically stable conduction-band electrons (e^-_{CB}). Continued illumination allows accumulation

of multiple e^-_{CB} per nanocrystal, which can be monitored by the appearance and growth of an absorption band in the IR.[10,11,13,16] Nanocrystals are referred to as fully reduced when continued photoexcitation no longer alters the intensity or position of the IR absorption peak. The number of conduction-band electrons can be determined via titration with $[FeCp^*_2][BAr_F]$.[12,13,16-18] The CW EPR spectrum of fully reduced 3.7 nm $Zn_{0.996}Mn_{0.004}O$ nanocrystals is shown in Figure 7.1a (blue). Introduction of e^-_{CB} leads to a broadening of the EPR signal and an increase in the total integrated intensity (Figure 7.1b). These changes have been observed previously and arise from new magnetic exchange interactions that are activated in the presence of the excess electrons.[8,10]

The broadening of the Mn^{2+} CW EPR spectrum upon photodoping is indicative of increased spin-spin and/or spin-lattice relaxation rates. To investigate the effect of conduction band electrons on Mn^{2+} spin relaxation times, pulsed EPR measurements were conducted at 4.2 K. Figure 7.2a shows electron spin echo spectra of the as-prepared 3.7 nm $Zn_{0.9997}Mn_{0.0003}O$ nanocrystals (red) and the same nanocrystals after maximum photochemical reduction (blue). A slight broadening of the signal and a decrease in overall intensity is observed upon photodoping. The sharp signal at ~360 mT is due to conduction band electrons in undoped ZnO nanocrystals that are present in the ensemble at very low Mn^{2+} concentrations. For 3.7 nm $Zn_{0.9997}Mn_{0.0003}O$ nanocrystals, there is an average of 0.33 Mn^{2+} per nanocrystal, meaning ~2/3 of the nanocrystals are undoped.

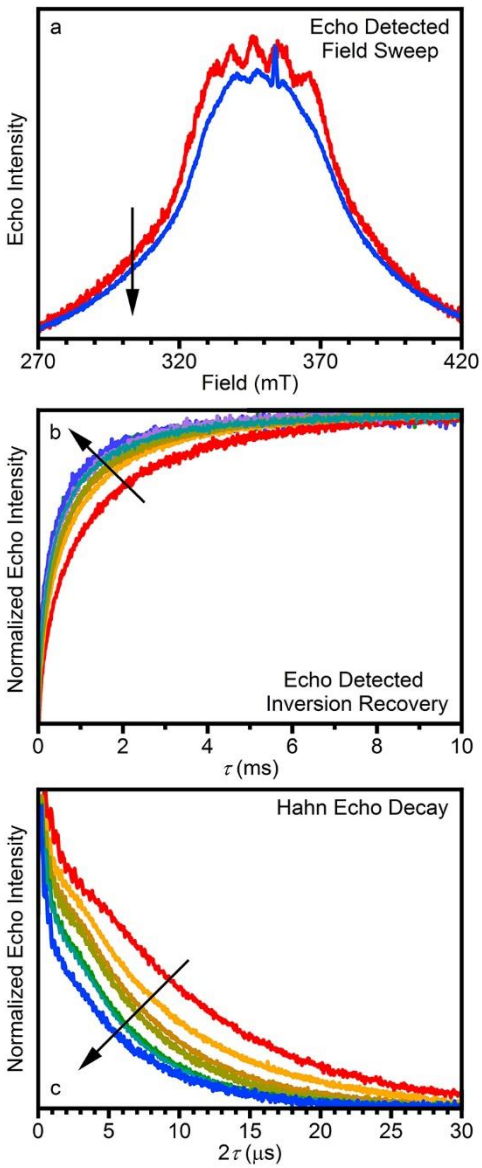

Figure 7.2. Effect of excess conduction-band electrons on the Mn^{2+} spin dynamics in $Zn_{1-x}Mn_xO$ nanocrystals. (a) Echo detected field sweep measurements of as prepared (red) and fully reduced (blue) d = 3.7 nm $Zn_{0.9997}Mn_{0.0003}O$ nanocrystals. (b) and (c) show measurements of T_1 and T_2, respectively, of the same nanocrystals at amounts of added electrons. Arrows show increased photochemical reduction.

To quantify spin-lattice relaxation times (T_1), the echo intensity was measured as a function of delay time (τ) using an echo-detected inversion recovery sequence ($\pi - \tau - \pi/2 - T_{fixed} - \pi - T_{fixed}$ – echo). These decays are shown in Figure 7.2b for the same nanocrystals as-prepared and

at various levels of photochemical reduction. With added electrons (arrow), a faster inversion recovery is observed. For the same electron levels, the spin-spin relaxation times (T_2) were also measured by monitoring the Hahn echo intensity as a function of delay time ($\pi/2 - \tau - \pi - \tau -$ echo). These curves are plotted in Figure 7.2c. Similar to T_1, T_2 becomes shorter with added electrons. With increased photochemical reduction, both the spin-lattice and spin-spin relaxation rates are accelerated. To estimate T_1 and T_2 from these measurements, the spectra in Figure 7.2b,c were fit to equations 7.1a and 7.1b, respectively. Neither data set follows purely single exponential decay, but for the purposes of this study an effective single exponential time is most useful for quantifying the changes in relaxation dynamics.

$$I(\tau) = 1 - A_1 \exp(-\tau / T_1) \tag{7.1a}$$

$$I(2\tau) = A_2 \exp(-2\tau / T_2) \tag{7.1b}$$

The effect of added electrons is most easily visualized by plotting the relaxation times as a function of the number of conduction-band electrons per nanocrystal. Figures 7.3a and 7.3b plot T_1 and T_2, respectively, as a function of average electron density (bottom axes) and of the average number of electrons per nanocrystal (top axes) for the 3.7 nm $Zn_{0.9997}Mn_{0.0003}O$ nanocrystals. The solid lines are guides to the eye. From these data, the addition of even one electron leads to a rapid decrease of both the spin-lattice and spin-spin relaxation times, causing both T_1 and T_2 to drop to around half of the initial values. The same experiments were performed on d = 3.7 nm $Zn_{0.996}Mn_{0.004}O$ nanocrystals and the results are plotted in Figure 7.3c,d. Again, a rapid decrease is seen in T_1 upon the addition of one electron. Interestingly, a similar trend is not observed for T_2. The same measurements were performed on 3.7 nm $Zn_{0.996}Mn_{0.004}O$ nanocrystals and 7.8 nm $Zn_{0.997}Mn_{0.003}O$ nanocrystals.

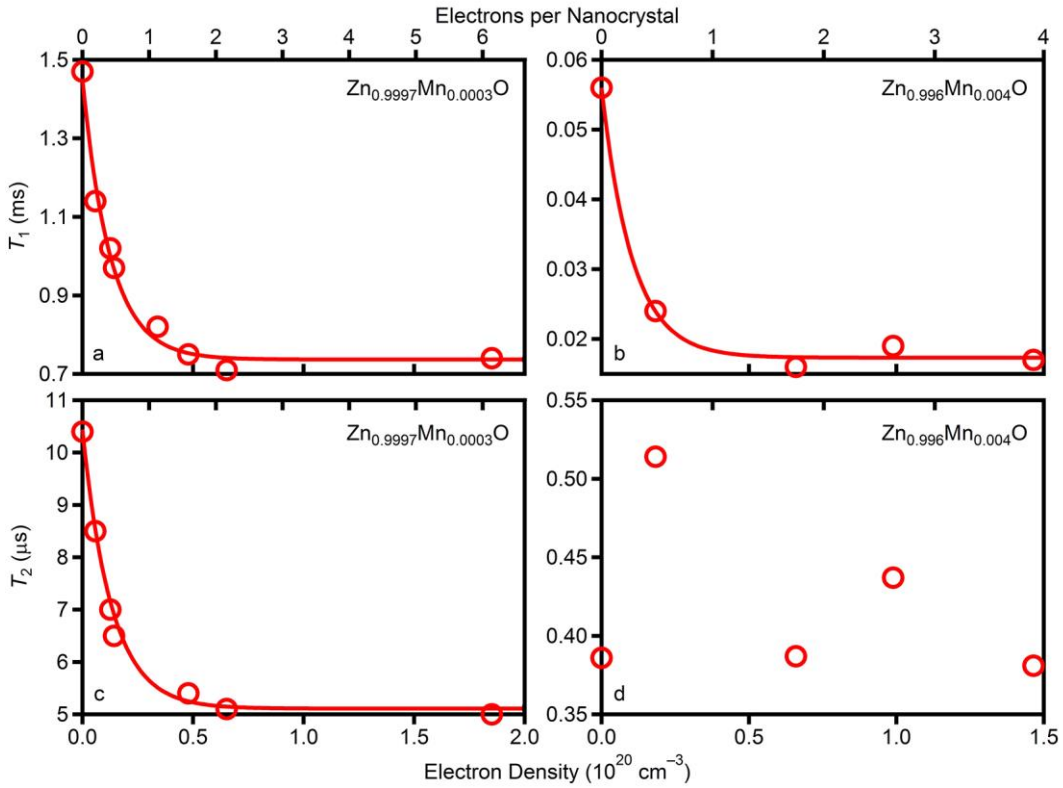

Figure 7.3. Dependence of Mn^{2+} spin dynamics on the number of conduction-band electrons in photochemically reduced $Zn_{1-x}Mn_xO$ nanocrystals. Change in (a,b) T_1 and (c,d) T_2 with increased photochemical reduction for (a,c) d = 3.7 nm $Zn_{0.9997}Mn_{0.0003}O$ and (b,d) d = 3.5 nm $Zn_{0.996}Mn_{0.004}O$ nanocrystals. The level of added electrons is given in terms of both electron density (bottom axes) and electrons per nanocrystal (top axes). The solid curves are guides to the eye.

Figure 7.4 plots normalized T_1 times as a function of electron density for each sample of $Zn_{1-x}Mn_xO$ nanocrystals. As mentioned above, both systems with d = 3.7 nm show a plateau in T_1 around 0.6×10^{20} cm^{-3}, corresponding to fewer than one e^-_{CB} per nanocrystal. For larger (d = 7.8 nm) nanocrystals, much smaller maximum electron densities were achieved, possibly due to competitive hole trapping. Despite the lower electron densities, the trend of T_1 decreasing with increasing electron densityis consistent with that of the smaller nanocrystals.

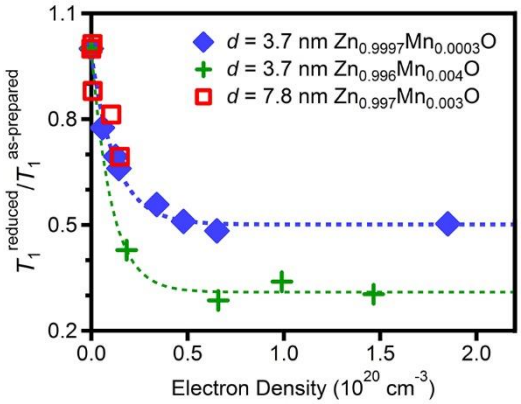

Figure 7.4. Normalized dependence of Mn^{2+} spin dynamics on the carrier density in *n*-type $Zn_{1-x}Mn_xO$ nanocrystals. Normalized Mn^{2+} spin-lattice relaxation in reduced nanocrystals ($T_1^{reduced}$/ $T_1^{as\text{-}prepared}$) as a function of carrier density for 3.7 nm $Mn_{0.0003}Zn_{0.9997}O$ (blue diamonds), 3.7 nm $Mn_{0.004}Zn_{0.996}O$ (green plus signs) and 7.8 nm $Mn_{0.003}Zn_{0.997}O$ (red squares) nanocrystals. The dashed curves are guides to the eye.

7.4 Analysis and discussion

In order to discuss the spin dynamics of *n*-type DMS nanocrystals, three coupled subsystems must be considered: (1) the magnetic ions (Mn^{2+} dopants), (2) the charge carriers (conduction-band electrons) and (3) lattice excitations (phonons). Spin and energy transfer between these subsystems is responsible for the spin dynamics of the DMS (Scheme 7.1, adapted from ref. 19). The impressive magneto-optical effects observed in DMSs, such as giant Zeeman splittings,[20-23] are a result of the strong exchange interactions between charge carriers and magnetic dopants.[7,8,10,20,23-37] The addition of charge carriers to the DMS nanocrystals opens up new coupling pathways between different Mn^{2+} dopants and between Mn^{2+} dopants and the lattice.

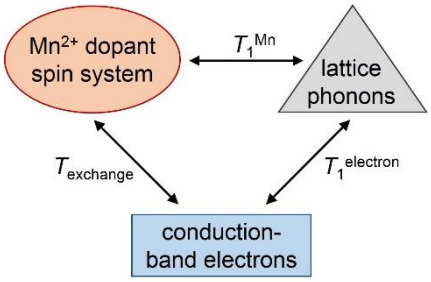

Scheme 7.1 Three coupled subsystems contributing to spin dynamics in *n*-type $Zn_{1-x}Mn_xO$ nanocrystals. Spin and energy transfer between Mn^{2+} electron spins, conduction-band electron spins and lattice phonons are responsible for the spin dynamics of the DMS.

The increase in intensity and broadening of the CW EPR spectrum (Figure 7.1) upon photochemical reduction has been shown to arise from interactions between the magnetic dopants and the conduction band electrons,[10] as well as electron-mediated interactions between dopants.[8] Excess electrons allow Mn^{2+} ions to overcome antiferromagnetic nearest-neighbor interactions, increasing the CW EPR intensity.[8] On the contrary, the electron spin echo (ESE) intensity decreased with added electrons (Figure 7.2a). This decreased intensity is due to fast relaxation, leading to reduced intensity at the first data point. For the reduced nanocrystals, the faster T_2 means that more of the signal decays before it is refocused, leading to a smaller measured echo intensity. Broadening of the spectrum is more pronounced in the CW spectrum than in the ESE spectrum, suggesting that some of the broadening is inhomogeneous and thus can be overcome by employing an echo sequence.

To first order, an isolated Mn^{2+} ion has zero orbital moment and does not interact directly with the lattice phonons, giving it a relatively long T_1. Therefore, the largest contribution to Mn^{2+} spin-lattice relaxation is due to interactions between adjacent Mn^{2+} ions, making T_1 highly dependent on Mn^{2+} concentration.[19] This concentration dependence is observed in the spin-lattice relaxation times of these $Zn_{1-x}Mn_xO$ nanocrystals: at higher Mn^{2+}concentrations T_1 is shorter

(Figure 7.3a,b). A similarly strong concentration dependence is also observed for T_2 (Figure 7.3c,d). At relatively low Mn^{2+} concentrations such as the ones in this study, spin-spin interactions are dominated by the magneto-dipole interaction.[19] This mechanism is inversely dependent on inter-dipole distance, consistent with smaller T_2 for higher Mn^{2+} concentrations. A strong dependence of T_1 and T_2 on Mn^{2+} concentration has been observed in a variety of bulk Mn^{2+}-doped II-VI semiconductors.[38-42]

Unlike Mn^{2+} spins, conduction-band electron spins are efficiently coupled to lattice phonons. These electron spins are also coupled strongly to Mn^{2+} spins, allowing efficient exchange scattering. They therefore open alternative channels for Mn^{2+} spin-lattice relaxation.[19] Such effects have been observed in (Cd, Mn)Te and (Zn, Mn)Se quantum wells in which spin-lattice relaxation is controlled by excess electrons or holes.[43,44] The introduction of this new pathway is depicted in Scheme 7.2. Here, $k_{\text{exch}} = 1/T_{\text{exch}}$ describes the efficiency of Mn^{2+} exchange scattering, which is generally very fast (10^{-12}–10^{-11} s).[29,45,46] Thus the Mn^{2+} excited spin state ($\left|Mn^{2+}*, e_{CB}^{-}\right\rangle$) and the electron excited spin state ($\left|Mn^{2+}, e_{CB}^{-}*\right\rangle$) reach thermal equilibrium before the instrument detection limit. The ground state can then be recovered via (1) direct coupling of Mn^{2+} spins with lattice phonons ($k_{\text{MnSLR}} = 1/T_1^{\text{as-prepared}}$) or (2) coupling of electron spins with lattice phonons ($k_{\text{eSLR}} = 1/T_1^{\text{electron}}$). The observed recovery of the ground state population is described by equation 7.2, where n_e is the number of conduction-band electrons. Equation 7.2 was used to model the dependence of T_1 on the number of conduction-band electrons for d = 3.7 nm $Zn_{0.9997}Mn_{0.0003}O$ and d = 3.5 nm $Zn_{0.996}Mn_{0.004}O$ nanocrystals (Figures 7.3a and 7.3b, respectively) and qualitatively reproduces the observed trend (Appendix I).

$$T_1^{\text{observed}} = \frac{1}{k_{\text{MnSLR}} + n_e k_{\text{eSLR}}} \tag{7.2}$$

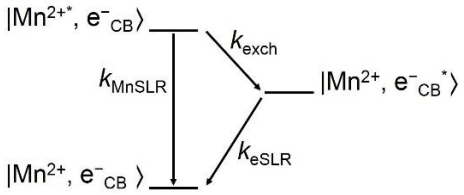

Scheme 7.2. Kinetic model for the acceleration of Mn^{2+} spin-lattice relaxation in *n*-type $Zn_{1-x}Mn_xO$ nanocrystals. Conduction-band electrons provide a new pathway for spin-lattice relaxation not available in intrinsic $Zn_{1-x}Mn_xO$ nanocrystals.

The ability of the spins to decay via electron spin-lattice relaxation relies on the very efficient exchange scattering. Since this interaction is exchange-mediated, it must conserve spin as well as the overall energy of the DMS. Therefore, the energy of the electrons must change by the difference in Mn^{2+} spin sublevels, $\Delta E_{Mn} = g_{Mn}\mu_B H$, where g_{Mn} is the Mn^{2+} g value, μ_B is the Bohr magneton and H is the applied magnetic field. The only electrons that may participate in spin-flips with Mn^{2+} are those within thermal reach of $E_F - \Delta E_{Mn}$ (E_F is the Fermi energy), since deeper electrons will not have enough energy to populate an unfilled level. This requirement leads to a saturation in the effect of excess electrons on Mn^{2+} spin dynamics. As E_F increases, the density of states available at $E_F - \Delta E_{Mn}$ becomes larger such that the addition of one more electron does not shift E_F significantly. For a spherical particle, E_F depends on the electron density, consistent with the data of Figure 7.4.

7. 5 Summary and conclusions

$Zn_{1-x}Mn_xO$ nanocrystals are model systems for probing spin interactions in DMS nanostructures. The effects of excess conduction-band electrons on Mn^{2+} spins in $Zn_{1-x}Mn_xO$ nanocrystals has been investigated by pulsed EPR spectroscopy. The addition of just one e^-_{CB} per nanocrystal leads to a large decrease in Mn^{2+} spin-lattice relaxation time. For all nanocrystals,

effects of excess electrons on spin-lattice relaxation time saturates around ~5 × 10^{-19} cm^{-3}. We attribute this to saturation of the number of filled conduction-band levels available for coupling to Mn^{2+} spin flips. This study represents the first in which the acceleration of spin dynamics has been measured in a zero-dimensional DMS containing both a magnetic dopant and excess charge carriers. These results provide a benchmark analysis of how electronic manipulation of zero-dimensional DMS systems will affect efficacy in devices for spin-based information processing technologies.

7.6 Experimental methods

Nanocrystal synthesis and general characterization is provided in Appendix A.1. Photodoping details are provided in Appendix B. EPR experimental details are provided in Appendix H.

7.7 References

1. Wolf, S. A.; Awschalom, D. D.; Buhrman, R. A.; Daughton, J. M.; von Molnár, S.; Roukes, M. L.; Chtchelkanova, A. Y.; Treger, D. M. Spintronics: A Spin-Based Electronics Vision for the Future. *Science* **2001**, *294*, 1488.

2. Zutic, I.; Fabian, J.; Das Sarma, S. Spintronics: Fundamentals and applications. *Rev. Mod. Phys.* **2004**, *76*, 323.

3. Hanson, R.; Kouwenhoven, L. P.; Petta, J. R.; Tarucha, S.; Vandersypen, L. M. K. Spins in Few-Electron Quantum Dots. *Rev. Mod. Phys.* **2007**, *79*, 1217.

4. Kobak, J.; Smoleński, T.; Goryca, M.; Papaj, M.; Gietka, K.; Bogucki, A.; Koperski, M.; Rousset, J. G.; Suffczyński, J.; Janik, E.; Nawrocki, M.; Golnik, A.; Kossacki, P.; Pacuski, W. Designing Quantum Dots for Solotronics. *Nat Commun.* **2014**, *5*.

5. Jonker, B. T.; Park, Y. D.; Bennett, B. R.; Cheong, H. D.; Kioseoglou, G.; Petrou, A. Robust Electrical Spin Injection into a Semiconductor Heterostructure. *Phys. Rev. B* **2000**, *62*, 8180.

6. Ohno, Y.; Young, D. K.; Beschoten, B.; Matsukura, F.; Ohno, H.; Awschalom, O. O. Electrical Spin Injection in a Ferromagnetic Semiconductor Heterostructure. *Nature* **1999**, *402*, 790.

7. Ruster, C.; Borzenko, T.; Gould, C.; Schmidt, G.; Molenkamp, L. W.; Liu, X.; Wojtowicz, T. J.; Furdyna, J. K.; Yu, Z. G.; Flatte, M. E. Very large Magnetoresistance in Lateral Ferromagnetic (Ga,Mn)As Wires with Nanoconstrictions. *Phys. Rev. Lett.* **2003**, *91*, 216602.

8. Ochsenbein, S. T.; Feng, Y.; Whitaker, K. M.; Badaeva, E.; Liu, W. K.; Li, X.; Gamelin, D. R. Charge-Controlled Magnetism in Colloidal Doped Semiconductor Nanocrystals. *Nat. Nanotechnol.* **2009**, *4*, 681.

9. Cohn, A. W.; Janßen, N.; Mayer, J. M.; Gamelin, D. R. Photocharging ZnO Nanocrystals: Picosecond Hole Capture, Electron Accumulation, and Auger Recombination. *J. Phys. Chem. C* **2012**, *116*, 20633.

10. Liu, W. K.; Whitaker, K. M.; Kittilstved, K. R.; Gamelin, D. R. Stable Photogenerated Carriers in Magnetic Semiconductor Nanocrystals. *J. Am. Chem. Soc.* **2006**, *128*, 3910.

11. Liu, W. K.; Whitaker, K. M.; Smith, A. L.; Kittilstved, K. R.; Robinson, B. H.; Gamelin, D. R. Room-Temperature Electron Spin Dynamics in Free-Standing ZnO Quantum Dots. *Phys. Rev. Lett.* **2007**, *98*, 186804.

12. Rinehart, J. D.; Schimpf, A. M.; Weaver, A. L.; Cohn, A. W.; Gamelin, D. R. Photochemical Electronic Doping of Colloidal CdSe Nanocrystals. *J. Am. Chem. Soc.* **2013**, *135*, 18782.

13. Schimpf, A. M.; Gunthardt, C. E.; Rinehart, J. D.; Mayer, J. M.; Gamelin, D. R. Controlling Carrier Densities in Photochemically Reduced Colloidal ZnO Nanocrystals: Size Dependence and Role of the Hole Quencher. *J. Am. Chem. Soc.* **2013**, *135*, 16569.

14. Schwartz, D. A.; Norberg, N. S.; Nguyen, Q. P.; Parker, J. M.; Gamelin, D. R. Magnetic Quantum Dots: Synthesis, Spectroscopy, and Magnetism of Co^{2+}- and Ni^{2+}-Doped ZnO Nanocrystals. *J. Am. Chem. Soc.* **2003**, *125*, 13205.

15. Norberg, N. S.; Kittilstved, K. R.; Amonette, J. E.; Kukkadapu, R. K.; Schwartz, D. A.; Gamelin, D. R. Synthesis of Colloidal Mn^{2+}:ZnO Quantum Dots and High-TC Ferromagnetic Nanocrystalline Thin Films. *J. Am. Chem. Soc.* **2004**, *126*, 9387.

16. Schimpf, A. M.; Thakkar, N.; Gunthardt, C. E.; Masiello, D. J.; Gamelin, D. R. Charge-Tunable Quantum Plasmons in Colloidal Semiconductor Nanocrystals. *ACS Nano* **2013**, *8*, 1065.

17. Schimpf, A. M.; Ochsenbein, S. T.; Buonsanti, R.; Milliron, D. J.; Gamelin, D. R. Comparison of Extra Electrons in Colloidal *n*-Type Al^{3+}-Doped and Photochemically Reduced ZnO Nanocrystals. *Chem. Commun.* **2012**, *48*, 9352.

18. Schrauben, J.; Hayoun, R.; Valdez, C.; Braten, M.; Fridley, L.; Mayer, J. Titanium and Zinc Oxide Nanoparticles Are Proton-Coupled Electron Transfer Agents. *Science* **2012**, *336*, 1298.

19. Yakovlev, D. R.; Merkulov, I. A. Spin and Energy Transfer Between Carriers, Magnetic Ions and Lattice In *Introduction to the Physics of Diluted Magnetic Semiconductors*; Gaj, J. A., Kossut, J., Eds.; Springer: 2011; Vol. 144.

20. Archer, P. I.; Santangelo, S. A.; Gamelin, D. R. Direct Observation of *sp–d* Exchange Interactions in Colloidal Mn^{2+}- and Co^{2+}-doped CdSe Quantum Dots. *Nano Lett.* **2007**, *7*, 1037.

21. Schimpf, A. M.; Gamelin, D. R. Thermal Tuning and Inversion of Excitonic Zeeman Splittings in Colloidal Doped CdSe Quantum Dots. *J. Phys. Chem. Lett.* **2012**, *3*, 1264.

22. Vlaskin, V. A.; Barrows, C. J.; Erickson, C. S.; Gamelin, D. R. Nanocrystal Diffusion Doping. *J. Am. Chem. Soc.* **2013**, *135*, 14380.

23. Beaulac, R.; Gamelin, D. R. Two-Center Formulation of Mn^{2+}-Electron *s–d* Exchange Coupling in Bulk and Quantum-Confined Diluted Magnetic Semiconductors. *Phys. Rev. B* **2010**, *82*, 224401.

24. Badaeva, E.; May, J. W.; Ma, J.; Gamelin, D. R.; Li, X. Characterization of Excited-State Magnetic Exchange in Mn2+-Doped ZnO Quantum Dots Using Time-Dependent Density Functional Theory. *J. Phys. Chem. C* **2011**, *115*, 20986.

25. Beaulac, R.; Archer, P. I.; Ochsenbein, S. T.; Gamelin, D. R. Mn^{2+}-Doped CdSe Quantum Dots: New Inorganic Materials for Spin-Electronics and Spin-Photonics. *Adv. Funct. Mater.* **2008**, *18*, 3873.

26. Beaulac, R.; Schneider, L.; Archer, P. I.; Bacher, G.; Gamelin, D. R. Light-Induced Spontaneous Magnetization in Colloidal Doped Quantum Dots. *Science* **2009**, *325*, 973.

27. Bradshaw, L. R.; Hauser, A.; McLaurin, E. J.; Gamelin, D. R. Luminescence Saturation via Mn^{2+}-Exciton Cross Relaxation in Colloidal Doped Semiconductor Nanocrystals. *J. Phys. Chem. C* **2012**, *116*, 9300.

28. Grumbach, N.; Rubin-Brusilovski, A.; Maikov, G. I.; Tilchin, E.; Lifshitz, E. Manipulation of Carrier-Mn2+ Exchange Interaction in CdTe/CdSe Colloidal Quantum Dots by Controlled Positioning of Mn2+ Impurities. *J. Phys. Chem. C* **2013**, *117*, 21021.

29. Kneip, M. K.; Yakovlev, D. R.; Bayer, M.; Maksimov, A. A.; Tartakovskii, I. I.; Keller, D.; Ossau, W.; Molenkamp, L. W.; Waag, A. Direct Energy Transfer from Photocarriers to Mn-Ion System in II-VI Diluted-Magnetic-Semiconductor Quantum Wells. *Phys. Rev. B* **2006**, *73*, 035306.

30. Merkulov, I. A.; Yakovlev, D. R.; Keller, A.; Ossau, W.; Geurts, J.; Waag, A.; Landwehr, G.; Karczewski, G.; Wojtowicz, T.; Kossut, J. Kinetic Exchange between the Conduction

Band Electrons and Magnetic Ions in Quantum-Confined Structures. *Phys. Rev. Lett.* **1999**, *83*, 1431.

31. Norberg, N. S.; Parks, G. L.; Salley, G. M.; Gamelin, D. R. Giant Excitonic Zeeman Splittings in Co^{2+}-doped ZnSe Quantum Dots. *J. Am. Chem. Soc.* **2006**, *128*, 13195.

32. Furdyna, J. K.; Kossut, J. *Diluted Magnetic Semiconductors*; Academic: New York, USA, 1988; Vol. 25.

33. Pandey, A.; Brovelli, S.; Viswanatha, R.; Li, L.; Pietryga, J. M.; Klimov, V. I.; Crooker, S. A. Long-Lived Photoinduced Magnetization in Copper-Doped ZnSe-CdSe Core-Shell Nanocrystals. *Nat. Nanotechnol.* **2012**, *7*, 792.

34. Sellers, I. R.; Oszwałdowski, R.; Whiteside, V. R.; Eginligil, M.; Petrou, A.; Zutic, I.; Chou, W.-C.; Fan, W. C.; Petukhov, A. G.; Kim, S. J.; Cartwright, A. N.; McCombe, B. D. Robust Magnetic Polarons in Type-II (Zn,Mn)Te/ZnSe Quantum Dots. *Phys. Rev. B* **2010**, *82*, 195320.

35. Seufert, J.; Bacher, G.; Scheibner, M.; Forchel, A.; Lee, S.; Dobrowolska, M.; Furdyna, J. K. Dynamical Spin Response in Semimagnetic Quantum Dots. *Phys. Rev. Lett.* **2002**, *88*, 027402.

36. Trojnar, A. H.; Korkusinski, M.; Kadantsev, E. S.; Hawrylak, P.; Goryca, M.; Kazimierczuk, T.; Kossacki, P.; Wojnar, P.; Potemski, M. Quantum Interference in Exciton-Mn Spin Interactions in a CdTe Semiconductor Quantum Dot. *Phys. Rev. Lett.* **2011**, *107*, 207403/1.

37. Yasuhira, T.; Uchida, K.; Matsuda, Y. H.; Miura, N.; Twardowski, A. Giant Faraday Rotation Spectra of $Zn_{1-x}Mn_xSe$ Observed in High Magnetic Fields up to 150 T. *Phys. Rev. B* **2000**, *61*, 4685.

38. Kneip, M. K.; Yakovlev, D. R.; Bayer, M.; Maksimov, A. A.; Tartakovskii, I. I.; Keller, D.; Ossau, W.; Molenkamp, L. W.; Waag, A. Spin-Lattice Relaxation of Mn Ions in ZnMnSe/ZnBeSe Quantum Wells Measured Under Pulsed Photoexcitation. *Phys. Rev. B* **2006**, *73*, 045305.

39. Dietl, T.; Peyla, P.; Grieshaber, W.; Daubigne, Y. M. Dynamics of Spin Organization in Diluted Magnetic Semiconductors. *Phys. Rev. Lett.* **1995**, *74*, 474.

40. Farah, W.; Scalbert, D.; Nawrocki, M. Magnetic Relaxation Studied by Transient Reflectivity in $Cd_{1-x}Mn_xTe$. *Phys. Rev. B* **1996**, *53*, R10461.

41. Scalbert, D. Spin-Lattice Relaxation in Diluted Magnetic Semiconductors. *Phys. Stat. Sol. B* **1996**, *193*, 189.

42. Scherbakov, A. V.; Akimov, A. V.; Yakovlev, D. R.; Ossau, W.; Landwehr, G.; Wojtowicz, T.; Karczewski, G.; Kossut, J. Spin-Lattice Relaxation in Semimagnetic CdMnTe/CdMgTe Quantum Wells. *Phys. Rev. B* **2000**, *62*, R10641.

43. Scherbakov, A.; Yakovlev, D.; Akimov, A.; Merkulov, I.; König, B.; Ossau, W.; Molenkamp, L.; Wojtowicz, T.; Karczewski, G.; Cywinski, G. Acceleration of the Spin-Lattice Relaxation in Diluted Magnetic Quantum Wells in the Presence of a Two-Dimensional Electron Gas. *Phys. Rev. B* **2001**, *64*, 155205.

44. Scherbakov, A. V.; Akimov, A. V.; Yakovlev, D. R.; Ossau, W.; Molenkamp, L. W.; Tatarenko, S.; Cibert, J. Spin-Lattice Relaxation in Semimagnetic CdMnTe/CdMgZnTe Quantum Wells with a Two-Dimensional Hole Gas Tuned by Optical Excitation. *Solid State Commun.* **2001**, *120*, 17.

45. Akimov, A. V.; Scherbakov, A. V.; Yakovlev, D. R.; Merkulov, I. A.; Bayer, M.; Waag, A.; Molenkamp, L. W. Multiple Transfer of Angular Momentum Quanta from a Spin-Polarized Hole to Magnetic Ions in $Zn_{1-x}Mn_xSe/Zn_{1-y}Be_ySe$ Quantum Wells. *Phys. Rev. B* **2006**, *73*, 165328.

46. Baumberg, J. J.; Crooker, S. A.; Awschalom, D. D.; Samarth, N.; Luo, H.; Furdyna, J. K. Ultrafast Faraday Spectroscopy in Magnetic Semiconductor Quantum Structures. *Phys. Rev. B* **1994**, *50*, 7689.

Chapter 8

Surface Contributions to Mn^{2+} Spin Dynamics in Colloidal Doped Quantum Dots

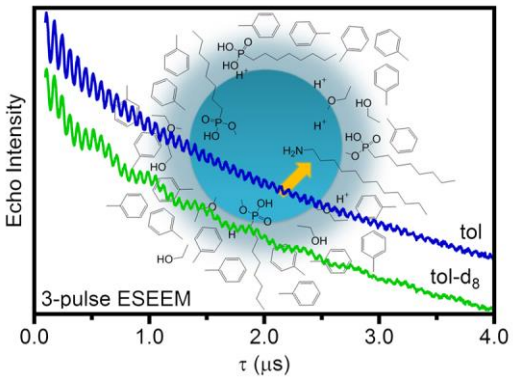

Adapted from: Schimpf, A. M.; Ochsenbein, S. T.; Gamelin, D. R. *In preparation.*

8.1 Overview

Colloidal impurity-doped quantum dots are attractive model systems for testing the fundamental spin properties of semiconductor nanostructures relevant to future spin-based information processing technologies. Although static spin properties of this class of materials have been studied extensively in recent years, their spin *dynamics* remain largely unexplored. Here, we use pulsed electron paramagnetic resonance (pEPR) spectroscopy to probe the spin relaxation dynamics of colloidal Mn^{2+}-doped ZnO, ZnSe, and CdSe quantum dots. pEPR spectroscopy is particularly powerful for identifying the specific nuclei that accelerate electron spin relaxation in these QDs. We show that the spin relaxation dynamics of these colloidal QDs are strongly influenced by dipolar coupling with proton nuclear spins outside the QDs, and especially those directly at the QD surfaces. Using this information, we demonstrate that spin relaxation times can be elongated significantly via ligand (or surface) deuteration or shell growth, providing two tools for chemical adjustment of spin dynamics in these nanomaterials. These findings advance our understanding of the spin properties of solution-grown semiconductor nanostructures relevant to spin-based information technologies.

8.2 Introduction

The manipulation of spins in diluted magnetic semiconductors (DMSs) is at the heart of various technologies in the nascent field of spin-based information processing.[1-5] Recently, coherent impurity spin manipulation was demonstrated in colloidal $Zn_{1-x}Mn_xO$ and $Pb_{1-x}Mn_xS$ quantum dots (QDs).[6,7] Colloidal doped QDs have impurity spin centers separated by the solution matrix (*i.e.*, solvent and ligands) in addition to the semiconductor host lattice, effectively isolating them and thereby reducing Mn^{2+}-Mn^{2+} spin-spin interactions relative to bulk semiconductors at the same Mn^{2+} doping level. Doped QDs have large surface-to-volume ratios, however, and the short distances between impurity ions and nanocrystal surfaces introduce new pathways for spin decoherence. For example, electron-nuclear double resonance (ENDOR) spectra of colloidal $Cd_{1-x}Mn_xS$ QDs showed resonances due to ^1H and ^{19}F nuclei of fluorothiophenol capping ligands,[8] and pulsed electron paramagnetic resonance (pEPR) measurements of colloidal $Zn_{1-x}Mn_xO$ and $Pb_{1-x}Mn_xS$ QDs showed electron spin echo envelope modulations (ESEEM) due to ^1H from solvent and ligand molecules.[6,7] The impact of such interactions between magnetic-dopant electron spins and external molecular nuclear spins on spin dynamics of the doped QDs, and strategies to mitigate or exploit such interactions, have not yet been extensively investigated.

Here, we use pEPR to probe the influence of nuclear spins on the spin relaxation dynamics of Mn^{2+} dopants in colloidal CdSe, ZnSe, and ZnO QDs. Nuclear spins from the host lattice as well as outside the QDs are observed to influence both the spin-lattice (T_1) and spin-spin (T_2) relaxation times of Mn^{2+} dopants, primarily via dipolar coupling. Experimental methods for decreasing this coupling are demonstrated to yield correspondingly increased relaxation times. pEPR spectroscopy thus provides a unique way to probe interactions between spins inside and

outside the QD. First, pEPR experiments were conducted to determine which nuclei contribute to Mn^{2+} spin relaxation in colloidal $Zn_{1-x}Mn_xSe$ and $Cd_{1-x}Mn_xSe$ QDs. Colloidal $Zn_{1-x}Mn_xO$ QDs are then used to evaluate the influence of nuclear spins on ligand and solvent molecules. Finally, we present a strategy to decrease the influence of surface nuclei by growing CdSe shells around $Cd_{1-x}Mn_xSe$ cores. The information gained from these experiments may be valuable not only for assessing spintronics functionalities but also for interpreting other QD relaxation processes involving surfaces.

8.3 Results and discussion

EPR experiments are detailed in Appendix H. Figure 8.1a shows room-temperature CW EPR spectra of $Zn_{0.995}Mn_{0.005}Se$ and $Cd_{0.995}Mn_{0.005}Se$ QDs. The hyperfine coupling constants of $|A| = 60 \times 10^{-4}$ cm^{-1} for $Zn_{1-x}Mn_xSe$ and $|A| = 62 \times 10^{-4}$ cm^{-1} for $Cd_{1-x}Mn_xSe$ are consistent with those previously reported for each material,[9] confirming substitutional Mn^{2+} doping. Figures 8.1b and c show 4.5 K electron spin echo intensities for the same samples measured following 2-pulse Hahn echo sequences ($\pi/2-\tau-\pi-\tau-$echo), plotted as a function of the transverse magnetic field. For both $Zn_{0.995}Mn_{0.005}Se$ and $Cd_{0.995}Mn_{0.005}Se$ QDs, modulations in the echo decay are observed that reflect coupling of the Mn^{2+} electron spins to nuclear spins.

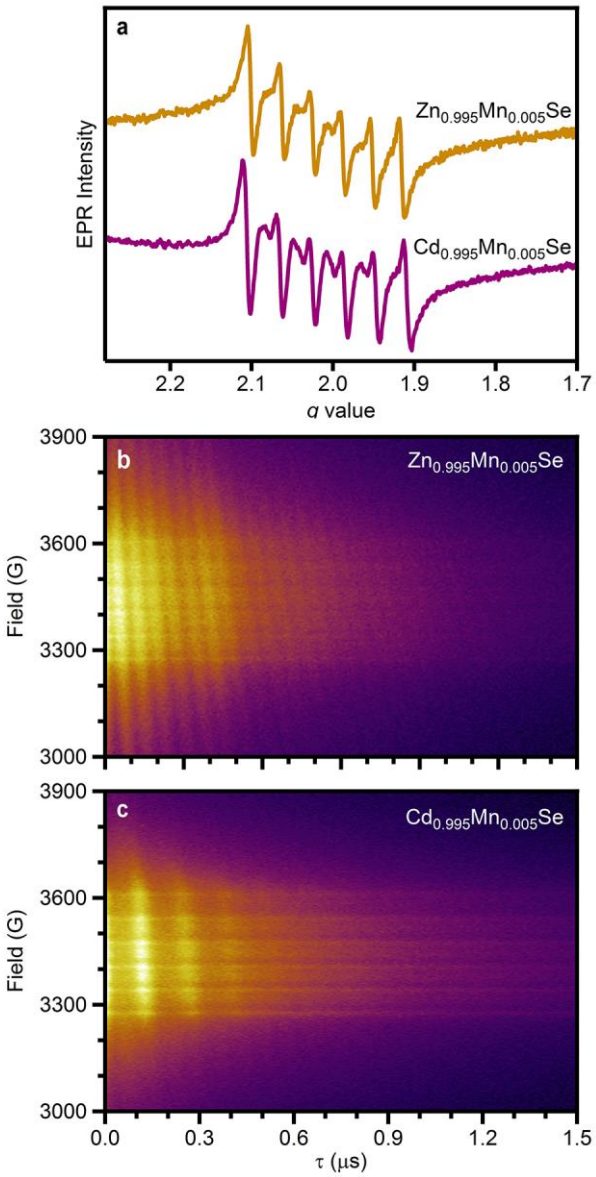

Figure 8.1. Representative CW and pulsed EPR of $Zn_{1-x}Mn_xSe$ and $Cd_{1-x}Mn_xSe$ quantum dots. (a) Room-temperature CW EPR spectra of d = 6 nm $Zn_{0.995}Mn_{0.005}Se$ (top) and d = 2.9 nm $Cd_{0.995}Mn_{0.005}Se$ (bottom) QDs. (b,c) 4.5 K 2-pulse ESEEM measurements on the same $Zn_{0.995}Mn_{0.005}Se$ and $Cd_{0.995}Mn_{0.005}Se$ QDs, respectively, as a function of delay time and magnetic field.

Fourier transform (FT) analysis of the time-domain data gives information about the energies of these couplings. Because the 2-pulse echo sequence is subject to combination frequencies and the data are limited by T_2, a 3-pulse stimulated echo sequence is more valuable

for obtaining information from the frequency domain. Echo-decay measurements using 3-pulse ESEEM sequences ($\pi/2-\tau-\pi/2-T-\pi/2-\tau$–echo) were therefore performed with a magnetic field of 3410 G for both samples. Figure 8.2 shows the resulting FT spectra from these measurements. In the $Zn_{0.995}Mn_{0.005}Se$ QDs, small peaks are seen around 0.9 and 2.8 MHz, consistent with the Larmor frequencies of ^{67}Zn and ^{77}Se, respectively. In the $Cd_{0.995}Mn_{0.005}Se$ QDs, a small peak around 3.2 MHz is observed, consistent with the Larmor frequencies of ^{111}Cd and ^{113}Cd. (The predicted Larmor frequencies are 3.1 and 3.2 MHz for the ^{111}Cd and ^{113}Cd isotopes, respectively.) This peak may also contain intensity from ^{77}Se. These peaks appearing at the Larmor frequencies are due to weak, dipolar coupling of the Mn^{2+} electron spins to nuclear spins on atoms inside the QD that are not directly bound to the Mn^{2+} dopant.

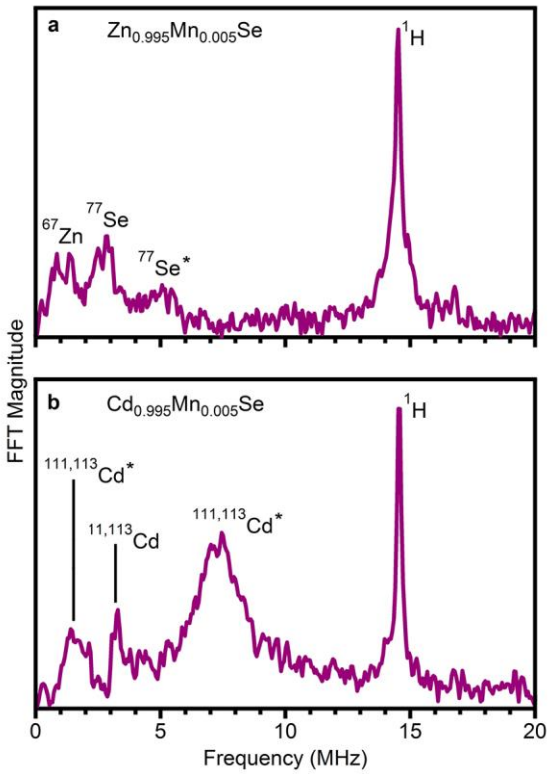

Figure 8.2. Coupling of Mn^{2+} spins to nuclear spins. Fourier transform spectra of the 4.5 K 3-pulse ESEEM data collected for (a) d = 6 nm $Zn_{0.995}Mn_{0.005}Se$ and (b) d = 2.9 nm $Cd_{0.995}Mn_{0.005}Se$ QDs. The Larmor frequencies of ^{1}H, ^{67}Zn, ^{77}Se, ^{111}Cd, and ^{113}Cd are indicated on the spectra. The starred features are attributed to strong coupling with neighboring ^{77}Se in $Zn_{0.995}Mn_{0.005}Se$ and $^{111,113}Cd$ in $Cd_{0.995}Mn_{0.005}Se$.

The $Cd_{0.995}Mn_{0.005}Se$ QDs also show a large feature centered around 7.3 MHz and a smaller one centered around 1.5 MHz. These peaks are attributed to coupling of the Mn^{2+} electron spins with nuclear spins on nearest-neighbor Cd^{2+} ions, mediated by covalency, and agree with what has been observed by CW EPR.[10,11] This interaction is much stronger than the dipolar coupling described above, serving to split and shift the peak away from the Cd Larmor frequency.[12] The $Zn_{0.995}Mn_{0.005}Se$ QDs also show a small peak around 5.2 MHz, which is attributed to covalent coupling of the Mn^{2+} electron spins to ^{77}Se nuclear spins. The relatively low intensity of this peak compared to the 7.3 MHz Cd peak in Figure 8.2b reflects the relative abundances of Cd and

Se isotopes containing nuclear spins (25% for Cd, 7.6% for Se) and the number of neighbors in the respective coordination shell (12 for Cd, 4 for Se). A similar peak is also expected in the $Cd_{0.995}Mn_{0.005}Se$ QDs but is occluded by the large Cd peak.

In both samples, a large feature is observed at 14.5 MHz, corresponding to the Larmor frequency of ^1H. This feature suggests long-range dipolar coupling of Mn^{2+} electrons to nuclear spins outside the QDs, likely on solvent or ligand molecules. Such coupling has been observed previously by ESEEM in $Zn_{1-x}Mn_xO$ and $Pb_{1-x}Mn_xS$ QDs[6,7] and by ENDOR in $Cd_{1-x}Mn_xS$ QDs.[8] In molecular magnets, nuclear spins of atoms not bound directly to the magnetic centers can significantly affect the coherence time.[13] Even solvent nuclear spins, despite the lack of through-bond coupling channels, influence spin-relaxation times in single molecule magnets.[14] Solvent and surface ligand protons are not relevant in bulk DMSs, however, so relaxation due to coupling with solvent and ligand nuclear spins is unique to the colloidal form of DMS QDs. Although doped QDs generally have longer spin relaxation times than their bulk counterparts at the same doping level,[6] these solvent and ligand nuclear spins introduce new pathways for spin decoherence not available in other semiconductor architectures.

To understand the impact of these new interactions, pEPR experiments were performed on DMS QDs to specifically probe solvent and ligand nuclear spins. These experiments were conducted on $Zn_{1-x}Mn_xO$ QDs because of their high colloidal solubility, which allows for high signal-to-noise ratios in the pEPR experiments. Figure 8.3 shows 4.5 K pEPR data collected on colloidal $Zn_{0.999}Mn_{0.001}O$ QDs suspended in frozen toluene (tol) and deuterated toluene (tol-d_8). A detailed fitting analysis of the inversion recovery and 2-pulse ESEEM data is provided in Appendix J. From the inversion recovery and echo decay data, there is a small change in T_1

(decreasing from 139 ± 2 μs to 117 ± 1 μs, Figure 8.3a) and no difference in T_2 (1.10 ± 0.02 μs versus 1.13 ± 0.03 μs, Figure 8.3b) when switching to the deuterated solvent.

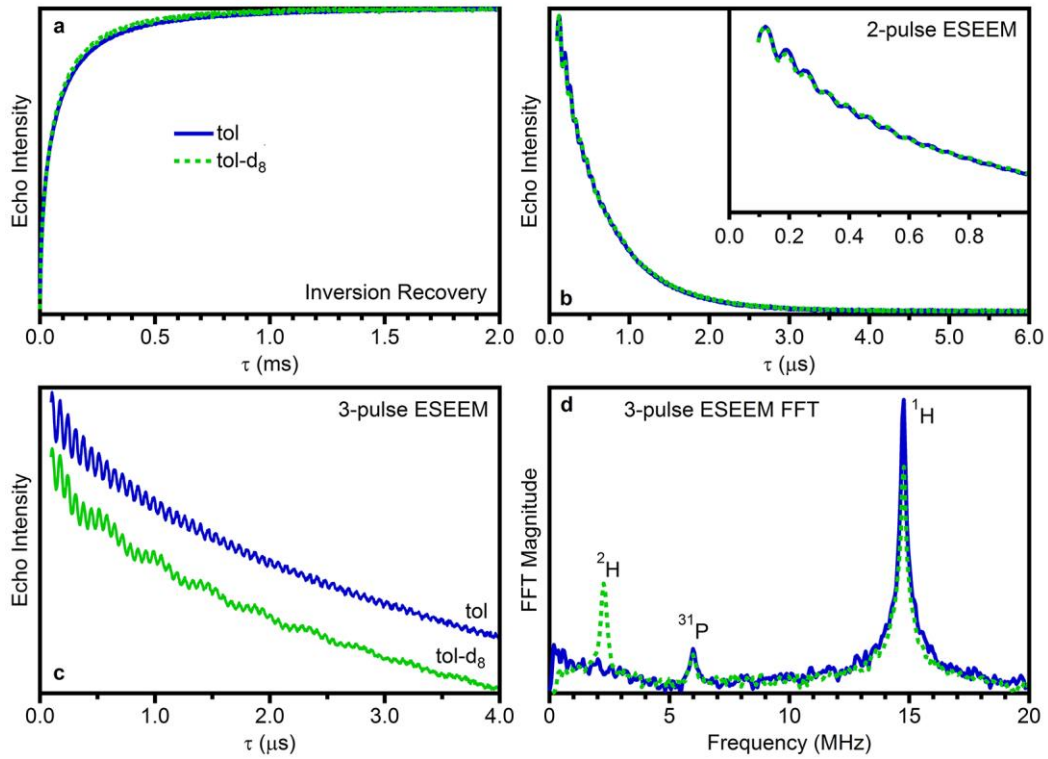

Figure 8.3. Effects of solvent deuteration on Mn^{2+} spin dynamics in $Zn_{1-x}Mn_xO$. 4.5 K pEPR data collected on d = 3.1 nm $Zn_{0.995}Mn_{0.005}O$ QDs suspended in toluene (tol) or in deuterated toluene (tol-d_8). (a) T_1, (b) T_2, (c) 3-pulse ESEEM, and (d) FT of 3-pulse ESEEM.

The 3-pulse ESEEM experiment reveals high-frequency modulations in both solvents. In addition, lower frequency modulations with relatively low amplitude are observed for the QDs suspended in deuterated toluene (Figure 8.3c). The FT spectra of these data (Figure 8.3d) reveal that the high frequency modulations are due to protons, which dominate the ESEEM of both samples. The FT spectrum of the QDs suspended in deuterated toluene shows a peak at the Larmor frequency of deuterium but, overall, changing the solvent nuclear spins does not have a

large influence on the Mn^{2+} electron spin relaxation times (Figure 8.3a,b). This result is reminiscent of that seen in molecules, where a change in spin relaxation times was observed when going to a solvent with no nuclear spins, but not upon deuterating the solvent.[14] The data in Figure 8.3d also show a peak due to coupling to ^{31}P (6.0 MHz) from the trioctylphosphine oxide (TOPO) or the related phosphonate capping ligands.

EtOH, used in the synthesis and washing of these ZnO QDs,[15] has been shown to adsorb to ZnO surfaces, binding dissociatively as ethoxide and a proton.[16-19] We hypothesized that such chemistry, if occurring here, should result in strong coupling of these surface proton nuclear spins with the Mn^{2+} electron spins inside the QDs. Figure 8.4 shows data from pEPR experiments conducted on colloidal $Zn_{0.995}Mn_{0.005}O$ QDs from the same synthesis, washed with EtOH or with EtOD. A detailed fitting analysis of the inversion recovery and 2-pulse ESEEM data is provided in Appendix J. Both T_1 and T_2 increase significantly when EtOD is used (from 48 ± 1 μs to 80 ± 1 μs and from 581 ± 1 ns to 760 ± 10 ns, respectively). Additionally, low-frequency modulations are seen in the 3-pulse ESEEM, and a correspondingly large peak in the FT spectra at the Larmor frequency of deuterium is observed when EtOD is used. Overall, this result is consistent with formation of O–H (or O–D) bonds at the ZnO surfaces upon washing with EtOH (or EtOD). The influence of direct surface deuteration on the Mn^{2+} spin relaxation times of these $Zn_{0.995}Mn_{0.005}O$ QDs is consistent with what has been with direct deuteration of molecules,[13] although smaller in magnitude because of the larger dimensions involved.

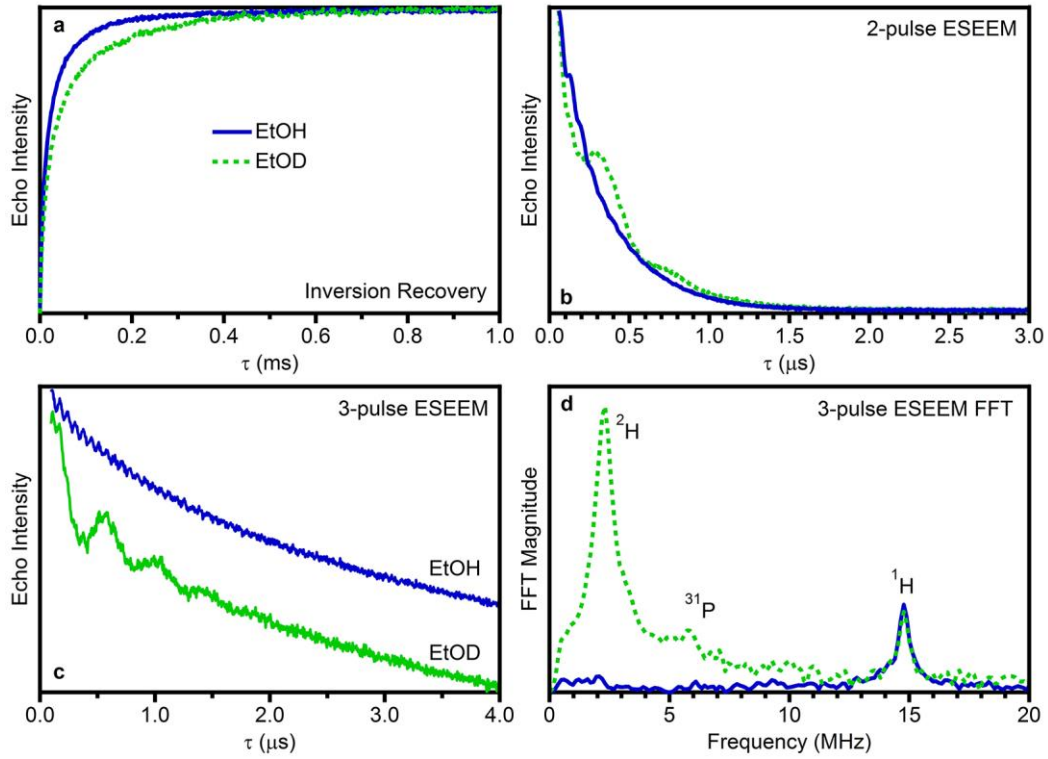

Figure 8.4. Effects of ethanol deuteration on Mn^{2+} spin dynamics in $Zn_{1-x}Mn_xO$. 4.5 K pEPR measurements on d = 3.3 nm $Zn_{0.990}Mn_{0.010}O$ QDs washed with EtOH or with EtOD. (a) T_1, (b) T_2, (c) 3-pulse ESEEM, and (d) FT of 3-pulse ESEEM.

We next hypothesized that it should be possible to decrease coupling between Mn^{2+} electron spins and ligand (or solvent) nuclear spins by growing an undoped semiconductor shell to increase the distances between Mn^{2+} dopant ions and the QD surfaces (Figure 8.5a). Growing a shell of the same material as the core should allow comparison of the core and core/shell structures without the complication of new nuclear spins. To test this hypothesis, $Cd_{1-x}Mn_xSe$ QDs were overcoated with isocrystalline CdSe shells. $Cd_{1-x}Mn_xSe$ was chosen for these measurements because the large Cd coupling peak at 7.3 MHz provides a convenient internal intensity reference. Because this peak is due only to Cd^{2+} nearest neighbors of the Mn^{2+} dopants, it is unaffected by shell growth.

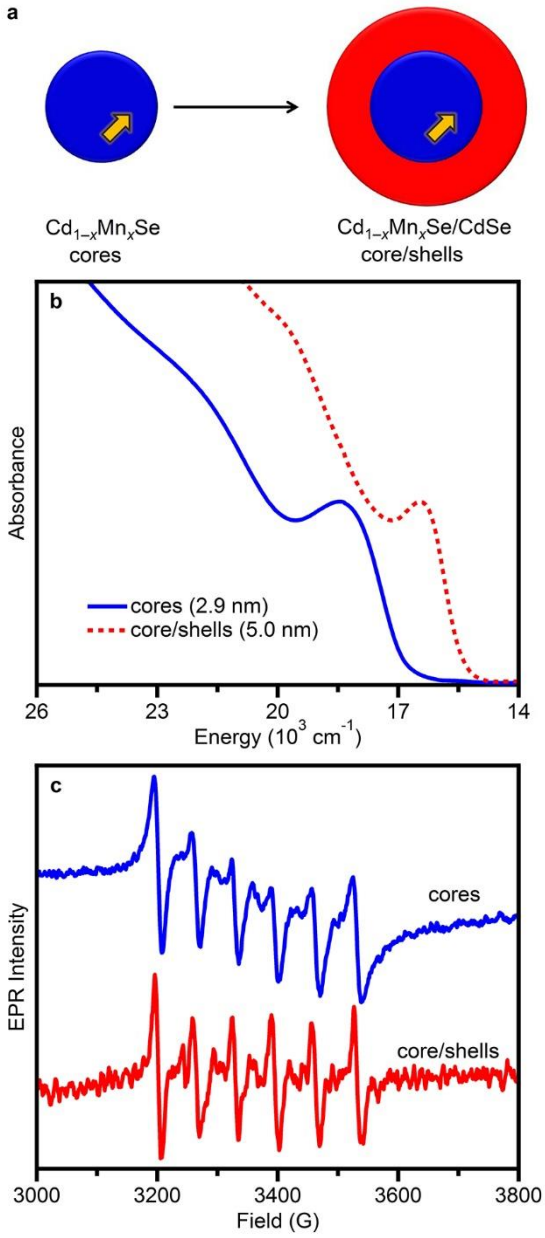

Figure 8.5. Overcoating $Cd_{1-x}Mn_xSe$ QDs with CdSe. (a) Schematic representation of core and core/shell QDs used to control the distance from Mn^{2+} dopants to the QD surfaces. Room-temperature (b) absorption and (c) CW EPR spectra of d = ~2.9 nm $Cd_{0.996}Mn_{0.004}Se$ core QDs and the same QDs after CdSe shell growth (core/shell d = ~5.0 nm).

The core QDs used in these experiments ($Cd_{0.996}Mn_{0.004}Se$) were prepared such that most would have only one Mn^{2+} ion per QD, to minimize interactions between Mn^{2+} spins. Figure 8.5b plots electronic absorption spectra collected before and after CdSe shell growth. From the

energies of the first excitonic maxima,[20] the $Cd_{0.996}Mn_{0.004}Se$ cores are ~2.9 nm in diameter, and the nanocrystals grow to ~5.0 nm in diameter with shell addition. The CW EPR spectra are similar before and after shell growth. Both spectra show hyperfine splittings consistent with substitutional Mn^{2+} in CdSe, indicating that both samples are free of surface Mn^{2+}, and both show sharp hyperfine lines consistent with the low Mn^{2+} concentrations. The hyperfine lines are noticeably sharper following shell growth (Figure 8.5c), however, suggesting slower relaxation dynamics, less inhomogeneous broadening (*e.g.*, less g or D strain), or both. Inductively coupled plasma- mass spectrometry (ICP-MS) measurements confirm the same number of Mn^{2+} per nanocrystal following shell growth, indicating that this change in relaxation dynamics does not come from a change in Mn^{2+}-Mn^{2+} interactions.

Figure 8.6 plots data from pEPR experiments conducted on the $Cd_{0.996}Mn_{0.004}Se$ core QDs before and after CdSe shell growth. Figure 8.6a plots the echo intensity as a function of time delay in the echo-detected inversion recovery, and Figure 8.6c plots the Hahn echo intensity as a function of delay time. From these data, there is an obvious increase in both spin-lattice and spin-spin relaxation times upon CdSe shell growth. Fits to obtain T_1 and T_2 are provided in Appendix J, and Table 8.1 summarizes the results. Both T_1 and T_2 increase by more than a factor of two upon shell growth.

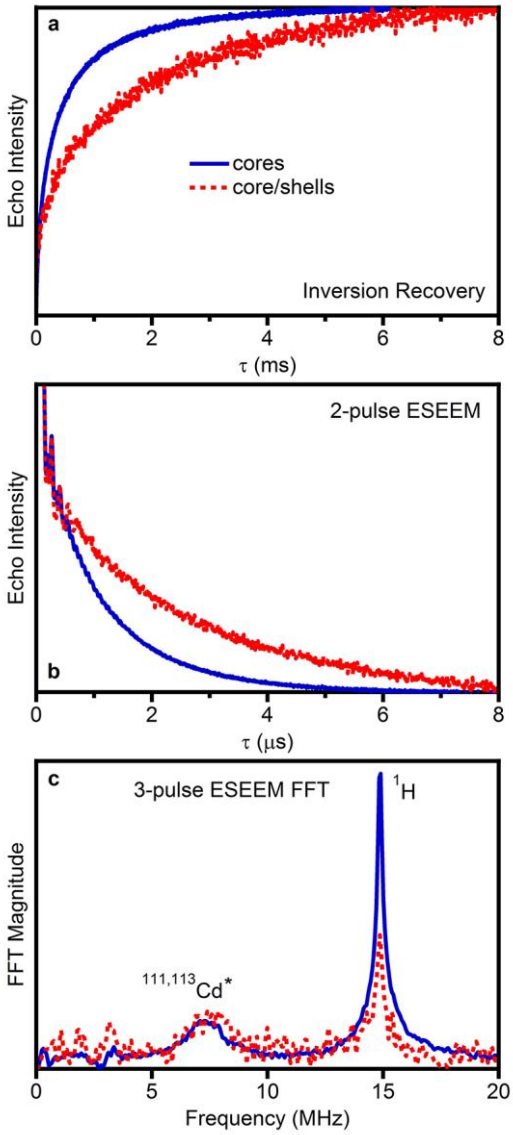

Figure 8.6. Effects of CdSe overcoating on Mn^{2+} spin dynamics in $Cd_{1-x}Mn_xSe$. 4.5 K pEPR data collected on $Cd_{0.996}Mn_{0.004}Se$ QDs before and after CdSe shell growth. (a) Echo-detected inversion recovery (T_1), (b) 2-pulse spin-echo decay (T_2), and (c) Fourier transform plot of 3-pulse ESEEM data. The QDs are the same as used in Figure 8.5.

Table 8.1. Spin relaxation times before and after shell growth

	Core (d = 2.9 nm)	Core/shell (d = 5.0 nm)	Increase Factor
Spin-lattice (T_1, ms)	0.725 ± 0.005	2.01 ± 0.01	2.8
Spin-spin (T_2, μs)	2.13 ± 0.01	4.70 ± 0.01	2.2

3-pulse ESEEM FT spectra of the same core and core/shell QDs are shown in Figure 8.6c. Because the 7.3 MHz peak due to Cd^{2+} nearest neighbors is unaffected by shell growth, these spectra were normalized to the integrated intensity of this peak. From this comparison, the peak at the ^{1}H Larmor frequency is smaller in the core/shell QDs than in the core QDs, reflecting a smaller contribution to decoherence from protons. This decrease in coupling with increasing distance between Mn^{2+} and the QD surfaces is consistent with the dipolar coupling mechanism expected for such long-range interactions.

The pEPR changes upon shell growth can be used to evaluate dipolar contributions to the observed spin-lattice and spin-spin relaxation. For both spin-lattice and spin-spin relaxation processes, the spin relaxation times are described by equation 8.1a, where T_{obs} is the measured spin relaxation time, T_0 is the intrinsic relaxation time, and T_{dip} is the contribution from dipole-dipole coupling. With the assumption that the intrinsic relaxation times do not change upon shell growth, equations 8.1b and 8.1c describe the core and core/shell relaxation times, respectively.

$$\frac{1}{T_{obs}} = \frac{1}{T_0} + \frac{1}{T_{dip}} \tag{8.1a}$$

$$\frac{1}{T_{obs}^{core}} = \frac{1}{T_0} + \frac{1}{T_{dip}^{core}} \tag{8.1b}$$

$$\frac{1}{T_{obs}^{core/shell}} = \frac{1}{T_0} + \frac{1}{T_{dip}^{core/shell}} \tag{8.1c}$$

For an ensemble of uniformly doped d = 2.9 nm cores containing one Mn^{2+} per nanocrystal, the average distance between Mn^{2+} and the surface of the QD is ~0.7 nm. The surface of the QD is where the nearest ligand or solvent molecules reside, and thus this distance represents the shortest distance between the Mn^{2+} and extrinsic nuclear spins and leads to the strongest dipolar

coupling. Upon shell growth, the distance to the surface increases to ~1.8 nm. Dipole-dipole coupling scales as $1/r^6$, implying $T_{dip}^{core/shell} / T_{dip}^{core} \approx 215$. With this information, the intrinsic and dipolar coupling contributions to the experimental T_1 and T_2 values can be estimated, and these values are summarized in Table 8.2. From this analysis, the intrinsic and dipolar contributions to both T_1 and T_2 are comparable in magnitude in the core nanocrystals, but in the core/shell nanocrystals the dipolar contributions have been reduced to such a large extent that they effectively no longer contribute, and the nanocrystal spin dynamics are determined solely by their intrinsic terms. This analysis thus demonstrates that extrinsic dipole-dipole contributions to spin relaxation can be simply and effectively eliminated by shell growth. This result is consistent with that observed in $Pb_{1-x}Mn_xS$ QDs, in which only ^1H within < 0.5 nm contributed significantly to Mn^{2+} decoherence.[7] Assuming a non-uniform Mn^{2+} spatial distribution or Mn^{2+} diffusion during shell growth yields nearly identical results (Appendix J), and hence the same overall conclusions. Similarly, because of the very strong distance dependence of the dipole-dipole interaction, consideration of Mn^{2+} coupling to nuclei beyond the QD surface may alter the quantitative values in Table 8.2, but not the central conclusion drawn from this analysis.

Table 8.2. Intrinsic and dipolar contributions to spin relaxation times in core and core/shell nanocrystals estimated using equation 8.1.

	T_0	T_{dip}^{core}	$T_{dip}^{core/shell}$
Spin-lattice (T_1)	2.03 ms	1.13 ms	34 s
Spin-spin (T_2)	4.70 μs	3.88 μs	116 ms

8.4 Summary and conclusions

In summary, pEPR was used to directly probe the factors influencing dopant spin relaxation in colloidal DMS QDs. The results demonstrate that the spin relaxation dynamics of magnetic impurities within colloidal QDs can be influenced by long-range dipolar coupling (and hence dipole-dipole energy transfer) to nuclear spins outside the QDs, and particularly those directly at the QD surfaces. We have demonstrated that Mn^{2+}-doped QD spin relaxation times can be elongated significantly by ligand (or surface) deuteration, which lowers the relevant Larmor frequency, or by shell growth, which reduces dipolar coupling between impurity electron spins and external nuclear spins. These results are reminiscent of the important role of dipole-dipole energy transfer from hot electrons to ligand vibrations in nonradiative electron cooling within photoexcited QDs.[21] Such cooling is slowed markedly in CdSe QDs by ZnSe shell growth[21] and is highly dependent on the ligand vibrational absorption cross sections.[22] The pEPR experiments described here are particularly powerful for probing the specific identities of the nuclei that participate in accelerating electron spin relaxation. Understanding these spin-spin interactions will assist the design and improvement of DMS-based nanostructures for spin-based information technologies.

8.5 Experimental methods

Nanocrystal syntheses are provided in Appendix A. EPR experiments are described in Appendix H.

8.6 References

1. Ardavan, A.; Blundell, S. J. Storing Quantum Information in Chemically Engineered Nanoscale Magnets. *J. Mater. Chem.* **2009**, *19*, 1754.

2. Bao, J.; Bragas, A. V.; Furdyna, J. K.; Merlin, R. Optically Induced Multispin Entanglement in a Semiconductor Quantum Well. *Nat. Mater.* **2003**, *2*, 175.

3. Engel, H. A.; Recher, P.; Loss, D. Electron Spins in Quantum Dots for Spintronics and Quantum Computation. *Solid State Commun.* **2001**, *119*, 229.

4. Leuenberger, M. N.; Loss, D. Quantum Computing in Molecular Magnets. *Nature* **2001**, *410*, 789.

5. Loss, D.; DiVincenzo, D. P. Quantum Computation with Quantum Dots. *Phys. Rev. A* **1998**, *57*, 120.

6. Ochsenbein, S. T.; Gamelin, D. R. Quantum Oscillations in Magnetically Doped Colloidal Nanocrystals. *Nature Nanotechnol.* **2011**, *6*, 112.

7. Moro, F.; Turyanska, L.; Granwehr, J.; Patanè, A. Spin Manipulation and Spin-Lattice Interaction in Magnetic Colloidal Quantum Dots. *Phys. Rev. B* **2014**, *90*, 205428.

8. Hofmann, D. M.; Hofstaetter, A.; Leib, U.; Meyer, B. K.; Counio, G. EPR and ENDOR investigations on CdS:Mn nanocrystals. *J. Cryst. Growth* **1998**, *184/185*, 383.

9. Beaulac, R.; Ochsenbein, S. T.; Gamelin, D. R. Colloidal Transition-Metal-Doped Quantum Dots In *Semiconductor Quantum Dots*; 2nd ed.; Klimov, V. I., Ed.; CRC Press: 2010, p 397.

10. Schneider, J.; Sircar, S. R.; Räuber, A. Elektronen-Spin-Resonanz von Mn^{2+}-Ionen im Kubischen und Trigonalen Kristallfeld des ZnS. *Z. Naturforsch.* **1963**, *18a*, 980.

11. Estle, T. L.; Holton, W. C. Electron-Paramagnetic-Resonance Investigation of the Superhyperfine Structure of Iron-Group Impurities in II-VI Compounds. *Phys. Rev.* **1966**, *150*, 159.

12. Schweiger, A. Pulsed Electron Spin Resonance Spectroscopy: Basic Principles, Techniques, and Examples of Applications. *Angew. Chem. Int. Edit.* **1991**, *30*, 265.

13. Ardavan, A.; Rival, O.; Morton, J. J. L.; Blundell, S. J.; Tyryshkin, A. M.; Timco, G. A.; Winpenny, R. E. P. Will Spin-Relaxation Times in Molecular Magnets Permit Quantum Information Processing? *Phys. Rev. Lett.* **2007**, *98*, 057201.

14. Schlegel, C.; van Slageren, J.; Manoli, M.; Brechin, E. K.; Dressel, M. Direct Observation of Quantum Coherence in Single-Molecule Magnets. *Phys. Rev. Lett.* **2008**, *101*, 147203.

15. Schwartz, D. A.; Norberg, N. S.; Nguyen, Q. P.; Parker, J. M.; Gamelin, D. R. Magnetic Quantum Dots: Synthesis, Spectroscopy, and Magnetism of Co^{2+}- and Ni^{2+}-Doped ZnO Nanocrystals. *J. Am. Chem. Soc.* **2003**, *125*, 13205.

16. Bowker, M.; Houghton, H.; Waugh, K. C. Temperature-Programmed Reaction Studies of the Interaction of Methyl Formate and Ethanol with Polycrystalline Zinc Oxide. *J. Chem. Soc. Farad. T. 1* **1982**, *78*, 2573.

17. Wöll, C. The Chemistry and Physics of Zinc Oxide Surfaces. *Prog. Surf. Sci.* **2007**, *82*, 55.

18. Bowker, M.; Petts, R. W.; Waugh, K. C. Temperature-Programmed Desorption Studies of Alcohol Decomposition on ZnO: 1-Propanol, 1-Butanol and 2-Butanol. *J. Catal.* **1986**, *99*, 53.

19. Cohn, A. W.; Janßen, N.; Mayer, J. M.; Gamelin, D. R. Photocharging ZnO Nanocrystals: Picosecond Hole Capture, Electron Accumulation, and Auger Recombination. *J. Phys. Chem. C* **2012**, *116*, 20633.

20. Yu, W. W.; Qu, L.; Guo, W.; Peng, X. Experimental Determination of the Extinction Coefficient of CdTe, CdSe, and CdS Nanocrystals. *Chem. Mater.* **2003**, *15*, 2854.

21. Pandey, A.; Guyot-Sionnest, P. Slow Electron Cooling in Colloidal Quantum Dots. *Science* **2008**, *322*, 929.

22. Guyot-Sionnest, P.; Wehrenberg, B.; Yu, D. Intraband Relaxation in CdSe Nanocrystals and the Strong Influence of the Surface Ligands. *J. Chem. Phys.* **2005**, *123*, 074709.

Chapter 9

Thermal Tuning and Inversion of Excitonic Zeeman Splittings in Colloidal Doped CdSe Quantum Dots

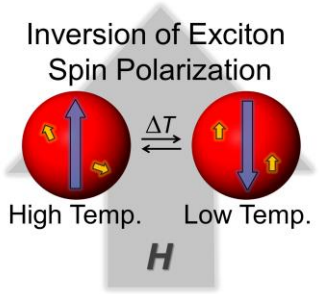

Adapted from: Schimpf, A. M.; Gamelin, D. R. *J. Phys. Chem. Lett.* **2012**, *3*, 1264.

9.1 Overview

Variable-temperature magnetic circular dichroism (MCD) spectroscopy is used to measure excitonic Zeeman splittings in colloidal Co^{2+}- and Mn^{2+}-doped CdSe quantum dots (QDs) with low dopant concentrations. The data demonstrate that the competition between intrinsic and exchange contributions to the excitonic Zeeman splittings in doped QDs can be tuned using temperature, from being dominated by exchange at low temperatures to being dominated by intrinsic Zeeman interactions at room temperature, with inversion at easily accessible temperatures and fields. These results may have relevance to spin-based information processing technologies that rely on manipulating carrier spins in QDs.

9.2 Introduction

The defining physical characteristic of a diluted magnetic semiconductor (DMS) is the so-called "giant" Zeeman splitting of their band structure, which arises from *sp–d* exchange coupling between delocalized charge carriers and localized spins on magnetic impurity ions embedded within the semiconductor.[1] These splittings lend DMSs a variety of extraordinary magnetic, magneto-optical, and magneto-transport properties that make them attractive for semiconductor-based spintronics or spin-photonics technologies.[2] Giant Zeeman splittings of

excitons give rise to the so-called giant Faraday rotation effect,[3-5] useful in Faraday optical isolators, and to spin-polarized excitonic photoluminescence,[6] in which magnetic fields control luminescence polarizations. Giant Zeeman splittings are also responsible for the spontaneous zero-field magnetization observed in excitonic magnetic polarons.[7-10]

This study demonstrates tuning and inversion of the excitonic Zeeman splittings in colloidal Mn^{2+}- and Co^{2+}-doped CdSe QDs at small magnetic fields, using temperature as the external variable. Excitonic Zeeman splittings probed by MCD spectroscopy are shown to follow a Curie temperature dependence, except that at elevated temperatures they pass through zero and actually invert in sign, in contrast with the MCD intensities of simple Curie paramagnets (like the Co^{2+} ligand-field MCD in the same Co^{2+}-doped CdSe QDs). Fitting the excitonic MCD temperature dependence allows quantitative parameterization of the microscopic factors underpinning this sign inversion. Specifically, these measurements yield an unusually clear illustration of the competition between intrinsic and exchange contributions to the excitonic Zeeman splittings of DMS QDs.

9.3 Results and discussion

Figure 9.1 shows room temperature absorption spectra and variable-temperature MCD spectra of $Cd_{1-x}Mn_xSe$ and $Cd_{1-x}Co_xSe$ QDs (x = 0.005 ± 0.001). Based on the empirical relationship between size and absorption maximum,[11] the QDs have radii of 1.5 nm and 2.1 nm, respectively. Although this relationship is altered by the presence of impurity atoms that lead to band gap engineering,[12] this is likely a small effect at such low dopant concentrations. For MCD measurements an external field of 0.63 T was applied using a small electromagnet. At 28 K, the MCD spectrum of the $Cd_{0.995}Mn_{0.005}Se$ QDs shows a large, derivative shaped feature at the CdSe

absorption edge. This feature has its positive intensity at lowest energy, indicative of a negative excitonic Zeeman splitting, ΔE_{Zeeman}.[13] The excitonic MCD intensity decreases with increasing temperature, reflecting loss of Mn^{2+} magnetization (*vide infra*). At ~80 K, this intensity passes through zero, and its sign is inverted at higher temperatures. It is worth noting that the MCD intensity does not pass through zero simultaneously at all wavelengths within the excitonic band, largely because of inhomogeneities in dopant concentration and QD diameter.

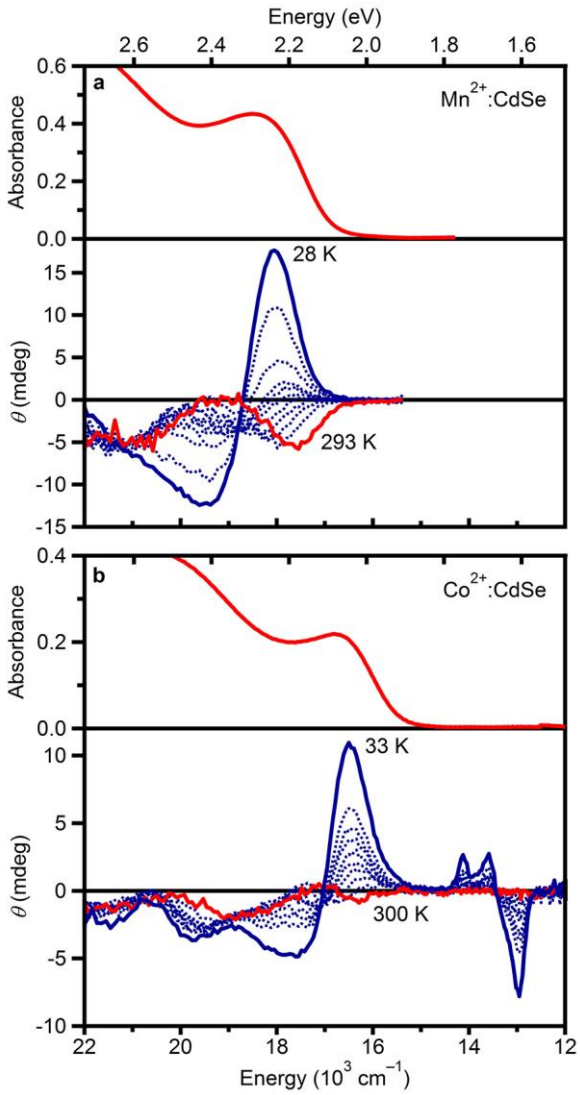

Figure 9.1. Variable-temperature MCD of Mn^{2+}- and Co^{2+}-doped CdSe QDs. Representative absorption and variable-temperature MCD spectra of colloidal (a) $Cd_{0.995}Mn_{0.005}Se$ and (b) $Cd_{0.995}Co_{0.005}Se$ QDs, collected at H = 0.63 T. The bold red and blue MCD spectra represent the highest and lowest temperatures, respectively. Absorption spectra were collected on colloidal suspensions and MCD spectra were collected on films drop-coated from these suspensions.

Similar results are obtained for $Cd_{0.995}Co_{0.005}Se$ QDs. The large, positive excitonic MCD feature dominant at 33 K loses its intensity with increasing temperature. In this sample, the excitonic MCD intensity inverts closer to room temperature. The structured MCD feature centered at ~13500 cm^{-1} derives from the $^4A_2(F) \rightarrow {}^4T_1(P)$ ligand-field transition of tetrahedral

Co^{2+} in CdSe.[14] This MCD intensity also decreases with increasing temperature, approaching zero at high temperatures but not inverting.

The strong temperature dependence and inversion of the excitonic MCD intensities in these DMS QDs can be understood by examination of the microscopic contributions to the excitonic Zeeman splittings. Formally, the magnitudes of the excitonic Zeeman splittings are determined by a competition between the intrinsic excitonic Zeeman splitting of the parent semiconductor (ΔE_{int}) and that arising from *sp–d* exchange (ΔE_{sp-d}), as described by equation 9.1a.[1]

$$\Delta E_{\text{Zeeman}} = \Delta E_{\text{int}} + \Delta E_{sp-d} \tag{9.1a}$$

$$= g\mu_{\text{B}}H + x\gamma N_0\left(\alpha - \beta\langle S_z\rangle\right) \tag{9.1b}$$

$$= g_{\text{eff}}\mu_{\text{B}}H \tag{9.1c}$$

These two contributions are expanded in equation 9.1b, and in the Curie regime their sum may be conveniently represented by a single (temperature-dependent) effective excitonic *g* value, g_{exc} (equation 9.1c). In equation 9.1b, ΔE_{int} is described by a simple Zeeman perturbation term, where *g* is the intrinsic Landé *g* factor of the exciton ($g_{\text{CdSe}} = +1.41$. ref. 15), μ_{B} is the Bohr magneton, and *H* is the external magnetic field. To first order, ΔE_{int} is thus independent of temperature and of the magnetic impurity ion concentration or magnetization. On the other hand, ΔE_{sp-d} reflects the splitting of the exciton induced by the collective action of an ensemble of magnetic impurity ions simultaneously exchange coupled with the exciton. As shown in the second term of equation 9.1b, ΔE_{sp-d} depends on the mole fraction of the magnetic ion (*x*), the cation density (N_0), the exciton-impurity overlap (γ), the *s–d* and *p–d* exchange energies (α and

β, respectively), and the spin expectation value of the magnetic ions ($\langle S_z \rangle$). For magnetic transition-metal impurity ions with spin-only ground states, such as tetrahedral Mn^{2+} and Co^{2+} (S = 5/2 and 3/2 Curie paramagnets, respectively), $\langle S_z \rangle$ follows Brillouin magnetization as represented by equation 9.2, where g_{TM} is the effective g value of the impurity's ground state, k_B is the Boltzmann constant, and T is temperature. At small magnetic fields, this function is inversely proportional to T (Curie behavior). The strong temperature dependence seen in Figure 9.1 is thus consistent with excitonic Zeeman splittings dominated by ΔE_{sp-d}.

$$\langle S_z \rangle = -\left[\frac{2S+1}{2} \coth\left(\frac{2S+1}{2} \frac{g_{TM}\mu_B}{k_B T} \right) - \frac{1}{2} \coth\left(\frac{1}{2} \frac{g_{TM}\mu_B}{k_B T} \right) \right] \tag{9.2}$$

An interesting feature of DMSs is that ΔE_{int} and ΔE_{sp-d} usually have opposite signs and thus compete with one another. Typically, ΔE_{Zeeman} is measured at low temperatures where ΔE_{sp-d} may become extremely large due to the inverse temperature dependence of $\langle S_z \rangle$. In this regime, there is little evidence of ΔE_{int}, and consequently it is widely neglected. For a particular magnetic field, however, equation 9.1 predicts the existence of a unique temperature for any given DMS at which $\Delta E_{int} = -\Delta E_{sp-d}$, and hence $\Delta E_{Zeeman} = 0$. Similarly, equation 9.1 predicts that at fixed temperature, the g value can be inverted by application of a magnetic field. Whereas inversion of DMS spin splittings has indeed been demonstrated at cryogenic temperatures using large magnetic fields and low dopant concentrations,[3,4,16,17] the use of temperature for this purpose has not been explored.

The data in Figure 9.1 were analyzed by plotting the integrated intensities of the first excitonic MCD peaks (I_{exc}) versus temperature for each sample. These plots are shown in Figure 9.2. The ligand-field MCD intensity (I_{LF}) in the $Cd_{0.995}Co_{0.005}Se$ spectra is also plotted versus temperature in Figure 9.2b. The inset in Figure 9.2b plots the ratio of excitonic to ligand-field MCD intensities (I_{exc} / I_{LF}) versus temperature for the $Cd_{0.995}Co_{0.005}Se$ QDs. This ratio is linear over a broad temperature range. The temperatures at which the excitonic MCD intensities invert are more clearly seen from these plots than from those in Figure 9.1. This crossing point occurs at ~80 K for the $Cd_{0.995}Mn_{0.005}Se$ QDs, and at ~160 K for the $Cd_{0.995}Co_{0.005}Se$ QDs. At these crossing points, the two contributions to ΔE_{Zeeman} cancel one another (*i.e.*, $\Delta E_{int} = -\Delta E_{sp-d}$). Doped QDs with small values of *x* were used for these measurements because their MCD inversion occurs at relatively low temperatures. This inversion temperature can be adjusted by altering *x* (equation 9.1).

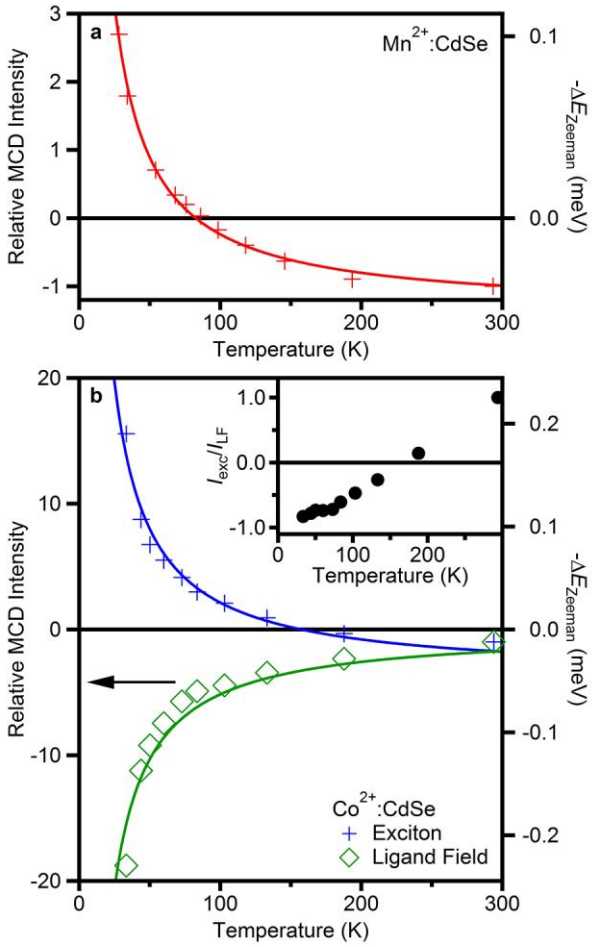

Figure 9.2. Temperature dependence of the MCD intensities in Mn^{2+}- and Co^{2+}-doped CdSe QDs. Temperature dependence of the MCD signal intensities in colloidal (a) $Cd_{0.995}Mn_{0.005}Se$ and (b) $Cd_{0.995}Co_{0.005}Se$ QDs, normalized at room temperature. The plus signs and open diamonds are the integrated MCD intensities of the lowest energy feature for the exciton and *d*–*d* transitions, respectively. The solid lines show fits to the data using equation 2.3. The right axes show the corresponding excitonic Zeeman splittings. The inset in (b) plots the ratio of excitonic to ligand-field MCD intensities in the $Cd_{0.995}Co_{0.005}Se$ QDs.

The solid curves in Figure 9.2 were obtained by fitting these data to equation 9.3.

$$I_{\text{exc}}(T) = A\Delta E_{\text{Zeeman}}(T) = A\left(g_{\text{CdSe}}\mu_{\text{B}}H + x\gamma N_0(\alpha-\beta)\langle S_z\rangle\right) \tag{9.3a}$$

$$I_{\text{LF}}(T) = B\langle S_z\rangle \tag{9.3b}$$

Equation 9.3a describes the excitonic Zeeman splitting, and therefore the excitonic MCD signal intensity, as a function of temperature, where *A* is a proportionality constant that relates the observed MCD signal intensity (in mdeg) to the actual Zeeman splitting energy (in eV). Similarly, *B* is the proportionality constant relating the ligand-field MCD intensity to Co^{2+} ground-state magnetization. When determining the fits, *A*, *B*, and the overlap factor γ were floated, while all other values were held constant. The values of g_{CdSe} and $N_0(\alpha-\beta)$ were fixed to that of bulk, and *x* was fixed to the value determined analytically. The linearity of $I_{\mathrm{exc}}/I_{\mathrm{LF}}$ versus *T* (Figure 9.2, inset) is consistent with a temperature-independent value of g_{CdSe}. From these fits, the values of $\Delta E_{\mathrm{Zeeman}}$ at saturation may be determined by taking the limit as $T \rightarrow 0$ (equation 9.4). Figure 9.3 plots the temperature dependence of $\Delta E_{\mathrm{Zeeman}}$ extended to saturation, with the analysis summarized in Table 9.1.

$$\Delta E_{\mathrm{Zeeman}}^{\mathrm{sat}} = \lim_{T \rightarrow 0}\left(\frac{I_{\mathrm{exc}}(T)}{A}\right) \tag{9.4}$$

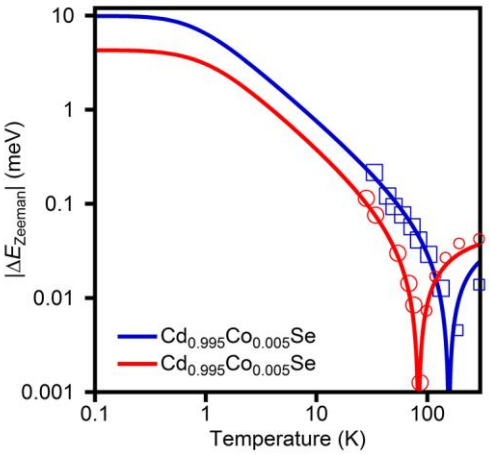

Figure 9.3. Temperature dependence of the Zeeman splittings in Mn^{2+}- and Co^{2+}-doped CdSe QDs extended to saturation. Temperature dependence of the magnitude of Zeeman splittings in colloidal $Cd_{0.995}Mn_{0.005}Se$ (red circles) and $Cd_{0.995}Co_{0.005}Se$ (blue squares) QDs extended to low temperatures to illustrate the saturation behavior. Zeeman energies are plotted as absolute values such that the dips at ~100 K represent changes in sign. Near this point, the curves deviate from Curie behavior and the contribution from the intrinsic Zeeman splitting is clearly observed.

Table 9.1. Results from analysis of excitonic Zeeman splittings.

Sample	Experimental ΔE_{Zeeman}^{sat} (meV)	Predicted ΔE_{Zeeman}^{sat} (meV)	Experimental $\gamma N_0(\alpha-\beta)$ (eV)	Literature $N_0(\alpha-\beta)$ (eV)	Overlap (γ)
$Cd_{0.995}Mn_{0.005}Se$	−4	−17	0.35	1.50[a]	0.23
$Cd_{0.995}Co_{0.005}Se$	−10	−16	1.32	2.15[b]	0.61

*Predicted values are calculated using equation 2.1 based on literature values of $N_0(\alpha - \beta)$. [a]Ref. 18. [b]Ref. 19.

The values of ΔE_{Zeeman}^{sat} extracted from the data in Figure 9.2 are smaller than expected from bulk exchange energies, yielding γ = 0.61 and 0.23 for the $Cd_{0.995}Co_{0.005}Se$ and $Cd_{0.995}Mn_{0.005}Se$ QDs, respectively. Because of the propensity for crystal nucleation to exclude dopants, colloidal DMS QDs generally have undoped cores,[20,21] precisely where the exciton probability density is greatest. The values of γ determined here are consistent with undoped cores of ~2 nm in both

samples, similar to the values measured in previous experiments.[20] The influence of such non-statistical dopant distributions is exacerbated in QDs because of the tight exciton confinement. The larger value of γ for the $Cd_{0.995}Co_{0.005}Se$ QDs than for the $Cd_{0.995}Mn_{0.005}Se$ QDs may be due in part to the larger size of the $Cd_{0.995}Co_{0.005}Se$ QDs. Additionally, until recently,[12] doping CdSe with large amounts of Mn^{2+} has proven more difficult than with Co^{2+}, suggesting that the $Cd_{0.995}Co_{0.005}Se$ QDs in this study may have a more uniform dopant distribution. Although some research[22-25] may suggest that γ should instead be interpreted in terms of confinement-induced changes in $N_0\alpha$,[22] recent theoretical work suggests that these QDs are too large to display significant kinetic *s-d* exchange.[26,27] The literature values for $N_0\alpha$ and $N_0\beta$ in bulk $Cd_{1-x}Mn_xSe$ and $Cd_{1-x}Co_xSe$ (Table 9.2) show substantial variation (up to ~15%,). Similarly, the value of g_{CdSe} taken from bulk may not be accurate for QDs,[28] and at such small *x* even small experimental uncertainties ($x = 0.005 \pm 0.001$) translate to large uncertainties in γ. The specific values of γ in Table 9.1 are thus influenced by uncertainties in $N_0(\alpha-\beta)$, g_{CdSe}, and *x*, and hence should not be overinterpreted. The primary finding from these data, namely of inversion of the sign of ΔE_{Zeeman} using temperature, is valid regardless of the value or interpretation of γ and provides a particularly clear experimental validation of the competition between ΔE_{int} and ΔE_{sp-d} formulated in equation 9.1.

Table 9.2. Literature values for mean-field exchange energies in bulk $Cd_{1-x}Mn_xSe$ and $Cd_{1-x}Co_xSe$.

Sample	$N_0\alpha$ (eV)	Ref.	$N_0\beta$ (eV)	Ref.	$N_0(\alpha-\beta)$ (eV)	Ref.
$Cd_{1-x}Mn_xSe$	0.26	18	-1.27	31		
	0.26	29	-1.24	18		
	0.28	30				
	0.23	31				
$Cd_{1-x}Co_xSe$	0.28	19	-1.87	19	2.52	34
	0.32	32	-2.12	33		

From equation 9.1c, these results further demonstrate that the effective excitonic g values (g_{eff}) of these QDs also invert over the temperature range explored here. At the crossing point, where $I_{\text{exc}} = 0$, g_{eff} is tuned to zero. In the high-temperature limit, $g_{\text{eff}} = g_{\text{CdSe}} \approx +1.41$. At ~30 K, $g_{\text{eff}} = -3g_{\text{CdSe}}$ (−4.2) for the $Cd_{0.995}Mn_{0.005}Se$ and $g_{\text{eff}} = -8g_{\text{CdSe}}$ (−11.3) for the $Cd_{0.995}Co_{0.005}Se$ QDs. At the liquid helium temperatures (4.2 K), these g_{eff} values increase to −25.9 and −50.2, respectively.

9.4 Summary and conclusions

In summary, variable-temperature MCD spectroscopy at small magnetic fields has been used to measure excitonic Zeeman splittings in colloidal Co^{2+}- and Mn^{2+}-doped CdSe QDs. The results clearly illustrate a competition between intrinsic and exchange contributions to these Zeeman splittings, and demonstrate that the exciton spin polarizations can be tuned and inverted within easily accessible temperature and magnetic field ranges, a finding that may be relevant to future spin-photonic information processing technologies reliant upon spin manipulation within QDs. Used in this way, variable-temperature MCD spectroscopy is demonstrated as a valuable tool for probing magnetic exchange interactions in DMSs.

9.5 Experimental methods

QD synthesis and general characterization are described in Appendix A.

9.5.1 Low-field, variable-temperature MCD. Concentrated QD solutions were drop-coated onto quartz discs that were mounted onto a Janis ST-300MS cryostat with a custom-made cold finger. The cryostat was placed between the poles of a GMW 45 mm electromagnet with a field of 0.63 T. The temperature of the cold finger near the sample was read with a Lakeshore CX-1030-SD-1.4L temperature sensor. MCD spectra were collected using an Aviv 40DS spectropolarimeter. All spectra were obtained at 0.63 T. MCD data are reported as θ(mdeg) = 32980ΔA, where $\Delta A = A_L - A_R$. A_L and A_R refer to the absorption of left and right circularly polarized photons, respectively, following the sign convention of Piepho and Schatz.[35]

9.6 References

1. Furdyna, J. K.; Kossut, J. *Diluted Magnetic Semiconductors*; Academic: New York, USA, 1988; Vol. 25.

2. Beaulac, R.; Archer, P. I.; Ochsenbein, S. T.; Gamelin, D. R. Mn^{2+}-Doped CdSe Quantum Dots: New Inorganic Materials for Spin-Electronics and Spin-Photonics. *Adv. Funct. Mater.* **2008**, *18*, 3873.

3. Yasuhira, T.; Uchida, K.; Matsuda, Y. H.; Miura, N.; Twardowski, A. Giant Faraday Rotation Spectra of $Zn_{1-x}Mn_xSe$ Observed in High Magnetic Fields up to 150 T. *Phys. Rev. B* **2000**, *61*, 4685.

4. Yasuhira, T.; Uchida, K.; Matsuda, Y. H.; Miura, N.; Twardowski, A. Magnetic and Non-Magnetic Faraday Rotation in ZnMnSe in High Magnetic Fields. *Semicond. Sci. Tech.* **1999**, *14*, 1161.

5. Bartholomew, D. U.; Furdyna, J. K.; Ramdas, A. K. Interband Faraday-Rotation in Diluted Magnetic Semiconductors - $Zn_{1-x}Mn_xTe$ and $Cd_{1-x}Mn_xTe$. *Phys. Rev. B* **1986**, *34*, 6943.

6. Beaulac, R.; Archer, P. I.; Liu, X.; Lee, S.; Salley, G. M.; Dobrowolska, M.; Furdyna, J. K.; Gamelin, D. R. Spin-Polarizable Excitonic Luminescence in Colloidal Mn^{2+}-Doped CdSe Quantum Dots. *Nano Lett.* **2008**, *8*, 1197.

7. Harris, J. H.; Nurmikko, A. V. Formation of the Bound Magnetic Polaron in (Cd,Mn)Se. *Phys. Rev. Lett.* **1983**, *51*, 1472.

8. Merkulov, I. A.; Yakovlev, D. R.; Kavokin, K. V.; Mackh, G.; Ossau, W.; Waag, A.; Landwehr, G. Hierarchy of Relaxation Times in the Formation of an Excitonic Magnetic Polaron in (CdMn)Te. *JETP Lett.* **1995**, *62*, 335.

9. Beaulac, R.; Schneider, L.; Archer, P. I.; Bacher, G.; Gamelin, D. R. Light-Induced Spontaneous Magnetization in Colloidal Doped Quantum Dots. *Science* **2009**, *325*, 973.

10. Sellers, I. R.; Oszwałdowski, R.; Whiteside, V. R.; Eginligil, M.; Petrou, A.; Zutic, I.; Chou, W.-C.; Fan, W. C.; Petukhov, A. G.; Kim, S. J.; Cartwright, A. N.; McCombe, B. D. Robust Magnetic Polarons in Type-II (Zn,Mn)Te/ZnSe Quantum Dots. *Phys. Rev. B* **2010**, *82*, 195320.

11. Yu, W. W.; Qu, L.; Guo, W.; Peng, X. Experimental Determination of the Extinction Coefficient of CdTe, CdSe, and CdS Nanocrystals. *Chem. Mater.* **2003**, *15*, 2854.

12. Vlaskin, V. A.; Barrows, C. J.; Erickson, C. S.; Gamelin, D. R. Nanocrystal Diffusion Doping. *J. Am. Chem. Soc.* **2013**, *135*, 14380.

13. Archer, P. I.; Santangelo, S. A.; Gamelin, D. R. Direct Observation of *sp–d* Exchange Interactions in Colloidal Mn^{2+}- and Co^{2+}-doped CdSe Quantum Dots. *Nano Lett.* **2007**, *7*, 1037.

14. Santangelo, S. A.; Hinds, E. A.; Vlaskin, V. A.; Archer, P. I.; Gamelin, D. R. Bimodal Bond-Length Distributions in Cobalt-Doped CdSe, ZnSe, and $Cd_{1-x}Zn_xSe$ Quantum Dots. *J. Am. Chem. Soc.* **2007**, *129*, 3973.

15. Madelung, O. *Semiconductors: Data Handbook*; Springer: New York, 2004.

16. Wojtowicz, T.; Kutrowski, M.; Karczewski, G.; Kossut, J.; Konig, B.; Keller, A.; Yakovlev, D. R.; Waag, A.; Geurts, J.; Ossau, W.; Landwehr, G.; Merkulov, I. A.; Teran, F. J.; Potemski, M. II-VI Quantum Structures with Tunable Electron g-Factor. *J. Cryst. Growth* **2000**, *214/215*, 378.

17. Wojtowicz, T.; Kutrowski, M.; Karczewski, G.; Kossut, J.; Teran, F. J.; Potemski, M. g-Factor Dependence of the Evolution of Magneto-Optical Spectra with the Density of Quasi-Two-Dimensional Electrons in $Cd_{1-x}Mn_xTe/Cd_{1-y}Mg_yTe$ Heterostructures. *Phys. Rev. B* **1999**, *59*, 10437.

18. Arciszewska, M.; Nawrocki, M. Determination of the Band-Structure Parameters of $Cd_{0.95}Mn_{0.05}Se$ from Magnetoabsorption Measurements. *J. Phys. Chem. Sol.* **1986**, *47*, 309.

19. Nawrocki, M.; Hamdani, F.; Lascaray, J. P.; Golacki, Z.; Deportes, J. Ion-Carrier Electron Exchange Constants for CdCoSe Semimagnetic Semiconductor. *Solid State Commun.* **1991**, *77*, 111.

20. Norberg, N. S.; Parks, G. L.; Salley, G. M.; Gamelin, D. R. Giant Excitonic Zeeman Splittings in Co^{2+}-doped ZnSe Quantum Dots. *J. Am. Chem. Soc.* **2006**, *128*, 13195.

21. Beaulac, R.; Ochsenbein, S. T.; Gamelin, D. R. Colloidal Transition-Metal-Doped Quantum Dots In *Semiconductor Quantum Dots*; 2 ed.; Klimov, V. I., Ed.; CRC Press: Boca Raton, USA, 2010, p 397.

22. Merkulov, I. A.; Yakovlev, D. R.; Keller, A.; Ossau, W.; Geurts, J.; Waag, A.; Landwehr, G.; Karczewski, G.; Wojtowicz, T.; Kossut, J. Kinetic Exchange between the Conduction Band Electrons and Magnetic Ions in Quantum-Confined Structures. *Phys. Rev. Lett.* **1999**, *83*, 1431.

23. Bussian, D. A.; Crooker, S. A.; Yin, M.; Brynda, M.; Efros, A. L.; Klimov, V. I. Tunable Magnetic Exchange Interactions in Manganese-Doped Inverted Core-Shell ZnSe-CdSe Nanocrystals. *Nat. Mater.* **2009**, *8*, 35.

24. Yu, J. H.; Liu, X. Y.; Kweon, K. E.; Joo, J.; Park, J.; Ko, K. T.; Lee, D.; Shen, S. P.; Tivakornsasithorn, K.; Son, J. S.; Park, J. H.; Kim, Y. W.; Hwang, G. S.; Dobrowolska, M.; Furdyna, J. K.; Hyeon, T. Giant Zeeman Splitting in Nucleation-Controlled Doped CdSe:Mn^{2+} Quantum Nanoribbons. *Nat. Mater.* **2010**, *9*, 47.

25. Myers, R. C.; Poggio, M.; Stern, N. P.; Gossard, A. C.; Awschalom, D. D. Antiferromagnetic *s–d* Exchange Coupling in GaMnAs. *Phys. Rev. Lett.* **2005**, *95*, 017204.

26. Beaulac, R.; Gamelin, D. R. Two-Center Formulation of Mn^{2+}-Electron *s–d* Exchange Coupling in Bulk and Quantum-Confined Diluted Magnetic Semiconductors. *Phys. Rev. B* **2010**, *82*, 224401.

27. Beaulac, R.; Feng, Y.; May, J. W.; Badaeva, E.; Gamelin, D. R.; Li, X. S. Orbital Pathways for Mn^{2+}-Carrier *sp–d* Exchange in Diluted Magnetic Semiconductor Quantum Dots. *Phys. Rev. B* **2011**, *84*, 195324.

28. Efros, A. L.; Rosen, M.; Kuno, M.; Nirmal, M.; Norris, D. J.; Bawendi, M. Band-Edge Exciton in Quantum Dots of Semiconductors with a Degenerate Valence Band: Dark and Bright Exciton States. *Phys. Rev. B* **1996**, *54*, 4843.

29. Shapira, Y.; Heiman, D.; Foner, S. Magnetization and Spin-Flip Energy in $Cd_{0.9}Mn_{0.1}Se$. *Solid State Comm.* **1982**, *44*, 1243.

30. Nawrocki, M.; Planel, R.; Fishman, G.; Galazka, R. Exchange-Induced Spin-Flip Raman Scattering in a Semimagnetic Semiconductor. *Phys. Rev. Lett.* **1981**, *46*, 735.

31. Arciszewska, M.; Nawrocki, M. Excitonic Magnetoabsorption of Cadmium Manganese Selenide In *Proc. of the XI Conf. of Physics of Semiconducting Compounds, Jaszowiec*; Pol. Acad. Sci.: Warsaw, Poland., 1982, p 225.

32. Bartholomew, D. U.; Suh, E. K.; Ramdas, A. K.; Rodriguez, S.; Debska, U.; Furdyna, J. K. Electronic Raman-Scattering in $Cd_{1-x}Co_xSe$. *Phys. Rev. B* **1989**, *39*, 5865.

33. Gennser, U.; Liu, X. C.; Vu, T. Q.; Heiman, D.; Fries, T.; Shapira, Y.; Demianiuk, M.; Twardowski, A. Exchange Energies, Bound Magnetic Polarons, and Magnetization in CdSe-Co and CdS-Co. *Phys. Rev. B* **1995**, *51*, 9606.

34. Inoue, M.; Adachi, N.; Mogi, I.; Kido, G.; Nakagawa, Y.; Oka, Y. An Optical Study of $Cd_{0.989}Co_{0.011}Se$ in High Magnetic Fields. *Phys. B* **1993**, *184*, 441.

35. Piepho, S. B.; Schatz, P. N. *Group Theory in Spectroscopy with Applications to Magnetic Circular Dichroism*; Wiley: New York, U.S.A., 1983.

Appendix A

Nanocrystal Synthesis and General Characterization Methods

A.1 ZnO nanocrystals

$Zn(OAc)_2$, TMAH, DDA and TOPO (90%) were purchased from Sigma-Aldrich and used without further purification.

A.1.1 ***Synthesis of colloidal ZnO nanocrystals.*** Colloidal ZnO nanocrystals were synthesized by base-initiated hydrolysis and condensation of Zn^{2+} as detailed previously.[1,2] In a typical synthesis, a solution of 22 mmol TMAH in 40 ml EtOH was added dropwise to a stirred solution of 13 mmol $Zn(OAc)_2 \bullet 2H_2O$ in 135 ml DMSO at room temperature. Nanocrystals were grown for 15-60 min, after which the reaction was stopped by precipitation with ~300 ml ethyl acetate. Nanocrystals were collected via centrifugation and resuspended in EtOH, followed by precipitation with heptane. To suspend the nanocrystals in nonpolar solvents, the surface ligands were exchanged by suspending the nanocrystals in excess of DDA that had been heated above the melting point (29 ºC), followed by precipitation with EtOH. Finally, the nanocrystals were heated in TOPO at 100 ºC for 30 minutes. The resulting TOPO-capped nanocrystals were then washed/resuspended with ~3:1 EtOH/toluene as described above.

A.1.2 ***Large ZnO nanocrystals.*** Large ZnO nanocrystals were made in a similar manner as described above, but were heated under N_2 in DDA at 180 ºC for 2-24 h prior to TOPO capping to promote growth to various sizes. Similar photodoping results are obtained for TOPO- and DDA-ligated nanocrystals, but TOPO-ligated nanocrystals retain their solubility better during titrations. We attribute this to the stronger binding of the phosphonate-type ligating groups in the 90%-purity TOPO, making it more compatible with the ionic $[FeCp^*_2][BAr_F]$ oxidant.

A.1.3 ***General characterization.*** The radii of small ZnO nanocrystals (r < 3.2 nm) were determined from the empirical correlation between radii and absorption spectra.[3] The radii of larger nanocrystals were determined by pXRD using a Bruker D8 Discover diffractometer and by statistical analysis of TEM images collected using a FEI Tecnai G2 F20.

A.1.4 ***Mg^{2+}- and Mn^{2+}-doped ZnO nanocrystals.*** ZnO nanocrystals doped with Mg^{2+} or Mn^{2+} were synthesized using the procedure described above, with the addition of $Mg(OAc)_2 \bullet 4H_2O$ or $Mg(OAc)_2 \bullet 4H_2O$, respectively. Sizes were determined by pXRD or by statistical analysis of TEM images.

A.2 Al^{3+}-doped ZnO (AZO) nanocrystals

AZO nanocrystals were synthesized following literature procedures.[4] Briefly, solutions of (A) 1 mmol zinc stearate, 3 mmol oleic acid and 0.05–0.2 mmol aluminum acetylacetonate in 4 ml ODE and (B) 10 mmol 1,2-hexadecanediol in 11 ml ODE were degassed at 140°C under argon for 1 h. The temperature of B was increased to 260 ºC and A was rapidly injected. Following injection, the temperature dropped to 240 ºC, where it was held for 5 h to allow nanocrystal growth. The resulting nanocrystals were precipitated with EtOH, collected by centrifugation, and resuspended in hexane. This procedure was repeated three times. On the third wash the nanocrystals were suspended in 1:1 hexane/octane. To prepare DDA-ligated AZO nanocrystals, excess DDA was added to the nanocrystal suspension and this solution was sonicated for 30 min. Following sonication, the nanocrystals were washed twice by precipitation with EtOH and resuspension in toluene. This process was repeated a total of three times to ensure effective ligand exchange. The AZO nanocrystals were sized via statistical analysis of TEM data collected using a JEOL 2100 microscope at Lawrence Berkeley National Laboratory.

A.3 CdSe nanocrystals

A.3.1 ***Synthesis of CdSe nanocrystals for photodoping.*** CdSe nanocrystals were synthesized according following a previously reported method.[5] For 4.6 nm nanocrystals, CdO (60 mg), ODPA (280 mg) and TOPO (3.0 g) were added to a 50 mL round bottom flask, heated to ~130 °C and degassed under vacuum for ~1.5 h. The reaction mixture was heated under nitrogen to above 350 °C to form an optically clear and colorless solution. After adding 1.0 ml TOP to the solution, the temperature was brought up to 375°C, at which point a solution of 60 mg Se in 0.5 ml TOP was swiftly injected into the flask. The CdSe cores were grown at ~370 °C until desired size was reached (2 – 5 min) at which point growth was halted by removing the heating mantle. The cooled CdSe nanocrystals were washed repeatedly by precipitating with EtOH and redissolving in toluene.

A.3.2 ***Synthesis of CdSe/ZnSe core/shell nanocrystals.*** CdSe/ZnSe nanocrystals were synthesized by modification of a literature method.[6] A 50 ml round bottom flask containing ~2×10^{-7} mol of washed CdSe cores, oleylamine (5 ml), and octadecane (5 ml) was heated to ~115 °C and degassed under vacuum for ~1.5 h. Stock solutions of ~0.2 M Se dissolved in TOP and ~0.2 M zinc oleate in 1:1 (m/m) ODE and decylamine were used as precursors for shell growth. The exact amount of precursors used for each monolayer of shell growth was calculated according to the increase in volume of each shell monolayer, taking into account the change in total nanocrystal size throughout growth. The reaction temperature was set at 200 °C under nitrogen. Growth times were 2.5 h for each cadmium addition and 1 h for each selenium addition. Aliquots were taken during growth and the amount for each addition of shell precursor was adjusted to take into account the lesser amount of remaining nanocrystals. The cooled CdSe/ZnSe nanocrystals were washed repeatedly by precipitating with EtOH and redissolving in toluene.

A.4 CdS and CdTe nanocrystals

CdS nanocrystals were synthesized by published methods.[7] CdTe nanocrystals were synthesized by a slight modification of published methods.[8] Briefly, CdO (13 mg), hexadecylphosphonic acid (60 mg), and octadecene (3.9 g) were degassed at 110 °C for 40 min and heated to 300 °C under nitrogen. To this stirring solution, an air-free solution of Te (25 mg) tributylphosphine (0.6 mL), and octadecene (1.5 g) was injected swiftly. The stirring solution cooled to ~270 °C and was held there for 3 min. The solution was cooled to room temperature and twice precipitated with acetone, centrifuged and redissolved in toluene.

A.5 Transition-metal-doped CdSe nanocrystals

A.5.1 $Cd_{1-x}Mn_xSe$ synthesis. $Cd_{1-x}Mn_xSe$ QDs were synthesized by cluster thermolysis.[9] Briefly, a solution of 0.015 mmol manganese chloride tetrahydrate in 11 g HDA was degassed under vacuum at 130 °C for 1.5 hours. The reaction flask was placed under N_2 and the temperature reduced to below 80 °C for the addition of 0.093 mmol $(Me_4N)_2[Cd_4(SePh)_{10}]$ and 0.260 mmol Se powder. The temperature was increased to 130 °C and maintained for 1.5 h, then increased to 220 °C and maintained for 1 h. After growth, the solution was rapidly cooled using a water bath. The QDs were suspended with the addition of ~4 ml toluene when the temperature dropped to ~70 °C.

A.5.1.1 Overcoating $Cd_{1-x}Mn_xSe$ with CdSe. CdSe shells were grown by the SILAR approach.[10] A Se precursor was made under anaerobic conditions with 0.16 g of Se powder in 10 ml of trioctylphosphine. A separate Cd precursor was made by dissolving 0.01 g of CdO and 0.38 g of oleic acid into 2.6 g of ODE and degassing at 200 °C until turning clear. In a separate flask, 0.8 g oleylamine and 5.6 g ODE were degassed before combining with degassed

$Cd_{1-x}Mn_xSe$ QDs and heating to 200 °C under N_2. Shells were grown with alternate additions of the Cd and Se precursors via syringe pump, starting with the Cd precursor. For each addition, 250 μl of precursor was added at a rate of 50 μl/minute. Because HDA was the capping ligand for the cores, the core/shell sample was sonicated with HDA and washed with toluene/EtOH in order to have HDA as the primary ligand for EPR measurements.

A.5.2 $Cd_{1-x}Co_xSe$ synthesis. $Cd_{1-x}Co_xSe$ QDs were synthesized by hot injection following literature procedures.[11] Briefly, a solution of the following was prepared and degassed at 130 °C: 80 mmol octadecene, 1.7 mmol oleic acid, 2.1 mmol HDA, 0.312 mmol cadmium acetate dehydrate, and 23 μmol cobalt(II) acetate tetrahydrate. A separate air-free solution of 25 mmol Se powder in 1 ml tributylphosphine was prepared. The former solution was heated to 310 °C and the latter solution was added quickly and anaerobically via syringe with vigorous stirring. The QDs were allowed to grow for ~7 min, after which they were cooled with a water bath.

A.5.3 Surface treatment and purification. QDs prepared by both methods were washed with EtOH, followed by centrifugation and resuspension in toluene. They were then sonicated in toluene with excess TOPO to remove surface cations, washed again, and resuspended as described above.

A.5.4 General characterization. Absorption spectra were collected in a 1 mm quartz cuvette using a Cary 500 (Varian) spectrophotometer. The dopant mole fraction (x) was determined by ICP-MS. QD sizes were determined from empirical correlation to absorption maxima.[12]

A.6 $Zn_{1-x}Mn_xSe$ nanocrystals

The $Zn_{1-x}Mn_xSe$ QDs were synthesized in the same manner as $Cd_{1-x}Mn_xSe$ QDs (section A.5.1), using $(Me_4N)_2[Zn_4(SePh)_{10}]$ and growing at 270 °C for 1.5 hours. All QDs were washed

with EtOH, followed by centrifugation and resuspension in toluene. They were then sonicated in toluene with excess TOPO (90%) to remove surface Mn^{2+} ions, washed again, and resuspended in toluene. QD sizes were determined from empirical correlation to absorption maxima.[13]

A.7 References

1. Schwartz, D. A.; Norberg, N. S.; Nguyen, Q. P.; Parker, J. M.; Gamelin, D. R. Magnetic Quantum Dots: Synthesis, Spectroscopy, and Magnetism of Co^{2+}- and Ni^{2+}-Doped ZnO Nanocrystals. *J. Am. Chem. Soc.* **2003**, *125*, 13205.

2. Norberg, N. S.; Gamelin, D. R. Influence of Surface Modification on the Luminescence of Colloidal ZnO Nanocrystals. *J. Phys. Chem. B* **2005**, *109*, 20810.

3. Meulenkamp, E. A. Synthesis and Growth of ZnO Nanoparticles. *J. Phys. Chem. B* **1998**, *102*, 5566.

4. Buonsanti, R.; Llordes, A.; Aloni, S.; Helms, B.; Milliron, D. Tunable Infrared Absorption and Visible Transparency of Colloidal Aluminum-Doped Zinc Oxide Nanocrystals. *Nano Lett.* **2011**, *11*, 4706.

5. Carbone, L.; Nobile, C.; De Giorgi, M.; Sala, F. D.; Morello, G.; Pompa, P.; Hytch, M.; Snoeck, E.; Fiore, A.; Franchini, I. R.; Nadasan, M.; Silvestre, A. F.; Chiodo, L.; Kudera, S.; Cingolani, R.; Krahne, R.; Manna, L. Synthesis and Micrometer-Scale Assembly of Colloidal CdSe/CdS Nanorods Prepared by a Seeded Growth Approach. *Nano Lett.* **2007**, *7*, 2942.

6. Ghosh, Y.; Mangum, B. D.; Casson, J. L.; Williams, D. J.; Htoon, H.; Hollingsworth, J. A. New Insights into the Complexities of Shell Growth and the Strong Influence of Particle Volume in Nonblinking "Giant" Core/Shell Nanocrystal Quantum Dots. *J. Am. Chem. Soc.* **2012**, *134*, 9634.

7. Yu, W. W.; Peng, X. G. Formation of High-Quality CdS and Other II-VI Semiconductor Nanocrystals in Noncoordinating Solvents: Tunable Reactivity of Monomers. *Angew. Chem. Int. Ed.* **2002**, *41*, 2368.

8. Yu, W. W.; Qu, L.; Guo, W.; Peng, X. Experimental Determination of the Extinction Coefficient of CdTe, CdSe, and CdS Nanocrystals. *Chem. Mater.* **2003**, *15*, 2854.

9. Archer, P. I.; Santangelo, S. A.; Gamelin, D. R. Direct Observation of *sp–d* Exchange Interactions in Colloidal Mn^{2+}- and Co^{2+}-doped CdSe Quantum Dots. *Nano Lett.* **2007**, *7*, 1037.

10. Li, J. J.; Wang, Y. A.; Guo, W. Z.; Keay, J. C.; Mishima, T. D.; Johnson, M. B.; Peng, X. G. Large-Scale Synthesis of Nearly Monodisperse CdSe/CdS Core/Shell Nanocrystals Using

Air-Stable Reagents via Successive Ion Layer Adsorption and Reaction. *J. Am. Chem. Soc.* **2003**, *125*, 12567.

11. Santangelo, S. A.; Hinds, E. A.; Vlaskin, V. A.; Archer, P. I.; Gamelin, D. R. Bimodal Bond-Length Distributions in Cobalt-Doped CdSe, ZnSe, and $Cd_{1-x}Zn_xSe$ Quantum Dots. *J. Am. Chem. Soc.* **2007**, *129*, 3973.

12. Ruster, C.; Borzenko, T.; Gould, C.; Schmidt, G.; Molenkamp, L. W.; Liu, X.; Wojtowicz, T. J.; Furdyna, J. K.; Yu, Z. G.; Flatte, M. E. Very large Magnetoresistance in Lateral Ferromagnetic (Ga,Mn)As Wires with Nanoconstrictions. *Phys. Rev. Lett.* **2003**, *91*, 216602.

13. Smith, C. A.; Lee, H. W. H.; Leppert, V. J.; Risbud, S. H. Ultraviolet-Blue Emission and Electron-Hole states in ZnSe Quantum Dots. *Appl. Phys. Lett.* **1999**, *75*, 1688.

Appendix B

Photodoping and Titration Methods

B.1 Chemicals

B.1.1 Photodoping chemicals. Toluene and THF were obtained from a solvent purification system, transferred to a N_2 glovebox, and placed over molecular sieves for 24 h prior to use. Anhydrous EtOH was purchased from Acros and stored in the glovebox. Li[Et_3BH], K[Et_3BH, Li[Me_2NBH_3], and Li[PF_6] were purchased from Sigma-Aldrich as 1 M solutions in THF and stored in the glovebox. [Bu_4N][Et_3BH] was synthesized by cation exchange. Briefly, 0.1 mmol [Bu_4N][PF_6] was added to a solution of 0.1 mmol K[Et_3BH] in 100 μl THF. 100 μl toluene was added with stirring to precipitate the K[PF_6] byproduct. The resulting solution was filtered through a 200 μm PTFE filter.

B.1.2 Titration chemicals. [$FeCp^*_2$][BAr_F] was synthesized following literature procedures.[1] The starting materials, sodium tetrakis[3,5-bis(trifluoromethyl)phenyl]borate, bis(pentamethylcyclopentadienyl)iron(II), and iron(III) chloride (99.9%) were purchased from Sigma-Aldrich and used without further purification.

B.2 Photodoping of colloidal ZnO nanocrystals

Colloidal ZnO nanocrystals were photodoped to their maximum level by prolonged exposure to UV irradiation from a 100 W Hg/Xe Oriel photolysis lamp (~2 W/cm^2, ~1.5 cm illumination diameter) in the presence of a hole quencher. Concentrated aqueous $CuSO_4$ was used as an IR filter to reduce sample heating. ZnO was successfully photodoped using EtOH, Li[Et_3BH], K[Et_3BH], Li[Me_2NBH_3] and [Bu_4N][Et_3BH] hole quenchers.

B.2.1 EtOH as a hole quencher. Photodoping in the presence of EtOH was performed on both TOPO- and DDA-ligated nanocrystals. Similar results were obtained for both, but TOPO-ligated nanocrystals retain their solubility better during titrations. We attribute this to the stronger binding of the phosphonate-type ligating groups in the 90%-purity TOPO, making it more compatible with the ionic $[FeCp^*_2][BAr_F]$ oxidant.

B.2.2 Borohydride hole quenchers. Photodoping in the presence of borohydrides was incompatible with amine ligands, and thus performed only on TOPO-ligated ZnO nanocrystals. Photodoping with the hydrides, especially $Li[Et_3BH]$ and $Li[Me_2NBH_3]$, sometimes resulted in formation of a brown/black byproduct that showed a pXRD pattern consistent with that of Zn^0 metal (Appendix D.6). The formation of this byproduct could be greatly reduced by periodically adding the hydride in small (~10–50 equivalents) aliquots during the photodoping process instead of introducing the entire amount at once so as to keep the unused hydride concentration low.

B.2.3 Spectroscopic measurements. Photodoping of ZnO nanocrystals was performed in (1) 1 cm air-free cuvettes for titrations, (2) an air-free IR cell to measure the IR and UV absorption, and (3) EPR tubes to measure the electron *g* value.

B.2.3.1 Photodoping in 1 cm air-free cuvettes. Nanocrystals were suspended in 1:1 toluene/THF. Typical nanocrystal concentrations were 10–100 μM, depending on nanocrystal size. Samples were considered maximally photodoped when the NIR absorption stopped increasing over ~20 min UV exposure. Under these conditions, maximum photodoping levels were typically reached within 2–4 h for EtOH or within ~20 min for borohydrides. Except for kinetic experiments, samples were not stirred during photodoping.

B.2.3.2 Photodoping in air-free IR cell. Nanocrystals were suspended in 1:1 toluene/THF. Typical nanocrystal concentrations were 1–10 μM, depending on nanocrystal size. Samples were loaded into an air-free IR cell containing a 100 μm Teflon spacer sandwiched between two CaF_2 windows. Spectra were obtained using Cary 500 and Bruker Vector 33 spectrometers for UV and IR measurements, respectively. Samples were considered maximally photodoped when the IR absorption stopped increasing over ~60 s. It should be noted that the UV absorption appeared to stop bleaching before the IR absorption maximized. Under these conditions, maximum photodoping levels were typically reached within ~30 min using EtOH and ~2 min using borohydrides. Prolonged UV irradiation after reaching the maximum photodoping level causes some irreversible photochemistry, manifested as diminished red shift in the IR absorption during re-oxidation, attributed to poor mixing in the IR cell.

B.2.3.3 Photodoping in air-free EPR tubes. CW EPR measurements were collected using a Bruker EMX X-band spectrometer with a SHQE resonator operating at 9.8 GHz. The *g* values were measured in reference to 2,2-diphenyl-1-picrylhydrazyl (DPPH, $g = 2.0036$). Nanocrystals were suspended in toluene with typical concentrations of 50–100 μM. Samples were considered maximally photodoped when the *g* value stopped increasing over ~10 min. Under these conditions, maximum photodoping levels were typically reached within 1–2 h using EtOH and ~ 20 min for borohydrides.

B.3 Electron counting in ZnO nanocrystals

B.3.1 Titration of photodoped ZnO nanocrystals. Electron counting in photodoped ZnO nanocrystals was performed by titration against $[FeCp^*_2][BAr_F]$.[2-5] Addition of $[FeCp^*_2][BAr_F]$ removes electrons from the ZnO nanocrystals, as described by equation B.1. Figure B.1a plots

NIR absorption spectra of photodoped r = 1.75 nm ZnO nanocrystals (TOPO-capped, 120 μM in 1:1 toluene/THF) at various stages of titration, using the NIR spectrum of the as-prepared nanocrystal solution as the baseline ($A = A_{\text{photodoped}} - A_{\text{as-prepared}}$). With each addition of $[FeCp^*_2][BAr_F]$ to the photodoped nanocrystals, the NIR absorption decreases due to nanocrystal oxidation. Once all of the ZnO electrons are removed, equation B.1 can no longer proceed in the forward direction. Instead, further addition of $[FeCp^*_2][BAr_F]$ leads to growth of $[FeCp^*_2]^+$ absorption centered around ~700 nm (Figure B.1b).

To determine $\langle n_{max} \rangle$, the decrease in NIR absorbance integrated from 800 to 1400 nm, and the subsequent increase in $[FeCp^*_2]^+$ absorption at 800 nm, are plotted versus equivalents of $[FeCp^*_2][BAr_F]$ added to the ZnO nanocrystals (Figure B.1c). The x intercepts of these two lines indicate $\langle n_{max} \rangle$. The use of integrated absorption was found to be more reliable than the absorption at a single wavelength, but both yield similar results (see section B.3.2).[3] Often the number of electrons determined by the decrease in NIR absorption was slightly smaller than that determined by $[FeCp^*_2]^+$ absorption due to shifting of the IR peak. The values reported here are averages of the two sides of the titration, and error bars encompass the upper and lower values. For r = 1.75 nm nanocrystals, $\langle n_{max} \rangle$ was determined to be 4.6 ± 0.6 e^-_{CB} per nanocrystal, which corresponds to an average maximum electron density of $\langle N_{max} \rangle = 1.9 \pm 0.3 \times 10^{20}$ cm^{-3}.

$$e^-_{CB}:ZnO + [FeCp^*_2]^+ \rightarrow ZnO + [FeCp^*_2] \qquad \text{(B.1)}$$

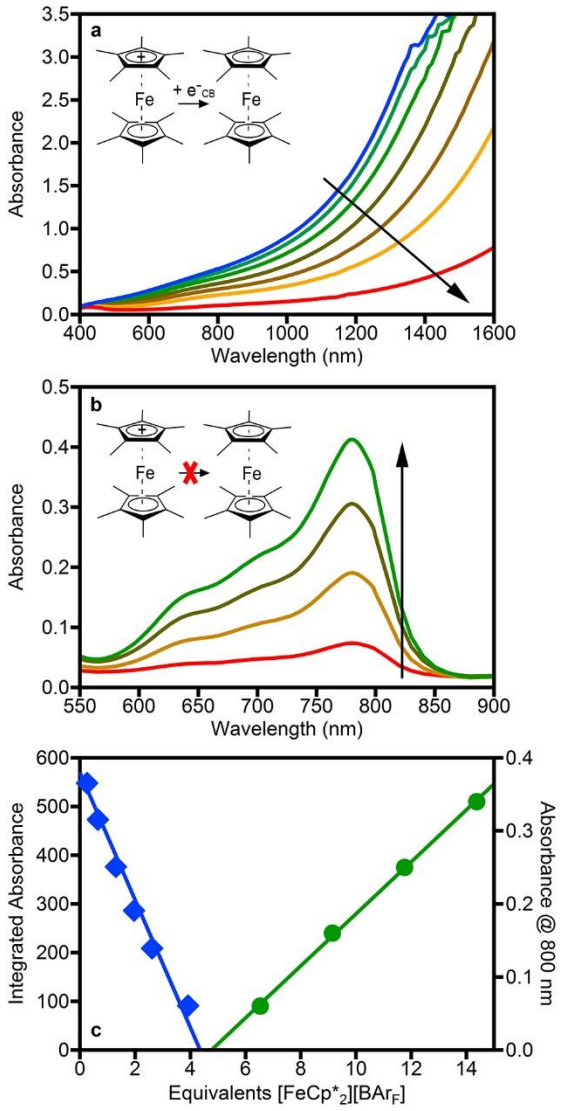

Figure B.1. Titration of photodoped ZnO nanocrystals. Absorption spectra of fully reduced r = 1.75 nm ZnO nanocrystals (top spectrum) with increasing amounts of $[FeCp^*_2][BAr_F]$ added, demonstrating (a) loss of the NIR absorption and (b) growth of $[FeCp^*_2]^+$ absorption. The arrows indicate increasing amounts of $[FeCp^*_2][BAr_F]$. (c) Integrated NIR absorption (800−1400 nm, blue diamonds) and $[FeCp^*_2]^+$ absorption at 800 nm (green circles) plotted as a function of $[FeCp^*_2][BAr_F]$ added to the nanocrystal solution. The solid lines are linear fits to the data. The equivalence point yields $\langle n_{max} \rangle$.

B.3.2 Use of single wavelength or integrated intensity to determine the equivalence point.

A 6 μM solution of dodecylamine-capped ZnO nanocrystals in 2 ml toluene/THF (1:1) was prepared anaerobically. THF was used to aid the solubility of $[FeCp^*_2][BAr_F]$. The nanocrystals were maximally photodoped as described above. To the fully reduced nanocrystals, several 20 μl aliquots of 4.9 mM $[FeCp^*_2][BAr_F]$ in THF were added and the reduction of the NIR absorption was monitored. Figure B.2a plots the absorption spectra of the as-prepared nanocrystals and fully reduced nanocrystals with sequential additions of $[FeCp_2^*][BAr_F]$. The NIR absorption decreases linearly in proportion to the added $[FeCp^*_2][BAr_F]$. Figure B.2b plots the difference in absorption between the as-prepared and fully reduced nanocrystals at each stage of titration.

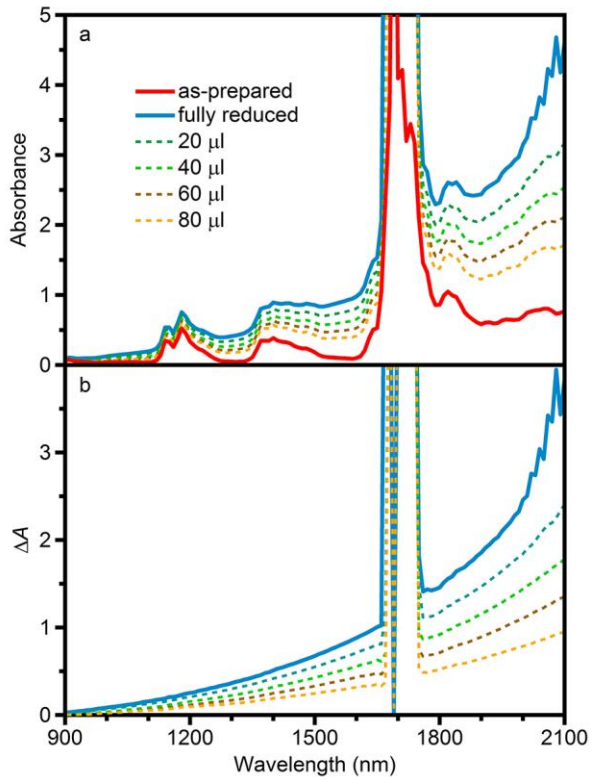

Figure B.2. Addition of $[FeCp^*_2]^+$ to photodoped ZnO monitored by NIR absorption. (a) NIR absorption spectra of as-prepared ZnO nanocrystals and photodoped ZnO nanocrystals in 1:1 toluene/THF (6 μM) with titration of $[FeCp^*_2][BAr_F]$. (b) Difference in absorption between reduced and as-prepared at each stage of titration.

To determine the equivalence point, the difference in absorption at various wavelengths was plotted as a function of added $[FeCp^*_2][BAr_F]$. This plot is shown in Figure B.3a. The solid lines are linear fits to the data. From these fits, the points at which there is no difference in absorption (*i.e.*, the nanocrystals are no longer reduced) were determined and used to calculate the average number of electrons per nanocrystal. There is some scatter when the data are analyzed this way, so the absorption differences integrated over low- and high-energy intervals were plotted (Figure B.3b). The integrated intensities should be less sensitive to small baseline shifts and solvent peaks. Both data sets converge to the same crossing point of 48 electrons per nanocrystal. The

nanocrystals were therefore concluded to contain an average of ~48 e^-_{CB} each. This amount corresponds to an electron density of 9.2×10^{19} cm^{-3} for a spherical 10 nm nanocrystal.

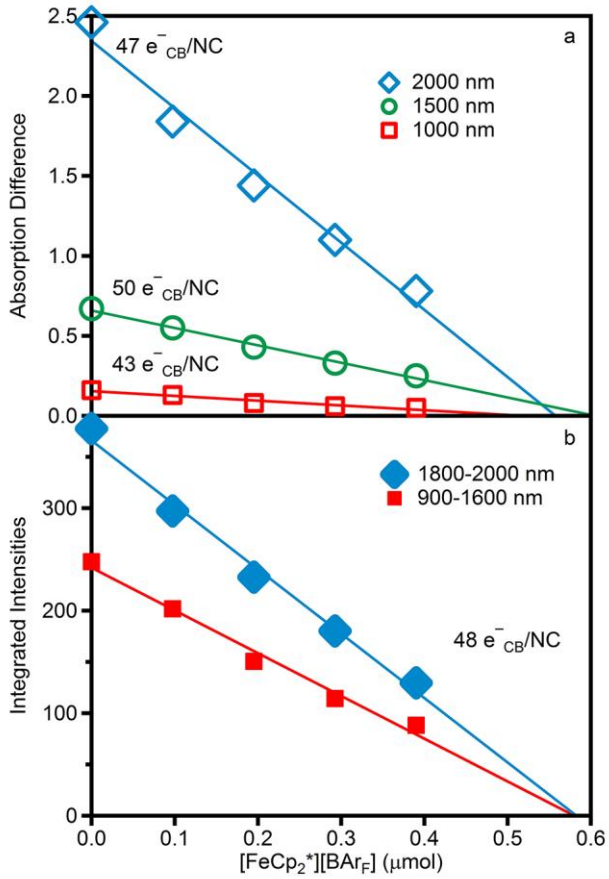

Figure B.3. Effect of single-wavelength versus integrated intensities on titration analysis. (a) Difference in absorption (from Figure B.2b) at various wavelengths plotted as a function of μmol [FeCp*$_2$][BAr_F] added. (b) Integrated absorption differences for two integration intervals, as a function of titration. The lines are fits to the data.

B.3.3 Electron counting in AZO nanocrystals. For the comparison with AZO by absorption and EPR spectroscopies presented in Chapter 2, a 6 μM anaerobic solution of the same nanocrystals in toluene was prepared. THF was not used in these experiments due to its incompatibility with room-temperature EPR experiments. The ZnO nanocrystals were charged to

an intermediate level such that the NIR absorption closely matched that of the AZO nanocrystals (Figure 2.2, referred to as the maximally photodoped or fully reduced ZnO nanocrystals). Figure B.4a shows the NIR absorption spectrum of these as-prepared and highly reduced ZnO nanocrystals. The difference compared to that of the highly photodoped nanocrystals is shown in Figure B.4b. The difference in absorption of the highly reduced nanocrystals is ~2/3 that of the fully reduced nanocrystals, from which these highly reduced nanocrystals were determined to contain 32 electrons per nanocrystal on average. It is noted that this analysis assumes the same extinction coefficient for e^-_{CB} in toluene and in 1:1 toluene/THF.

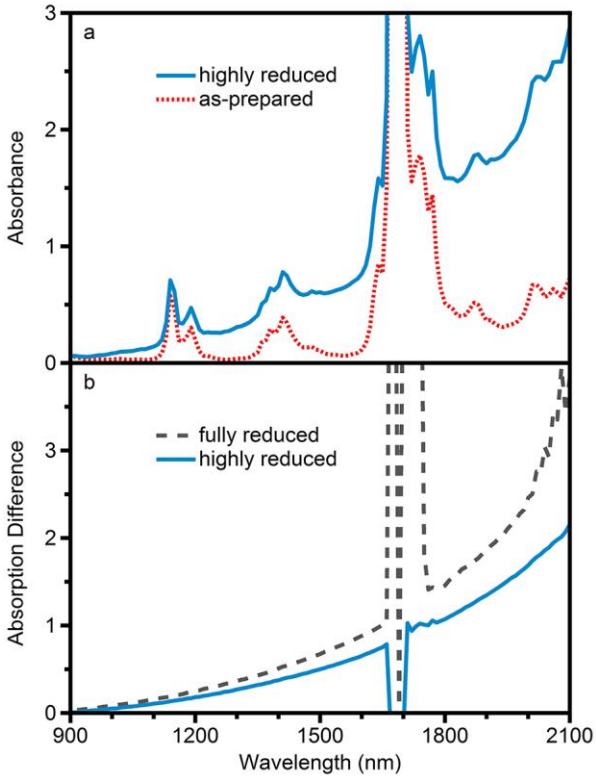

Figure B.4. Comparison of AZO and highly reduced ZnO nanocrystals by NIR absorption. (a) NIR absorption spectra of as-prepared and highly reduced ZnO nanocrystals in toluene (6 μM). (b) Difference in absorption for maximally photodoped (taken from Figure B.2b) and highly reduced ZnO nanocrystals.

B.4 Photodoping of CdSe and CdS nanocrystals

B.4.1 Photodoping of CdSe and CdS colloidal nanocrystals. CdS and CdSe were photodoped using $Li[Et_3BH]$ Photodoping experiments could be done under a wide range of conditions, but typically worked best with 10-100 equivalents of $Li[Et_3BH]$ per CdSe nanocrystal. CdSe nanocrystal concentrations were determined by absorption.[6] Solutions were prepared and kept in the dark until photodoping. Without exposure to visible light (beyond the low-level excitation used in the absorption measurement), no measureable nanocrystal absorption bleach or IR absorption was detected (Appendix E.1). Photodoping was achieved with a variety of light sources. Many samples could be photodoped in the presence of ambient room light, but more efficient photodoping could be achieved using a white light LED or photolysis lamp with a λ = 450 nm cutoff filter (to prevent UV illumination) and a water IR filter (to prevent sample heating).

B.4.1.1 IR absorption of photodoped CdSe colloids. For IR absorption measurements, nanocrystal solutions were prepared in the dark in a nitrogen glove box to be 10–100 μM in toluene with 250–1000 equivalents $Li[Et_3BH]$. These solutions were loaded into an air-free IR cell comprised of a 100 μm spacer between two CaF_2 windows, which was kept in the dark until background absorption measurements were taken. The as-prepared nanocrystal solutions were used as a background. The IR cell was then exposed to visible light using the white light LED on a Galaxy Nexus by Samsung smartphone (λ_{max} = 436, 535 nm) for short times (1−20 s between spectra). The IR absorption was monitored until no further increase was observed.

B.4.2 Photodoping of CdSe nanocrystal films. CdSe quantum dots (d = 7.0 nm) were drop cast onto a FTO substrate and dried under inert atmosphere. A solution of $Li[Et_3BH]$ (20 μl of 0.1 M in THF) was dropped onto the dried CdSe film and allowed to evaporate.

B.5 Titration of photodoped CdSe nanocrystals

For comparison with numbers determined by fitting of the optical bleach, the average number of excess electrons per nanocrystal ($\langle n_{max} \rangle$) was determined by titration against $[FeCp^*_2][BAr_F]$.[7] Direct reaction of $[FeCp^*_2][BAr_F]$ with excess $Li[Et_3BH]$ was found to be slow compared to the nanocrystal oxidation, ruling out the possibility of anomalously large electron counts due to the titration method. Additionally, a nanocrystal-catalyzed reaction of $[FeCp^*_2][BAr_F]$ with excess $Li[Et_3BH]$ can be ruled out because both d = 3.8 and 4.6 nm nanocrystals showed much lower electron counts than the d = 7.0 nm nanocrystals despite similar concentrations of $Li[Et_3BH]$. All titrations, including absorption measurements, were conducted in a nitrogen glove box. A solution of 1–50 μM CdSe nanocrystals in 1:1 toluene/THF was prepared in a 1 cm quartz cuvette with a 2 mm sample path-length. Excess trioctylphosphine oxide was added to aid in solubility. A starting absorption spectrum (denoted "as prepared") was measured using an Ocean Optics 2000+ spectrometer with an absorption attachment. To the cuvette, 20–100 equivalents $Li[Et_3BH]$ was added as a solution in 10 μl THF. The absorption was monitored using the Ocean Optics, which simultaneously provided light for photodoping. The nanocrystal solutions were left in the Ocean Optics lamp until the first exciton absorption stopped decreasing. To these maximally photodoped nanocrystals, 10 μl aliquots of $[FeCp^*_2][BAr_F]$ in THF were added and recovery of the first exciton absorption was monitored. To analyze the titration data, difference spectra ($\Delta A = A_{photodoped} - A_{as\text{-}prepared}$) were integrated over the first exciton, and the amount of bleach was plotted as a function of added $[FeCp^*_2][BAr_F]$. The data were fit to a line, with the x-intercept representing the equivalence point.

B.6 References

1. Le Bras, J.; Jiao, H.; Meyer, W. E.; Hampel, F.; Gladysz, J. A. Synthesis, Crystal Structure, and Reactions of the 17-Vvalence-Electron Rhenium Methyl Complex $[(\eta^5\text{-}C_5Me_5)Re(NO)(P(4\text{-}C_6H_4CH_3)_3)(CH_3)]^+$ $B(3,5\text{-}C_6H_3(CF_3)_2)_4^-$: Experimental and Computational Bonding Comparisons with 18-Electron Methyl and Methylidene Complexes. *J. Organomet. Chem.* **2000**, *616*, 54.

2. Schimpf, A. M.; Gunthardt, C. E.; Rinehart, J. D.; Mayer, J. M.; Gamelin, D. R. Controlling Carrier Densities in Photochemically Reduced Colloidal ZnO Nanocrystals: Size Dependence and Role of the Hole Quencher. *J. Am. Chem. Soc.* **2013**, *135*, 16569.

3. Schimpf, A. M.; Ochsenbein, S. T.; Buonsanti, R.; Milliron, D. J.; Gamelin, D. R. Comparison of Extra Electrons in Colloidal *n*-Type Al^{3+}-Doped and Photochemically Reduced ZnO Nanocrystals. *Chem. Commun.* **2012**, *48*, 9352.

4. Schimpf, A. M.; Thakkar, N.; Gunthardt, C. E.; Masiello, D. J.; Gamelin, D. R. Charge-Tunable Quantum Plasmons in Colloidal Semiconductor Nanocrystals. *ACS Nano* **2013**, *8*, 1065.

5. Schrauben, J.; Hayoun, R.; Valdez, C.; Braten, M.; Fridley, L.; Mayer, J. Titanium and Zinc Oxide Nanoparticles Are Proton-Coupled Electron Transfer Agents. *Science* **2012**, *336*, 1298.

6. Yu, W. W.; Qu, L.; Guo, W.; Peng, X. Experimental Determination of the Extinction Coefficient of CdTe, CdSe, and CdS Nanocrystals. *Chem. Mater.* **2003**, *15*, 2854.

7. Rinehart, J. D.; Schimpf, A. M.; Weaver, A. L.; Cohn, A. W.; Gamelin, D. R. Photochemical Electronic Doping of Colloidal CdSe Nanocrystals. *J. Am. Chem. Soc.* **2013**, *135*, 18782.

Appendix C

Supplementary Material for

Chapter 2: Comparison of Extra Electrons in n-Type Al^{3+}-Doped Photochemically Reduced ZnO Nanocrystals

Adapted from: Schimpf, A. M.; Ochsenbein, S. T.; Buonsanti, R.; Milliron, D. J.; Gamelin, D. R. *Chem. Comm.* **2012**, *48*, 9352.

C.1 Addition of $[FeCp^*_2][BAr_F]$ to AZO nanocrystals

The titration of AZO nanocrystals with $[FeCp^*_2][BAr_F]$ described in Chapter 2 (Figure 2.3) was performed under the same conditions as the titration of photodoped ZnO nanocrystals. Figure C.1 shows the absorption spectrum of anaerobically prepared dodecylamine-capped 5.4% AZO nanocrystals suspended in 1:1 toluene/THF and mixed with various amounts of $[FeCp^*_2][BAr_F]$. No loss of NIR absorption is observed upon addition of $[FeCp^*_2][BAr_F]$ to the nanocrystals. As $[FeCp^*_2]$ is added, absorption from $[FeCp^*_2]^+$ appears with a maximum at ~780 nm. The immediate appearance of $[FeCp^*_2]^+$ absorption without loss of AZO NIR absorption indicates that no electrons are transferred from AZO to $[FeCp^*_2]^+$ (to form the colorless $FeCp^*_2$). To rule out slow electron-transfer kinetics, the final titration point (most $[FeCp^*_2][BAr_F]$) was monitored for 24 h but still showed no loss of NIR absorption.

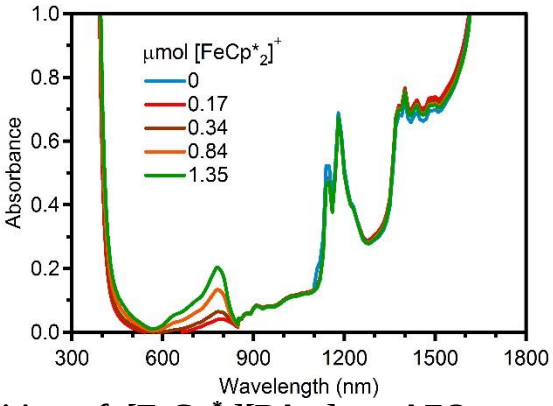

Figure C.1. Addition of [FeCp*$_2$][BAr$_F$] to AZO nanocrystals. Electronic absorption spectra of 5.4% AZO nanocrystals mixed with the various amounts of [FeCp*$_2$][BAr$_F$] as indicated. Addition of [FeCp*$_2$]$^+$ does not lead to decrease in AZO NIR absorption, but is accompanied by an increase in absorption of the [FeCp*$_2$]$^+$ band centered at ~780 nm.

C.2 Comparison of reactivity toward methylene blue

Methylene blue (MB^+) undergoes facile two-electron proton-coupled reduction in the presence of electron donors to form the doubly reduced leucomethylene blue (LMB, equation C.1a). LMB formation can be reversed upon reoxidation (equation C.1b).[1] Equation C.1b is not intended to literally identify the fate of the reduced O_2, which has not been investigated here. In contrast with the reactions with [FeCp*$_2$]$^+$ described above, this reaction (like that with O_2 in air) involves proton-coupled electron transfer.

$$2e^- + H^+ + MB^+ \rightarrow LMB \qquad \text{(C.1a)}$$

$$LMB + \tfrac{1}{2}O_2 \rightarrow MB^+ + OH^- \qquad \text{(C.1b)}$$

To illustrate the difference in reactivities of AZO and photochemically charged ZnO nanocrystals, samples of each were mixed with MB^+ under anaerobic conditions. MB^+ dissolved in EtOH was added to the nanocrystals suspended in toluene. Figure C.1a shows the absorption

spectrum collected after anaerobic mixing of reduced ZnO nanocrystals with excess MB^+ (solid line). Exposing this mixture to air increases the MB^+ absorption (circles), indicating formation of MB^+ via re-oxidation of LMB. LMB shows no absorption in this spectral range. Figure C.2b shows the MB^+ absorption spectra obtained from the same experiment performed with AZO nanocrystals. In this case, exposing the reaction mixture to air does not increase the MB^+ absorption, indicating that no LMB was present and therefore that no electron transfer from the AZO nanocrystals occurred. This experiment is solely intended to illustrate the reactivity difference, and no attempt was made to quantify the number of electrons in the photodoped ZnO using MB^+ as the acceptor.

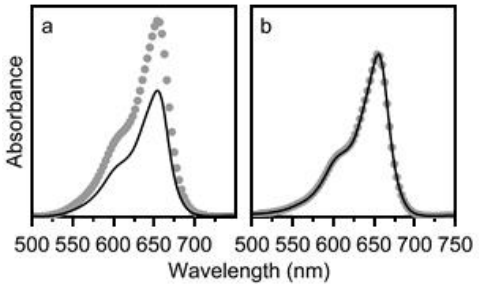

Figure C.2. Difference in reactivities of photodoped ZnO and AZO toward methylene blue. MB^+ absorption spectra (solid lines) collected after anaerobic mixing with (a) photodoped ZnO and (b) AZO nanocrystals suspended in toluene. The gray circles show the absorption spectra of the same mixtures after exposure to air. LMB shows no absorption in this spectral range.

C.3 References

1. de Tacconi, N. R.; Carmoba, J.; Rajeshwar, K. Reversibility of Photoelectrochromism at the TiO_2/Methylene Blue Interface. *J. Electrochem. Soc.* **1997**, *144*, 2486.

Appendix D

Supplementary Material for

Chapter 3: Controlling Carrier Densities in Photochemically Reduced Colloidal ZnO Nanocrystals: Size Dependence and Role of the Hole Quencher

Adapted from: Schimpf, A. M.; Gunthardt, C. E; Rinehart, J. D.; Gamelin, D. R. *J. Am. Chem. Soc.* **2013**, *135*, 16569.

D.1 Titration results

Table D.1 summarizes the titration data for all of the nanocrystals described in Figure 3.2, some of which are from previously published reports. The surface capping ligands and solvent are listed for each sample. All of these nanocrystals were reduced by photoexcitation in the presence of EtOH, but other experimental conditions were different. All of these samples follow the same trend in $\langle n_{max} \rangle$ versus r, as summarized in Figure 3.2. Figure D.1 plots the data in Figure 3.2 using symbols to represent the different surface ligands and solvents used in each experiment.

Table D.1. Values for maximum number of electrons per nanocrystal and corresponding electron densities for the data presented in Figure 3.2.

Radius	Ligand, Solvent	$\langle n_{max} \rangle$	$\langle N_{max} \rangle$ (10^{20} cm^{-3})	Ref.
1.75	TOPO, toluene/THF	4.6 ± 0.6	2.0 ± 0.3	this work
1.95	DDA, toluene/THF	4	1.3	1
2.15	TOPO, toluene/THF	5.0 ± 0.9	1.3 ± 0.3	this work
2.3	TOPO, toluene	5.7	1.1	2
2.5	Hydroxide, EtOH	10	1.5	3
2.8	TOPO, toluene/THF	16 ± 3	1.7 ± 0.4	this work
3.9	DDA, toluene/THF	42 ± 6	1.7 ± 0.3	this work
4.85	TOPO, toluene/THF	51 ± 7	1.0 ± 0.2	this work
5	DDA, toluene/THF	50	0.9	4
6.15	TOPO, toluene/THF	110 ± 20	1.4 ± 0.2	this work

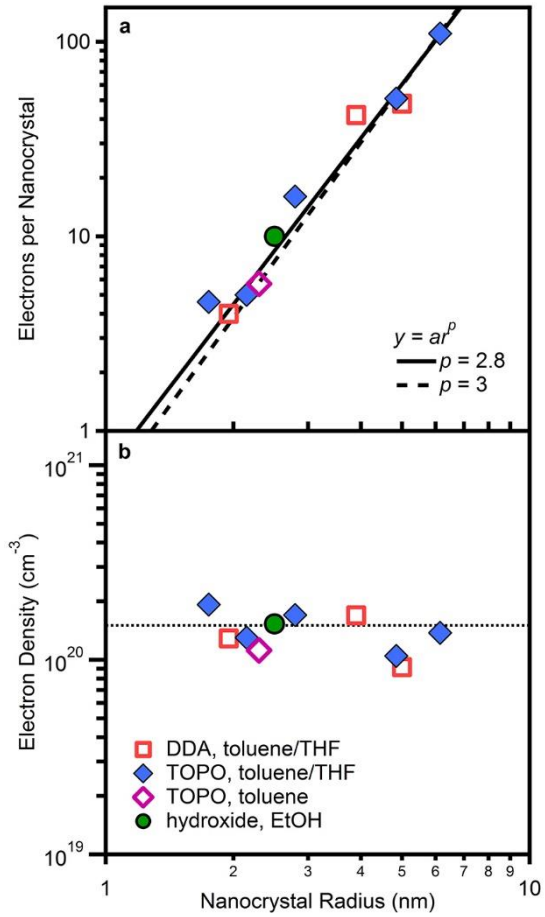

Figure D.1. Size dependence of the maximum photodoping level in colloidal ZnO nanocrystals using EtOH as the hole quencher with various ligands/solvents. (a) Maximum number of electrons per nanocrystal ($<n_{max}>$) plotted versus nanocrystal radius on logarithmic scales. The red open squares are for DDA-capped nanocrystals suspended in 1:1 toluene THF. The solid blue diamonds are for TOPO-capped nanocrystals suspended in 1:1 toluene/THF. The open purple diamond is for TOPO-capped nanocrystals suspended in toluene. The filled green circle is for nanocrystals capped with hydroxides and suspended in EtOH. The solid line represents the best fit to equation 3.2, which yields p = 2.8. The dashed line shows the best fit for p = 3.0. (b) The data from (a) re-plotted as the maximum electron density ($<N_{max}>$) versus nanocrystal radius on logarithmic scales. The dotted line is the maximum carrier density averaged over all nanocrystal sizes ($<<N_{max}>> = 1.4 \pm 0.4 \times 10^{20}$ cm^{-3}).

D.2 Comparison between EtOH and hydride hole quenchers

D.2.1 Photodoping. A stock solution containing ~50 μM r = 2.15 nm ZnO nanocrystals (TOPO-capped in 1:1 toluene/THF) was prepared anaerobically. For photodoping with EtOH, 1

ml of the stock solution was combined with 1 ml THF. For photodoping with Li[Et_3BH], 1 ml of the stock solution was combined with 1 ml of 10 mM Li[Et_3BH] in THF. Both solutions were illuminated with UV light until the maximum photodoping level was reached.

D.2.2 Electron counting by titration with [FeCp*$_2$][BAr$_F$]. Both solutions were titrated as described in Appendix B. The nanocrystals photodoped using EtOH were determined to have $\langle n_{max} \rangle$ = 5.4 e^-_{CB} per nanocrystal. Figure F.3 shows the decrease in NIR absorption with added [FeCp*$_2$][BAr_F] for the ZnO nanocrystals irradiated in the presence of Li[Et_3BH]. The equivalence point of this titration yields $\langle n_{max} \rangle$ = 19 e^-_{CB} per nanocrystal, corresponding to 3.5 times more electrons than in the nanocrystals photodoped using EtOH. After complete loss of the NIR absorption, further addition of [FeCp*$_2$][BAr_F] did not lead to the expected linear increase in absorption of $[FeCp^*_2]^+$. We hypothesize that this result is due to direct reaction between [FeCp*$_2$][BAr_F] and the excess Li[Et_3BH] when no more conduction band electrons are present in the nanocrystals.

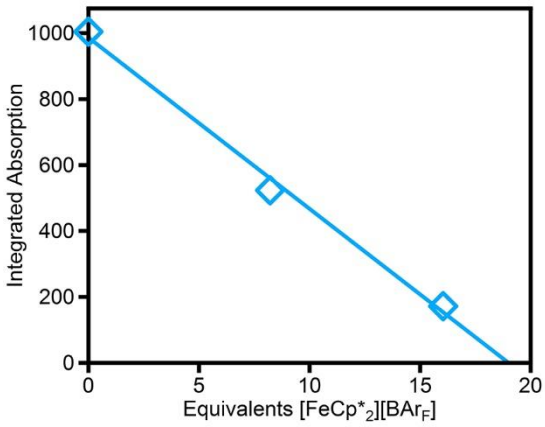

Figure D.2. Titration of ZnO nanocrystals photodoped with Li[Et_3BH]. Integrated NIR absorption (800−1400 nm) plotted as a function of [$FeCp^*_2$][BAr_F] added to the solution of ZnO nanocrystals photodoped using Li[Et_3BH] as the hole quencher.

D.2.3 Electron counting by optical determination. To rule out the concern that reaction between $[FeCp^*_2][BAr_F]$ and excess $Li[Et_3BH]$ affects the decrease in NIR intensity, the number of electrons in ZnO nanocrystals photodoped using $Li[Et_3BH]$ was also determined spectroscopically. Figure D.3 shows absorption difference spectra ($A_{photodoped} - A_{as\text{-}prepared}$) for the fully photodoped nanocrystals prepared using EtOH (dotted blue line) and $Li[Et_3BH]$ (solid purple line). The ratio of integrated absorption between 800 and 1400 nm yields a ratio of 1:3.9 for the EtOH:$Li[Et_3BH]$ spectra, meaning that the nanocrystals reacted with $Li[Et_3BH]$ should contain ~22 e^-_{CB} per nanocrystal. These numbers agree well with those determined above by titration using $[FeCp^*_2][BAr_F]$ ($<n_{max}>$ = 19 e^-_{CB} per nanocrystal, a ratio of 1:3.5 for the EtOH:$Li[Et_3BH]$ solutions), validating the use of such absorbance ratios for estimating the number of added electrons when photodoping with different hole quenchers.

The data in Figure 3.3 and Table 3.1 were obtained by analyzing the absorbance of nanocrystals photodoped using hydride hole quenchers relative to the same nanocrystals photodoped using EtOH. For the data presented in this figure and table, the nanocrystals photodoped using EtOH were assumed to have ($<N_{max}> = 1.4 \pm 0.4 \times 10^{20}$ cm^{-3}, and the average carrier density of nanocrystals photodoped using a hydride was estimated by multiplying 1.4×10^{20} cm^{-3} by the ratio of integrated NIR absorption intensities. For example, if the integrated intensity between 800-1400 nm was three times more when photodoping was performed in the presence of $Li[Et_3BH]$ than in the presence of EtOH, the nanocrystals were estimated to have a maximum carrier density of $<N_{max}> = 3 \times (1.4 \times 10^{20}$ $cm^{-3}) = 4.2 \times 10^{20}$ cm^{-3}. The estimated densities were then converted to numbers of electrons per nanocrystal.

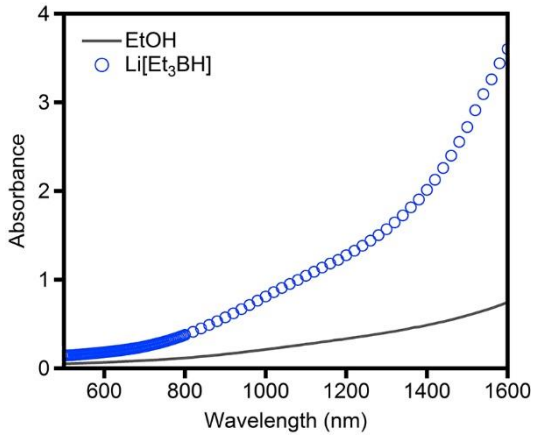

Figure D.3. Determination of photodoping level in ZnO nanocrystals photodoped using Li[Et$_3$BH] by comparison with ZnO nanocrystals photodoped using EtOH. Absorption difference ($A_{photodoped}$ - $A_{as\text{-}prepared}$) of r = 2.15 nm ZnO nanocrystals photodoped to the maximum extent in the presence of EtOH (solid gray line) and Li[Et$_3$BH] (blue circles).

D.3 Size dependence of the maximum photodoping level with various hole quenchers

The data in Figure 3.3, which describe the size dependence of the maximum photodoping using various hole quenchers, were fit to equation 3.2. This was done both by holding p = 3, which facilitates interpretation of the fit paramater a in terms of the relative maximum electron density achieveble with each hole quencher. Fixing p = 3 biases the fitting slightly toward the larger nanocrystals, however, because in most cases these have slightly larger electron densities. Figure D.4 shows fits of the same data, obtained when p is allowed to float. The values of p from these fits are summarized in Table 3.2, and in all cases are close to 3. This fitting was performed using a log-log representation of the data, but the data are presented on linear scales here for clarity.

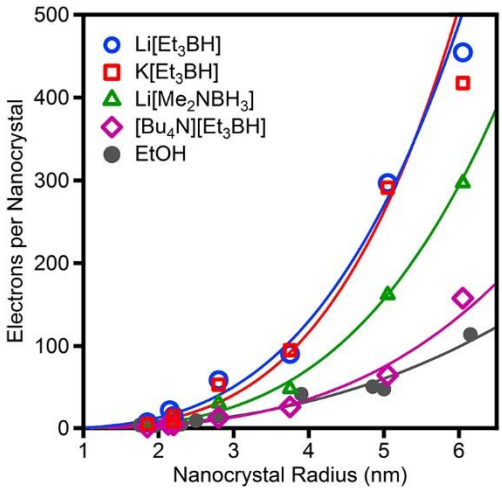

Figure D.4. Size dependence of <n_{max}> of ZnO nanocrystals photodoped using various hole quenchers. The solid lines show fits to equation 5.2 in which *p* is allowed to float.

Table D.2. Summary of the size dependence of ZnO nanocrystal photodoping using various hole quenchers. Parameters were obtained by fitting the data in Figure 5.3b to equation 3.2and allowing *p* to float.

ZQ	*p*
EtOH	2.7 ± 0.3
$[Bu_4N][Et_3BH]$	3.3 ± 0.3
$Li[Me_2NBH_3]$	3.5 ± 0.2
$K[Et_3BH]$	3.3 ± 0.4
$Li[Et_3BH]$	3.6 ± 0.4

D.4 Photodoping in the presence of acid

Figure D.5 shows the NIR absorption spectra of TOPO-capped *r* = 2.8 nm ZnO nanocrystals photodoped using EtOH as the hole quencher, under different conditions. Sample **1** contains as prepared nanocrystals that were maximally photodoped (~3 h). To prepare sample **2,** the nanocrystals were fully photodoped, and to them added 10 equivalents of $[H(Et_2O)^+][BAr_F]$.[5] This mixture was then photodoped for an additional 1 h. Sample **3** contains a mixture of as prepared nanocrystals and 10 equivalents of $[H(Et_2O)^+][BAr_F]$ that was maximally photodoped (~4 h). All samples contain the same concentration of nanocrystals in 1:1 toluene/THF. In

contrast to chemically reduced nanocrystals,[5] added protons have no effect on the maximum number of electrons introduced photochemically by EtOH oxidation.

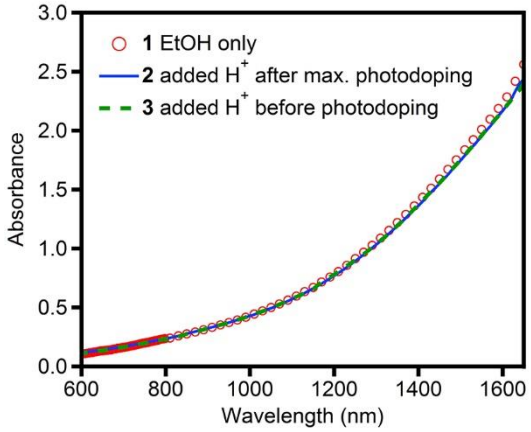

Figure D.5. Photodoping in the presence of acid. Comparison of NIR absorption spectra of TOPO-capped r = 2.8 nm ZnO nanocrystals photodoped using EtOH hole quencher, with and without additional acid, $[H(Et_2O)][BAr_F]$.

D.5 Analysis of kinetic photodoping data

Kinetic photodoping data (Figure 3.5a) were fit to a double exponential (equation D.2a) and initial rates determined by evaluating the initial slope (equation D.2b). Tables D.3a and D.3b give a summary of the fitting parameters and analysis. The ratios $A_{max}^{ZQ}/A_{max}^{EtOH}$, which reflect $\langle N_{max}^{ZQ}\rangle/\langle N_{max}^{EtOH}\rangle$, are slightly smaller than the ratios $\langle\langle N_{max}^{ZQ}\rangle\rangle/\langle\langle N_{max}^{EtOH}\rangle\rangle$ obtained from analysis of the size dependence and reported in Table 3.1. This difference is likely due to two factors: (1) The absorbance values here are measured at a single wavelength, which may be slightly different than the integrated intensities used in Table 3.1, and (2) these data represent only a single nanocrystal sample.

$$A = A_{max} - A_1 e^{-k_1 t} - A_2 e^{-k_2 t} \qquad \text{(D.2a)}$$

$$R_0 = \left(\frac{dA}{dt} \right)\Bigg|_{t=0} = A_1 k_1 + A_2 k_2 \qquad \text{(D.2b)}$$

Table D.3a. Summary of rate constants and weighting coefficients obtained from fitting kinetic data to equation F.2a.

ZQ	A_1	k_1	A_2	k_2
EtOH	0.138 ± 0.007	0.037 ± 0.005	0.044 ± 0.007	0.9 ± 0.4
EtOH + $Li[PF_6]$	0.186 ± 0.004	0.078 ± 0.004	0.037 ± 0.004	4 ± 1
$[Bu_4N][Et_3BH]$	0.11 ± 0.02	8 ± 1	0.05 ± 0.02	30 ± 10
$Li[Me_2NBH_3]$	0.10 ± 0.01	4.6 ± 0.5	0.21 ± 0.01	25 ± 2
$Li[Et_3BH]$	0.29 ± 0.01	3.2 ± 0.5	0.30 ± 0.02	35 ± 3
$K[Et_3BH]$	0.26 ± 0.03	1.9 ± 0.4	0.32 ± 0.03	29 ± 5

Table D.3b. Summary of initial rates and photodoping levels. Maximum photodoping levels were obtained from fitting kinetic data to equation D.2a. Initial rates were obtained by evaluating equation D.2b.

ZQ	R_0^{ZQ}	R_0^{ZQ} / R_0^{EtOH}	A_{max}^{ZQ}	$A_{max}^{ZQ} / A_{max}^{EtOH}$
EtOH	0.04 ± 0.02	1	0.21 ± 0.02	1
EtOH + $Li[PF_6]$	0.18 ± 0.05	4 ± 1	0.23 ± 0.02	1.1 ± 0.1
$[Bu_4N][Et_3BH]$	2 ± 1	50 ± 20	0.16 ± 0.01	0.8 ± 0.1
$Li[Me_2NBH_3]$	5.6 ± 5	130 ± 10	0.31 ± 0.2	1.5 ± 0.2
$Li[Et_3BH]$	11 ± 1	250 ± 30	0.59 ± 0.05	2.8 ± 0.3
$K[Et_3BH]$	10 ± 2	220 ± 40	0.59 ± 0.05	2.8 ± 0.3

D.6 Formation of Zn^0 metal

Figure F.6 shows typical examples of the black/brown coloration observed in ZnO nanocrystal suspensions following anaerobic exposure to UV illumination (~15 min) in the presence of excess (~500 equivalents) $Li[Et_3BH]$ or $Li[Me_2NBH_3]$. When these samples were precipitated in air, pXRD showed only ZnO, and Zn^0 was not detectable.

Figure D.6. Coloration of ZnO nanocrystal suspensions when exposed to UV illumination in the presence of $Li[Et_3BH]$ or $Li[Me_2NBH_3]$.

The formation of metallic Zn^0 was observed following prolonged UV exposure (24 h) in the presence of a large excess of $Li[Et_3BH]$ (~3×10^4 equivalents). The resulting black, cloudy solution was centrifuged and the ZnO nanocrystals could be washed away with hexanes while the black pellet would not resuspend. The black pellet was dried and pressed between two pieces of Kapton tape for pXRD analysis. Figure D.7 shows the pXRD pattern obtained for a drop-coated film of r = 3.75 nm ZnO nanocrystals before photodoping (top spectrum, dotted black line). Following extensive UV irradiation (24 h) of the colloids in the presence of excess $Li[Et_3BH]$ (>10^4 equivalents), coloration was observed, and a brown/black byproduct could be separated from the nanocrystals by centrifugation and washing with hexanes. The resultant pellet was placed between two pieces of Kapton tape and the pXRD spectrum measured (bottom spectrum, solid black line). The patterns for ZnO and Zn^0 are shown at the bottom (blue and red, respectively). Before photodoping, the sample shows only ZnO peaks. The byproduct of photodoping shows both ZnO and Zn^0 metal peaks, plus some additional peaks that could be due to a Li_xZn intermetallic.[6] The large amorphous peak below 30 degrees is due to Kapton tape.

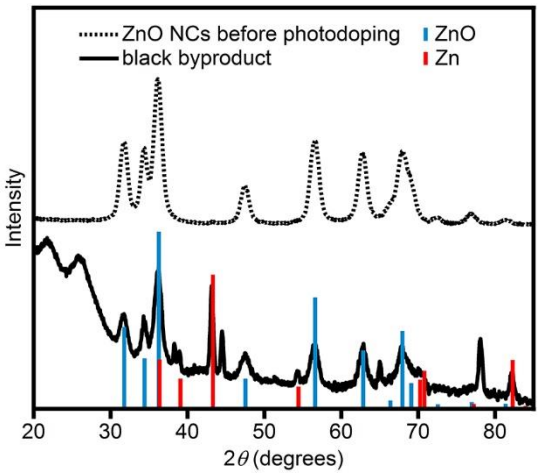

Figure D.7. Formation of Zn^0 metal detected by pXRD. pXRD spectra of r = 3.75 ZnO nanocrystals before photodoping (top spectrum, dotted black line) and of the black byproduct generated during photochemical doping with $Li[Et_3BH]$. The ZnO (blue) and Zn^0 (red) patterns are given for reference.

D.7 Stability of the photolysis lamp

The stability of the lamp used during the kinetics experiments was examined by monitoring the lamp output over time (data point taken every 10 s, averaged for 10 ms) using an Ocean Optics 2000+ fiber-coupled spectrometer. Figure D.8a shows the lamp intensity (integrated from 340-380 nm) as a function of time. Figure D.8b plots a histogram of the data in Figure D.8a. The black curve shows a Gaussian fit to the data (equation D.3), yielding a standard deviation that is ~8% of the mean. This difference is small compared to the differences in initial photodoping rates using EtOH and the hydride hole quenchers shown in Figure 3.5. Lamp intensity variations could possibly contribute to differences between initial photodoping rates among the different hydride hole quenchers or between those observed using EtOH with and without added $Li[PF_6]$.

$$y = y_0 + A\exp\left(-\frac{(x-x_0)^2}{2\sigma^2}\right) \tag{D.3}$$

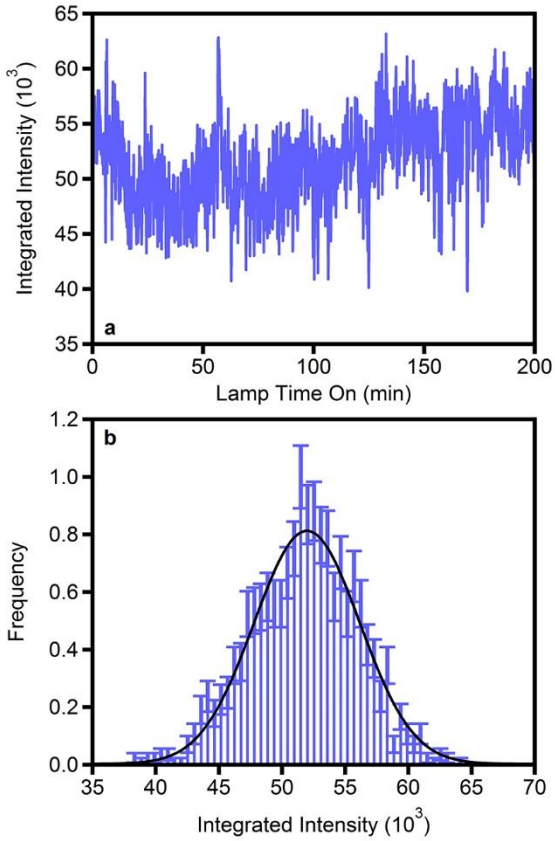

Figure D.8. Stability of the photolysis lamp used in photodoping. (a) Output of the UV photolysis lamp over time. Each data point represents the integrated intensity between 340−380 nm, averaged for 10 ms. A data point was collected every 10 s. (b) Histogram of data from (a). The solid black curve shows a Gaussian fit to the data, yielding a standard deviation that is ~8% of the mean.

D.8 References

1. Schrauben, J.; Hayoun, R.; Valdez, C.; Braten, M.; Fridley, L.; Mayer, J. Titanium and Zinc Oxide Nanoparticles Are Proton-Coupled Electron Transfer Agents. *Science* **2012**, *336*, 1298.

2. Liu, W. K.; Whitaker, K. M.; Smith, A. L.; Kittilstved, K. R.; Robinson, B. H.; Gamelin, D. R. Room-Temperature Electron Spin Dynamics in Free-Standing ZnO Quantum Dots. *Phys. Rev. Lett.* **2007**, *98*, 186804.

3. Wood, A.; Giersig, M.; Mulvaney, P. Fermi Level Equilibration in Quantum Dot-Metal Nanojunctions. *J. Phys. Chem. B* **2001**, *105*, 8810.

4. Schimpf, A. M.; Ochsenbein, S. T.; Buonsanti, R.; Milliron, D. J.; Gamelin, D. R. Comparison of Extra Electrons in Colloidal *n*-Type Al^{3+}-Doped and Photochemically Reduced ZnO Nanocrystals. *Chem. Commun.* **2012**, *48*, 9352.

5. Valdez, C. N.; Braten, M.; Soria, A.; Gamelin, D. R.; Mayer, J. M. Effect of Protons on the Redox Chemistry of Colloidal Zinc Oxide Nanocrystals. *J. Am. Chem. Soc.* **2013**, *135*, 8492.

6. Kushima, A.; Liu, X. H.; Zhu, G.; Wang, Z. L.; Huang, J. Y.; Li, J. Leapfrog Cracking and Nanoamorphization of ZnO Nanowires During In Situ Electrochemical Lithiation. *Nano Lett.* **2011**, *11*, 4535.

Appendix E

Supplementary Material for

Chapter 4: Photochemical Electronic Doping of CdSe Nanocrystals

Adapted from: Rinehart, J. D.; Schimpf, A. M.; Weaver, A. L.; Cohn, A. W.; Gamelin, D. R. *J. Am. Chem. Soc.* 2013, *135*, 18782.

E.1 Addition of Li[Et_3BH] to CdSe nanocrystals in the dark

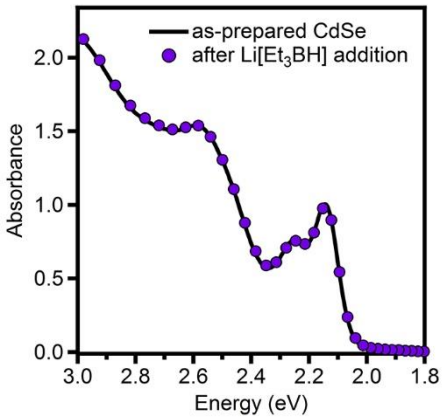

Figure E.1. Addition of Li[Et_3BH] to CdSe nanocrystals in the dark. Absorption spectra of d = 3.8 nm CdSe nanocrystals before and after the addition of Li[Et_3BH] but without exposure to light other than the spectrometer source used for the measurement of these spectra.

E.2. Gaussian deconvolution of the excitonic absorption bleach

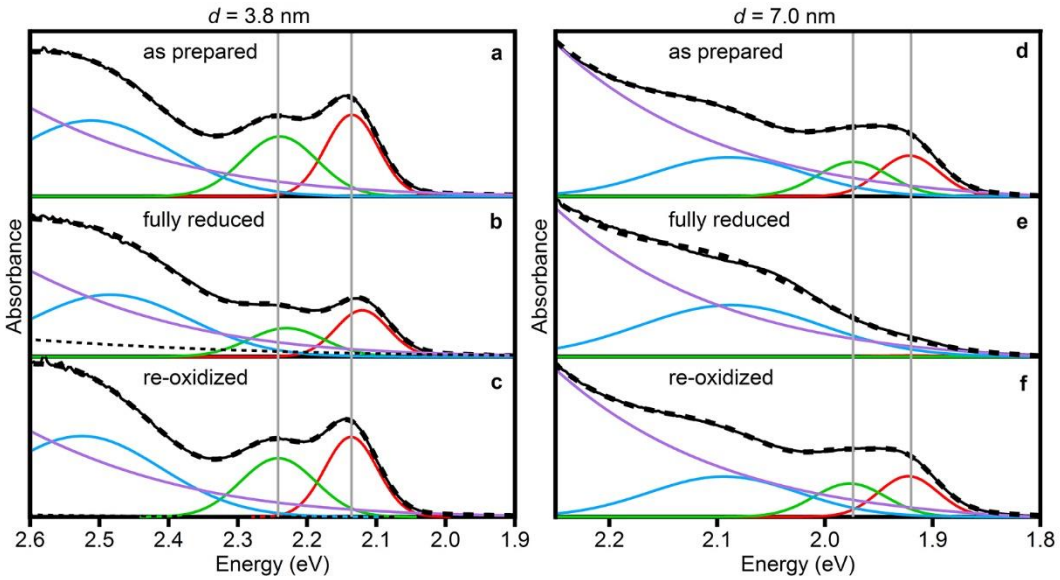

Figure E.2. Gaussian deconvolution of the excitonic absorption bleach in photodoped CdSe nanocrystals. Multi-Gaussian fits (thick black dashed) of absorption spectra (thin black) of d = 3.8 nm (a,b,c) and d = 7.0 nm (d,e,f) CdSe nanocrystals before photodoping (a,d), at maximum photodoping (b,e), and after re-oxidation (c,f). All absorption spectra are fitted with a sum of four Gaussians. The magnitudes, positions, and widths of the three lowest-energy Gaussians (red, green, blue) were allowed to float during fitting. The highest-energy Gaussian (purple) accounts for rising absorption in the high-energy region, and its amplitude, position, and width were fixed to be equal across all three panels for a given nanocrystal. The fitting of the smaller nanocrystals also incorporated a small additional Gaussian (thin black dashed) to account for the slight pre-edge tail that appears after photodoping.

E.3 Extinction coefficient of conduction-band electrons in CdSe nanocrystals

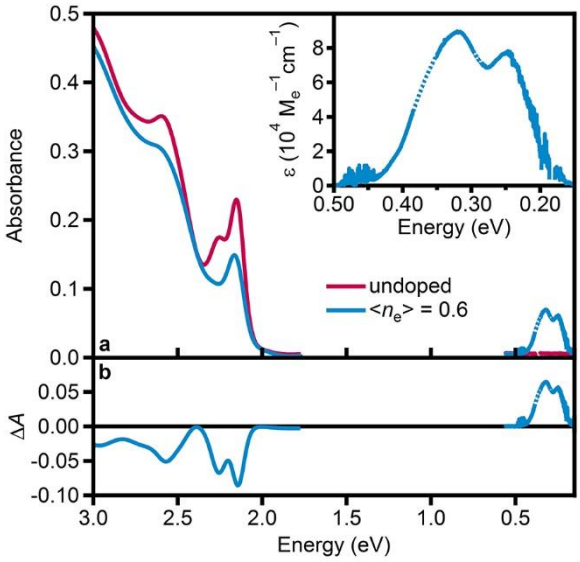

Figure E.3. Extinction coefficient of conduction-band electrons in CdSe nanocrystals. (a) Visible/IR absorption spectra for undoped (purple) d = 3.8 nm CdSe nanocrystals and the same nanocrystals photodoped to $\langle n_e \rangle$ = 0.6 electrons per nanocrystal (blue). Regions of intense C-H and CO_2 vibrational absorption are interpolated (dotted lines). (b) Difference spectra ($\Delta A = A_{\text{photodoped}} - A_{\text{as-prepared}}$), from the spectra in (a). Inset: Extinction coefficient plot for the IR absorption in units of $M_e^{-1}cm^{-1}$, where M_e is the molar concentration of conduction-band electrons. The per-electron molar extinction coefficient for the IR absorption maximum in these nanocrystals is $8.9 \pm 0.6 \times 10^4$ $M_e^{-1}cm^{-1}$ at 0.32 eV. Note that this extinction coefficient is for this specific nanocrystal diameter, because the spectrum changes with nanocrystal diameter (Figure 4.1).

E.4 Titrations on photodoped CdSe nanocrystals

For comparison with numbers determined by fitting of the optical bleach, the average number of excess electrons per nanocrystal ($\langle n_{max} \rangle$) was determined by titration against $[FeCp^*_2][BAr_F]$.[1-4] Direct reaction of $[FeCp^*_2][BAr_F]$ with excess $Li[Et_3BH]$ was found to be slow compared to the nanocrystal oxidation, ruling out the possibility of anomalously large electron counts due to the titration method. Additionally, a nanocrystal-catalyzed reaction of $[FeCp^*_2][BAr_F]$ with excess $Li[Et_3BH]$ can be ruled out because both d = 3.8 and 4.6 nm

nanocrystals showed much lower electron counts than the d = 7.0 nm nanocrystals despite similar concentrations of Li[Et_3BH].

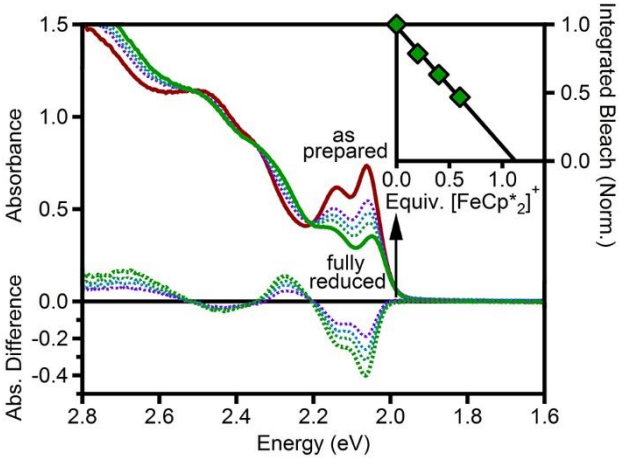

Figure E.4. Titration of small photodoped CdSe nanocrystals. Absorption spectra of d = 4.6 nm (10.6 μM) CdSe nanocrystals collected during redox titration in 1:1 toluene/THF. The red spectrum shows data collected before introduction of Li[Et_3BH]. The solid green spectrum is of the maximally photodoped nanocrystals. The other spectra were collected following addition of various amounts of $[FeCp^*_2]^+$ (increasing with direction of arrow). The corresponding difference spectra ($A_{photodoped} - A_{as\text{-}prepared}$) are plotted as dotted lines. Inset: The integrated absorption bleach of the first excitonic feature as a function of equivalents of $[FeCp^*_2]^+$. The solid line shows a linear fit to the data. The crossing of this line with zero indicates the equivalence point, corresponding to 1.1 electrons per nanocrystal.

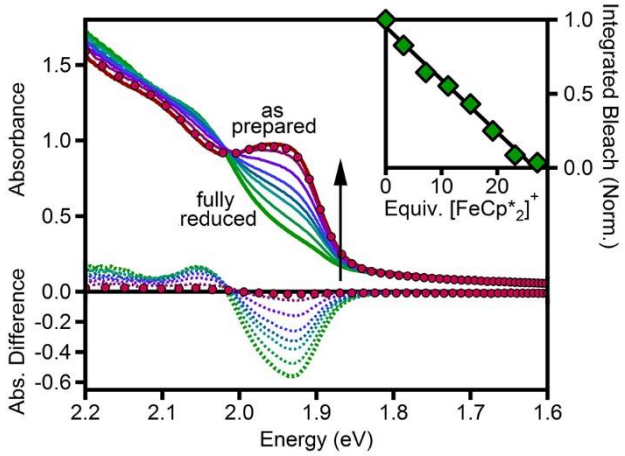

Figure E.5. Titration of large photodoped CdSe nanocrystals. Absorption spectra of d = 7.0 nm (4.4 μM) CdSe nanocrystals collected during redox titration in 1:1 toluene/THF. The red spectrum shows data collected before introduction of Li[Et_3BH]. The solid green spectrum is of the maximally photodoped nanocrystals. The other spectra were collected following addition of various amounts of $[FeCp^*_2]^+$ (increasing with direction of arrow). The red circles show the solution after reoxidation with air. The corresponding difference spectra ($A_{photodoped} - A_{as\text{-}prepared}$) are plotted as dotted lines. Inset: The integrated absorption bleach of the first excitonic feature as a function of equivalents of $[FeCp^*_2]^+$. The solid line shows a linear fit to the data. The crossing of this line with zero indicates the equivalence point, corresponding to 27 electrons per nanocrystal.

E.4.1 Effect of storage environment on titration results. Figure G.6 shows the absorption bleach and titration data for two sets of the same nanocrystal batch with different handling/storage. Sample A (red) was stored immediately in the N_2 glove box, while sample B was stored in air until the titration measurement. The absorption data for the two samples before and after photodoping are essentially indistinguishable, but the titration data show a significant difference in the number of electrons retrieved from these nanocrystals (~7 electrons/nanocrystal more in sample B). These data support the conclusion that the absorption bleach reports on the delocalized conduction electrons, whereas the chemical titration is also sensitive to other (trapped) electrons.

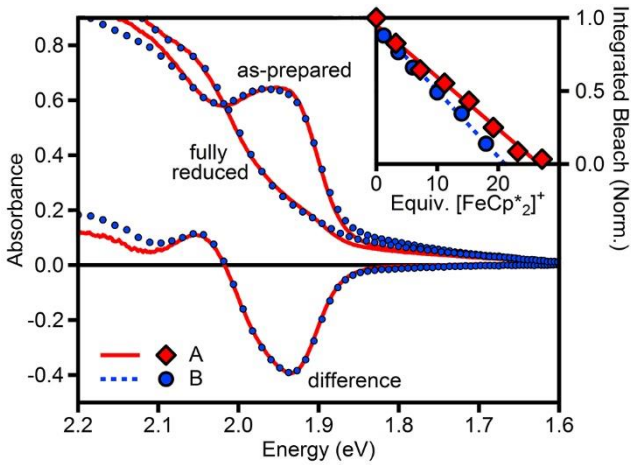

Figure E.6. Effects of storage environment on titration results. Absorption spectra and titration data for two different sets of the same d = 7.0 nm (4.4 μM) CdSe nanocrystals with different storage/handling histories.

E.5 ZnSe shell growth

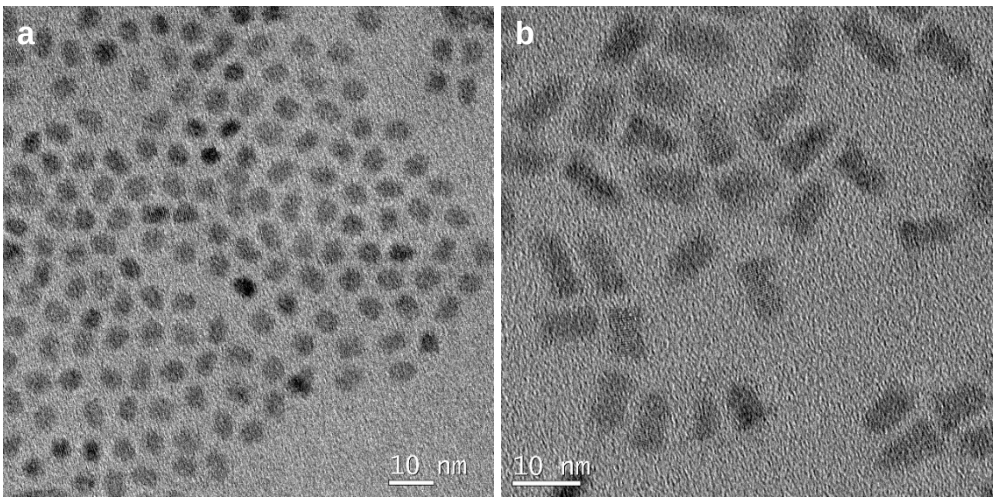

Figure E.7. Representative TEM images of core and core/shell CdSe and CdSe/ZnSe nanocrystals. (a) 4.6 nm CdSe nanocrystals and (b) the same nanocrystals with a ZnSe shell. Because of shape anisotropy, an average shell thickness was estimated by distributing the total shell volume equally around the central CdSe core. Core/shell volumes were modeled as rectangular cuboids with $a = b < c$, estimated from TEM data.

E.6 Extension of photodoping methods to other nanocrystal systems

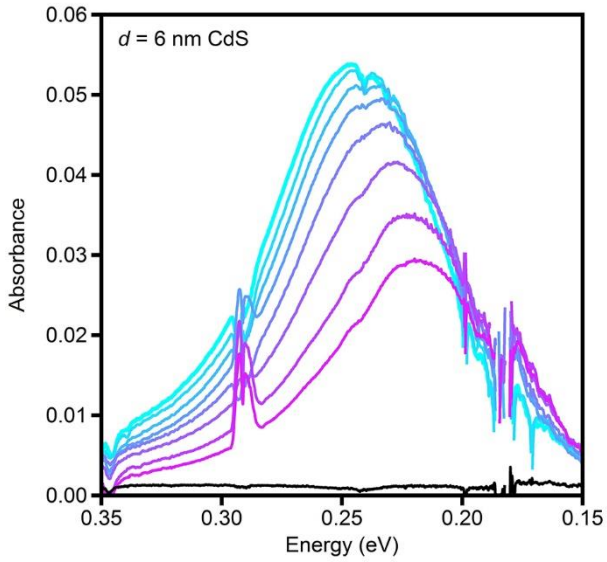

Figure E.8. Photodoping in CdS nanocrystals observed by IR absorption. IR spectra demonstrating the introduction of electrons into the conduction band of a 1:1 THF:toluene CdS nanocrystal colloidal suspension after introduction of Li[Et_3BH] and incremental exposure to 405 nm light.

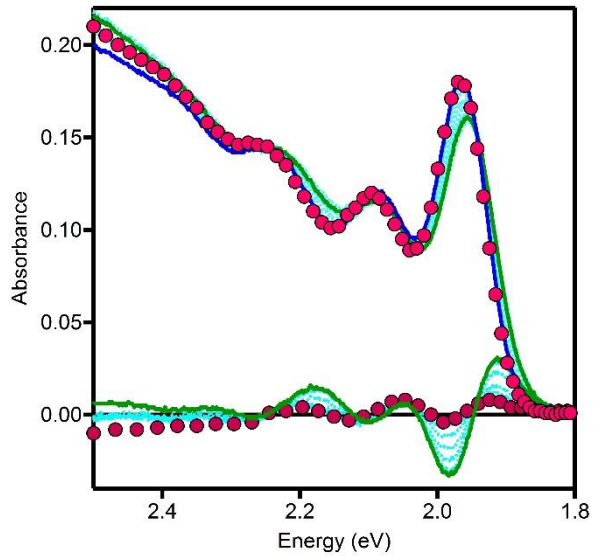

Figure E.9. Photodoping in CdTe nanocrystals observed by exciton bleach. Absorption spectra of CdTe (d = 4 nm) in THF solution (1 μM) as prepared (blue line), after addition of 40 equivalents of Li[Et_3BH] and $\lambda > 450$ nm light exposure (dotted blue and green lines), and after reoxidation in air (red circles). Difference spectra of matching colors are shown below.

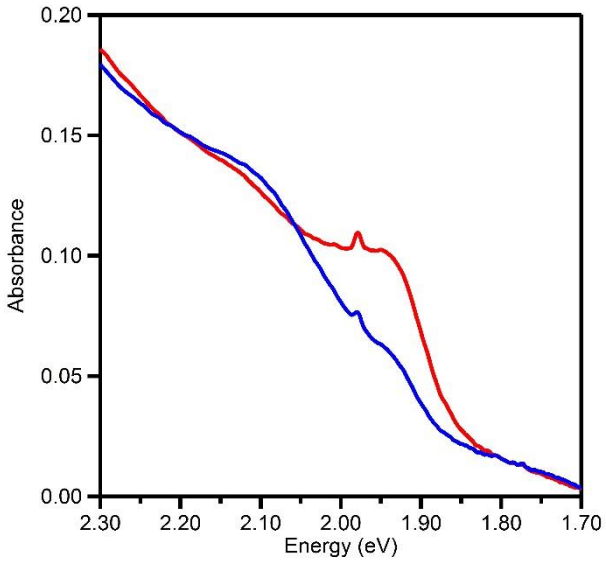

Figure E.10. Photodoping of CdSe nanocrystal films. Absorption spectra of d = 7.0 nm quantum dot film on FTO maximally photodoped (blue) and reoxidized (red). The small sharp peak at ~1.98 eV is due to film reflections.

E.7 References

1. Rinehart, J. D.; Schimpf, A. M.; Weaver, A. L.; Cohn, A. W.; Gamelin, D. R. Photochemical Electronic Doping of Colloidal CdSe Nanocrystals. *J. Am. Chem. Soc.* **2013**, *135*, 18782.

2. Schimpf, A. M.; Gunthardt, C. E.; Rinehart, J. D.; Mayer, J. M.; Gamelin, D. R. Controlling Carrier Densities in Photochemically Reduced Colloidal ZnO Nanocrystals: Size Dependence and Role of the Hole Quencher. *J. Am. Chem. Soc.* **2013**, *135*, 16569.

3. Schimpf, A. M.; Ochsenbein, S. T.; Buonsanti, R.; Milliron, D. J.; Gamelin, D. R. Comparison of Extra Electrons in Colloidal *n*-Type Al^{3+}-Doped and Photochemically Reduced ZnO Nanocrystals. *Chem. Commun.* **2012**, *48*, 9352.

4. Schrauben, J.; Hayoun, R.; Valdez, C.; Braten, M.; Fridley, L.; Mayer, J. Titanium and Zinc Oxide Nanoparticles Are Proton-Coupled Electron Transfer Agents. *Science* **2012**, *336*, 1298.

Appendix F

Supplementary Material for

Chapter 5: Photodoped In_2O_3 and Sn-doped In_2O_3 Nanocrystals

Adapted from: Schimpf, A. M.; Lounis, S. D.; Runnerstrom, E. L.; Milliron, D. J.; Gamelin, D. R. *J. Am. Chem. Soc.* **2014**, *Accepted Manuscript*, doi: 10.1021/ja5116953.

F.1 Absorption of In_2O_3 and ITO nanocrystals

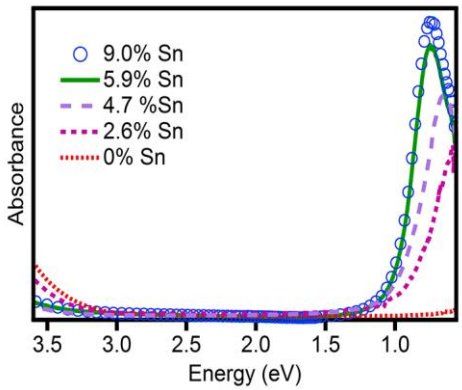

Figure F.1. Absorption spectra of In_2O_3 nanocrystals containing various Sn dopant concentrations.

F.2 Oxidation of ITO nanocrystals with $(NH_4)_2Ce(NO_3)_6$

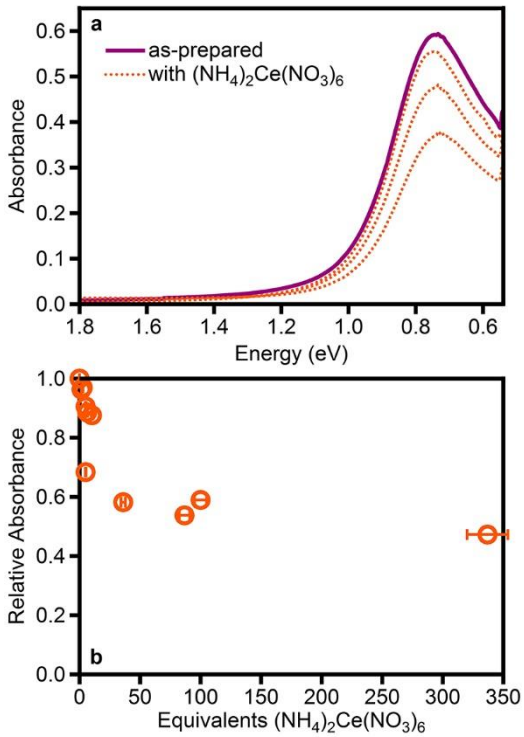

Figure F.2. Oxidation of ITO nanocrystals with $(NH_4)_2Ce(NO_3)_6$. (a) Absorption spectra of 5.9% Sn-doped In_2O_3 nanocrystals (top purple, 0.6 mM in heptane) with various amounts of added $(NH_4)_2Ce(NO_3)_6$ (dotted orange). (b) Plot of relative LSPR absorption versus equivalents of added $(NH_4)_2Ce(NO_3)_6$. Even with a large excess of this strong oxidant, some electrons remained in the ITO nanocrystals.

F.3 Evidence for electron transfer between In_2O_3 and ITO nanocrystals

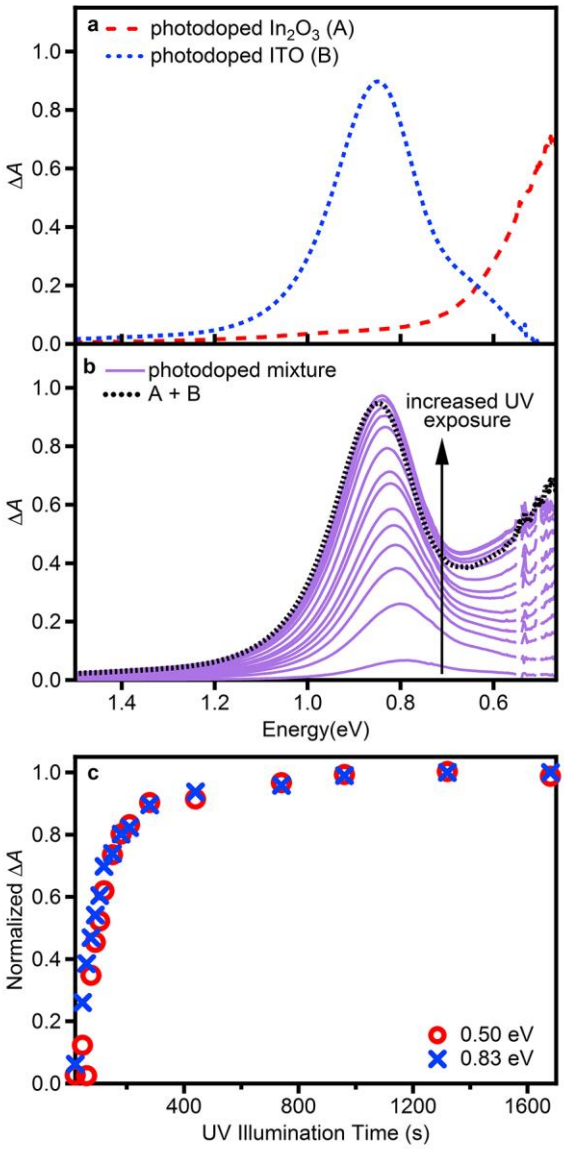

Figure F.3. Simultaneous photodoping of a mixture of In_2O_3 and ITO nanocrystals. (a) In_2O_3 (dashed red) and 9.0% Sn-doped In_2O_3 (dotted blue) nanocrystals photodoped to their maximum extents (both ~1 μM in 1:1 toluene/THF). The spectra are plotted as the difference in absorption from the as-prepared nanocrystals ($\Delta A = A_{\text{photodoped}} - A_{\text{as-prepared}}$). (b) Mixture of the nanocrystals from panel (a), photodoped together (purple). The arrow shows increased UV exposure. The dotted black line represents the numerical summation of the two nanocrystal absorption spectra after photodoping each to its maximum extent individually. (c) Plot of the absorption (normalized) at 0.50 eV and at 0.83 eV measured as a function of time. Absorption from both nanocrystals increases concurrently.

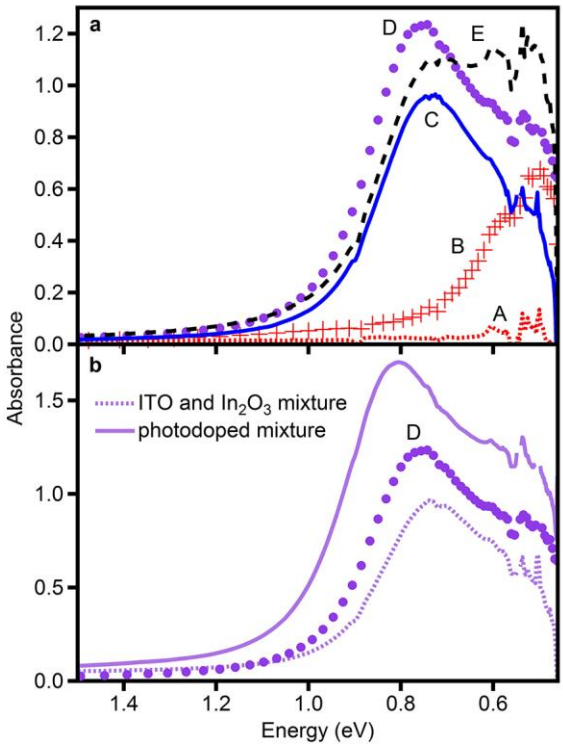

Figure F.4. Electron transfer between In_2O_3 and ITO nanocrystals. (a) Reproduced from Figure 5.3b. Absorption spectra of: (A) As-prepared In_2O_3 nanocrystals (1μM in 1:1 toluene/THF with ~3×10^5 equivalents EtOH, anaerobic); (B) The same nanocrystals after maximal photodoping; (C) As-prepared 9.0% Sn:In_2O_3 nanocrystals; (D) After adding one equivalent of maximally photodoped In_2O_3 nanocrystals to a solution of as-prepared 9.0% Sn:In_2O_3 nanocrystals. Spectrum E is a numerical summation of absorption spectra B and C. (b) Spectra of a mixture of as-prepared ITO and In_2O_3 nanocrystals before (dotted) and after (solid) maximal concurrent photodoping. The absorption spectrum of as-prepared ITO nanocrystals added to maximally photodoped In_2O_3 nanocrystals (spectrum D from part (a)) falls roughly halfway between the two endpoints, confirming electron equilibration between the ITO and In_2O_3 nanocrystals in part (a).

F.4 Absorption of ITO-PLMA films

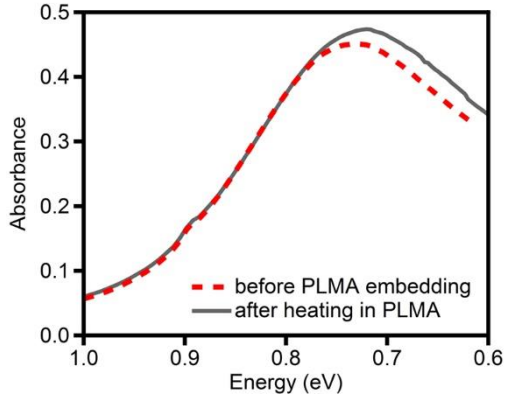

Figure F.5. LSPR absorption in solution versus films. Room-temperature absorption spectra of 9.0% Sn-doped In_2O_3 nanocrystals before (dashed red) and after (solid gray) incorporation into a PLMA matrix.

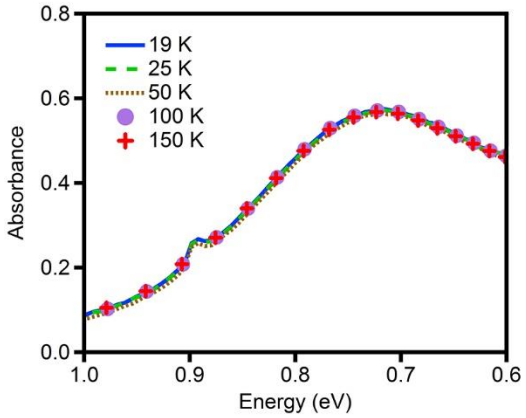

Figure F.6. Variable-temperature absorption spectra of ITO nancrystals. Absorption of 9.0% Sn-doped In_2O_3 nanocrystals embedded in a PLMA matrix.

F.5 Variable-temperature magnetic circular dichroism of ITO nanocrystals

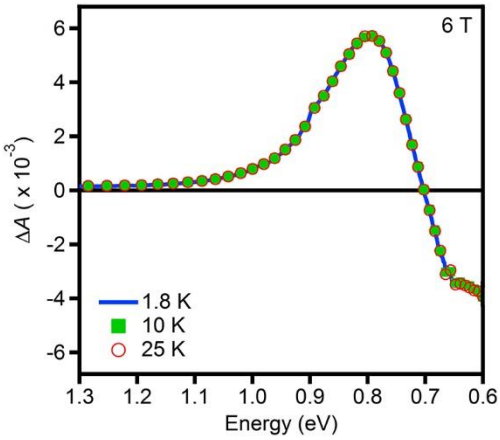

Figure F.7. Variable-temperature magnetic circular dichroism of ITO nancrystals. MCD spectra of 9.0% Sn-doped In_2O_3 nanocrystals embedded in a PLMA matrix.

Appendix G

Supplementary Material for

Chapter 6: Charge-Tunable Quantum Plasmons in Colloidal Semiconductor Nanocrystals

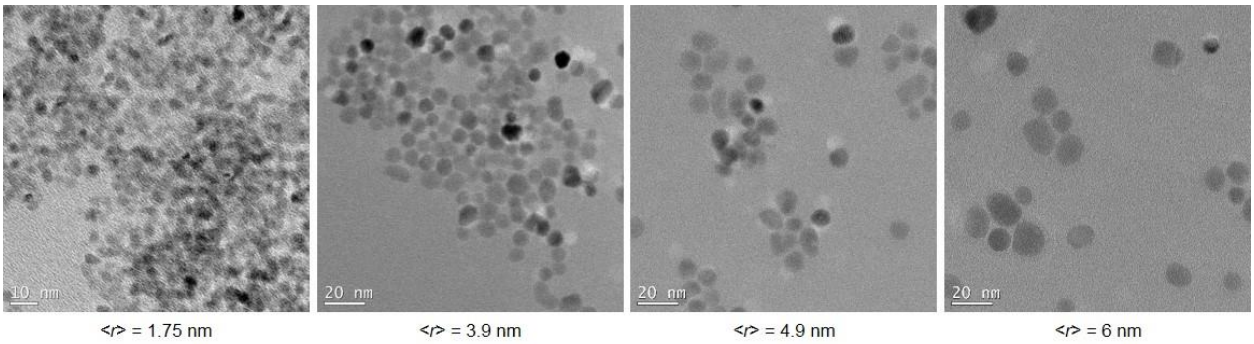

Figure G.1. Representative TEM Images of colloidal ZnO nanocrystals of various sizes.

G.1 Determination of electron densities

Electron densities in photodoped ZnO nanocrystals have been determined via titration against a mild oxidant, as described in detail in Appendix B.[1-5] Figure G.2 illustrates representative titration data, from which carrier densities were determined. A solution of 3.7 μM r = 6 nm ZnO nanocrystals was anaerobically prepared in 1:1 toluene/THF with EtOH as the hole quencher. The solution was illuminated with UV light and the NIR absorption monitored until it stopped increasing, at which point the nanocrystals are considered to be maximally photodoped. Figure G.2a shows the NIR absorption tail of the maximally photodoped nanocrystals (top spectrum). To the maximally photodoped nanocrystals, aliquots of 8 mM $[FeCp^*_2][BAr_F]$ were added. Electron transfer from the photodoped ZnO nanocrystals to $[FeCp^*_2]^+$ (equation G.1, Figure G.2a inset) results in a decrease of the NIR absorption.[3-5] When all of the electrons are removed, the

reaction described by equation G.1 no longer proceeds, and growth of $[FeCp^*_2]^+$ absorption centered around 1.75 eV is observed (Figure F.2b). Figure G.2c plots the decrease in ZnO NIR absorption (integrated intensity, 0.9–1.5 eV) and the growth in $[FeCp^*_2]^+$ absorption as a function of added equivalents of $[FeCp^*_2][BAr_F]$. The solid lines show linear fits to the data. The *x*-intercepts of these lines determine the equivalence point. The values determined by the two *x*-intercepts are averaged, and their values used to determine uncertainties in the number of electrons per nanocrystal. In this case, 116 ± 22 electrons were added to the r = 6 nm ZnO nanocrystals, corresponding to an electron density of $1.3 \pm 0.3 \times 10^{20}$ cm^{-3}.

$$e^-_{CB}:ZnO + [FeCp^*_2]^+ \rightarrow ZnO + [FeCp^*_2] \quad (G.1)$$

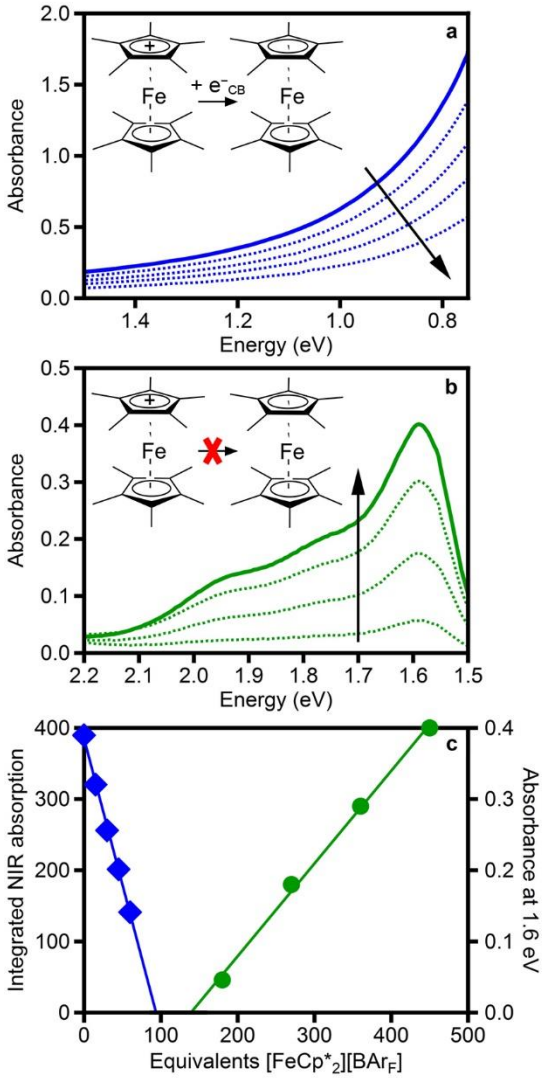

Figure G.2. Representative titration data for photodoped ZnO nanocrystals. (a) Reduction of the ZnO NIR absorption due to electron transfer from the photodoped ZnO nanocrystals to $[FeCp^*_2]^+$. (b) Growth of absorption due to excess $[FeCp^*_2]^+$, after all ZnO electrons have been removed. (c) Plot of the decrease in NIR absorption (blue diamonds) and increase in $[FeCp^*_2]^+$ absorption (green circles) versus added equivalents of $[FeCp^*_2][BAr_F]$. ZnO nanocrystals are 6 nm in radius. The solid lines are linear fits to the data and their *x*-intercepts determine the equivalence point.

Figure G.3 plots the maximum number of electrons that can be added to various sized ZnO nanocrystals by photochemical reduction using EtOH as the hole quencher, titrated as described above (adapted from ref. 5). The maximum photodoping level scales with nanocrystal volume,

meaning that *all sizes of nanocrystals reach the same electron density*, determined to be 1.4 ± 0.4 × 10^{20} cm^{-3}. The solid line plots equation G.2 for N_e = 1.4 × 10^{20} cm^{-3}.

$$n_e = N_e V = N_e \frac{4}{3}\pi r^3 \tag{G.2}$$

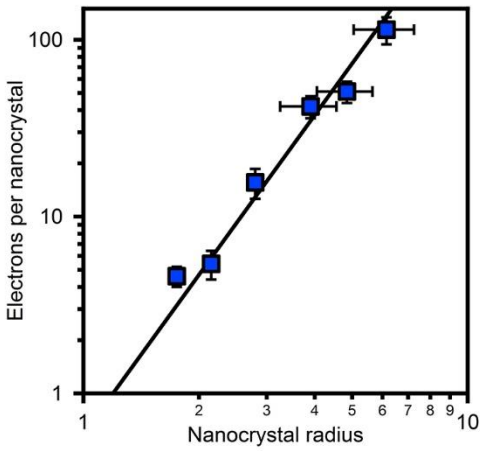

Figure G.3. Size dependence of photodoping in ZnO nanocrystals. Maximum number of electrons that can be added to ZnO via photodoping using EtOH as the hole quencher, plotted as a function of nanocrystal radius. The solid line plots the number of electrons per nanocrystal at a fixed electron density of 1.4 × 10^{20} cm^{-3}. Adapted from ref. 5.

G.2 Dependence of IR absorption energy on size and electron density

Figure G.4a plots the IR absorption peak energy (purple squares) as a function of electron density for colloidal r = 6 ± 1 nm nanocrystals (top spectrum, Figure 6.1). From Figure G.3, the maximum photodoping is 1.4 ± 0.4 × 10^{20} cm^{-3}, and the electron densities of the other spectra were estimated by equation G.3, where I is the integrated absorption intensity from 0.14–0.50 eV (excluding regions of intense absorption from ligand or solvent). The error bars in electron density are based on the 20% error for the maximum photodoping level. The error bars in peak energy are set at 5% based on the breadth of the absorption band. The black line plots the peak energy calculated for various electron densities from the Drude model (equation 6.1). It should

be noted that the spectral integration range does not encompass the entire IR absorption band. The lowest electron densities are thus lower limits to the actual electron densities.

$$N_e = \frac{I}{I_{\text{maximally doped}}} \times N_{\text{maximally doped}} \tag{G.3}$$

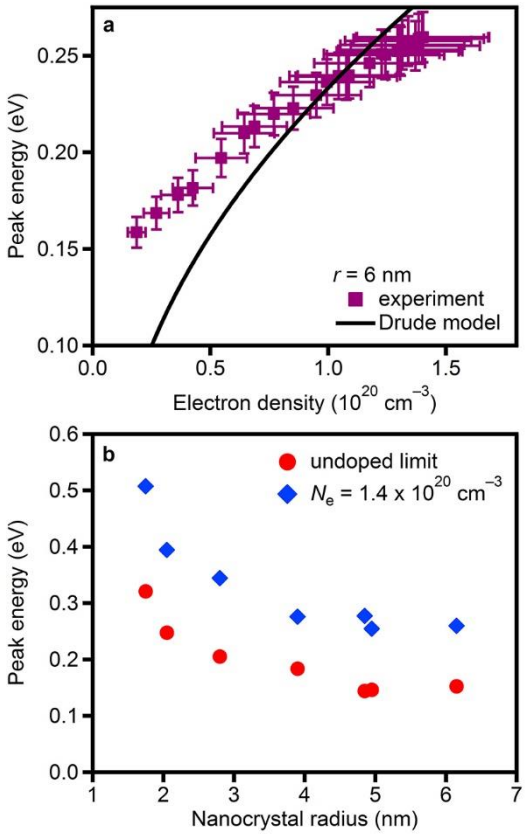

Figure G.4. Size- and electron-dependence of the IR absorption in photodoped ZnO nanocrystals. (a) IR absorption maximum (purple squares) as a function of electron density for r = 6 nm ZnO nanocrystals. The black line shows the dependence predicted by the Drude model (equation 1). (b) Size dependence of the IR absorption peak maxima for ZnO nanocrystals photodoped to an electron density of 1.4 ± 0.4 × 10^{20} cm^{-3} (blue diamonds) and in the low electron density limit (red circles).

Figure G.4b plots IR absorption peak energies versus radius for photodoped ZnO nanocrystals with N_e = 1.4 ± 0.4 × 10^{20} cm^{-3} (blue diamonds) and in the low-photodoping limit

(red circles). This low-electron-density limit was estimated by plotting the peak energy versus electron density and determining the *y*-intercept.

G.4 Magnetic circular dichroism spectroscopy

Figure G.5a shows the 2 K MCD spectra for the same nanocrystals as in Chapter 6. The difference in intensity is attributed to depolarization induced by sample freezing. Once frozen, the sample shows no temperature dependence (Figure G.5b).

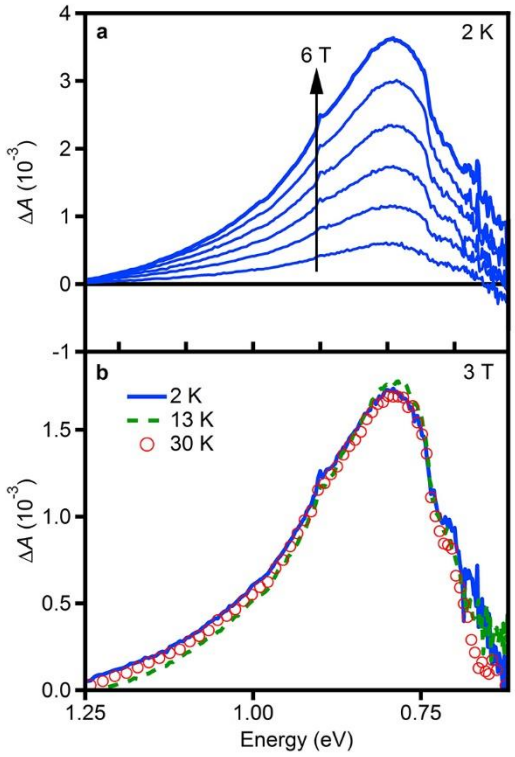

Figure G.5. Temperature-independent magnetic circular dichroism in photodoped ZnO. (a) 2 K MCD spectra of photodoped r = 1.55 nm ZnO nanocrystals. The arrow indicates increasing magnetic field. (b) 3 T MCD spectra collected at three temperatures, illustrating temperature independence of this MCD signal.

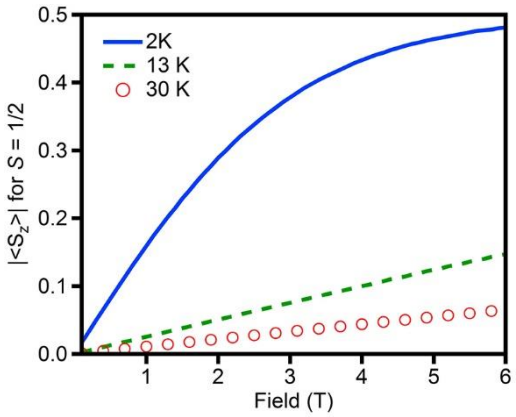

Figure G.6. Calculated spin expectation values for an *S* = ½ paramagnet as a function of applied magnetic field. Plotted at the three temperatures used in Figure G.5b. *C*-term MCD intensities are proportional to spin expectation value. The lack of temperature dependence in Figure G.5b indicates that this MCD intensity does not come from the *C*-term mechanism.

G.5 Theoretical model

Resonance behavior in photodoped ZnO quantum dots is modeled by constructing a quantum-mechanically modified Lorentz approximation to the dielectric function.[6] This process begins at the single electron level, where electron response to an external electric field is modeled as a damped and driven harmonic oscillator. Thus, the equation of motion for a single electron is specified via Newton's Second Law as

$$\ddot{x} + \gamma \dot{x} + \omega_0^2 x = \frac{1}{m} F(x,t) \qquad \text{(G.4)}$$

where ω_0 is the resonance frequency of the restoring force and γ is the measure of damping force (known as the scattering frequency, see Chapter 6 for details). Classically, the driving force is dependent only on the electric field of the incident photon, generally taken to be a plane wave. However, boundary effects, due to the confined nature of the nanocrystals, serve to give the system preferential modes similar to modes found in classical waveguides. This modal structure both discretizes the set of available resonance frequencies in the restoring force and modifies the

strength of the driving force. These effects are treated quantum mechanically and separately, but they modify the equation of motion above. Then,

$$\ddot{\mathrm{x}}+\gamma\dot{\mathrm{x}}+\omega_0^2\mathrm{x}=\frac{e}{m}\mathrm{S}_{if}\mathrm{E}(\mathrm{x})e^{-i\omega t} \tag{G.5}$$

where *i* and *f* are composite indices representing the quantum numbers associated with some initial and some final state, respectively. This equation can be solved in the frequency domain and simply summed to model a system of many, non-interacting electrons. In that case, the dielectric function is written as

$$\varepsilon(\omega)=\varepsilon_{\mathrm{IB}}(\omega)-\omega_{\mathrm{p}}^2\sum_{i,f}\frac{S_{if}}{\omega^2+i\gamma\omega-\omega_{if}^2} \tag{G.6}$$

where ω_{p} is the bulk plasma frequency and $\varepsilon_{\mathrm{IB}}(\omega)$ represents contributions from interband transitions. In ZnO, interband transitions occur far from the near-IR plasmons, and are expected to have little contribution to the dielectric function in this region. We thus replace $\varepsilon_{\mathrm{IB}}(\omega)$ with ε_∞.

A quantum model of a ZnO nanocrystal is required to specify parameters in the equation above. TEM images show that the quantum dots are quasi-spherical, motivating the choice to model the conduction electrons as a degenerate Fermi gas in an infinite, spherical potential well of radius *R*. In that case, single electron wave functions are known to be

$$\psi_{n,l,m}(\mathrm{x})=j_l(\kappa r)Y_{lm}\left(\hat{r}\right),\quad r<R. \tag{G.7}$$

Here, j_l is the *l*th spherical Bessel function, κ is the wavenumber ($\kappa=x_{n,l}/R$, where $x_{n,l}$ is the *n*th root of the *l*th spherical Bessel function) and Y_{lm} is a spherical harmonic. The set (n,l,m) is a given state's principle, angular, and projection quantum numbers.

For the semi-conductor case, the number of electrons in the conduction band is, compared to a conductor, relatively small, and this limits the angular quantum number, *l*, accordingly. In this case, using the Lorch lower bound[7] for $x_{n,l}$, one can show that $\kappa r > l$ and, thus,

$$\psi_{n,l,m} \approx \frac{2}{\sqrt{R}} \frac{\sin\left(\kappa r - (l+1)\frac{\pi}{2}\right)}{r} Y\left(\hat{r}\right). \tag{G.8}$$

Meanwhile, eigenvalues of the spherical potential well specify single-electron energies. Thus, the discretized set of resonance frequencies, ω_{if}, is

$$\omega_{if} = \frac{E_f - E_i}{\hbar} \approx \frac{\hbar\pi^2}{8m_e r^2}\left[\left(2n_f + l_f + 2\right)^2 - \left(2n_i + l_i + 2\right)^2\right]. \tag{G.9}$$

Finally, the interaction strengths, S_{if}, are computed using the well-known Thomas-Reiche-Kuhn sum rules. The expression used for the harmonic oscillator is

$$S_{if} = \frac{2m_e\omega_{if}}{\hbar n_e}\left|\left\langle f\left|z\right|i\right\rangle\right|^2, \tag{G.10}$$

where the matrix element above is simply the integral

$$\left\langle f\left|z\right|i\right\rangle = \int \psi_f^* r\cos\theta\psi_i \mathrm{d}^3x. \tag{G.11}$$

Thus, contributions to the sum in equation S6 can, using the quantum mechanically derived equations above, be computed as needed. The quantum numbers that contribute most to the physics are dependent on the Fermi level, n_F. Computation of the Fermi level is described in the paper and amounts to finding the roots of a cubic polynomial. Given a Fermi level, all other quantum numbers have specified ranges:[8,9]

$$|\Delta l| = 1$$
$$\frac{1-\Delta l}{2} \le \Delta n \le n_{\mathrm{F}}$$
$$0 \le n_i \le n_{\mathrm{F}} - \frac{1-\Delta l}{2}$$
$$2\left(n_{\mathrm{F}} - n_i - \Delta n + \frac{1-\Delta l}{2} \right) \le l \le 2\left(n_{\mathrm{F}} - n_i \right)$$

where $\Delta l = l_f - l_i$ and $\Delta n = n_f - n_i$.

The absorption efficiencies for the dielectric functions were calculated as the ratio of the diffractive absorption cross section to the geometric cross section and normalized at each radius:

$$Q_{\mathrm{abs}}(\omega) = \frac{4\pi k}{\pi r^2} \mathrm{Im}\left\{ r^3 \frac{\varepsilon(\omega) - \varepsilon_{\mathrm{m}}}{\varepsilon(\omega) + 2\varepsilon_{\mathrm{m}}} \right\}. \tag{G.12}$$

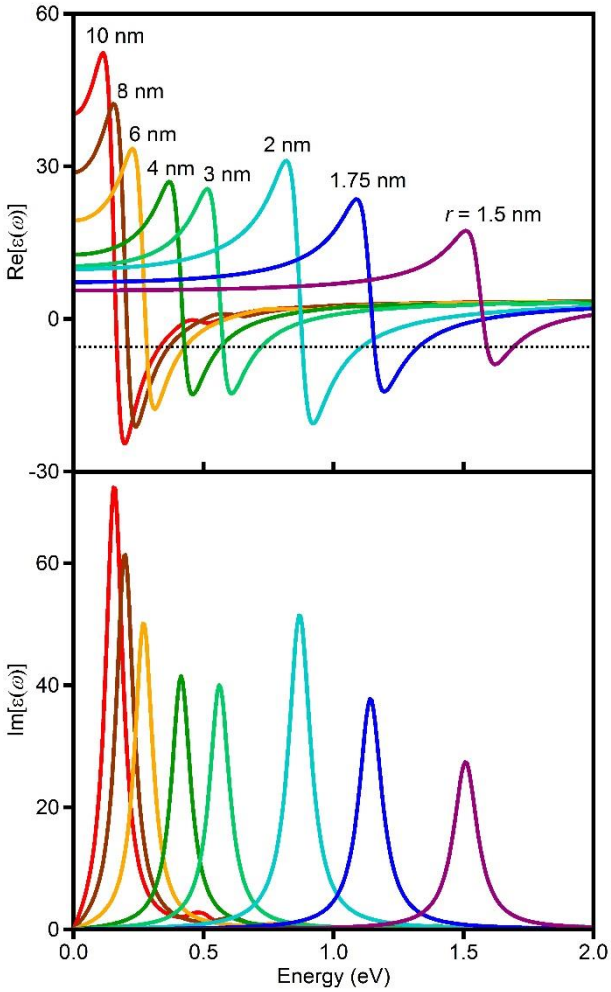

Figure G.7. Calculated spectral dependences of the ZnO dielectric function for various nanocrystal radii. (a) real (reproduced from Figure 6.4a) and (b) imaginary parts The imaginary parts are smaller for solutions of $\mathrm{Re}[\varepsilon(\omega)] = -2\varepsilon_m$ in regions of normal dispersion, as opposed to those in regions of anomalous dispersion, validating the former as the proper solutions**.**

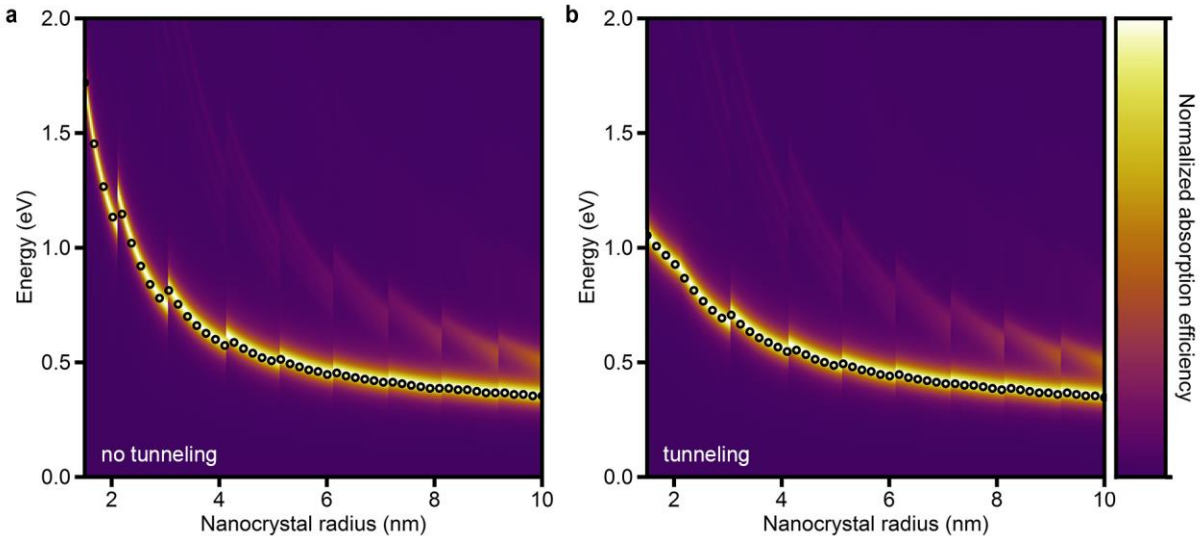

Figure G.8. Effects of electron tunneling on LSPR energies. Comparison of calculated LSPR energies (a) without and (b) with inclusion of a phenomenological tunneling ("spill-out") parameter. Panel (a) is the same as Figure 6.4b. Panel (b) has been calculated modeling the ZnO nanocrystals with effective radii of $r_{eff} = r(1 + C^2/r^2)$,[10] where C is a fit parameter chosen to be 1 nm, to illustrate the effect of tunneling beyond the nanocrystal surface. This r_{eff} was not used in calculation of the Fermi level in order to keep the same number of conduction-band electrons for calculations with and without tunneling. The effect of tunneling is to make the smallest nanocrystals effectively larger and weaken the LSPR size dependence. This description of tunneling is arbitrary and is solely intended to illustrate the general effect of introducing spill-out into the model. In reality, tunneling is only one of several factors neglected in the idealized model of Chapter 6 that could prove significant.

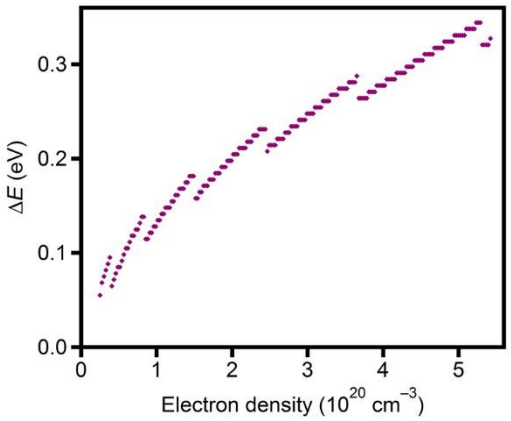

Figure G.9. Convergence of LSPR and single-electron transitions and low carrier densities. Calculated difference between LSPR and dominant single-electron transition energies ($\Delta E = \hbar(\omega_{sp} - \omega_{if})$) as a function of electron density in an r = 6 nm ZnO nanocrystal. These results demonstrate convergence of the two types of transitions in the low-carrier-density limit. The calculations use the parameters described in Chapter 6.

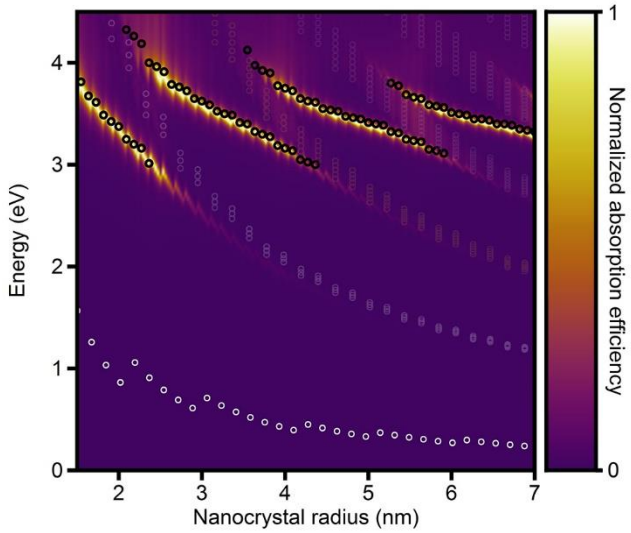

Figure G.10. Calculated absorption efficiencies for Ag nanoparticles. The single-electron transitions are shown as white circles, with opacities proportional to their oscillator strengths. The LSPRs are plotted in open black circles. Discontinuities in the curve of highest absorption efficiency are a result of our approximate shell-filling scheme. This figure illustrates that LSPRs in Ag, and metal nanoparticles in general, are spectrally remote from the most allowed single-electron transitions.

G.6 References

1. Wood, A.; Giersig, M.; Mulvaney, P. Fermi Level Equilibration in Quantum Dot-Metal Nanojunctions. *J. Phys. Chem. B* **2001**, *105*, 8810.

2. Liu, W. K.; Whitaker, K. M.; Smith, A. L.; Kittilstved, K. R.; Robinson, B. H.; Gamelin, D. R. Room-Temperature Electron Spin Dynamics in Free-Standing ZnO Quantum Dots. *Phys. Rev. Lett.* **2007**, *98*, 186804.

3. Schrauben, J.; Hayoun, R.; Valdez, C.; Braten, M.; Fridley, L.; Mayer, J. Titanium and Zinc Oxide Nanoparticles Are Proton-Coupled Electron Transfer Agents. *Science* **2012**, *336*, 1298.

4. Schimpf, A. M.; Ochsenbein, S. T.; Buonsanti, R.; Milliron, D. J.; Gamelin, D. R. Comparison of Extra Electrons in Colloidal *n*-Type Al^{3+}-Doped and Photochemically Reduced ZnO Nanocrystals. *Chem. Commun.* **2012**, *48*, 9352.

5. Schimpf, A. M.; Gunthardt, C. E.; Rinehart, J. D.; Mayer, J. M.; Gamelin, D. R. Controlling Carrier Densities in Photochemically Reduced Colloidal ZnO Nanocrystals: Size Dependence and Role of the Hole Quencher. *J. Am. Chem. Soc.* **2013**, *135*, 16569.

6. Dressel, M.; Grüner, G. *Electrodynamics of Solids*; Cambridge University Press: United Kingdom, 2002.

7. Qu, C. K.; Wong, R. "Best Possible" Upper and Lower Bounds for the Zeros of the Bessel Function. *Trans. Amer. Math. Soc.* **1999**, *351*, 2833.

8. Genzel, L.; Martin, T. P.; Kreibig, U. Dielectric Function and Plasma Resonances of Small Metal Particles. *Z. Phys. B Con. Mat.* **1975**, *21*, 339.

9. Scholl, J. A.; Koh, A. L.; Dionne, J. A. Quantum Plasmon Resonances of Individual Metallic Nanoparticles. *Nature* **2012**, *483*, 421.

10. Monreal, R. C.; Antosiewicz, T. J.; Apell, S. P. Competition Between Surface Screening and Size Quantization for Surface Plasmons in Nanoparticles. *New J. Phys.* **2013**, *15*, 083044.

Appendix H

Electron Paramagnetic Resonance Measurements

H.1 CW EPR

CW EPR spectra were collected using a Bruker E580 X-band spectrometer with a Bruker SHQE resonator operating at 9.8 GHz.

H.2 Pulsed EPR

pEPR experiments (4.5 K) were performed on a Bruker E580 X-band spectrometer with an ER 4118 X-MD5 resonator operating at a microwave frequency of 9.7 GHz. The sample and probe were mounted inside an Oxford Instruments CF935O dynamic continuous flow cryostat. The temperature was controlled and monitored with an Oxford Instruments ITC5035 temperature controller and a Cernox Resistor CX-1050-AA-1.4L temperature sensor (LakeShore). T_1 was measured using an echo detected inversion recovery pulse sequence ($\pi - T - \pi/2 - \tau - \pi/2 - \tau$–echo). T_2 was measured using a standard 2-pulse Hahn echo sequence ($\pi/2 - \tau - \pi - \tau$–echo). A stimulated echo sequence ($\pi/2 - \tau - \pi/2 - T - \pi/2 - \tau$–echo) was used to obtain well-resolved frequencies in the ESEEM experiments. The length of the $\pi/2$ (π) pulse for all experiments was 16 ns (32 ns).

Appendix I

Supplementary Material for

Chapter 7: Acceleration of Mn^{2+} Spin Relaxation by Excess Charge Carriers in Colloidal *n*-type $Zn_{1-x}Mn_xO$ Nanocrystals

Adapted from: Schimpf, A. M.; Rinehart, J. D. Ochsenbein, S. T.; Gamelin, D. R. *In preparation.*

I.1. Kinetic model of the acceleration of Mn^{2+} spin-lattice relaxation by excess electrons.

The dependence of T_1 on the number of conduction-band electrons, n_e, was modeled using equation S1. Here, $T_1^{Mn} = T_1^{as\text{-}prepared}$ and $T_1^{electron} = 0.1$ ms was measured independently (I.2).

$$T_1^{observed} = \frac{1}{1/T_1^{Mn} + n_e / T_1^{electron}} \quad \text{(I.1)}$$

Figure I.1 presents $T_1^{observed}$ (circles) compared to T_1^{calc} (crosses) calculated with equation I.1. The calculations qualitatively reproduce the observed trend, and are close to the actual values for $Zn_{0.996}Mn_{0.004}O$ nanocrystals.

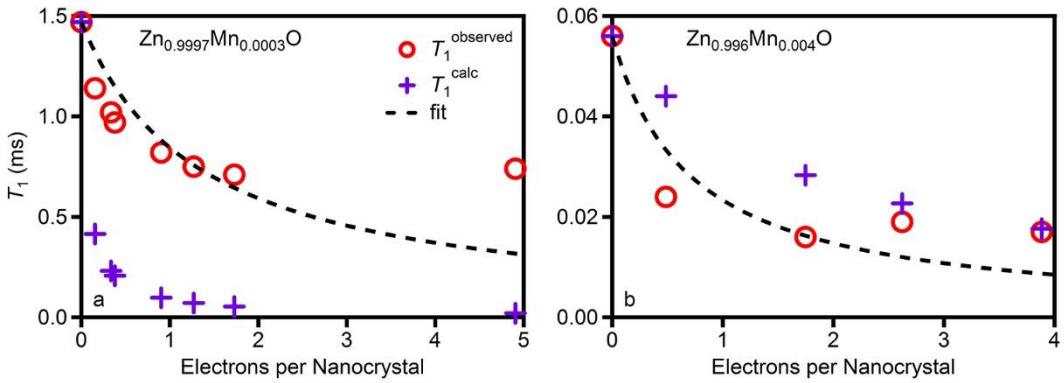

Figure I.1. Kinetic model of the acceleration of Mn^{2+} spin-lattice relaxation by excess electrons. Observed (circles) and calculated (crosses) dependence of T_1 on the number of conduction-band electrons for (a) d = 3.7 nm $Zn_{0.9997}Mn_{0.0003}O$ and (b) d = 3.5 nm $Zn_{0.996}Mn_{0.004}O$ nanocrystals. The solid line is a fit to the experimental data allowing $T_1^{electron}$ to float.

Equation I.1 was also used to fit the experimental data, allowing $T_1^{electron}$ to float (dashed line). The results of the fitting are presented in Table I.1. The best fit produced $T_1^{electron}$ that was ~18 times longer than the measured $T_1^{electron}$ for $Zn_{0.9997}Mn_{0.0003}O$ and 0.35 times shorter for $Zn_{0.996}Mn_{0.004}O$. The small decrease factor of 0.35 could be due to differences in size or sample homogeneity. It is unlikely, however, that such differences could account for an increase of 18 times. The T_1^{calc} suggest that this effect should actually be much more efficient at decreasing T_1.

Table I.1. $T_1^{electron}$ obtained by fitting the experimental data in Figure I.1 to equation I.1.

	$T_1^{electron}$ (fit)	$T_1^{electron}$ (measured)/ $T_1^{electron}$ (fit)
$Zn_{0.9997}Mn_{0.0003}O$	2.0 ± 0.5 ms	17.7
$Zn_{0.996}Mn_{0.004}O$	40 ± 13 μs	0.35

I.2. Measurement of electron spin-lattice relaxation in colloidal ZnO nanocrystals

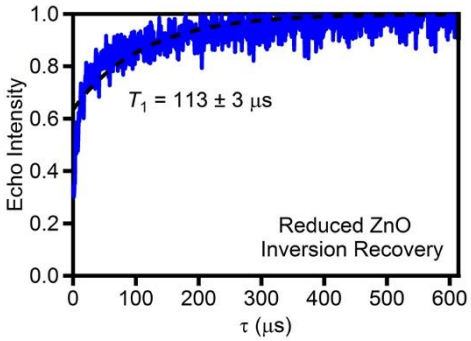

Figure I.2. Measurement of electron spin-lattice relaxation in colloidal ZnO nanocrystals. 4.5 K inversion recovery measured on photochemically reduced *d* = 6.9 nm ZnO nanocrystals.

Appendix J

Supplementary Material for

Chapter 8: Surface Contributions to Mn^{2+} Spin Dynamics in Colloidal Doped Quantum Dots

Adapted from: Schimpf, A. M.; Ochsenbein, S. T.; Gamelin, D. R. *In preparation.*

J.1 Fitting analysis to obtain T_1 and T_2

Figure J.1 shows inversion recovery data for $Zn_{0.995}Mn_{0.005}O$ QDs in toluene (tol, a) or deuterated toluene (tol-d_8, b), and for $Zn_{0.900}Mn_{0.010}O$ QDs washed with ethanol (EtOH, c) or deuterated ethanol (EtOD, d). The data were fit to both single (equation J.1a, dashed blue) and double (equation J.1b, dotted orange) exponentials[1] to obtain T_1. From the double exponential fits, an effective spin-lattice relaxation time was calculated ($T_{1\text{eff}}$) using equation J.1c. The results of this analysis are presented in Table J.1. The $T_{1\text{eff}}$ values determined from this analysis are reported in Chapter 8 as T_1 values.

$$V(\tau) = 1 - V_0 \exp(-\tau / T_1) \tag{J.1a}$$

$$V(\tau) = 1 - A\exp(-\tau / T_{1A}) - B\exp(-\tau / T_{1B}) \tag{J.1b}$$

$$T_{1\text{eff}} = \frac{A}{A+B}T_{1A} + \frac{B}{A+B}T_{1B} \tag{J.1c}$$

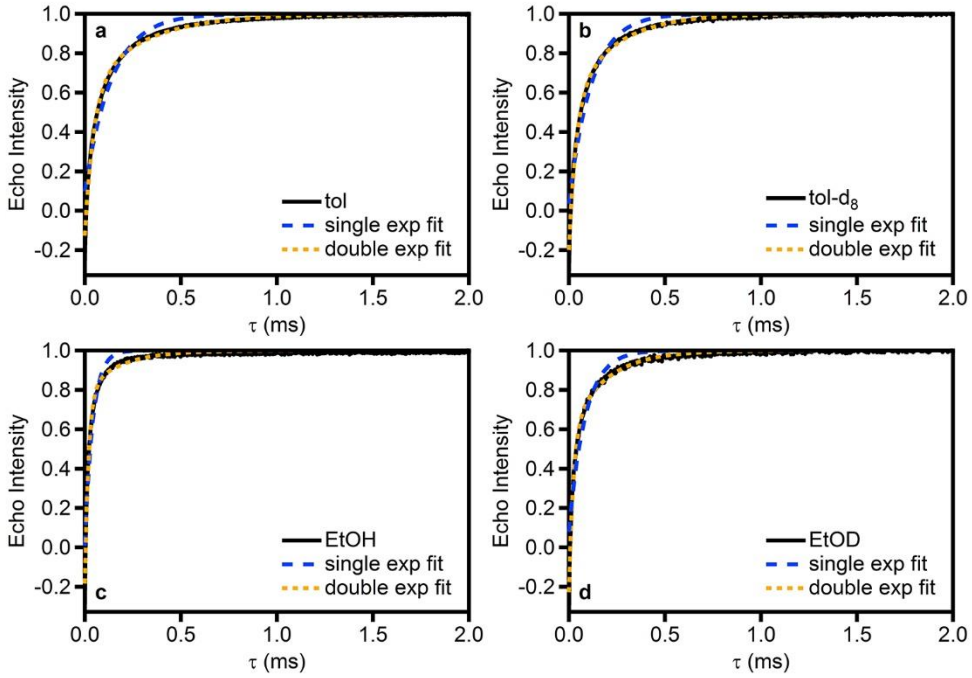

Figure J.1. Spin-lattice relaxation measurements in $Zn_{1-x}Mn_xO$ QDs. Inversion recovery data (solid black) with single (dashed blue) and double (dotted orange) exponential fits following equations J.1a and J.1b, respectively. Data are shown for $Zn_{0.995}Mn_{0.005}O$ QDs in tol (a) or tol-d_8 (b) and for $Zn_{0.900}Mn_{0.010}O$ QDs washed with EtOH (c) or EtOD (d).

Table J.1. Spin-lattice relaxation times in $Zn_{0.995}Mn_{0.005}O$ (tol versus tol-d_8) and $Zn_{0.990}Mn_{0.010}O$ (EtOH versus EtOD) QDs.

	Single Exponential Fits	Double Exponential Fits				
	T_1 (μs)	T_{1A} (μs)	A	T_{1B} (μs)	B	T_{1eff} (μs)
In tol	139 ± 2	298 ± 3	0.342 ± 0.004	46.6 ± 0.6	0.658 ± 0.005	151 ± 2
In tol-d_8	117 ± 1	230 ± 2	0.374 ± 0.005	37.4 ± 0.5	0.625 ± 0.005	109 ± 1
With EtOH	41 ± 1	179 ± 5	0.177 ± 0.005	19.7 ± 0.3	0.823 ± 0.007	48 ± 1
With EtOD	84 ± 1	184 ± 2	0.338 ± 0.004	22.4 ± 0.4	0.662 ± 0.006	80 ± 1

Figure J.2 shows 2-pulse ESEEM data for $Zn_{0.995}Mn_{0.005}O$ QDs in toluene (tol, a) or deuterated toluene (tol-d_8, b), and for $Zn_{0.900}Mn_{0.010}O$ QDs washed with ethanol (EtOH, c) or deuterated ethanol (EtOD, d). The data were fit to both single (equation J.2a, dashed blue) and double (equation J.2b, dotted orange) exponentials[1] to obtain T_2. From the double exponential fits, effective spin-lattice relaxation times were calculated ($T_{2\text{eff}}$) using equation J.2c. The results of this analysis are presented in Table J.2. For EtOD, a double exponential fit does not converge when $T_{1\text{A}} \neq T_{1\text{B}}$, so a single exponential fit was used. In Chapter 8, $T_{2\text{eff}}$ from this analysis is reported for comparison between tol and tol-d_8, and T_2 from this analysis is reported for comparison between EtOH and EtOD.

$$V(\tau) = V_0 \exp(-2\tau / T_2) \tag{J.2a}$$

$$V(\tau) = A\exp(-2\tau / T_{2\text{A}}) + B\exp(-2\tau / T_{2\text{B}}) \tag{J.2b}$$

$$T_{2\text{eff}} = \frac{A}{A+B} T_{2\text{A}} + \frac{B}{A+B} T_{2\text{B}} \tag{J.2c}$$

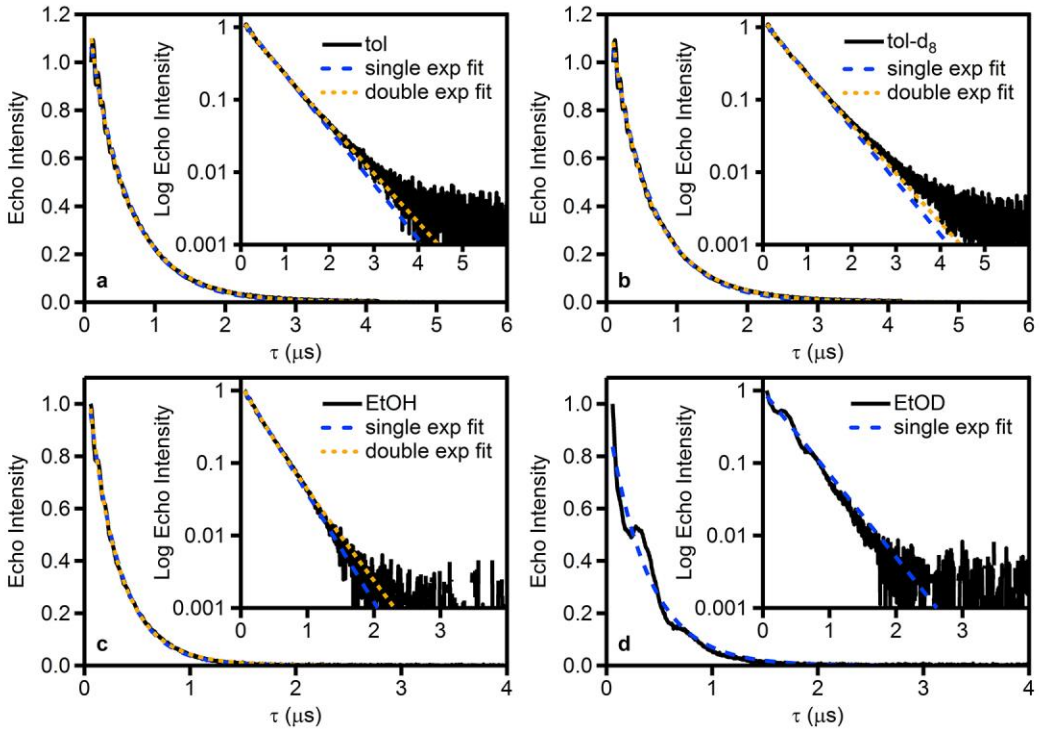

Figure J.2. Spin-spin relaxation measurements in $Zn_{1-x}Mn_xO$ QDs. Hahn echo decay data (solid black) with single (dashed blue) and double (dotted orange) exponential fits following equations J.2a and J.2b, respectively. Decays are shown for $Zn_{0.995}Mn_{0.005}O$ QDs in tol (a) or tol-d_8 (b) and for $Zn_{0.900}Mn_{0.010}O$ QDs washed with EtOH (c) or EtOD (d).

Table J.2. Spin-lattice relaxation times in $Zn_{0.995}Mn_{0.005}O$ (tol versus tol-d_8) and $Zn_{0.990}Mn_{0.010}O$ (EtOH versus EtOD) QDs.

	Single Exponential Fits	Double Exponential Fits				
	T_2 (μs)	T_{2A} (μs)	A	T_{2B} (μs)	B	T_{2eff} (μs)
In tol	1.150 ± 0.002	1.28 ± 0.01	0.77 ± 0.01	0.49 ± 0.02	0.23 ± 0.01	1.10 ± 0.02
In tol-d_8	1.176 ± 0.002	1.36 ± 0.01	0.70 ± 0.02	0.60 ± 0.03	0.30 ± 0.02	1.13 ± 0.03
With EtOH	0.581 ± 0.001	0.73 ± 0.03	0.47 ± 0.02	0.43 ± 0.02	0.53 ± 0.02	0.57 ± 0.03
With EtOD	0.76 ± 0.01					

Figure J.3 shows inversion recovery (a) and 2-pulse ESEEM data (b) collected on $Cd_{0.996}Mn_{0.004}Se$ QDs before (blue) and after (red) CdSe shell growth. To obtain T_1 and T_2 the inversion recovery and 2-pulse ESEEM spectra were fit to equations J.1a and J.2a, respectively.

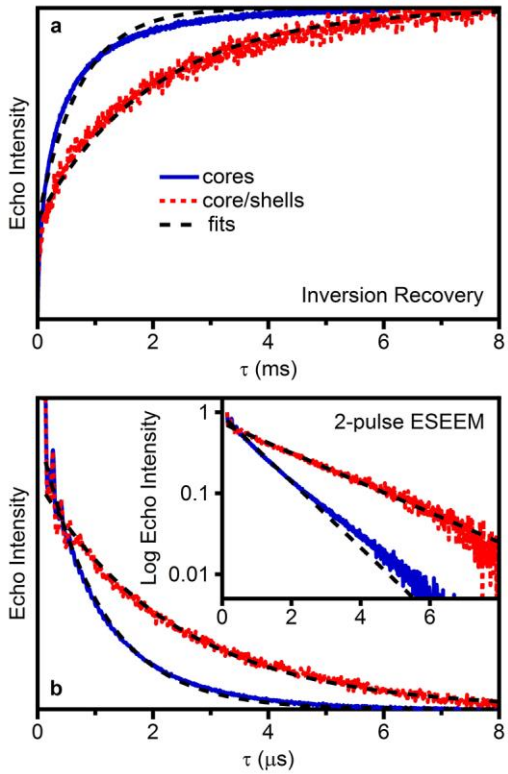

Figure J.3. Measurement of Mn^{2+} spin dynamics in $Cd_{1-x}Mn_xSe$ core and $Cd_{1-x}Mn_xSe/CdSe$ core/shell QDs. pEPR data collected on $Cd_{0.996}Mn_{0.004}Se$ QDs before (blue) and after (red) CdSe shell growth. (a) Echo-detected inversion recovery (T_1) and (b) 2-pulse spin-echo decay (T_2). The dashed black lines are single exponential fits to the inversion recovery and 2-pulse ESEEM data following equations J.1a and J.2a, respectively.

J.2 References

1. Schweiger, A.; Jeschke, G. *Principles of Pulse Electron Paramagnetic Resonance*; Oxford University Press: United Kingdom, 2001.